

Aus der Klinik und Poliklinik für Neurologie
Direktor: Herr Prof. Dr. Heinz Reichmann

Modeling of *FUS*- and *C9ORF72*-associated cortical neuropathology using patient-specific induced pluripotent stem cells

Dissertationsschrift

zur Erlangung des akademischen Grades
Doktor der Biomedizin
Doctor rerum medicinalium (Dr. rer. medic.)
vorgelegt
der Medizinischen Fakultät Carl Gustav Carus
der Technischen Universität Dresden

von

Master of Science
Julia Japtok

geboren am 30.05.1989
in Stollberg/Erzg.

Dresden, 2019

Gutachter

1. Gutachter: Prof. Dr. Dr. Andreas Hermann
2. Gutachter: Prof. Dr. Marius Ader

Tag der mündlichen Prüfung: 12.06.2020

gez.: -----

Vorsitzender der Promotionskommission

Table of contents

1	Introduction	10
1.1	Characteristics of Amyotrophic lateral sclerosis (ALS).....	10
1.2	ALS-associated genes <i>FUS</i> and <i>C9ORF72</i>	12
1.2.1	Fused in sarcoma (<i>FUS</i>)	12
1.2.2	Chromosome 9 open reading frame 72 (<i>C9ORF72</i>).....	14
1.3	Putative disease mechanisms in ALS.....	16
1.3.1	Protein aggregation.....	16
1.3.1.1	FUS.....	17
1.3.1.2	C9ORF72.....	18
1.3.2	DNA damage	20
1.3.2.1	FUS.....	20
1.3.2.2	C9ORF72.....	21
1.3.3	Organelle trafficking	21
1.4	ALS disease modeling.....	22
1.4.1	Animal models	22
1.4.2	Patient-specific models	23
1.4.3	CRISPR/Cas9 gene editing.....	25
1.5	Objective of the thesis.....	27
2	Materials and methods	28
2.1	Materials	28
2.1.1	Instruments	28
2.1.2	Chemicals and reagents.....	29
2.1.3	Commercial available kits.....	30
2.1.4	Enzymes	30
2.1.5	Antibodies	31
2.1.6	Primer	32
2.1.7	Plasmids	32
2.1.8	Cell culture media, supplements, and consumables.....	33

2.1.9	Software.....	35
2.1.10	Cell lines.....	35
2.2	Molecular biology	37
2.2.1	Plasmid design and generation for CRISPR/Cas9n-mediated gene editing of <i>FUS</i>	37
2.2.1.1	Design of sgRNA sequences.....	37
2.2.1.2	Screening for CRISPR/Cas9n-related Off-targets.....	38
2.2.1.3	Cloning of DNA oligos into the pX335B plasmid	39
2.2.1.4	Design & Generation of <i>FUS</i> correction plasmids.....	40
2.2.2	Plasmid preparation	42
2.2.2.1	Transformation	42
2.2.2.2	Mini-culture and plasmid preparation.....	43
2.2.3	Isolation of genomic DNA.....	43
2.2.4	Polymerase chain reaction (PCR).....	43
2.2.4.1	Colony PCR	43
2.2.4.2	Screening PCR for <i>FUS</i> -EGFP.....	44
2.2.4.3	Genotyping PCR of <i>FUS</i> -EGFP positive clones.....	45
2.2.5	Sequencing.....	46
2.2.5.1	Sequencing of <i>FUS</i> -EGFP positive iPSC clones	46
2.2.6	Agarose gel electrophoresis.....	46
2.2.7	Gel extraction of PCR fragments.....	46
2.3	Cell culture.....	47
2.3.1	Cell culture media	47
2.3.2	Coatings.....	48
2.3.2.1	Matrigel™ coating.....	48
2.3.2.2	Poly-L-ornithine/ Laminin coating	49
2.3.3	Cell count.....	49
2.3.4	Cultivation of human induced pluripotent stem cells	50
2.3.4.1	Expansion and maintenance of human iPSCs.....	50

2.3.4.2	Freezing and thawing of iPSCs	50
2.3.5	CRISPR/Cas9n-mediated gene editing of iPSCs	51
2.3.5.1	Transfection of feeder-free iPSCs.....	51
2.3.5.2	Single colony selection	51
2.3.6	Differentiation of human iPSCs into three germ layer	52
2.3.7	Differentiation of human iPSCs into spinal and cortical neural cell types	53
2.3.7.1	Expansion of human small molecule neuronal precursor cells.....	53
2.3.7.2	Differentiation of human smNPCs into spinal motor neurons	53
2.3.7.3	Differentiation of human iPSCs into cortical neurons and astrocytes	54
2.3.7.4	Splitting of NPCs, spinal MNs, and cortical cells using accutase	55
2.4	Microscopy.....	56
2.4.1	Immunofluorescence staining.....	56
2.4.2	Fluorescence microscopy.....	57
2.4.3	Live cell imaging	57
2.5	Investigation of patient-specific <i>in vitro</i> cultures.....	57
2.5.1	DNA damage analysis.....	57
2.5.1.1	Analysis of γ H2AX and 53BP1	58
2.5.1.2	DNA damage laser cut assay	59
2.5.2	Axonal organelle trafficking analysis	59
2.5.3	FUS-EGFP localization	61
2.5.4	Evaluation of <i>C9ORF72</i> -associated DPRs	62
2.6	Quantifications and Statistics	64
3	Results.....	65
3.1	Cortical differentiation of patient-specific iPSCs	65
3.2	CRISPR/Cas9n-mediated gene editing of <i>FUS</i>	69
3.2.1	Generation of isogenic WT and P525L FUS-EGFP iPSC lines.....	69
3.2.2	Characterization of isogenic WT and P525L FUS-EGFP iPSC lines	71
3.2.2.1	Screening and Genotyping of isogenic FUS-EGFP iPSCs.....	71
3.2.2.2	Pluripotency of isogenic FUS-EGFP iPSCs.....	73

3.2.2.3	Off-targets	74
3.3	Analysis disease-associated proteins	76
3.3.1	FUS-EGFP localization in cortical neurons and astrocytes	76
3.3.2	Characterization of <i>C9ORF72</i> -associated DPRs	77
3.3.2.1	ELISA for Poly-GP	78
3.3.2.2	Immunofluorescence staining for Poly-GP	79
3.3.2.3	Immunofluorescence staining for Poly-GA	83
3.3.2.4	Immunofluorescence staining for Poly-GR	86
3.3.3	DPRs versus DNA damage	86
3.3.4	TDP43 neuropathology in <i>C9ORF72-HRE</i> cortical cultures	88
3.4	Analysis of DNA damage in patient-specific <i>in vitro</i> models of ALS	91
3.4.1	Analysis of DNA damage marker γ H2AX and 53BP1	91
3.4.1.1	Evaluation of DSB markers in cells with <i>C9ORF72-HRE</i> mutation	91
3.4.1.2	Evaluation of DSB marker in cells with <i>FUS-NLS</i> mutation	100
3.4.1.3	Effect of etoposide on cell survival	103
3.4.2	Analysis of laser-induced DNA damage	104
3.5	Axonal organelle trafficking analysis within patient-specific cortical neurons	105
3.5.1	Directed axonal outgrowth of cortical neurons	106
3.5.2	Motility of mitochondria and lysosomes	107
4	Discussion	110
4.1	Control and mutant iPSCs differentiate into cortical neurons and astrocytes	111
4.2	Isogenic iPSC lines allow the analysis of mutation-dependent effects independent of patient's genetic background	111
4.3	Disease-associated proteins	112
4.3.1	Cytoplasmic mislocalization of mutant FUS depends on cell type	112
4.3.2	<i>C9ORF72</i> -associated DPR pathology can only be recapitulated partially within iPSC-derived cortical neurons	113
4.3.3	DPR accumulation and DNA damage do not correlate in iPSC-derived cortical neurons	116

4.3.4	ALS-associated TDP43 pathology can be recapitulated partially within iPSC-derived cortical neurons	116
4.4	Characterization of DNA damage	117
4.4.1	<i>C9ORF72-HRE</i> and <i>FUS-NLS</i> mutations do not affect DSB levels in unstressed cortical neurons and astrocytes	117
4.4.2	<i>C9ORF72-HRE</i> and <i>FUS-NLS</i> mutations do not affect DDR signaling and DSB repair upon DNA damage induction	120
4.4.3	Recruitment of FUS-EGFP to laser-induced DNA damage sites depends on cell- and genotype	121
4.5	<i>FUS-NLS</i> mutations affect axonal organelle trafficking differently as in spinal MNs 122	
4.6	Conclusion	124
5	Summary	127
6	Zusammenfassung	128
7	References	130
8	List of Figures	145
9	List of Tables	147
10	Acknowledgments	149
11	Appendix	150
11.1	Supplementary Movies	150
11.2	Supplementary Tables	151
11.3	Declarations	162
11.3.1	Erklärungen zur Eröffnung des Promotionsverfahrens	162
11.3.2	Erklärung über Einhaltung gesetzlicher Vorgaben	163

Abbreviations

AA	<i>Ascorbic acid</i>
ALS	<i>Amyotrophic lateral sclerosis</i>
C9ORF72	<i>Chromosome 9 open reading frame 72</i>
Cas9	<i>CRISPR-associated system 9</i>
Cas9n	<i>Cas9 nickase</i>
CHIR	<i>CHIR99021</i>
conc.	<i>concentration</i>
CRISPR	<i>Clustered Regularly Interspaced Short Palindromic Repeat</i>
DDR	<i>DNA damage repair</i>
DDS	<i>DNA damage sites</i>
DNA	<i>Deoxyribonucleic acid</i>
DPR	<i>Dipeptide repeat</i>
DSB	<i>Double strand break</i>
EB	<i>Embryoid body</i>
EGFP	<i>Enhanced Green Fluorescent Protein</i>
ELISA	<i>enzyme linked immunosorbent assay</i>
Eto	<i>Etoposide</i>
EWS	<i>Ewing's sarcoma</i>
fALS	<i>Familial ALS</i>
FDA	<i>Food and Drug Administration</i>
FTD	<i>Frontotemporal dementia</i>
FTLD	<i>Frontotemporal lobar degeneration</i>
FUS	<i>Fused in sarcoma</i>
gDNA	<i>genomic DNA</i>
GFAP	<i>Glial fibrillary acid protein</i>
HDR	<i>Homology directed repair</i>
h-iPSCs	<i>human induced Pluripotent Stem Cell</i>
homologous recombination	<i>Homologous recombination</i>
HRE	<i>Hexanucleotide repeat expansion</i>
iPSCs	<i>induced pluripotent stem cells</i>
LMN	<i>Lower motor neuron</i>
MAP2	<i>Microtubule-associated protein 2</i>
min	<i>minutes</i>
MNs	<i>motor neurons</i>

NDM	<i>neural differentiation medium</i>
NHEJ	<i>Non-homologous end joining</i>
NLS	<i>Nuclear localization signal</i>
NPCs	<i>neural progenitor cells</i>
PCR	<i>Polymerase chain reaction</i>
PFA	<i>Paraformaldehyde</i>
PMA	<i>Purmorphamine</i>
PY-NLS	<i>proline-tyrosine NLS</i>
RA	<i>Retinoic acid</i>
RAN	<i>Repeat-associated non-ATG dependent</i>
RNA	<i>Ribonucleic acid</i>
ROCKi	<i>ROCK inhibitor, Siehe</i>
rpm	<i>rounds per minute</i>
RRM	<i>RNA-recognition motif</i>
RT	<i>Room Temperature</i>
sALS	<i>Sporadic ALS</i>
sgRNA	<i>single guide RNA</i>
SGs	<i>Stress granules</i>
SOD1	<i>Superoxide dismutase 1</i>
SSBs	<i>Single strand breaks</i>
TAF15	<i>TATA box-binding protein (TBP)-associated factor</i>
TDP43	<i>TAR DNA-binding protein 43</i>
TLS	<i>Translocated in liposarcoma</i>
UMN	<i>Upper motor neuron</i>
WT	<i>wild type, Wild type</i>
yH2AX	<i>phosphorylated H2A.X</i>
ZnF	<i>zinc finger</i>

1 Introduction

1.1 Characteristics of Amyotrophic lateral sclerosis (ALS)

Amyotrophic lateral sclerosis (ALS) belongs to the spectrum of neurodegenerative diseases, which also include Alzheimer's, Parkinson's, Huntington's disease, and Frontotemporal dementia (FTD). Most neurodegenerative diseases are age-dependent disorders affecting the nervous system. They are incurable diseases that are becoming more prevalent as the elderly population has increased in recent years (Heemels 2016). The underlying pathophysiology is diverse with some disorders causing primarily memory and cognitive impairment as seen in Alzheimer's and FTD, while others affect mainly the motor system (movement, speech, and breathing) as in ALS (Abeliovich and Gitler 2016, Canter, Penney et al. 2016, Taylor, Brown et al. 2016, Wyss-Coray 2016).

In ALS, neurodegeneration specifically affects upper (corticospinal) and lower (spinal) motor neurons (Van Langenhove, van der Zee et al. 2012, Vance, Scotter et al. 2013). The selective death of motor neurons (MNs) results in a progressive muscular weakness and palsy. The clinical symptoms of ALS consist of a characteristic combination of signs of upper motor neuron (UMN) degeneration, which includes muscular spasticity and hyperreflexia, together with signs of lower motor neuron (LMN) degeneration, which comprises muscular atrophy and fasciculation (Van Langenhove, van der Zee et al. 2012). ALS patients differ significantly in presentation of clinical symptoms including site of onset, rate of progression, presence of cognitive dysfunction, and comorbidity with frontotemporal lobar degeneration (FTLD) (Lomen-Hoerth 2011).

ALS occurs with an incidence of 1 to 2 cases per 100,000/year and a prevalence of 3 to 8 per 100,000 (Worms 2001, Van Damme, Robberecht et al. 2017). Symptoms most commonly develop in the age between 55 and 75. Death, usually through respiratory failure, occurs on average 2 to 5 years after symptom onset (Van Damme, Robberecht et al. 2017). At present, ALS remains an incurable disease. Riluzole is one of two FDA-approved drugs to treat patients suffering ALS. It can increase lifetime for 3 to 6 months but cannot entail any cure of disease (Bensimon, Lacomblez et al. 1994, Gurney, Cutting et al. 1996). Edaravone (trading name: Radicava®) was approved by FDA for treating ALS only in 2017. However, clinical trials only showed an effect on subgroups of ALS patients and further studies need to be conducted to clarify the benefits of edaravone on ALS disease progression (Abe, Itoyama et al. 2014, Writing and Edaravone 2017).

ALS neuropathology is characterized by axon retraction, the loss of cell bodies of upper and lower MNs and the occurrence of astro- and microgliosis (Saber, Stauffer et al. 2015).

Reactive astrocytes were shown to surround degenerating neurons (McGeer and McGeer 2002); (Boillee, Yamanaka et al. 2006); (Yamanaka, Chun et al. 2008). Microglia become activated as response to neuronal distress and lead to higher degree of inflammation. The effects of neuroinflammation in disease progression are still under debate, as it was shown to protect neurodegeneration but also to drive it (Boillee, Vande Velde et al. 2006); (McGeer and McGeer 2002); (Boillee, Yamanaka et al. 2006). Another neuropathological hallmark in sporadic and familial ALS patient's tissue are ubiquitin-positive cytoplasmic inclusion (Saber, Stauffer et al. 2015). They are observed most commonly in neurons but occasionally also occur in glial cells. Ubiquitin-positive inclusion in ALS are negative for proteins commonly associated with neurodegenerative disease such as TAU or α -SYNUCLEIN. In 95% of patients, TDP43 is the main component of such inclusions (Arai, Hasegawa et al. 2006); (Neumann, Sampathu et al. 2006). In addition to pathological cytoplasmic redistribution of the protein, a loss of nuclear TDP43 can be observed (Giordana, Piccinini et al. 2010). Even though most neuropathological hallmark characteristics can be associated with sporadic and familial ALS, a number of genetic causes exist that demonstrate distinctive molecular and neuropathological features.

About 90% are sporadic cases (sALS) with largely unknown genetic etiology and 10% are familial cases (fALS) (Rowland and Shneider 2001, Pasinelli and Brown 2006, Debray, Race et al. 2013, Al-Chalabi, van den Berg et al. 2017). It is of great interest to investigate monogenetic forms causing fALS to understand its underlying disease pathologies and mechanisms to be able to develop new treatments (Dion, Daoud et al. 2009, Bento-Abreu, Van Damme et al. 2010). Disease causing gene mutation are typically inherited in an autosomal dominant manner and over 20 genes have been linked to ALS until now (Bento-Abreu, Van Damme et al. 2010, Al-Chalabi, Jones et al. 2012, Al-Chalabi, van den Berg et al. 2017). In 1993, Superoxide dismutase 1 (*SOD1*) was the first gene to be identified to cause ALS (Rosen 1993). ALS-causing mutations were also found in *TARDBP* coding for TAR DNA-binding protein 43 (TDP43) (Kabashi, Valdmanis et al. 2008, Sreedharan, Blair et al. 2008, Van Deerlin, Leverenz et al. 2008) and shortly after in the gene Fused in sarcoma (*FUS*) (Kwiatkowski, Bosco et al. 2009, Vance, Rogelj et al. 2009). Only some years later, chromosome 9 open reading frame 72 (*C9ORF72*) was found to be the most common disease-causing gene (Renton, Majounie et al. 2011).

1.2 ALS-associated genes *FUS* and *C9ORF72*

1.2.1 Fused in sarcoma (*FUS*)

FUS, also known as Translocated in liposarcoma (*TLS*), was initially identified as a fusion oncogene in human myxoid liposarcomas (Croizat, Aman et al. 1993). *FUS* is located on chromosome 16, consists of 16 exons, and codes for a 526 amino acid long protein (Lagier-Tourenne, Polymenidou et al. 2010, Dormann and Haass 2011, Dormann and Haass 2013). The protein structure of *FUS* contains an N-terminal serine, tyrosine, glycine and glutamine-rich domain (transcriptional activation domain), followed by an RNA-recognition motif (RRM) and a zinc finger domain (ZnF) (Figure 1.1). Interspaced between those domains are three RRG-repeat regions. Moreover, *FUS* contains a C-terminal non-classical nuclear localization signal (NLS) which consists of a proline-tyrosine NLS (PY-NLS) and the RGG3 domain (Lee, Cansizoglu et al. 2006, Dormann, Rodde et al. 2010, Dormann, Madl et al. 2012).

FUS belongs to the FET (*FUS*, *EWS* and *TAF15*) family of proteins, which also includes Ewing's sarcoma (*EWS*) and TATA box-binding protein (TBP)-associated factor (*TAF15*) (Powers, Mathur et al. 1998, Andersson, Stahlberg et al. 2008). FET proteins are RNA-binding and structurally similar multifunctional proteins. *FUS* is a ubiquitously expressed protein that predominantly localizes to the nucleus but is able to shuttle between nucleus and cytoplasm (Zinszner, Sok et al. 1997). It was found to be a DNA-/RNA-binding protein which is involved in the regulation of gene expression, RNA metabolism, and DNA processing (Zinszner, Sok et al. 1997, Powers, Mathur et al. 1998, Lagier-Tourenne, Polymenidou et al. 2012, Ling, Polymenidou et al. 2013). Moreover, *FUS* regulates its own gene expression by alternative splicing and nonsense-mediated decay (Zhou, Liu et al. 2013). Even though *FUS* is known to play a role in various cellular processes, its precise function is still poorly understood.

About 4% of fALS cases are caused by dominant mutations within *FUS* (Kwiatkowski, Bosco et al. 2009, Vance, Rogelj et al. 2009, Kaneb, Dion et al. 2012) representing the third most common fALS form in Germany. Figure 1.1 shows that the C-terminus of *FUS* is a hotspot for disease-causing mutations (Zhang and Chook 2012). Two-thirds of known *FUS* mutations cluster within exon 12 to 15, which encode for ZnF-motif, RGG2+3 domain, and PY-NLS (Deng, Gao et al. 2014). One-third of mutations cluster within exon 3 to 6, encoding for SYGQ- and RGG1-domains. *R521C* and *R521H* are the most common ALS-causing *FUS*-NLS mutations and lead to a typical late disease onset (Kwiatkowski, Bosco et al. 2009). In contrast, *FUS-P525L* mutation is associated with an early onset (in the 20s or even earlier) and rapid disease progression (Dormann, Rodde et al. 2010, Conte, Lattante et al. 2012). Thus, disease onset and course of disease highly depend on the severity of the underlying *FUS* mutation.

Neuropathological features in *FUS*-associated ALS include the loss of MN. It was found, that MN loss in *FUS*-ALS patients is most severe in the spinal cord, while within brainstem MN loss occurs to a lesser degree, and loss of UMN within the motor cortex occurs at moderate to mild levels only (Deng, Gao et al. 2014). Hallmark neuropathology of *FUS*-ALS is a cytoplasmic mislocalization of mutant *FUS*, followed by formation of cytoplasmic inclusions (Vance, Rogelj et al. 2009, Bosco, Lemay et al. 2010, Dormann, Rodde et al. 2010, Gal, Zhang et al. 2011, Kino, Washizu et al. 2011, Niu, Zhang et al. 2012, Zhang and Chook 2012, Vance, Scotter et al. 2013, Wang, Pan et al. 2013, Deng, Gao et al. 2014). *FUS* positive inclusions can be found within the nucleus as well, however to a much lesser extent than cytoplasmic ones (Vance, Rogelj et al. 2009, Verbeeck, Deng et al. 2012). Moreover, the severity of the underlying *FUS* mutation was found to affect *FUS* inclusion formation. *FUS-R521C* mutation, causing a rather slow disease progression, is associated with a more widespread *FUS* pathology, including glial and neuronal cells (Blair, Williams et al. 2010, Hewitt, Kirby et al. 2010, Rademakers, Stewart et al. 2010, Suzuki, Aoki et al. 2010). In general, *FUS* positive inclusion were distributed more widely in neurons and glia from patient with longer disease progression than observed in fast progressing cases (Suzuki, Kato et al. 2012, Deng, Gao et al. 2014). Severity of *FUS* mutation also affects the type of aggregates, e.g. if rather round inclusions are formed, as associated with *FUS-P525L*, or if more tangle-like inclusion can be found as observed in *FUS-R521C* carriers (Mackenzie, Ansorge et al. 2011). *FUS*-associated neuropathology in ALS needs further characterization, given the variability of *FUS* pathology in patients with different mutations (and even among individuals with the same mutation)(Huang, Zhang et al. 2010, Mackenzie, Rademakers et al. 2010, Deng, Gao et al. 2014).

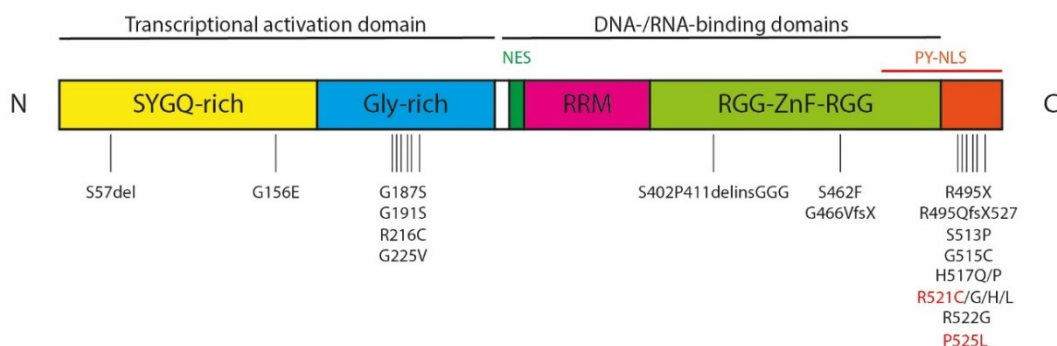


Figure 1.1 FUS domain structure.

The illustration shows human *FUS* protein domain structure and ALS-associated mutations. Red marked mutations are object of this study. The illustration was adopted by Dormann & Haas 2011 and modified by the author of this study.

1.2.2 Chromosome 9 open reading frame 72 (*C9ORF72*)

The gene *C9ORF72*, located on chromosome 9, confers for three transcriptional variants that can be translated into two possible protein isoforms (Rohrer, Isaacs et al. 2015). *C9ORF72* contains a hexanucleotide GGGGCC (G4C2) repeat region either in the promoter region or in intron 1 of the gene, depending on the transcript variant (Figure 1.2). The normal repeat size in healthy individuals, in most cases, is in the range of 1 to 40 G4C2 repeat units (Renton, Majounie et al. 2011). Repeat lengths larger than 50 units are considered to be pathogenic. Of note, in individual cases repeat lengths of only 20 to several hundred have been linked to ALS (Buchman, Cooper-Knock et al. 2013, Dobson-Stone, Hallupp et al. 2013, Gomez-Tortosa, Gallego et al. 2013, Byrne, Heverin et al. 2014, Dols-Icardo, Garcia-Redondo et al. 2014) but also to healthy control individuals (Simon-Sanchez, Dopper et al. 2012, Beck, Poulter et al. 2013). Clear pathogenic repeats consist of several hundred to several thousand G4C2 repeat units (Renton, Majounie et al. 2011, Beck, Poulter et al. 2013, van Blitterswijk, DeJesus-Hernandez et al. 2013).

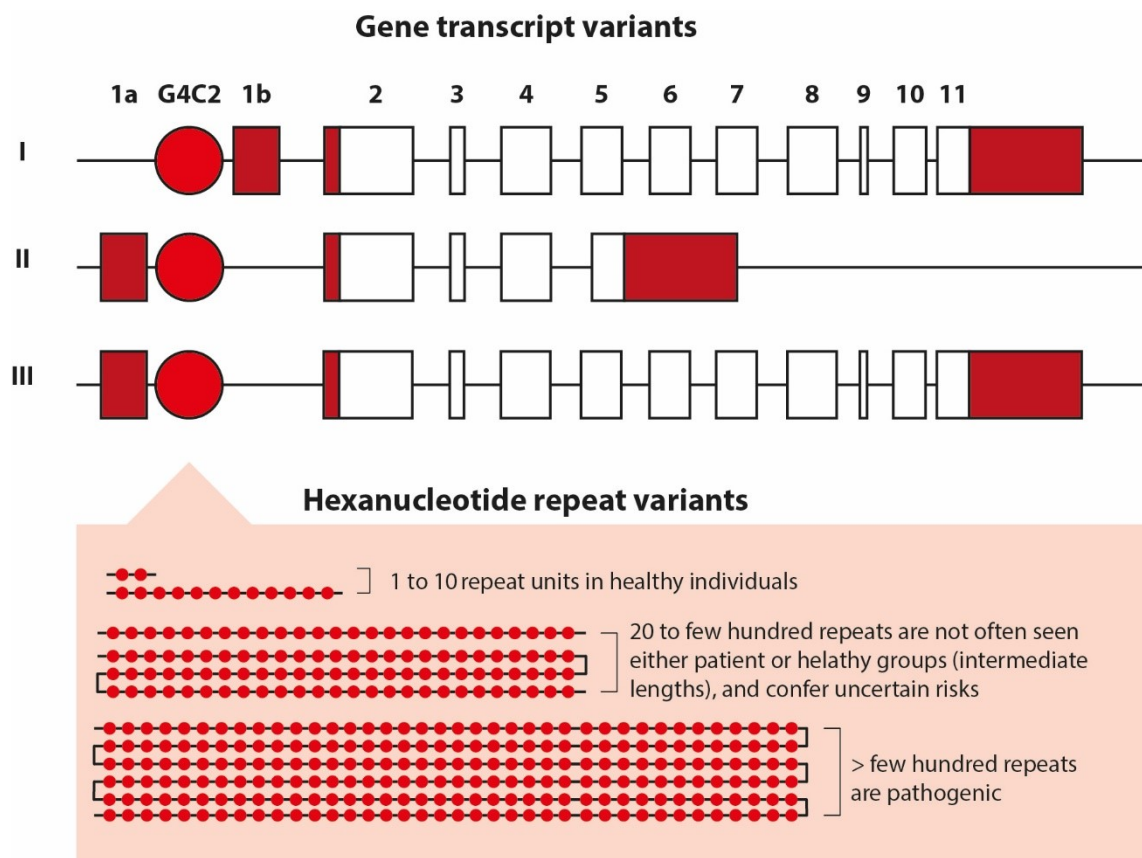


Figure 1.2 The *C9ORF72* gene and transcript variants.

The illustration shows the *C9ORF72* gene and its three possible transcription variants. Exons are depicted as boxes and the G4C2 hexanucleotide repeat region is depicted as a red circle. Possible repeat lengths are depicted below as chains of red circles with their pathogenic relation. The illustration was adopted from Rohrer et al. 2015 and modified by the author of this study.

The G4C2 hexanucleotide repeat expansion (HRE) in the *C9ORF72* gene is the most common cause for FTD and ALS (DeJesus-Hernandez, Mackenzie et al. 2011, Renton, Chio et al. 2014). *C9ORF72-HRE* mutations can cause either FTD or ALS alone, or a combination of both (Rohrer, Isaacs et al. 2015). Cognitive or behavioral impairment seem to be much more common in ALS with *C9ORF72-HRE* than in those cases caused by other mutations (Millecamps, Boillee et al. 2012, Montuschi, Iazzolino et al. 2015). Patients with *C9ORF72-HRE*, who present initial ALS-associated symptoms, are often indistinguishable from classic ALS (Rohrer, Isaacs et al. 2015). On a cellular level, *C9ORF72-HRE* carriers typically show the formation of neuronal inclusions containing TDP43, irrespective of the clinical phenotype. Unique for *C9ORF72*-associated neuropathology is the formation of ubiquitin and p62 positive neuronal inclusions that are negative for TDP43 (Ash, Bieniek et al. 2013, Mackenzie, Arzberger et al. 2013, Mori, Weng et al. 2013, Schludi, May et al. 2015). Those inclusions are typically positive for *C9ORF72*-specific dipeptide repeat (DPR) proteins.

How *C9ORF72-HRE* causes neurodegeneration is controversially discussed and loss- and gain-of-function hypotheses exist (Gendron, Bieniek et al. 2013, Gendron, Belzil et al. 2014, Rohrer, Isaacs et al. 2015, Taylor, Brown et al. 2016)(Figure 1.3). Loss of function is associated with a decreased expression of *C9ORF72* in various cell types carrying the G4C2 repeat expansion (Donnelly, Zhang et al. 2013, Sivadasan, Hornburg et al. 2016). Gain of function mechanisms are thought to be conferred by the accumulation of toxic RNA foci (DeJesus-Hernandez, Mackenzie et al. 2011, Gendron, Bieniek et al. 2013) and DPR-mediated toxicity (Mori, Arzberger et al. 2013, Mori, Weng et al. 2013, Zu, Liu et al. 2013).

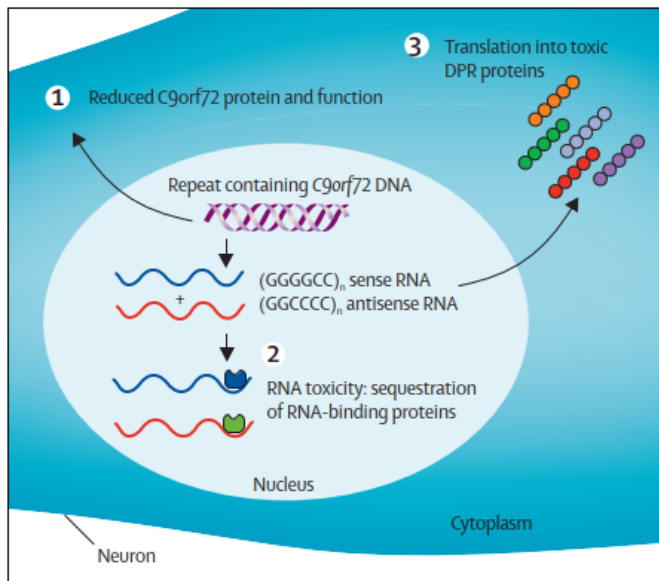


Figure 1.3 Potential mechanism of neurodegeneration due to C9ORF72 G4C2 repeat expansion.

Potential mechanisms leading to neurodegeneration in *C9ORF72-HRE*-associated ALS include: loss of function (1), toxicity conferred by accumulating RNA (2), and DPR-mediated toxicity (3). The illustration was adopted from Rohrer et al. 2015.

1.3 Putative disease mechanisms in ALS

The identification of mutant *SOD1* as an ALS-causing gene set the start point of an era of investigation of possible molecular pathomechanisms underlying ALS (Rosen 1993). Despite 26 years of research on *SOD1*, no consensus of the main toxicity conferred by mutant *SOD1* has emerged. Similar is true for ALS-associated genes *C9ORF72* and *FUS*. The precise mechanisms by which mutations in those genes cause ALS are still poorly understood. Nevertheless, various possible mechanisms have been identified (some depending on the underlying mutation, some independent of it), including protein aggregation, non-cell autonomous toxicity, axonal transport defects, prion-like spreading, and impaired RNA metabolism (Taylor, Brown et al. 2016). The following chapters will summarize putative mechanisms involved in ALS neurodegeneration with relevance to *FUS*- and *C9ORF72*-associated ALS.

1.3.1 Protein aggregation

The formation of cytoplasmic protein aggregates is a hallmark pathology of sporadic and familial ALS (Nishihira, Tan et al. 2008, Zhang, Tan et al. 2008, Blokhuis, Groen et al. 2013, Mori, Arzberger et al. 2013, Ederle and Dormann 2017). The accumulation of proteins is thought to be a key event in ALS neuropathology. Various mechanisms have been proposed how protein aggregates form and how they contribute to disease. However, if aggregation is

cause or consequence of ALS pathology is still under debate. Predominately, ubiquitinated aggregates can be found in ALS patients (Blokhuis, Groen et al. 2013), but otherwise protein aggregation seems to depend on the underlying mutation.

1.3.1.1 FUS

The formation of FUS positive cytoplasmic protein aggregates is a hallmark of *FUS*-associated ALS. Nuclear import defects that are caused by a disrupted NLS are thought to be a key event in ALS pathology (Dormann, Rodde et al. 2010, Dormann and Haass 2011, Dormann, Madl et al. 2012, Zhang and Chook 2012). As aforementioned, most *FUS* mutations cluster in the C-terminal part of the protein. Those mutations typically lead to a cytoplasmic mislocalization of FUS, which is followed by the formation of cytoplasmic FUS positive inclusions (Vance, Rogelj et al. 2009, Bosco, Lemay et al. 2010, Dormann, Rodde et al. 2010, Gal, Zhang et al. 2011, Kino, Washizu et al. 2011, Zhang and Chook 2012, Vance, Scotter et al. 2013, Wang, Pan et al. 2013). The amount of mislocalized FUS was shown to depend on the severity of the underlying mutation (Dormann, Rodde et al. 2010, Japtok, Lojewski et al. 2015, Higelin, Demestre et al. 2016). Mutant *FUS* causing an early disease onset (e.g. *FUS-P525L* and *FUS-R495X*) shows a severe cytoplasmic mislocalization, while typical late-onset mutations (*FUS-R521C/G/H*) show only mild cytoplasmic expression and remain mainly nuclear.

FUS also contains a prion-like domain within its SYGQ- and RGG2 region (King, Gitler et al. 2012). Even though, mutations within this region are associated with ALS, this domain was shown to be necessary but not sufficient to induce FUS aggregation and toxicity (Sun, Diaz et al. 2011). This means that the prion-like domain within FUS makes it prone for aggregation. Sun et al. and others hypothesize furthermore, that *FUS*-associated pathology is caused by a prion-like propagation of misfolded or aggregated FUS protein (Figure 1.4)(Polymenidou and Cleveland 2011, King, Gitler et al. 2012). Aggregation transmission can be explained by the ability of prion-like proteins to convert normal protein conformation into an infectious state that is susceptible to aggregation (Blokhuis, Groen et al. 2013).

Moreover, mutant FUS proteins are shown to incorporate into stress granules (SGs) upon different types of cellular stress, where mutant FUS can bind and sequester normal FUS into SGs (Figure 1.4) (Andersson, Stahlberg et al. 2008, Bosco, Lemay et al. 2010, Dormann, Rodde et al. 2010, Bentmann, Neumann et al. 2012, Li, King et al. 2013, Vance, Scotter et al. 2013). If stress is sustained, FUS-positive SGs are thought to turn into irreversible protein aggregates (Ling, Polymenidou et al. 2013). However, it was also shown that recruitment into SGs rather protects cytoplasmic FUS from irreversible aggregation (Shelkovnikova, Robinson

et al. 2013). Thus, if SGs function as a disease initiating event followed by aggregation during disease progression needs to be further investigated.

Various mechanisms, such as SG formation and prion-like spreading, are proposed to cause neurodegeneration in FUS-ALS. However, the precise underlying functional mechanisms are still unclear. Therefore, further investigations are needed to find the consensus of how pathological FUS aggregates confer toxicity in ALS.

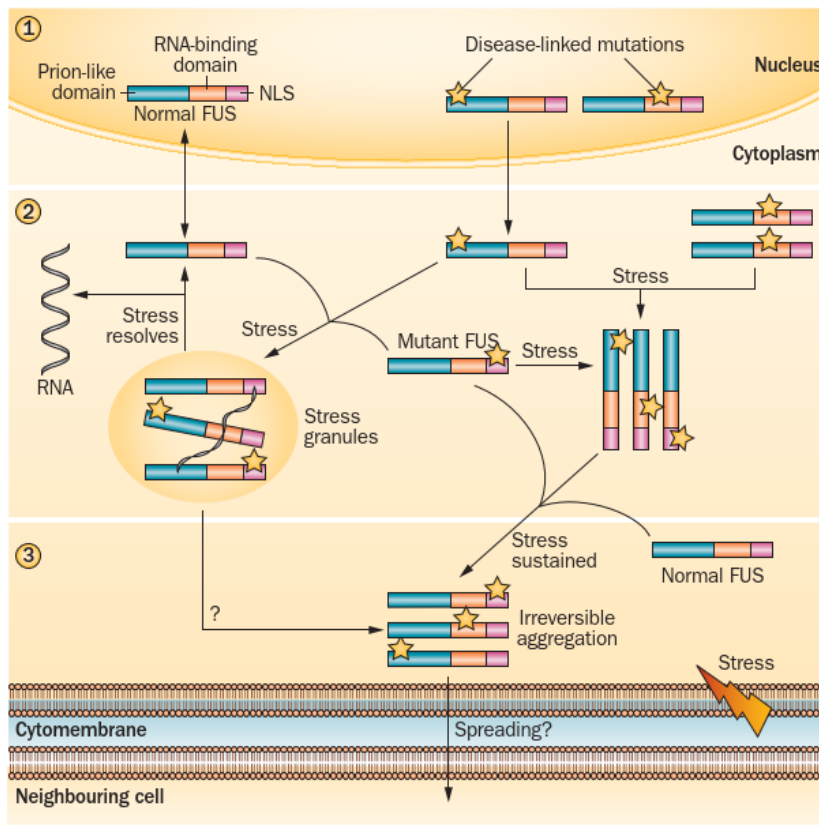


Figure 1.4 Potential mechanisms of FUS-associated neuropathology.

Normal FUS localizes to the nucleus but is also able to shuttle to the cytoplasm (1). Mutations within the nuclear localization signal (NLS) of FUS make the protein prone to cytoplasmic mislocalization. Cytoplasmic FUS is incorporated into stress granules upon cellular stress (2). When stress resolves, the stress granules rapidly dissociate and release sequestered RNAs and FUS protein, which resume their normal function. Sustained stress causes mutant FUS to form irreversible aggregates either directly or because FUS mutations impair SG disassembly (3). A prion-like transmission from cell to cell of FUS aggregates possibly causes FUS-associated pathology. The illustration was adopted from Deng et al. 2014.

1.3.1.2 C9ORF72

The G4C2 repeat sequence, located upstream of the *C9ORF72* coding region, does not possess an ATG start codon. In carriers with *C9ORF72-HRE*, the expanded repeat sequence is unconventionally translated via repeat-associated non-ATG dependent (RAN) translation. RAN translation of *C9ORF72-HRE* furthermore results in the generation of five DPR species:

glycine-alanine (GA) and glycine-arginine (GR) DPRs from the sense RNA strand; glycine-proline (GP), proline-alanine (PA), and proline-arginine (PR) DPRs from the antisense RNA strand (Ash, Bieniek et al. 2013, Gendron, Bieniek et al. 2013, Mori, Arzberger et al. 2013, Mori, Weng et al. 2013, Zu, Liu et al. 2013). All five DPR species can be found in neuronal inclusion in *C9ORF72-HRE* carriers.

Various cell- and animal models showed the toxicity induced by the expression of DPRs (Wen, Tan et al. 2014, Freibaum, Lu et al. 2015, Ohki, Wenninger-Weinzierl et al. 2017). However, those models work with an overexpression, which exceeds endogenous levels and can cause an aggravation of observed pathologies. In post-mortem tissue, DPRs are detectable at high levels in cortical regions, hippocampus and cerebellum but only at low amount in spinal cord (Ash, Bieniek et al. 2013, Mackenzie, Arzberger et al. 2013, Schludi, May et al. 2015). DPRs predominantly accumulate in cytoplasmic aggregates. Thereby, Poly-GA, Poly-GP, and Poly-GR are shown to be far more abundant than Poly-PR and Poly-PA (Gendron, Bieniek et al. 2013, Mori, Weng et al. 2013). The role of DPRs in the pathophysiology in patients with *C9ORF72-HRE* mutation is yet unclear since it was shown that the anatomical distribution of DPR inclusions does not correlate with neurodegeneration measured by classical neuropathology techniques as well as TDP43 aggregation (Mackenzie, Arzberger et al. 2013).

DPR positive inclusions were shown to be positive for ubiquitin and p62 but negative for TDP43, which makes them a unique characteristic of *C9ORF72-ALS* (Ash, Bieniek et al. , Mackenzie, Arzberger et al. 2013, Mori, Arzberger et al. , Schludi, May et al. 2015). Nevertheless, TDP43-positive ubiquitinated cytoplasmic inclusions are a hallmark pathology of ALS (Neumann, Sampathu et al. 2006, Mackenzie, Neumann et al. 2009) and are also found in neurons and glial cells of almost all *C9ORF72-HRE* carriers (Zu, Liu et al. 2013, Gendron, Belzil et al. 2014, Mann 2015). In contrast to DPR positive inclusions, TDP43 positive aggregates are most abundant in spinal MNs and are found to lesser extent in cortical regions. This TDP43 pattern much better correlates with neurodegeneration in these ALS patients. (Mackenzie, Arzberger et al. 2013). Cytoplasmic mislocalization and aggregation of TDP43 are, moreover, associated with the nuclear clearance of the protein (Lee, Lee et al. 2011) (Neumann, Sampathu et al. 2006).

In summary, the accumulation of DPRs is a characteristic pathology in *C9ORF72*-associated disease. Overexpression *in vitro* models show a DPR-induced toxicity while its role in human neuropathophysiology is still unclear, since only the aggregation formation of TDP43 in *C9ORF72-HRE* carriers is correlated with motor neuron degeneration not DPR accumulation. As post-mortem tissue only recapitulates the end-stage of the disease and overexpression models possibly accelerate phenotypes, *in vitro* models are needed that express endogenous levels of *C9ORF72-HRE*.

1.3.2 DNA damage

The human genome is constantly modified by endogenous (e.g. mitochondrial respiratory metabolites) and exogenous/environmental factors (e.g. air pollutants, chemicals, UV light) (Lindahl 1993). It is estimated that, in a mammalian genome, each day $\sim 10^5$ DNA lesions are produced due to spontaneous decay, replication errors, and cellular metabolism (Hoeijmakers 2009). Persisting DNA damage can cause mutagenesis and can further lead to cell death (Iyama and Wilson 2013). To avoid this, cells evolved multiple DNA damage repair (DDR) pathways to maintain their genome integrity.

Different types of DNA damage can occur, including double strand breaks (DSBs), single strand breaks (SSBs), DNA-protein cross-links, or insertion/deletion mismatches (Rao 1993), each repaired by specialized DDR pathways. DSBs are the most deleterious form of DNA damage, as they promote genome instability and cell death if unrepaired (Jackson and Bartek 2009, Bohgaki, Bohgaki et al. 2010). DSBs are repaired via two major pathways: homologous recombination (HR) or non-homologous end joining (NHEJ) (Iyama and Wilson 2013). HR is considered to be error-free and acts in particular in dividing cells, as it requires a sister chromatid for repair (Rulten and Grundy 2017). NHEJ is considered an error-prone pathway, because it directly ligates broken ends and does not require a template as replication-dependent HR (Madabhushi, Pan et al. 2014). NHEJ is independent of cell cycle and can act in dividing and non-dividing cells.

This difference is of note, because the human body consists of various cell types which are either in a dividing or non-dividing state (Iyama and Wilson 2013). Most cells in the body are in a non-dividing state, e.g. terminally differentiated such as neurons. They are post-mitotic cells that under physiological conditions do not re-enter cell cycle. This makes them highly vulnerable to DNA damage (Penndorf, Witte et al. 2018) and makes DNA damage a crucial pathomechanism causing neurodegenerative disease and particularly ALS (Coppede 2011, Madabhushi, Pan et al. 2014, Coppede and Migliore 2015).

The investigation of DNA damage as a possible pathomechanism underlying ALS is a very wide field itself. The analyzed cell type (proliferative or post-mitotic), the type of DNA damage (SSB, DSB, etc.), and responsible DDR pathways need to be taken into account. Further research is needed to determine precise mechanisms of how DNA damage causes neurodegeneration and if it is cause or consequence of ALS-associated mutations.

1.3.2.1 FUS

Wild type (WT) FUS was shown to play an active role in DDR (Wang, Pan et al. 2013). FUS is recruited to laser-induced DNA damage sites (Mastrocola, Kim et al. 2013, Naumann, Pal

et al. 2018) and binds to DSBs marked by γ H2AX staining (Mastrocola, Kim et al. 2013, Wang, Pan et al. 2013). Similar to *C9orf72-HRE* mutant cells, ALS-associated *FUS* mutations lead to increased DNA damage in patient-specific spinal MNs (Higelin, Demestre et al. 2016, Naumann, Pal et al. 2018). There as well, an accumulation of DNA damage could only be observed in post-mitotic neurons, but not in iPSCs (Higelin, Demestre et al. 2016). Moreover, Qiu et al. could show increased DNA damage in mouse primary cortical neurons overexpressing mutant *FUS* as well as in human cortical postmortem tissue (Qiu, Lee et al. 2014). Wang et al. further showed increased γ H2AX levels in transgenic mice spinal cord and cortex (Wang, Pan et al. 2013).

1.3.2.2 C9ORF72

The exact underlying mechanisms of how *C9ORF72-HRE* causes ALS is still unclear but various studies implicate a role of DNA damage in *C9ORF72*-ALS pathology (Konopka and Atkin 2018). Elevated levels of DNA damage were reported in *C9ORF72-HRE* mutant postmortem tissue as well as in iPSC-derived motor neurons (Lopez-Gonzalez, Lu et al. 2016, Farg, Konopka et al. 2017, Walker, Herranz-Martin et al. 2017, Higelin, Catanese et al. 2018). Farg and colleagues found increased DNA damage levels in lumbar MNs from *C9ORF72*-ALS patients (Farg, Konopka et al. 2017). Further they showed, that overexpression of DPRs in mouse primary cortical neurons and in human neuroblastoma cells induced accumulation of DNA damage. Higelin and colleagues could show that patient-specific iPSC-derived spinal MNs, but not induced pluripotent stem cells (iPSCs), show increased DNA damage in *HRE* expressing cells (Higelin, Catanese et al. 2018), highlighting the vulnerability of neurons to mutation-mediated DNA damage or mutation-mediated insufficiency of DDR. *C9ORF72* is not known to be directly involved in DDR pathway, however it was shown that accumulation together with defective ATM-signaling is a pathological consequence of *C9ORF72-HRE* (Walker, Herranz-Martin et al. 2017).

1.3.3 **Organelle trafficking**

With axons reaching over one meter in length, MNs are one of the most asymmetrical cell type in the human body (Millecamps and Julien 2013, Taylor, Brown et al. 2016). Due to these long cell processes, they rely on functional transport of various cellular organelles from the cell body (soma) to the distal axons and synapses. This includes for example the transport of mRNA, ribosomes, and translational factors for local protein synthesis at distal sites. Organelle trafficking also includes functional clearance of recycled or misfolded proteins. Two categories of axonal transport exits: fast axonal transport for membrane-bound organelles (vesicles and

mitochondria) and slow axonal transport of cytoplasmic and cytoskeletal proteins (Millecamps and Julien 2013).

Various studies in recent years showed axonal trafficking defects in neurodegenerative diseases (Sheetz, Pfister et al. 1998, Millecamps and Julien 2013, Guo, Naujock et al. 2017, Hasegawa, Sugeno et al. 2017, Kreiter, Pal et al. 2018, Naumann, Pal et al. 2018). In ALS models, mutations within *TARDBP* and *SOD1* lead to impaired axonal organelle trafficking (Williamson and Cleveland 1999, Perlson, Jeong et al. 2009, Perrot and Julien 2009, Alami, Smith et al. 2014, Kreiter, Pal et al. 2018). In a *SOD1* ALS model, axonal trafficking defects could be observed before onset of neurodegeneration.

The same is true for the ALS-associated gene *FUS*. Severe distal axonal trafficking defects of mitochondria and lysosomes precede neurodegeneration in patient-specific *FUS* mutant MN cultures (Naumann, Pal et al. 2018). In this context, Guo and colleagues could show progressive axonal transport defect, accumulating during aging of patient-specific MN cultures (Guo, Naujock et al. 2017).

With regard to *C9ORF72*, the protein was found to regulate endosomal trafficking and possibly affect trafficking in ALS patients (Farg, Sundaramoorthy et al. 2014). Aoki et al. found an interaction between *C9ORF72* and *RAB7L1* which is disrupted in presence of *HRE* mutation due to downregulation of *C9ORF72*. This disrupted interaction results further in defect intracellular and extracellular trafficking (Aoki, Manzano et al. 2017). Impaired axonal trafficking is thought to be a key pathological event causing ALS. However, how exactly defects in organelle trafficking cause neurodegeneration is still under debate.

1.4 ALS disease modeling

1.4.1 Animal models

Various model systems exist in ALS research. Rodent models (mouse and rat) have been the gold standard to investigate ALS disease pathology for decades (Van Damme, Robberecht et al. 2017). Due to their high homology to humans, rodent models allow detailed mechanistic studies with relevance to human physiology. The first ALS mouse model, overexpressing human mutant *SOD1*, came up in 1994 and was intensively investigated since then (Gurney, Pu et al. 1994). Even though there are new rodent models existing for ALS-associated proteins such as *SOD1*, *TDP43*, *FUS*, and *C9ORF72* (Turner and Talbot, Gendron and Petrucelli, Philips and Rothstein, Nolan, Talbot et al.), much of our current understanding of disease mechanisms is still based on this first *SOD1* model (Gurney, Pu et al. 1994). Rodent models are expensive to maintain, complicated to generate, and do not allow to test for multiple

hypotheses at the same time (Van Damme, Robberecht et al. 2017). Therefore, model systems are needed that are easier to access.

Small animal models are the second model system important in ALS research. The generation of transgenic strains is fast and cheap, and various tools for genomic modification exist (Van Damme, Robberecht et al. 2017). The most widely used small animal model in ALS research is *Drosophila melanogaster*, followed by *Ceanorhabditis elegans* and *Danio rerio*. All three possess a rapid life cycle and are well-suited for high throughput analysis, e.g. for drug testing screens. However, small animal models lack the complex interplay between MNs and their environment as it is found in rodents or even human beings. It is also of note that many small animal models, as well as rodent models, most often use overexpression of mutant proteins to mimic human disease. Furthermore, treatments developed in both, small animal and rodent models, never lead to effective therapeutics in human trials (Swarup and Julien 2011, Van Damme, Robberecht et al. 2017). To overcome these issues, cellular patient-derived models have been upcoming in recent years to investigate disease mechanisms *in vitro* on a patient-specific basis.

1.4.2 Patient-specific models

The breakthrough discovery to reprogram human somatic cells to an embryonic-like state has been of great interest for the medical and scientific communities. So called induced pluripotent stem cells (iPSCs) can be derived by the overexpression of pluripotency genes in human somatic cells such as fibroblasts (Takahashi, Tanabe et al. 2007, Yu, Vodyanik et al. 2007). The pluripotent nature of iPSCs allows them to become any cell type of the adult human body. This is of great interest for scientific investigations, because iPSCs can be differentiated into any cell type of interest including MNs to study ALS pathology *in vitro* (Burkhardt, Martinez et al. 2013, Matus, Medinas et al. 2014, Maury, Come et al. 2015, Sances, Bruijn et al. 2016). As shown in Figure 1.5, many aspects of ALS neuropathology could be recapitulated and putative underlying mechanisms have already been determined by the use of patient-specific iPSC-derived MNs.

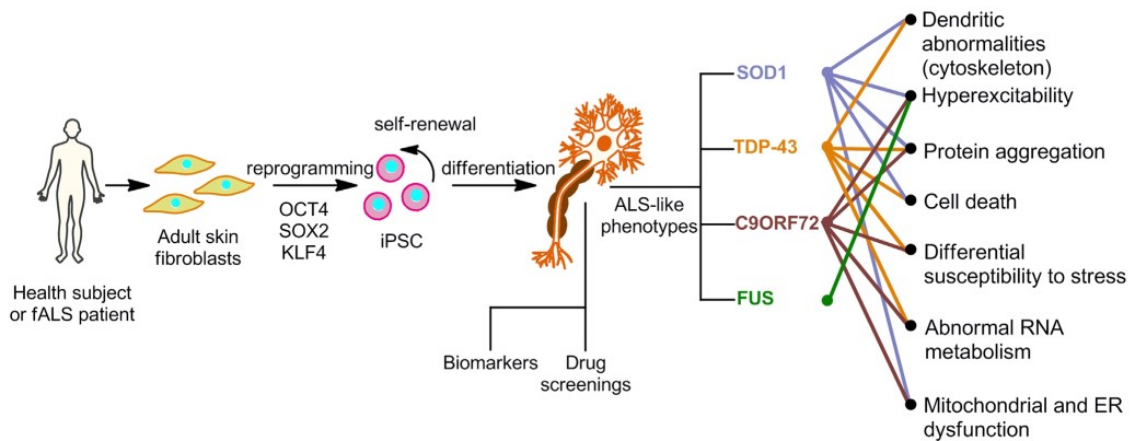


Figure 1.5 Discovery of molecular mechanisms underlying ALS pathology using patient-specific iPSC-derived motor neurons.

Fibroblast, derived from humans, can be used to generate iPSCs by the overexpression of pluripotency genes. iPSCs can be used further for differentiation into motor neurons, which are affected in ALS pathology. Recent studies using human motor neuron cultures from ALS patients with distinct genetic mutations have identified transversal pathological mechanisms, including abnormal protein and RNA aggregation, hyperexcitability, morphological alterations, and cell death. The illustration was adopted from Matus et al. 2014.

Various protocols exist for the differentiation of iPSCs into spinal and cortical MNs (Burkhardt, Martinez et al. 2013, Reinhardt, Glatza et al. 2013, Sances, Bruijn et al. 2016). Most studies in recent years concentrated on the investigation of spinal MNs, for which many protocols exist which result in a good MN outcome. Spinal MNs can be differentiated using iPSC-derived neural progenitor cells (NPCs) (Reinhardt, Glatza et al. 2013). This makes them relatively easily accessible, because once patient-specific NPCs are generated, they can be expanded in culture or frozen away if not needed. Furthermore, fully mature spinal MNs can be derived already after 2 to 3 weeks of differentiation. The modeling of ALS in cortical MNs (also upper MNs) is not this straightforward. The cerebral cortex consists of various types of projection neurons, from which upper MNs are only a relatively rare subtype (Molyneaux, Arlotta et al. 2007, Sances, Bruijn et al. 2016). Furthermore, the generation of cortical neurons is more complex due to long differentiation times (2 to 4 months) and the need to use iPSCs (not NPCs) as starting cell type (Mariani, Simonini et al. 2012, Shi, Kirwan et al. 2012, Shi, Kirwan et al. 2012, Burkhardt, Martinez et al. 2013). This makes the evaluation of cortical neurons in ALS research rare, until now. Nevertheless, the use of patient-specific iPSCs is nowadays an important tool for modeling disease because they can be generated relatively easy and provide a good balance between throughput and relevance to human disease (Matus, Medinas et al. 2014).

1.4.3 CRISPR/Cas9 gene editing

One challenge remains if patient-specific iPSC models are used to study disease-associated pathology: the patient's genetic background. For scientific investigation it is state-of-the-art to compare several iPSC lines derived from different healthy individuals and different diseased patients. As abovementioned, pathological phenotypes associated with ALS-causing mutations highly depend on the underlying mutation. Some mutations might only cause a subtle phenotype. Due to that, sometimes it could be difficult to determine if such a phenotype is caused by the mutation itself or by the genetic background of the patient. To overcome this problem, the use of isogenic iPSC lines is recently becoming a crucial tool in ALS research and disease modeling systems altogether (Higelin, Demestre et al. 2016, Marrone, Poser et al. 2018, Naumann, Pal et al. 2018). An isogenic line is a cell line that has been generated from a parental line in which a gene modification was introduced (either induction of mutation or correction of mutation) (StemCell 2018). The generated modified iPSC line and the unmodified parental line can be easily compared with each other because both lines possess the same genetic background (=isogenic). Thus, phenotypes observed in experimental approaches most likely represent the result from the genotype and not the patient's genetic background.

Only recently, a new versatile and robust tool for targeted gene editing was established to easily generate isogenic iPSC lines: the Clustered Regularly Interspaced Short Palindromic Repeat (CRISPR)-associated 9 system (short CRISPR/Cas9). Cas9 nuclease, derived from *Streptococcus pyogenes*, can be directed by single guide RNAs (sgRNA) to any genomic locus of interest (Deveau, Garneau et al. 2010, Deltcheva, Chylinski et al. 2011, Jinek, Chylinski et al. 2012, Hsu, Scott et al. 2013, Ran, Hsu et al. 2013)(Figure 1.6). To improve specificity of Cas9-mediated gene editing, the D10A mutant nickase version of Cas9 (Cas9n) can be used (Gasiunas, Barrangou et al. 2012, Jinek, Chylinski et al. 2012, Cong, Ran et al. 2013, Ran, Hsu et al. 2013) (Figure 1.7). By nicking both DNA strands at the target site by a pair of sgRNA-Cas9n complexes, the introduction of DSBs can be mimicked which triggers DDR pathways such as NHEJ and HR. This, in turn, can be used to correct disease-causing gene mutations or to generate ALS-associated mutations in WT iPSC lines to generate isogenic lines (Kiskinis, Sandoe et al. 2014, Sances, Bruijn et al. 2016).

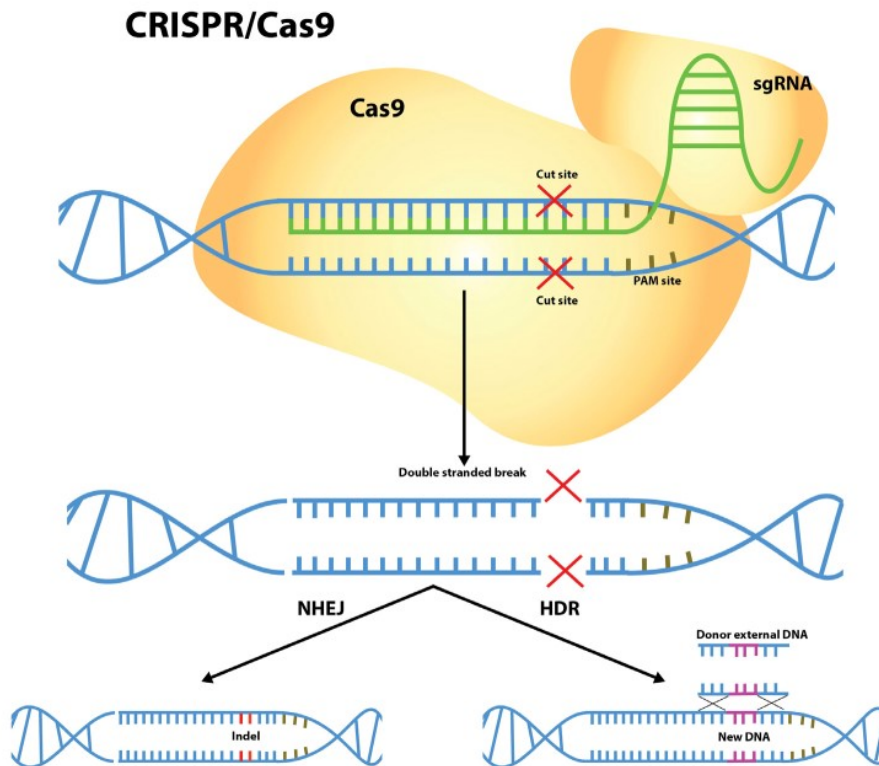


Figure 1.6 CRISPR/Cas9-mediated gene editing.

Single guide RNA (sgRNA) can be designed to specifically target the genomic locus of interest. sgRNAs recognize the genomic sequence followed by a PAM sequence, which recruits Cas9 endonuclease to the target site. Cas9 then introduces DSBs that are either repaired by NHEJ or HDR. NHEJ is error-prone and can result in the formation of indels that disrupt the gene. HDR, in the presence of a donor construct, can be used to introduce aimed genomic modifications as it needs a template for DSB repair. The illustration was adopted from Cribbs and Perera 2017.

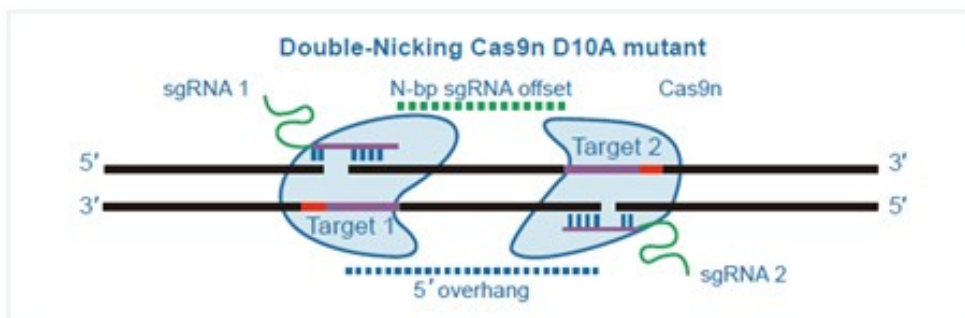


Figure 1.7 D10A mutant nickase version of Cas9 (Cas9n).

By the use of Cas9n, specificity of Cas9-mediated gene editing can be improved because two individual sgRNAs are used to guide two Cas9n enzymes to the target site. By the nicking of both DNA strands by a pair of Cas9 nickases, site-specific DSBs can be mimicked further triggering HDR (Ran, Hsu et al. 2013). The illustration was adopted from GenScript website (GenScript 2019).

1.5 Objective of the thesis

Overall aim of this thesis work is the modeling of *FUS*- and *C9ORF72*-associated ALS in a disease-related *in vitro* model of particularly cortical neuropathology using patient-derived iPSCs.

Specific questions of this thesis are:

- Can hallmark neuropathology of *FUS*- and *C9ORF72*-associated ALS be recapitulated in patient-specific iPSC-derived cortical neurons and astrocytes?
- Are there differential cell type dependent phenotypes between cortical neurons vs. astrocytes and cortical vs. spinal neurons?

To achieve abovementioned aim, human iPSCs derived from healthy controls and ALS patients carrying mutations within *FUS* or *C9ORF72* were used for directed cortical and spinal differentiation. Additionally, two new *FUS*-WT and *FUS*-P525L EGFP-tagged isogenic iPSC lines were generated by CRISPR/Cas9n gene editing. To analyze disease-related phenotypes in patient-specific *in vitro* cultures, immunofluorescence staining followed by fluorescence microscopy were conducted. Analysis included the evaluation of cortical differentiation potential, DNA damage markers γ H2AX and 53BP1, *FUS*-EGFP cellular localization, and aggregation of *C9ORF72*-associated DPRs and TDP43. Live cell imaging approaches were used to analyze DNA damage in the context of *FUS* mutation by the analysis of *FUS*-EGFP recruitment to laser-induced DNA damage sites. Moreover, compartmentalized culture systems were used to evaluate motility parameters of axonal organelle trafficking by live imaging of lysosomes and mitochondria.

The results of these experiments should help to augment knowledge on cortical neuropathology in ALS and highlighting differences and importance of the herein analyzed cell types. Using patient-specific iPSCs, disease-related phenotypes can be analyzed on physiological conditions without any need of overexpression or knockdown of ALS-associated proteins. Therewith, the presented thesis work is the first to use patient-specific iPSCs to model in particular cortical neuropathology of *FUS*- and *C9orf72*-associated ALS.

2 Materials and methods

2.1 Materials

2.1.1 Instruments

Table 2.1 Instruments

Instrument	Company
Analytical Balance - CP225D-0CE	Satorius AG, Göttingen, GER
Balance - SBA 52	Scaltec Instruments GmbH, Heiligenstadt, GER
Cell culture Microscope – Axiovert 35	Carl Zeiss, Jena, GER
Centrifuge – 5403	Eppendorf, Hamburg, GER
Centrifuge - Biofuge Pico	Thermo Fisher Scientific, Massachusetts, USA
Centrifuge - Biofuge Primo	Thermo Fisher Scientific, Massachusetts, USA
Centrifuge - MiniSpinPlus	Eppendorf, Hamburg, GER
Fluorescence Microscope - AFLX6000 TIRF	Leica Camera, Wetzlar, GER
Fluorescence Microscope – Axiovert 200M	Carl Zeiss, Jena, GER
Fluorescence Microscope - Observer.Z1	Carl Zeiss, Jena, GER
Gel documentation - Dunkelhaube D4	Biostep GmbH, Burkhardtsdorf, GER
Gel electrophoresis - E865	Consort, Turnhout, BEL
Gel electrophoresis PSU - EPS 600	Pfizer, New York, USA
Hemocytometer - Neubauer improved	Paul Marienfeld GmbH Co. KG, Lauda-Königshofen, GER
Hybridization oven - HB-1000	UVP, Upland, CAN
Hybridization oven - OV3	Biometra GmbH, Göttingen, GER
Imager - LAS3000	Fujifilm, Tokyo, JPN
Incubator - Heracell 150	Thermo Fisher Scientific, Massachusetts, USA
Incubator - Heracell 150i	Thermo Fisher Scientific, Massachusetts, USA
Laminar Flow hood - Clean Wizard V 100	Kojair Tech Oy, Vilppula, FIN
Laminar Flow hood – Herasafe HS	Thermo Fisher Scientific, Massachusetts, USA
Multichannel multistep pipette-Transferringpipette-8	Brand GmbH & Co. KG, Wertheim, GER
PCR cycler – Mastercycler gradient	Eppendorf, Hamburg, GER
pH meter - inoLab ph 720	Wtw GmbH, Weilheim, GER
Photometer - Biophotometer	Eppendorf, Hamburg, GER
Real time PCR cycler - MX3000P	Agilent, Santa Clara, USA
Shaker – incubating orbital shaker 3500i	VWR International, Radnor Township, USA
Shaker – RotaMax 150	Heidolph, Schwabach, GER

Stereo preparation microscope - Stemi DV4SteREO CL 1500 ECO	Carl Zeiss, Jena, GER
Thermomixer – Thermomixer 5436	Eppendorf, Hamburg, GER
Thermomixer – Thermomixer Comfort	Eppendorf, Hamburg, GER
Transiluminator – BioView UST 30M-8R	Biostep GmbH, Burkhardtsdorf, GER
Water bath	Memmert GmbH & Co. KG, Schwabach, GER
Water bath - Julambo SW22	JULAMBO Labortechnik GmbH, Seelbach, GER
Water purification system - GenePure	Thermo Fisher Scientific, Massachusetts, USA
Qubit Fluorometer	Thermo Fisher Scientific, Massachusetts, USA

2.1.2 Chemicals and reagents

Table 2.2 Chemicals and reagents

Chemical	Manufacturer
Agarose	Biozym Biotech Trading GmbH, Oldendorf, GER
Ampicillin	Carl Roth GmbH & Co. KG, Karlsruhe, GER
BSA Fraction V	Thermo Fisher Scientific, Massachusetts, USA
Collagenase Type IV	Thermo Fisher Scientific, Massachusetts, USA
DMSO	Sigma Aldrich, St. Louis, USA
DNA ladder	Thermo Fisher Scientific, Massachusetts, USA
Donkey Serum	Jackson ImmunoResearch Laboratories Inc., West Grove, USA
Ethanol	VWR International GmbH, Dresden, GER
Fetal bovine serum	Sigma Aldrich, St. Louis, USA
Fetal calf serum	Merck Group, Darmstadt, GER
Fluoromount	SouthernBiotech, Birmingham, USA
FuGene® HD	Promega, Madison, USA
Gelatine	Sigma Aldrich, St. Louis, USA
Glycerol	MP biomedicals, Santa Ana, USA
Glycine	Carl Roth GmbH & Co. KG, Karlsruhe, GER
Isopropanol	VWR International GmbH, Darmstadt, GER
Kanamycin	Carl Roth GmbH & Co. KG, Karlsruhe, GER
Laminin	Roche Holding AG, Basel, CHE
Laminin	Sigma Aldrich, St. Louis, USA
LB Medium	Thermo Fisher Scientific, Massachusetts, USA
Matrigel	BD Bioscience, Bedford, USA (556320)
Mikrozid	Schülke&Mayr, Norderstedt, GER
Midori Green Advance DNA stain	Nippon Genetics Europe GmbH, Dueren, GER

NaCl	Merck Group, Darmstadt, GER
PBS	Thermo Fisher Scientific, Massachusetts, USA
Paraformaldehyde 4% solution	Seipt, Klinikapotheke UKD,
Poly-L-orthnitine	Sigma Aldrich, St. Louis, USA
Protamin Sulfat	Sigma Aldrich, St. Louis, USA
Penicillin and streptomycin	Thermo Fisher Scientific, Massachusetts, USA
Penicillin, streptomycin, glutamine	Thermo Fisher Scientific, Massachusetts, USA
Sterile RNase-free water	Thermo Fisher Scientific, Massachusetts, USA
Tris-HCL	Carl Roth GmbH & Co. KG, Karlsruhe, GER
TritonX-100	Thermo Fisher Scientific, Massachusetts, USA
Tween 20	Serva Elektrophoresis GmbH, Heidelberg, GER

2.1.3 Commercial available kits

Table 2.3 Commercial available kits

Name	Company
DNeasy Blood & Tissue Kit	Qiagen, Hilden, GER
QIAquick® Gel Extraction Kit	Qiagen, Hilden, GER
Qubit™ dsDNA BR Assay Kit	Thermo Fisher Scientific, Massachusetts, USA
ZR Plasmid Miniprep Kit	Zymo Research, Irvine, USA

2.1.4 Enzymes

Table 2.4 Enzymes for cell culture

Name	Company
Accutase	Sigma Aldrich, St. Louis, USA
Dispase	Thermo Fisher Scientific, Massachusetts, USA
Trypsin	Thermo Fisher Scientific, Massachusetts, USA

Table 2.5 Restriction enzymes for cloning

Name	Company
FastDigest Bpil	Thermo Fisher Scientific, Massachusetts, USA
FastDigest Lgul	Thermo Fisher Scientific, Massachusetts, USA

2.1.5 Antibodies

Table 2.6 Primary antibodies

Antibody	Host	Dilution	Company	Reference Number
53BP1	Rabbit	1:1000	Novusbio	NB100-304
CTIP2	Rat	1:1000	Abcam	ab18465
FUS	Mouse	1:3000	Sigma	AMAB90549-100UL
GATA4	Rabbit	1:500	Abcam	ab61170
GFAP	chicken	1:1000	Abcam	ab46674
GFAP	Rabbit	1:1000	Abcam	ab33922
MAP2	Chicken	1:2000	Abcam	ab5392
OCT4	Rabbit	1:500	Abcam	ab19857
phHistone H2A.X(Ser139)	Mouse	1:500	Millipore	#05-636
Poly-GA (IAI2)	Mouse	1:500	Provided by	Prof. Dr. D. Edbauer
Poly-GP (18H8)	Rat	1:1000	Provided by	Prof. Dr. D. Edbauer
Poly-GR (5H9)	Rat	1:1000	Provided by	Prof. Dr. D. Edbauer
SATB2	Mouse	1:600	Abcam	ab51502
SMA	Mouse	1:100	Dako	M0851
SMI32	Chicken	1:10,000	Covance	PCK-592P
SOX2	Mouse	1:200	Millipore	MAB4343
SSEA4	Mouse	1:500	Abcam	ab16287
TARDBP	Rabbit	1:300	Abcam	ab41972
TBR1	Rabbit	1:3000	Abcam	ab31940
TRA-1-60	Mouse	1:500	Abcam	ab16288
TUJ1	Mouse	1:1000	Covnce	MMS-435P

Table 2.7 Secondary antibodies

Antibody	Host & reactive species	Dilution	Company	Reference Number
Alexa Fluor 488	donkey anti mouse IgG	1:500	Molecular Probes	A21202
Alexa Fluor 555	donkey anti mouse IgG	1:500	Molecular Probes	A31570
Alexa Fluor 647	donkey anti mouse IgG	1:500	Molecular Probes	A31571
Alexa Fluor 488	donkey anti rabbit IgG	1:500	Molecular Probes	A21206
Alexa Fluor 555	donkey anti rabbit IgG	1:500	Molecular Probes	A31572
Alexa Fluor 594	donkey anti rabbit IgG	1:500	Molecular Probes	A21207
Alexa Fluor 488	goat anti-chicken IgG	1:500	Molecular Probes	A11039
Alexa Fluor 647	donkey anti-Chicken IgY	1:500	Dianova	703295155
Alexa Fluor 488	donkey anti rat IgG	1:500	Dianova	703605155
Alexa Fluor 594	donkey anti rat IgG	1:500	Molecular Probes	A21208
Alexa Fluor 647	goat anti-rat IgG	1:500	Dianova	712165150

Table 2.8 Fluorescence reporters

Name	Dilution	Manufacturer (catalog number)
LysoTracker Red (L7528)	1:20000	Thermo Fisher Scientific, Massachusetts, USA
MitoTracker DeepRed (M22426)	1:20000	Thermo Fisher Scientific, Massachusetts, USA
Hoechst33342 (H3570)	1:1333	Thermo Fisher Scientific, Massachusetts, USA

2.1.6 Primer

Table 2.9 List of primer

Primer Name	Forward/ Reverse	Sequence (5'-3')	Used for...
pX335_seq_R	Reverse	GGAAAGTCCCTATTGGCGTT	Sequencing (2.2.1.3)
FUS-1.3-F	Forward	CTTGCCTATTCCCCATCGCT	Screening PCR (2.2.4.2)
EGFP Rev 1	Reverse	CGGTGGTGCAGATGAACTT	Screening PCR (2.2.4.2) and Sequencing (2.2.5.1)
FUS-2.1-F	Forward	CAGTTGAACAGAGGCCATAGG	Genotyping PCR (2.2.4.3)
FUS-2.1-R	Reverse	CTCTCTACCTTCCTGATCGGG	Genotyping PCR (2.2.4.3)
FUS-seq-R	Reverse	TGGGTGATCAGGAATTGGAAGG	Sequencing (2.2.5.1)

2.1.7 Plasmids

Table 2.10 List of plasmids

Plasmid name	Description	Source
pX335B_hCas9_2x sgRNA	Cas9n plasmid w/o sgRNAs	Dr. Boris Greber (Max Planck Institute for Molecular Biomedicine, 48149 Münster, GER)
pX335B_FUS_T1+T2	Cas9n plasmid containing sgRNA for FUS targeting	Cloned as part of this thesis work
pEX-K4-FUS-WT-EGFP	Plasmid containing template for FUS modification	Synthesized <i>de novo</i> by Eurofins Genomics
pEX-K4-FUS-P525L-EGFP	Plasmid containing template for FUS modification	Synthesized <i>de novo</i> by Eurofins Genomics

2.1.8 Cell culture media, supplements, and consumables

Table 2.11 Cell culture media and supplements

Name	Company
B27-Supplement w/o Vitamin A	Thermo Fisher Scientific, Massachusetts, USA
β -Mercaptoethanol	Thermo Fisher Scientific, Massachusetts, USA
DMEM	Thermo Fisher Scientific, Massachusetts, USA
DMEM F12	Thermo Fisher Scientific, Massachusetts, USA
Etoposide	Sigma Aldrich, St. Louis, USA
GlutaMAX	Thermo Fisher Scientific, Massachusetts, USA
mTeSR1	Stemcell Technologies, Vancouver, CAN
N2-Supplement	Thermo Fisher Scientific, Massachusetts, USA
Non Essential Amino Acids	Thermo Fisher Scientific, Massachusetts, USA
Neurobasal	Thermo Fisher Scientific, Massachusetts, USA
ReLeSR	Stemcell Technologies, Vancouver, CAN
TeSR-E8	Stemcell Technologies, Vancouver, CAN

Table 2.12 Growth factors and small molecules

Name	Company
Activin A	Biomol GmbH, Hamburg, GER
Ascorbic Acid	Sigma Aldrich, St. Louis, USA
BDNF	Promega, Madison, USA
cAMP	Sigma Aldrich, St. Louis, USA
CHIR 99021	Cayman chemical company, Ann Arbor, USA
Dorsomorphin	Tocris Bioscience, Bristol, UK
GDNF	Sigma Aldrich, St. Louis, USA
Insulin	Sigma Aldrich, St. Louis, USA
PMA	Cayman chemical company, Ann Arbor, USA
ROCK Inhibitor Y-27632	Abcam, Cambridge, United Kingdom
SAG	Cayman chemical company, Ann Arbor, USA
SB431542	Tocris Bioscience, Bristol, UK
TGF β -3	Peptidech, London, UK

Table 2.13 Consumables

Material	Company
BD Falcon™ Round-Bottom Tube	BD Bioscience, New Jersey, USA
Bottle-top vacuum filters	Corning Inc., Corning, USA
Cell culture Dishes	Corning Inc., Corning, USA
(4-,6-,12-,24-,96-well)	Thermo Fisher Scientific, Massachusetts, USA
	Sarstedt AG & Co., Nümbrecht, GER

Cell culture Flasks	TPP Techno Plastic Products AG, Trasadingen, CHE
Cell scraper	Corning Inc., Corning, USA
	Carl Roth, Karlsruhe, GER
	TPP Techno Plastic Products AG, Trasadingen, CHE
Centrifuge tubes	Greiner Bio-One GmbH, Kremsmünster, AUT
Costar® Stripette®	Corning Inc., Corning, USA
Cryo preservation tubes, 2 ml	Greiner Bio-One GmbH, Kremsmünster, AUT
Eppendorf tubes 1.5 ml, 2 ml	Eppendorf, Hamburg, GER
Glass Cover Slips	Thermo Fisher Scientific, Massachusetts, USA
Microscope slide glass	Thermo Fisher Scientific, Massachusetts, USA
Microfluidic chambers	Xona Microfluidics LLC, Temecula, USA
Millex HV low binding PVDV membrane filters 0.45 µm	Merck Millipore, Billerica, USA
Nalgene® Mr. Frosty Freezing Container	Sigma Aldrich, St. Louis, USA
Nunc™ glass base dish, 27mm	Thermo Fisher Scientific, Massachusetts, USA
Pipette tips (w & w/o filter)	Sarstedt AG & Co., Nümbrecht, GER
	Biozym Scientific, Hessisch Oldendorf, GER
	Corning Inc., Corning, USA
Pipettes	Gilson Inc., Middleton, USA
	Eppendorf, Hamburg, GER
	VWR International, Radnor Township, USA
SafeSeal reaction tubes	Sarstedt AG & Co., Nümbrecht, GER
Serological pipette 5, 10, 25 and 50ml	Greiner Bio-One GmbH, Kremsmünster, AUT
Surgery cap Barrier®	Mönlycke Health Care, Erkrath-Unterfeldhaus, GER
Surgical mask	Paul Hartmann AG, Heidenheim,

2.1.9 Software

Table 2.14 Software

Software	Type	Company
CellProfiler 2.2.0	Image analysis	Open Source (Carpenter, Jones et al. 2006)
FIJI 1.48a and 1.52b	Image and video analysis	Open Source (Schindelin, Arganda-Carreras et al. 2012)
GraphPad Prism 7	Statistics	GraphPad Software Inc., La Jolla, USA
KNIME 3.1.2	Data mining and organization	KNIME.COM AG, Zurich, CHE
Photoshop CS6	Image processing	Adobe Systems, San Jose, USA
Photoshop Illustrator CS6	Graphics design	Adobe Systems, San Jose, USA
SerialCloner 2.6.1	Sequence design	Open Source
Snap Gene Viewer 4.0.7	Plasmid design and maps	GSL Biotech, Chicago, USA
Zen 2011	Image acquisition	Carl Zeiss AG, Oberkochen, GER

2.1.10 Cell lines

Cell lines used in this thesis work were either generated previously by members of the group or obtained from collaborators. All iPSC lines were already fully established and the generation and basic characterization was not topic of this theses. An exception from this are the lines FUS-WT and FUS-P525L, which were generated as a part of this thesis work. Non-isogenic cell lines as well as isogenic once were used to analyze disease-associated phenotypes. The study was approved by the local ethics committee (EK45022009).

Table 2.15 Cell lines

C9-WT	C9-HRE 2	C9-HRE 3	C9-HRE 1	FUS- P525L	FUS-WT	FUS- R521C	Ctrl 4	Ctrl 3	Ctrl 2	Ctrl 1	Name
Corrected C9- HRE 2 (isogenic)	C9-HRE (ca. 1800 rep.)	C9-HRE (ca. 1800 rep.)	C9-HRE (>50 rep.)	Modified FUS- R521C	Corrected FUS- R521C	FUS- R521C	control	control	control	control	Mutation
WT / WT	C9-HRE / WT	C9-HRE / WT	C9-HRE / WT	FUS- P525L- EGFP / WT	FUS-WT- EGFP / WT	FUS- R521C / WT	WT / WT	WT / WT	WT / WT	WT / WT	Genotype
AG	AG	AG	AG	AG	AG	AG	AG	AG	AG	AG	Source
Sterneckert	Sterneckert	Böckers, Ludolph	Hermann	Hermann	Hermann	Hermann	Hermann	Hermann	Hermann	Sterneckert	
M	M	M	F	F	F	F	M	M	F	F	Gender
1944	1944	1951	1944	1952	1952	1952	1976	1976	1963	1959	Year of birth
65	65	NA	68	58	58	58	34	34	48	NA	Age at biopsy
(Abo-Rady 2018)	(Donnelly, Zhang et al. 2013)	(Higelin, Catanese et al. 2018)	(Sivadasan , Hornburg et al. 2016)	(Naumann, Pal et al. 2018)	(Naumann, Pal et al. 2018)	(Japtok, Pal et al. 2015)	(Glass, Pal et al. 2018)	(Glass, Pal et al. 2018)	(Glass, Pal et al. 2018)	(Reinhardt, Glatza et al. 2013)	Reference

2.2 Molecular biology

2.2.1 Plasmid design and generation for CRISPR/Cas9n-mediated gene editing of *FUS*

For CRISPR/Cas9n-mediated genome editing an approach described by Ran et al. (2013) was used. The CRISPR vector pX335B_hCas9_2x sgRNA (short pX335B) containing the D10A mutant nickase version of Cas9 (Cas9n) and a pair of sgRNA was used to create a double strand break (DSB) at the target site (Ran, Hsu et al. 2013). The pX335B vector was kindly provided by the laboratory of Dr. Boris Greber (Table 2.10).

2.2.1.1 Design of sgRNA sequences

Single-guide RNAs were manually selected by screening of the coding strand of *FUS* for suitable sgRNA target sequences upstream of *FUS-R521C* mutation site (Figure 2.1). DNA motifs screened for were CCN(N)19C for target one (T1) and G(N)20NGG for target two (T2). Target specific sgRNAs listed in Table 2.16 were selected for CRISPR/Cas9n-mediated gene editing of *FUS*. Each guide consisted of annealed pairs of forward and reverse oligonucleotides. Specific 5'-overhanging sequences (CACC- and AAC-) were introduced in each oligo to enable successful cloning within pX335B. The *PAM* sequence is not part of the designed sgRNAs.

Table 2.16 Target specific sgRNA sequences for *FUS* gene editing

Target	Target sequence on + strand (PAM)	sgRNA sequence 5'→3'	Forward Oligo (a)	Reverse Oligo (b)
T1	CCCACTTGAGATAAGATAC TCGC	gcgagtatcttatctcaagt	CACCgcgagt atcttatctcaagt	AAACacttgagata agatactcgc
T2	GTTAGGTAGGAGGGGCAG ATAGG	gtaggtaggaggggcag at	CACCgtaggt aggaggggcag at	AACatctgccctcc tacctaac

FUS coding strand

CTCCTTAGCACCTGTGAGAATATGAACTTCTCTTGGAGGAATGAATGCAACCAGTGTAAAGGCCCTAAACCA
 GATGGCCAGGAGGGGGACCAGGTGGCTCTCATATGGTAAGAAAGGCAGACCTGGTGCTAGGGAGCTGG
 GACCAAAGAATCCTTAATTTTCAGCGGGGAGGCTCGGGGAACATAGGGGAATGGGAATATGATAGATCTTG
 TTTCTTTTGTCTAGGGGTAACACGGGGATGATCGTGTGGTGGCAGAGGAGGCTATGATCGAGGGCGC
 TACCGGGGCGCGGGGACCGTGGAGGCTCCGAGGGGGCCGGGGTGGTGGGACAGAGGTGGCTTT
 GGCCCTGGCAAGATGGATTCCAGGTAAGACTTTAAATCAGAATAAAAAAGTAGAGCAGTTGAACAGAGGCCA
 TAGGATAACAGGGTTTTGTTGAGAAAGTGGTTTCATTTGAGGGCTAGGTGGAAGACCTGAGGTTGTAACCA
 GTAGTGGAGAGGGGAGGAAATTAACACAGGGGGAGTGAATCTGTAGA **CCCACTTGAGATAAGATACTCGCT**
 GG **TTAGCCTGGCTGAGTAACTCAAAATATAATGGATACTTA** ATATCTAGGCTTGGAGAGGCTGGTAACCAATATAATGGATACTTA
 ATTTTTTTTTTTTTTTTGCAGGGGTGAGCACAGACAGGATCGCAGGGAGAGGCCGTATTAATTAGCCTGGCT
 CCCAGGTTCTGGAACAGCTTTTTGTCTGTACCCAGTGTACCCCTGTTATTTTGTAACTTCCAATTCCTGATC
 ACCCAAGGGTTTTTTGTGTCGGACTATGTAATTGTAACCTACCTCTGGTCCCATTAAGGTGACCATTTTAG
 TAAATTTTGTCTCTTCCCTTTTCACTTTCCTGGAAGATCGATGCCGATCAGGAAGGTAGAGAGTTTTTC
 CTGTTACAGATTACCTGCCAGCAGGA

Offset: +3bp

Target1: CCCACTTGAGATAAGATACTCGC

gRNA sequence 5'->3': gcgagtatcttatctcaagt

Oligo a: CACCgcgagtatcttatctcaagt

Oligo b: AAACacttgagataagataactcgc

Target2: GTTAGGTAGGAGGGGCAGATAGG

gRNA sequence 5'->3': gttaggtaggaggggcagat

Oligo a: CACCgttaggtaggaggggcagat

Oligo b: AACatctgcccctcctacctaac

Legend

Target 1 exon
 Target 2 intron
 PAM stopp codon
 AA position 521
 AA position 525
 UTR
 Restriction sites for cloning into pX335B

Figure 2.1 Design of sgRNAs targeting *FUS*.

“FUS coding strand” shows part of the *WT* sequence of *FUS*. sgRNA sequences were manually designed by screening the coding strand of *FUS* for the motifs CCN(N)19C for target 1 (T1) and G(N)20NGG for target 2 (T2). Each sgRNA is assembled from two complementary DNA oligonucleotides (“a” & “b”) containing a distinct 4bp-overhang at the 5'-end to allow ligation into the expression vector. The *PAM* sequence is not part of the sgRNA.

2.2.1.2 Screening for CRISPR/Cas9n-related Off-targets

A theoretical approach was used in order to screen for any possible off-target effects of Cas9n for target specific sgRNAs (T1 and T2, see Table 2.16). In this thesis work two different online tools were used for screening (see Table 2.17).

Table 2.17 Online tools for Off-target detection

Online Tool	Reference
CRISPR Design (Zhang laboratory)	http://crispr.mit.edu
Off-spotter	Pliatsika et al., 2015

2.2.1.3 Cloning of DNA oligos into the pX335B plasmid

Target specific sgRNAs (T1 and T2) were cloned into the pX335B_hCas9_2x sgRNA vector (short pX335B) vector in two cloning steps. To linearize the plasmid, it was digested with *BbsI* (*Bpil*) for 30 min at 37°C (see Table 2.19). In parallel, the sgRNA specific oligos “a” and “b” (Table 2.16) were phosphorylated by T4 Polynucleotide kinase for 30 min at 37°C (Table 2.20). The phosphorylated oligo mixture was directly used for annealing at 95°C for 5 min with subsequent cooling to 25°C at a cooling rate of 5°C/min. Annealed Oligos and linearized vector were then ligated using QuickLigase (NEB) for 20 min at RT (Table 2.21). Finally, unspecific recombination products were degraded via Plasmid-Safe™ DNase.

Table 2.18 Materials for cloning

Name	Company
10x T4 DNA Ligase Buffer with 10 mM ATP	NEB, Massachusetts, USA
T4 Polynucleotide Kinase	NEB, Massachusetts, USA
10x T4 Polynucleotide kinase Buffer	NEB, Massachusetts, USA
2x Quick Ligase Reaction Buffer	NEB, Massachusetts, USA
ATP Solution 25 mM	Epicentre, Wisconsin, USA
10x Plasmid-Safe™ Buffer	Epicentre, Wisconsin, USA
Plasmid-Safe™ ATP-dependent DNase 1000U	Epicentre, Wisconsin, USA

Table 2.19 Mixture for restriction digestion

1 µg	pX335B_hCas9_2x sgRNA plasmid
1 µl	FastDigest <i>BbsI</i> (<i>Bpil</i>) or <i>SapI</i> (<i>Lgul</i>)
1 µl	10x FastDigest Buffer
X µl	H ₂ O
20 µl	Total

Table 2.20 Mixture for annealing of oligos

1 µl	Oligo “a” (10 µM)
1 µl	Oligo “b” (10 µM)
1 µl	10x T4 Ligation Buffer
0.5 µl	T4 PNK
6.5 µl	H ₂ O
10 µl	Total

Table 2.21 Mixture for ligation

1 μ l	Annealed Oligo dilution (1:200)
x μ l	Digested pX335B (50 ng)
5 μ l	10x T4 Ligation Buffer
1 μ l	T4 QuickLigase
X μ l	H ₂ O
11 μl	Total

Table 2.22 Mixture for degradation of unspecific recombination products

11 μ l	Ligation reaction from Table 2.21
1.5 μ l	10x Plasmid-Safe™ Buffer
1 μ l	25 mM ATP
1 μ l	Plasmid-Safe™ Exonuclease
14.5 μl	Total

Ligated plasmids were transformed into JM109 competent *E. coli* (see section 2.2.2.1). After each ligation and transformation step, successfully cloned vectors were identified via colony PCR (see section 2.2.4.1). In order to put the second sgRNA for T2 into pX335B plasmid, the procedure was repeated with the obtained plasmid (containing sgRNA for T1). The second round *SapI* (*Lgul*) was used for restriction digestion (see Table 2.19). Positive clones, containing both target sgRNAs, were amplified, sequenced using pX335_seq_R primer (Table 2.9). Successful sequenced clones were used for targeting of h-iPSC (see section 2.3.5.1).

2.2.1.4 Design & Generation of FUS correction plasmids

The *FUS* genomic DNA sequence of the iPSC line FUS-R521C was aimed to be modified (Table 2.15). The *FUS* correction sequences were designed according to the *WT* sequence of *FUS* (NCBI Ref. Seq. NC_000016.10). Homology arms covering the *FUS-R521C* mutation site of the parental cell line (AA position 521), and in a size of 500 bp upstream and 400 bp downstream of the induced DSB, were used. The *EGFP*-Tag was added to the last exon of *FUS* with a 12 bp linker-DNA sequence (5'-GCCGCCAAATTC-3'). In the FUS-WT-EGFP correction construct, the codon at AA position 521 coding for *R521C* mutation (Tgc) was replaced with its *WT* counterpart (Cgc). In the FUS-P525L-EGFP correction construct, the codon at AA position 521 coding for *R521C* mutation (Tgc) was replaced with its *WT* counterpart (Cgc) and the codon at AA position 525 coding for *WT* sequence (cCg) was replaced with its mutant counterpart (cTg). For detailed sequences used for correction see below. Synthesis of *FUS-EGFP* correction constructs was outsourced to Eurofins Genomics

(Table 2.10). The sequences for *FUS-WT-EGFP* and *FUS-P525L-EGFP* were synthesized *de novo* and cloned into the pEX-K4 backbone by the company.

FUS-WT-EGFP

TCCTTAGCACCTGTGAGAATATGAACTTCTCTTGGAGGAATGAATGCAACCAGTGTAAAGGCC
CCTAAACCAGATGGCCCAGGAGGGGGACCAGGTGGCTCTCACATGGGTAAGAAAGGCAGACC
 TGGTGCTAGGGAGCTGGGACCAAAGAATCCTTAATTTTTTCAGCGGGGAGGCTCGGGGAACATAG
 GGGAAATGGGAATATGATAGATCTTGTTTCTTTTGCCTAG**GGGGTAACTACGGGGATGATCGTC**
GTGGTGGCAGAGGAGGCTATGATCGAGGCGGCTACCGGGGCCGCGGCGGGGACCGTGGAGG
CTTCCGAGGGGGCCGGGGTGGTGGGGACAGAGGTGGCTTTGGCCCTGGCAAGATGGATTCCA
GGTAAGACTTTAAATCAGAATAAAAAAGTAGAGCAGTTGAACAGAGGCCATAGGATAACAGGGTT
 TTGTTGAGAAAGTGGTTTCATTTTGAGGGCTAGGTGGAAAGACCTGAGGTTGTAACCAGTAGTGG
 AGAGGGAAGGAAATTAACCTCAGGGGGAGTGAATCTGTAGACCCACTTGAGATAAGATACTCGCT
 GGGTTAGGTAGGAGGGGCAGATAGGATATCTAGGCTTGGAGAGGCTGGTAACTCAAATATAATG
 GATACTTAATTTTTTTTTTTTTTTTTTGCAGGGGTGAGCACAGACAGGAT**CGCAGGGAGAGGCCGT**
AT **SCCGCCAAATTC** ATGGTGAGCAAGGGCGAGGAGCTGTTACCGGGGTGGTGCCATCCTGG
 TCGAGCTGGACGGCGACGTAAACGGCCACAAGTTCAGCGTGTCCGGCGAGGGCGAGGGCGAT
 GCCACCTACGGCAAGCTGACCCTGAAGTTCATCTGCACCACCGCAAGCTGCCCGTGCCCTGG
 CCCACCCTCGTGACCACCCTGACCTACGGCGTGCAGTGCTTACGCCGCTACCCCGACCACATGA
 AGCAGCACGACTTCTTCAAGTCCGCCATGCCGAAGGCTACGTCCAGGAGCGCACCATCTTCTT
 CAAGGACGACGGCAACTACAAGACCCGCGCCGAGGTGAAGTTCAGAGGGCGACACCCTGGTGAA
 CCGCATCGAGCTGAAGGGCATCGACTTCAAGGAGGACGGCAACATCCTGGGGCACAAGCTGGA
 GTACAACACTACAACAGCCACAACGTCTATATCATGGCCGACAAGCAGAAGAACGGCATCAAGGTG
 AACTTCAAGATCCGCCACAACATCGAGGACGGCAGCGTGCAGCTCGCCGACCACTACCAGCAGA
 ACACCCCATCGGGCAGCGCCCGTGCTGCTGCCCGACAACCACTACCTGAGCACCCAGTCCG
 CCCTGAGCAAAGACCCCAACGAGAAGCGCGATCACATGGTCTGCTGGAGTTCGTGACCGCCG
 CCGGATCACTCTCGGCATGGACGAGCTGTACAAG**TAA**TTAGCCTGGCTCCCGAGTTCTGGAA
 CAGCTTTTTGTCTGTACCCAGTGTTACCCTCGTTATTTGTAACCTTCCAATCCTGATCACCCA
 AGGGTTTTTTGTGTCGACTATGTAATTGTAACCTATACTCTGGTTCCCATTAAGTGACCATT
 TAGTTAAATTTTGTCTCTTCCCTTTTCACTTCTGGAAGATCGATGTCCCGATCAGGAAGG
 TAGAGAGTTTTCTGTTTCAGATTACCCTGCCAGCAGGA

Legend: Intron (*FUS*), **Exon (*FUS*)**, UTR (*FUS*), *EGFP*, **Linker DNA**, **Stop**, **Codon AA position 521**, **Codon AA position 525**

FUS-P525L-EGFP

CTCCTTAGCACCTGTGAGAATATGAACTTCTCTTGGAGGAATGAATGCAACCAGTGTAAAGGCC
CCCTAAACCAGATGGCCCAGGAGGGGGACCAGGTGGCTCTCACATGGGTAAGAAAGGCAGAC
 CTGGTGCTAGGGAGCTGGGACCAAAGAATCCTTAATTTTTTCAGCGGGGAGGCTCGGGGAACATA
 GGGGAATGGGAATATGATAGATCTTGTTTCTTTTGCCTAGGGGGTAACTACGGGGATGATCGT
CGTGGTGGCAGAGGAGGCTATGATCGAGGCGGCTACCGGGGCCGCGGCGGGGACCGTGGAG

GCTTCGAGAGGGGGCCGGGGTGGTGGGGACAGAGGTGGCTTTGGCCCTGGCAAGATGGATTCC
AGGTAAGACTTTAAATCAGAATAAAAAAGTAGAGCAGTTGAACAGAGGCCATAGGATAACAGGGT
 TTTGTTGAGAAAGTGGTTTCATTTTGAGGGCTAGGTGGAAAGACCTGAGGTTGTAACAGTAGTG
 GAGAGGGAAGGAAATTAACCTAGGGGGAGTGAATCTGTAGACCCACTTGAGATAAGATACTCG
 CTGGGTTAGGTAGGAGGGGCAGATAGGATATCTAGGCTTGGAGAGGCTGGTAACTCAAATATAA
 TGGATACTTAATTTTTTTTTTTTTTTTTTGCAG**GGGTGAGCACAGACAGGATCGCAGGGAGAGGCT**
GTAT**CCCGCCAAATTC**ATGGTGAGCAAGGGCGAGGAGCTGTTACCGGGGTGGTGCCCATCCT
 GGTGAGCTGGACGGCGACGTAACCGGCCACAAGTTCAGCGTGTCCGGCGAGGGCGAGGGCG
 ATGCCACCTACGGCAAGCTGACCCTGAAGTTCATCTGCACCACCGGCAAGCTGCCCGTGCCCTG
 GCCCACCTCGTGACCACCTGACCTACGGCGTGACGTGCTTCAGCCGCTACCCCGACCACATG
 AAGCAGCAGACTTCTTCAAGTCCGCCATGCCGAAGGCTACGTCCAGGAGCGCACCATCTTCT
 TCAAGGACGACGGCAACTACAAGACCCGCGCCGAGGTGAAGTTCGAGGGCGACACCCTGGTGA
 ACCGCATCGAGCTGAAGGGCATCGACTTCAAGGAGGACGGCAACATCCTGGGGCACAAGCTGG
 AGTACAACACTACAACAGCCACAACGTCTATATCATGGCCGACAAGCAGAAGAACGGCATCAAGGT
 GAACTTCAAGATCCGCCACAACATCGAGGACGGCAGCGTGACGCTCGCCGACCACTACCAGCA
 GAACACCCCATCGGCGACGGCCCGTGCTGCTGCCCGACAACCACTACCTGAGCACCCAGTC
 CGCCCTGAGCAAAGACCCCAACGAGAAGCGCGATCACATGGTCCTGCTGGAGTTCGTGACCGC
 CGCCGGGATCACTCTCGGCATGGACGAGCTGTACAAG**TAA**TTAGCCTGGCTCCCCAGGTTCTGG
 AACAGCTTTTTGTCTGTACCCAGTGTTACCCTCGTTATTTGTAACCTTCCAATTCCTGATCACC
 CAAGGGTTTTTTGTGTCGGACTATGTAATTGTAACCTATACTCTGGTTCCCATTAAGTGACCA
 TTTTAGTTAAATTTTGTTCCTCTTCCCCCTTTTCACTTTCTGGAAGATCGATGTCCCGATCAGGAA
 GGTAGAGAGTTTTCTGTTGAGATTACCCTGCCAGCAGGA

Legend: Intron (*FUS*), **Exon (*FUS*)**, UTR (*FUS*), *EGFP*, **Linker DNA**, **Stop**, **Codon AA position 521**, **Codon AA position 525**

2.2.2 Plasmid preparation

2.2.2.1 Transformation

Chemical competent E.coli JM109 (Promega) were thawed on ice. To transform, 50 µl of bacteria were aliquoted into 1.5 ml tube and 0.4 µl β-Mercaptoethanol were added. E.coli were incubated on ice for 10 min and swirled every 2 min. Then, 50 ng plasmid DNA were added and incubated on ice for 30 min. Heat shock was applied at 42°C for 45 sec after which tubes were immediately placed on ice for 2 min. 500 µl S.O.C medium was added to the tubes which were then incubated at 37°C, 300 rpm for 60 min in thermomixer. Bacteria transformed with plasmid were plated on agar plates containing appropriate antibiotics (Ampicillin or Kanamycin) and incubated at 37°C overnight.

2.2.2.2 Mini-culture and plasmid preparation

E.coli colonies on agar plates were picked (5 to 10 colonies) and directly added into a conical flask (one colony per flask) containing 15 ml LB medium with appropriate antibiotics and cultured overnight at 37°C, 210rpm.

The ZR Plasmid Miniprep kit was used for plasmid purification following manufacturer's protocol. Obtained plasmid were either used for further cloning (see section 2.2.1.3) or for transfection (see section 2.3.5.1), after successful confirmation via sequencing (see section 2.2.5).

2.2.3 Isolation of genomic DNA

For the isolation of genomic DNA (gDNA), cells were grown on 1w/6w format. Cells were washed once with DPBS and 1 ml fresh DPBS was added to the cells. Using a cell scraper cells were detached from the plate and transferred to 1.5 ml tube. The cells were centrifuged down and supernatant was removed. The cell pellet was either directly used for gDNA isolation or stored at -20°C for later extraction. To isolate gDNA, the DNeasy Blood & Tissue Kit (Table 2.3) was used and gDNA was isolated according to manufacturer's instructions.

2.2.4 Polymerase chain reaction (PCR)

2.2.4.1 Colony PCR

Positive clones of pX335B plasmid, containing sgRNAs for T1 and T2, were identified by colony PCR using the respective "a"-oligo as forward primer and pX335_seq_R as reverse primer (Table 2.9 and Table 2.16).

Bacterial colonies were resuspended in 30µl of H₂O and, simultaneously, a backup-plate for eventual inoculation was prepared. Cells were lysed at 95°C for 5 min and 3µl of the lysate were used as template for the PCR reaction (see Table 2.23 and Table 2.24). After amplification, 10µl of the PCR were analyzed on a 1% agarose gel for 20min at 120V (see section 2.2.6).

Table 2.23 Mixture for Colony PCR

Component	25 μ l reaction	Final conc.
OneTaq 2x Master Mix with Standard Buffer	12.5 μ l	1X
10 μ M Forward Primer	0.5 μ l	0.2 μ M
10 μ M Reverse Primer	0.5 μ l	0.2 μ M
Template DNA	3 μ l	<1 ng
Nuclease-Free Water	8.5 μ l	

Table 2.24 Program for Colony PCR

Step	Temp	Time
Initial Denaturation	94°C	1 min
	94°C	30 sec
30x cycles	64°C	30 sec
	68°C	30 sec
Final Extension	68°C	5 min
Hold	4°C	

2.2.4.2 Screening PCR for FUS-EGFP

To confirm the presence of the *EGFP*-Tag within the genomic sequence of *FUS*, genomic DNA of previously picked clones (see section 2.3.5.2) was analyzed. A forward primer (FUS-1.3-F) targeting *FUS* upstream of the used homology arms was used and a reverse primer (EGFP Rev 1) targeting *EGFP* (Table 2.9), resulting in amplification of a 909 bp long PCR fragment. After amplification, 10 μ l of the PCR were analyzed on a 1% agarose gel (see section 2.2.6).

Table 2.25 Mixture for Screening PCR

Component	25 μ l reaction	Final conc.
10x <i>Pfx</i> Amplification Buffer	3.75 μ l	1.5X
dNTPs	2 μ l	0.8 mM
MgSO ₄	0.5 μ l	1 mM
10 μ M Forward Primer	1.25 μ l	12.5 pmol
10 μ M Reverse Primer	1.25 μ l	12.5 pmol
Template DNA	1.5 μ l	>40 ng
Platinum™ <i>Pfx</i> Polymerase	0.2 μ l	0.5 U
Nuclease-Free Water	14.55 μ l	

Table 2.26 Program for Screening PCR

Step	Temp	Time
Initial Denaturation	94°C	5 min
	94°C	15 sec
30x cycles	58°C	30 sec
	68°C	45 sec
Final Extension	68°C	5 min
Hold	4°C	

2.2.4.3 Genotyping PCR of FUS-EGFP positive clones

To determine the genotype of FUS-EGFP positive iPSC clones, genomic DNA was amplified using the primer pair FUS-2.1-F/-R (Table 2.9) resulting in the generation of three possible PCR product combinations (Table 2.27).

Table 2.27 Possible PCR products of FUS-EGFP Genotyping PCR

Genotype	WT allele	CRISPR allele
heterozygous	528 bp	1257 bp
homozygous	/	1257 bp
homozygous	528 bp	/

Table 2.28 Mixture for Genotyping PCR

Component	25 µl reaction	Final conc.
10x <i>Pfx</i> Amplification Buffer	3.75 µl	1.5X
dNTPs	2 µl	0.8 mM
MgSO ₄	0.5 µl	1 mM
10µM Forward Primer	1.25 µl	12.5 pmol
10µM Reverse Primer	1.25 µl	12.5 pmol
Template DNA	1 µl	>40 ng
Platinum™ <i>Pfx</i> Polymerase	0.3 µl	0.75 U
Nuclease-Free Water	14.95 µl	

Table 2.29 Program for Genotyping PCR

Step	Temp	Time
Initial Denaturation	94°C	5 min
	94°C	15 sec
30x cycles	58°C	30 sec
	68°C	1 min 45 sec

Final Extension	68°C	5 min
Hold	4°C	

2.2.5 Sequencing

Purified plasmids or PCR fragments were analyzed via Sanger sequencing method. For that, 5 µl template DNA and 5 µl primer (5 pmol/µl) were mixed in a 1.5 ml tube. The tube was labeled and send to GATC Biotech (Konstanz, GER) for LIGHTrun sequencing. Returned sequences were analyzed with SnapGene Viewer software and NCBI nucleotide blast.

2.2.5.1 Sequencing of FUS-EGFP positive iPSC clones

In order to confirm successful CRISPR/Cas9n-mediated gene editing, a genotyping PCR with 50 µl reaction mixture was run (section 2.2.4.3). After amplification, the complete reaction mixture was run on a 1% agarose gel (section 2.2.6) and extracted from it (section 2.2.7). The extracted PCR fragments were send to sequencing. The Primer FUS-seq-R (Table 2.9) was used to sequence PCR fragments representing the *WT* allele of *FUS*. To sequence PCR fragments representing the CRISPR (*FUS-EGFP*) allele the primer EGFP Rev 1 was used (Table 2.9).

2.2.6 Agarose gel electrophoresis

Analysis of PCR products was performed using agarose gel electrophoresis. To prepare 1% gel (w/v), 0.5 g agarose and 50 ml 1xTAE buffer were mixed in a conical flask and heated in microwave until the agarose dissolved. Agarose solution was briefly cooled to which 2.5 µl Midori Green was added and mixture was swirled to distribute evenly. The gel was filled into chamber fitted with 1.5 mm comb and air-bubble free gel was the allowed to polymerize at RT. Gel was then placed in electrophoresis chamber and covered with 1xTAE buffer. 2 µl of 6 x loading buffer was added to 10 µl of sample and filled into wells of the gel. All gel electrophoresis were performed at 70 mAmps, 120V. Bands were detected and imaged using UV transilluminator and biostep argus X1 software, respectively.

2.2.7 Gel extraction of PCR fragments

To extract PCR fragments, the fragments of interest were cut out from the agarose gel and transferred to a 1.5 ml tube. The QIAquick® Gel Extraction Kit (Table 2.3) was used to isolate PCR product from an agarose gel according to manufacturer's instructions.

2.3 Cell culture

All cells used in this work were cultivated at 37°C in a tissue culture incubator maintaining a stable content of 21 % O₂ and 5 % CO₂. Cell culture procedures described in this chapter were all performed under a sterile biosafety cabinet. All media and solutions used, were prewarmed in a 37°C water bath prior to use unless described otherwise.

2.3.1 Cell culture media

Culture media and additives for culturing eukaryotic cells were applied as sterile solution. Media supplement working stocks were stored as aliquots at -20°C. In order to avoid multiple freeze and thaw cycles, aliquots of freshly prepared media were stored at 4°C, if not indicated otherwise by the manufacturer. Growth factors were always added prior to use of pre-warmed media.

iPSC freezing medium

TeSR-E8 or mTeSR1	90 % (v/v)
DMSO	10 % (v/v)
Y-27632	10 µM

Neural Differentiation Medium (NDM) (Burkhardt, Martinez et al. 2013)

DEMEM/F-12	47.6 % (v/v)
Neurobasal	47.6 % (v/v)
GlutaMAX-Supplement (100x)	1% (v/v)
Penicillin-Streptomycin (100x)	1% (v/v)
MEM Non-essential Amino Acids (100x)	1% (v/v)
N2-Supplement (100x)	0.5% (v/v)
B27-Supplement without Vitamin A (50x)	0.5% (v/v)
β – mercaptoethanol (50 mM)	100 µM
Insulin	5 µg/ml

EB medium for ectodermal differentiation

DMEM/F-12	48.6% (v/v)
Neurobasal	48.6% (v/v)
N2-Supplement (100x)	1% (v/v)
B27-Supplement without Vitamin A (50x)	0.5% (v/v)
Penicillin-Streptomycin-Glutamine (100x)	1% (v/v)

2-Mercaptoethanol (50 nM)	0.1% (v/v)
BSA Fraction V 7.5%	0.2% (v/v)

EB medium for endodermal and mesodermal differentiation

DMEM (Hi-glucose)	76.9% (v/v)
Fetal Calf Serum (FCS)	20% (v/v)
Penicillin-Streptomycin-Glutamine (100x)	1% (v/v)
MEM Non-Essential Amino Acids (100x)	1% (v/v)
2-Mercaptoethanol (50 nM)	0.1% (v/v)
1-Thioglycerol (0.04 M stock solution)	1% (v/v)

N2B27 medium

DMEM/F12	48.75% (v/v)
Neurobasal	48.75% (v/v)
N2-Supplement (100x)	0.5% (v/v)
B27-Supplement without Vitamin A (50x)	1% (v/v)
Penicillin-Streptomycin-Glutamine (100x)	1% (v/v)

N2B27 freezing medium

N2B27 medium	90% (v/v)
DMSO	10% (v/v)

2.3.2 Coatings

The following coatings were used to allow cell attachment and growth of monolayer cell cultures. The volume used for the following coating procedures was 250µl per well of a 4-well plate. For coating of 12-well and 6-well plates the amount used was increased twofold and fourfold respectively. 10 cm cell culture dishes were coated with 5 - 7 ml of coating solution.

2.3.2.1 Matrigel™ coating

Matrigel™ was pre-diluted 1:5 in DMEM/F12 and working aliquots were stored at -20°C. For coating, pre-diluted Matrigel™ was thawed at RT and further diluted 1:20 in cold DMEM/F12. Unused working aliquots were immediately stored at -20°C after use, to prevent polymerization. Culture plates were coated with Matrigel™ solution and incubated at 37°C for 15-30 minutes. Plates could be directly used. Coated plates also could be stored for up to two weeks at 4°C. Cold plates (4°C) were allowed to equilibrate to RT for at least 30 minutes prior

to use. Matrigel™ solution was then removed and cells were plated on the coated culture vessels without any further washing steps.

2.3.2.2 Poly-L-ornithine/ Laminin coating

Neural precursor cells (NPCs) and cortical cultures were differentiated on Poly-L-ornithine (PLO)/ Laminin coated culture vessels. PLO-solution was diluted in DPBS to a total amount of 15% (v/v). Culture plates were coated with 15% PLO-solution and incubated overnight at 37°C. The next day, plates were washed three times with DPBS and shortly dried at RT. Dried PLO pre-coated plates were incubated with 1% (v/v) Laminin (Sigma-Aldrich) solution in DPBS overnight at 37°C. Prior to use, plates were washed three times with DPBS. PLO/Laminin coated plates could be stored at 4°C in DPBS for up to four weeks or used directly.

Microfluidic chamber (MFC) systems were assembled as previously established in our group (Naumann, Pal et al. 2018). In brief, Nunc™ glass bottom dishes were coated with 30% (v/v) PLO in DPBS at 37°C overnight. Xona silicon MFC units were stored in 70% (v/v) ethanol in water for sterilization. PLO pre-coated dishes were washed three times with sterile water. Dishes and silicon chambers were dried for ~30 min under UV light under the laminar flow bench. Dried silicon chambers were carefully attached to the dry PLO-coated glass bottom dishes. The system was perfused with 2% (v/v) Laminin (Roche) in DPBS. Assembled and perfused MFCs were incubated overnight at 37°C. Prior to use, MFCs were washed once with corresponding medium.

2.3.3 Cell count

To plate cells at a defined density, cells needed to be count. For that, cells were detached from culture vessels using accutase as described under 2.3.7.4. The cell pellet was resuspended in 1 ml culture medium. For better counting, a dilution of this cell suspension was prepared. Most often, a 1:100 dilution was prepared by adding 1 µl of cell suspension to 99 µl medium.

Cells were counted using a hemocytometer. 10 µl of diluted cell suspension were given to the hemocytometer and cells were counted with an inverted microscope under 10 x magnification. Cells within each of the four corner squares were count and the average value was calculated. Thereafter, the cell number could be calculated by using the following formula:

$$\text{Average value} \times \text{dilution factor} \times 10,000 \text{ cell/ml} = \text{total cells/ml}$$

Finally, the needed dilution factor of the current cell suspension for plating could be calculated by using the following formula:

$$\text{Measured cells concentration} / \text{desired cell concentration} = \text{dilution factor}$$

2.3.4 Cultivation of human induced pluripotent stem cells

2.3.4.1 Expansion and maintenance of human iPSCs

Human iPSCs were cultured on matrigel and maintained in feeder-free, animal component-free culture medium. In general, iPSCs used for gene editing or simple expansion culture were maintained in TeSR-E8. iPSCs needed for neural differentiation were cultured in mTeSR1. Expansion cultures were cultured in 12-well or 6-well format. Medium was changed every day, except on weekends/holidays on which iPSCs were double fed (e.g. from Friday to Sunday).

Cells typically were passaged when they reached 70-90% confluence (usually once a week) in a splitting ratio 1:10 to 1:50. Prior to splitting, matrigel coated plates were prepared (see section 2.3.2.1) and medium containing 10 μM of the ROCK inhibitor Y-27632 (ROCKi) was pre-warmed. iPSC were splitted using ReLeSR. For that, culture medium was removed and ReLeSR was added (500 μl per 1w/6w, 250 μl per 1w/12w). Cells were briefly rocked back and forth with the solution for 30 sec. Then ReLeSR was removed and iPSC were incubated without any solution for 5 min at RT. After incubation, feeder-free medium containing Y-27632 was added to the cells. iPSC colonies were detached by holding the plate with one hand and using the other hand to firmly tap the side of the plate for approximately 30 - 60 seconds. Detached cells were transferred in the respective splitting ratio onto a new plate containing pre-warmed feeder-free medium containing Y-27632. The following day, medium was replaced by feeder-free medium without Y-27632.

2.3.4.2 Freezing and thawing of iPSCs

In order to freeze iPSCs, colonies were detached and collected as described in

Section 2.3.4.1. Colonies were then resuspended in feeder-free medium containing 10% DMSO and 10 μM Y-27632. iPSC were then immediately placed at -80°C using a Nalgene™ Cryo freezing container which ensures a cooling rate of $1^{\circ}\text{C}/\text{min}$. For long term storage, iPSCs were kept in a liquid nitrogen tank. As a rule, one confluent well of a 6-well plate was frozen down into 1 to 4 cryovial using 1 ml of freezing media.

To thaw iPSCs, 1 to 6 wells of a 6-well plates were prepared with matrigel as described above. The iPSCs were then partially thawed at 37°C . Colonies were resuspended in 5 ml cold

feeder-free media, collected in a 15 ml falcon tube and centrifuged at 1200 rpm for 1 minute. Supernatant was removed, cells were resuspended in 1 ml warm feeder-free medium containing Y-27632 and evenly distributed throughout the well. The next day, medium was replaced by feeder-free medium without Y-27632 and iPSCs were maintained as described under section 2.3.4.1.

2.3.5 CRISPR/Cas9n-mediated gene editing of iPSCs

For gene targeting of iPSCs, feeder-free iPSCs cultured in TeSR-E8 medium were co-transfected with pX335B vector (containing the Cas9n cassette, two sgRNAs and a puromycin selection cassette) and pEX-K4 vector (containing the *FUS-WT-EGFP* or *FUS-P525L-EGFP* sequence) using FuGENE HD transfection reagent (see 2.3.5.1). 24 h after transfection, cells containing the pX335B vector were selected by treatment with 0.4 µg/µl Puromycin (InvivoGen) for another 16h to 24h. Following selection, cells were allowed to recover for 3-7 days in TeSR-E8 with daily medium changes. After recovery, iPSCs were passaged onto a new 6-well plate in a clonal dilution (2000 cells per 6-well) in Y-27632-containing medium. After 10-14 days EGFP-positive clones were picked as described in section 2.3.5.2 and further cultured for characterization.

2.3.5.1 Transfection of feeder-free iPSCs

The day before transfection 175,000 iPSC were plated onto 1w/6w into TeSR-E8 + Y-27632. Prior to transfection, transfection reagent Fugene HD ® was allowed to adapt to RT and iPSC medium was replaced with fresh TeSR-E8 + Y-27632 (2 ml per 1w/6w). Then transfection mixture was prepared. For that, 200 µl OptiMEM were mixed with 2 µg plasmid DNA (1 µg pX335B and 1 µg correction plasmid) in a 1.5 ml tube and vortexed. Then, 7 µl Fugene HD ® were added to the mixture and vortexed immediately. Transfection mixture was incubated for 15 min at RT. Then the mixture was added dropwise to the iPSC and cells were incubated overnight. After 24h, transfection medium was replaced with new TeSR-E8 or selection medium.

2.3.5.2 Single colony selection

Prior to picking iPSC colonies, matrigel coated 12-well plates were prepared (2.3.2.1). At least two plates were prepared per cell line. TeSR-E8 medium containing Y-27632 was pre-warmed at 37°C water bath. Shortly before picking, matrigel solution was exchanged by the pre-warmed medium. Under a fluorescence microscope EGFP-positive iPSC colonies were

detected and marked on the plates. The EGFP-positive colonies were then picked under an inverted bright-field microscope as described below.

Using 10 μ l pipette tips, previously marked colonies were carefully detached using the tip of 10 μ l pipette tips. Floating colonies were collected with the 10 μ l pipette tip directly plated into one well of 12-well plate (one colony per well). About 12-24 colonies were picked per cell line. Colonies were titrated using 1 ml pipette tips about 2-4 times within the wells.

The next day medium was replaced with TeSR-E8 without Y-27632. Colonies were allowed to grow for 3-7 days with daily medium changes. iPSCs were splitted as described in section 2.3.4.1 onto new wells of 12-well plate for further expansion and characterization.

2.3.6 Differentiation of human iPSCs into three germ layer

Three germ layer formation of human iPSCs was obtained via embryoid body (EB) differentiation. iPSCs were cultured as described under 2.3.4. For EB formation, iPSCs were expanded on 2w/6w or 3w/6w format. When colonies reached 70 to 90 % confluency, iPSCs were washed once with DPBS and 1mg/ml dispase diluted in iPSC medium was added to the cells. iPSCs were incubated with the enzyme for 30 to 45 min. Every 10 min iPSCs were checked for detachment. Once colonies detached completely, they were collected in a 15 ml falcon and centrifuged for 10 sec at 1200 rpm. For all following pipetting steps the cells were pipetted carefully and not titrated because the colonies were aimed to be collected as a whole (not as small fragments). The supernatant was removed and the cells were additionally washed twice with DMEM/F12 to further dilute remaining dispase. The cell pellet was then resuspended carefully in 6 ml DMEM/F12 and iPSCs were split 1/3 and 2/3 into two 15 ml falcons. Cells were again centrifuged for 10 sec at 1200 rpm and the supernatant was removed.

For ectodermal differentiation, 1/3 of the cells were resuspended in mTeSR1 supplemented with 5 μ M Y-27632, 10 μ M SB431542, and 1 μ M Dorsomorphin plated. For meso-/endodermal differentiation, 2/3 of the cells were resuspended in mTeSR1 supplemented with only 5 μ M Y-27632. Colonies were plated onto two 6 cm dishes. Two days later, medium was changed to same condition but without Y-27632. Another 2 days later, EBs were collected and centrifuged for 10 sec at 1200 rpm and supernatant was removed. EBs were resuspended in ectodermal differentiation medium and plated on Matrigel coated 4-well plate (). For meso- and endodermal differentiation, EBs were resuspended in meso-/endodermal differentiation medium and plated on gelatine coated 4-well plate (). Medium was changed every other day for 14 days. At day 14, cells were fixed for immunocytochemical analysis.

2.3.7 Differentiation of human iPSCs into spinal and cortical neural cell types

2.3.7.1 Expansion of human small molecule neuronal precursor cells

Supplements for NPC expansion:

CHIR	3 μ M
AA	150 μ M
PMA	0.5 μ M

Expansion and differentiation of small molecule neuronal precursor cells (smNPCs) is basing on protocols established by Dr. Peter Reinhardt (Reinhardt, Glatza et al. 2013). The smNPCs were grown on matrigel coated plates in N2B27 media supplemented with 3 μ M CHIR99021 (CHIR), 150 μ M ascorbic acid (AA) and 0.5 μ M purmorphamine (PMA). Medium was changed every other day during expansion phase. NPCs were passaged once a week or when they reached 70-90% confluence. For passaging, cells were splitted using accutase (see section 2.3.7.4). NPCs were plated onto new matrigel coated plates in fresh N2B27 media supplemented with growth factors.

2.3.7.2 Differentiation of human smNPCs into spinal motor neurons

Supplements for differentiation induction:

BDNF	1 ng/ml
AA	0.2 mM
RA	1 μ M
GDNF	1 ng/ml
SAG	0.5 μ M

Supplements for maturation:

Activin A	5 ng/ml (just the first day)
cAMP	0.1 mM
BDNF	2 ng/ml
TGF β -3	1 ng/ml
GDNF	2 ng/ml

To induce differentiation into spinal MNs, smNPCs were splitted in a 1:10 ratio (see section 2.3.7.4) onto new matrigel coated plates (day 0 of differentiation process). Figure 2.2 shows a schematic overview of the differentiation steps. NPCs were plated in N2B27 medium containing growth factors for differentiation induction (see above). In differentiation phase (day 0 to 5), medium was changed every other day. On day 6, medium for differentiation induction was changed to N2B27 medium containing factors for maturation (see above). Only on the first day of medium change to maturation (day 6 to 7) Activin A was added. On day 7 medium was

changed to N2B27 maturation medium without Activin A. On day 8 to 10, cells were then splitted into their desired format onto POL/Laminin coated plates (see section 2.3.2.2). Cells were split using accutase (see section 2.3.7.4). Prior to seeding, cells were counted (see section 2.3.3) and plated into N2B27 maturation medium at the following densities: 1×10^6 cells/6 well, 4×10^4 cells/4 well, and $10 \mu\text{l}$ of 30×10^6 concentrated cell suspension per MFC. Spinal MNs were allowed to further mature/age from this time point on with medium changes every other day.



Figure 2.2 Workflow chart of smNPC differentiation into spinal MNs.

Differentiation of human smNPCs was induced by BDNF, AA, RA, GDNF, and SAG. After 6 days of differentiation spinal MN maturation was promoted by cAMP, BDNF, TGF β -3, and GDNF. On day 8 to 10 spinal MNs were re-plated onto their final format for further maturation and aging. © Julia Japtok

2.3.7.3 Differentiation of human iPSCs into cortical neurons and astrocytes

Supplements for neural induction:

Dorsomorphin	1.5 μM
SB431542	10 μM

Supplements for neural maintenance:

BDNF	2 ng/ml
GDNF	2 ng/ml
RA	0.05 μM

Supplements for neural maintenance in MFC:

Seeding site (proximal):

RA	0.05 μM
----	--------------------

Exit site (proximal):

BDNF	2 ng/ml
GDNF	2 ng/ml
Retinoic acid	0.05 μM

Human iPSCs were split using ReLeSR (see section 2.3.4.1) and plated at a high density on matrigel coated 6-well plates in mTeSR1 containing 10 μM Y-27632. iPSCs were cultured for another 3 to 5 days in mTeSR1 without Y-27632 to obtain confluent cell layer for neural induction, with medium changes every day. When iPSCs reached a confluence of 80 to 90 %, differentiation into cortical lineage was induced by changing the medium to neural differentiation medium (NDM, see section 2.3.1) containing factors Dorsomorphin and SB431542 for neural induction (day 0 of differentiation process). Figure 2.3 shows a schematic

overview of the differentiation steps. Cells were differentiated for 10 days in NDM induction medium. From day 11 to 14 the thereby derived neuroepithelial cells/ neural progenitor cells (NPCs) were fed with NDM only (not containing any growth factors). From days 15 to 19 NDM was supplemented with 0.05 μM retinoic acid (RA). From day 0 to 20 medium was changed daily, supplemented with the respective growth factors.

At day 20 cultures were dissociated using accutase (see section 2.3.7.4). The cells were replated at a density of 19.2×10^4 cells per cm^2 onto PLO/Laminin coated cell culture 6-well plates in NDM maintenance medium containing BDNF, GDNF, and RA. For splitting, 10 μM Y-27632 were added to the medium only for one day. Differentiating NPCs were cultured from day 21 to 45 in NDM supplemented with growth factors for neural maintenance. Medium was changed every other day.

At day 40 to 45, cells were passaged into their final format for experimental analysis onto new PLO/Laminin coated plates (see section 2.3.2.2). Prior to seeding, cells were counted (see section 2.3.3) and plated into NDM maintenance medium supplemented with 10 μM Y-27632 at the following densities: 30.000 cells/ cm^2 for immunostaining approaches and laser cutter experiments. For axonal trafficking analysis 10 μl of 30×10^6 concentrated cell suspension per MFC were plated. For protein-dependent approaches (e.g. ELISA) 60.000 cells/ cm^2 cells were plated. The next day, Y-27632 was removed and cortical culture were allowed to further mature and age from this time point on. For cortical MFC cultures, on the seeding site (proximal) 50 μl medium per well were applied while on the exit sites (distal) 100 μl medium per well were added. NDM maintenance medium was changed 2 to 3 times a week.

In general, cortical neurons are already detectable from day 20 to 30 on, mainly consisting of lower layer neurons. Upper layer cortical neurons can be detected between day 40 to 50 earliest. To obtain astrocytes, cortical cultures need to be matured for at least 70 to 80 days. Therefore, all experimental analysis was implemented between maturation day 80 to 150, if not stated otherwise.



Figure 2.3 Workflow chart of iPSC differentiation into cortical cells.

Differentiation of human iPSCs was induced by SB431542 (SB) and Dorsomophin (D) for 10 days. On days 11 to 15 RA was applied. Differentiating cells were re-plated on day 20 and further cultured in neural maintenance medium supplied with RA, BDNF, and GDNF. On day 45, cortical cells were re-plated onto their final format for further maturation and aging. © Julia Japtok

2.3.7.4 Splitting of NPCs, spinal MNs, and cortical cells using accutase

To obtain a single cell suspension, as for instance required for cell counting, cells were split using accutase. To detach cells, culture medium was replaced by accutase solution. In general

0.5 ml were used to detach cells from 1w/6w format. Cells were incubated for 10 minutes at 37°C with accutase solution. Cells thereafter were dissociated into single cells clumps by pipetting up and down 6 to 10 times in accutase solution. The solution containing the cells, was then transferred to 15 ml falcon and diluted with 4 volumes of pre-warmed medium. Cells were centrifuged for 2 minutes at 160xg. Supernatant was discarded and cells were resuspended in the required amount of pre-warmed culture medium for plating onto new plates.

2.4 Microscopy

2.4.1 Immunofluorescence staining

Blocking solution (in DPBS)

BSA	1%
Donkey serum	5%
Glycine	0.3M
Triton-X	0.02%

The following specifications refer to one well of a 4-well plate. Prior staining, cells needed to be fixed. For that, media was removed, cells were washed twice with DPBS and fixed with 4% PFA for 10 min at RT. PFA was aspirated and cells were washed three times with DPBS. Fixed cells could be stored in DPBS at 4°C for up to one week or stained directly.

Fixed cells were first permeabilised for 10 minutes in 250 µl 0.2 % Triton X solution. Cells then were incubated for 1 hour at RT in 250 µl blocking solution. Following blocking, primary antibodies (Table 2.6) were diluted in blocking solution and cells were incubated with 250 µl primary antibody solution overnight at 4°C. The next day, cells were washed 4 to 5 times for 5 minutes in DPBS. Secondary antibodies (Table 2.7) were diluted in blocking solution and cells were incubated for 1 hour at RT in 250µl secondary antibody solution. Secondary antibody solution was aspirated and samples were washed three times for 5 min in DPBS. During all steps involving secondary antibodies, the sample was protected from light. Nuclei from cells were stained using Hoechst (Table 2.8). 0.75 µl of Hoechst solution were mixed with 1 ml DPBS and cells were incubated in 250 µl Hoechst solution for 5 minutes at RT. Cells were washed three times with PBS. Cells were finally covered with a glass coverslip. For that 1 to 2 drops of mounting medium were given to the cells and a coverslip was carefully mounted onto the cells. In contrast, cells that were already grown on coverslips were mounted onto glass slides. One drop of mounting medium was put onto a glass slide for each coverslip with stained cells and coverslips were carefully removed from the wells and mounted onto the glass slide. Covered cells were sealed with nail polish the next day. Immunofluorescence stained cells were stored at 4°C.

2.4.2 Fluorescence microscopy

Images of immunofluorescence staining or *in vitro* fluorescence for qualitative analysis were obtained with the fluorescence microscope Observer.Z1. Images of cortical marker (Figure 3.2), FUS-EGFP expression in iPSCs (Figure 3.4), pluripotency marker (Figure 3.5), and germ layer marker (Figure 3.6), and distal axonal outgrowth (Figure 3.33) were taken with this microscope.

For quantitative analyses (including DNA damage, C9-HRE associated DPRs, FUS-EGFP expression in cortical cultures, and TDP43), images were obtained using the fluorescence microscope Axiovert 200M from Light Microscopy Facility (a Core Facility of the CMCB Technology Platform at TU Dresden). Apotome microscopy was conducted using either a 63x oil or 40x air objective. If not stated otherwise, 5x Apotome projection images per channel were taken to obtain one optical-sectioned image. Randomly assigned images of different experiments were evaluated either qualitative or quantitative using CellProfiler image analysis software (Table 2.14).

2.4.3 Live cell imaging

Live cell imaging approaches were conducted for the analysis of organelle trafficking in MFC cultures (see section 2.5.2) and laser cut assays of FUS-EGFP expressing iPSCs and cortical neurons (see section 2.5.1.2). Dr. Arun Pal. implemented all live cell imaging microscopy. Both approaches, live cell imaging of compartmentalized cultures and DNA damage laser cut assay, were implemented as published by Naumann and Pal, 2018 (Naumann, Pal et al. 2018).

2.5 Investigation of patient-specific *in vitro* cultures

The characterization of human iPSCs, spinal MNs, and cortical cells was performed on 24-well plates with glass coverslips for immunofluorescence staining. For axonal trafficking analysis, cortical cultures were grown in MFC culture system. Laser cut live cell imaging was implemented with cells grown on Nunc glass bottom dishes. Cells required for isolation of protein or DNA were cultured on 6-well plates. For cell densities plated see sections 2.3.7.2 and 2.3.7.3.

2.5.1 DNA damage analysis

DNA damage within patient-specific *in vitro* cultures was assessed by immunofluorescence staining for γ H2AX or 53BP1 and by laser cut live cell imaging approach.

2.5.1.1 Analysis of γ H2AX and 53BP1

Phosphorylated H2A.X (γ H2AX) and 53BP1 can be used to detect DSBs via immunofluorescence staining. Once the cell detects DSBs, DDR signaling is initiated including the phosphorylation of serine 139 of histone H2A.X (Kinner, Wu et al. 2008, Grabarz, Barascu et al. 2012). This is followed by the recruitment of 53BP1. The amount of nuclear DNA damage within neurons and astrocytes was assessed by the evaluation of immunofluorescence images.

As a DNA damage positive control, cells were treated with 2 μ M etoposide for 1h to induce DNA damage. To assess whether cells are able to recover after DNA damage induction, etoposide was removed from the medium and cells were allowed to recover for 24h prior to fixation.

Neurons and astrocytes were stained using antibodies against MAP2 or GFAP (Table 2.6). DSBs were detected by staining against γ H2AX or 53BP1 (Table 2.6). Both marker can be visualized as nuclear foci in immunofluorescence staining. Apotome microscopy using a 63x oil objective was conducted to obtain images of one focal plane for analysis (see section 2.4.2). To identify and quantify DSBs, a semi-automated workflow using CellProfiler image analysis software was used (Table 2.14). Analysis pipeline was designed as follows:

1. For Apotome images stained for four markers (e.g. γ H2AX / 53BP1/ MAP2/ Hoechst):
 - a. Loading of images in czi- or tif-format
 - b. Extract metadata
 - c. Split channels into greyscale components
2. Identify nuclei automatically via Hoechst staining
3. Identify MAP2 region automatically via MAP2 staining
4. Overlay MAP2 and Heochst channels with detected outlines in point 2 and 3
5. Manually select nuclei positive for MAP2, using overlay created in point 4
6. Mask γ H2AX channel with manually selected MAP2 positive nuclei (point 5)
7. Mask 53BP1 channel with manually selected MAP2 positive nuclei (point 5)
8. Identify γ H2AX foci within MAP2 positive nuclei automatically (point 6), by using a robust background tresholding within each assigned nuclei
9. Identify 53BP1 foci within MAP2 positive nuclei automatically (point 7), by using a robust background tresholding within each assigned nuclei
10. Measure object size, shape, and number of identified γ H2AX foci (point 8), 53BP1 foci (point 9), and MAP2 region (point 3)
11. Relate identified objects
 - a. γ H2AX foci (point 8) and MAP2 positive nuclei (point 5)

- b. 53BP1 foci (point 9) and MAP2 positive nuclei (point 5)
- 12. Overlay outlines of identified object to create merged images (e.g. overlay γ H2AX and MAP2 channel with outlines detected in point 8 and 5)
- 13. Save images of interest
- 14. Export measurements as excel spreadsheets

Results derived from semi-automated CellProfiler analysis were assembled and post-filtered in KNIME (Table 2.14). Further, the foci numbers per nuclei and normalized values were calculated using KNIME and exported as excel spreadsheets. Those results were further loaded in Graphpad PRISM 7 for creation of graphs and statistical analysis (see section 2.6).

2.5.1.2 DNA damage laser cut assay

Another approach used in this work was the DNA damage laser cut assay, in which nuclear DNA damage at defined positions within nuclei was induced. FUS, as an ALS-associated protein (Kwiatkowski, Bosco et al. 2009, Vance, Rogelj et al. 2009) and known to be involved in DDR (Mastrocola, Kim et al. 2013, Wang, Pan et al. 2013, Qiu, Lee et al. 2014, Rulten, Rotheray et al. 2014, Naumann, Pal et al. 2018), was tagged with EGFP using CRISPR/Cas9n gene editing technique. The generation of EGFP-tagged FUS-WT and FUS-P525L iPSC lines (see section 2.3.5) enabled, concomitant, the live cell imaging of FUS recruitment to DNA damage sites (see section 2.4.3). Aim was to analyze the effect of *FUS* mutation on recruitment in iPSCs and cortical neurons. The UV laser cutter experimental setup was implemented as previously published by our group (Naumann, Pal et al. 2018). Dr. Arun Pal implemented imaging and data evaluation shown in Figure 3.31.

2.5.2 Axonal organelle trafficking analysis

In order to analyze the motility of mitochondria and lysosomes in distal vs. proximal axonal parts, cortical neurons were cultured in compartmentalized microfluidic chambers (MFCs) (Figure 2.4). In general, the experimental set up, including MFC preparation, live cell imaging, and track analysis, was implemented as previously established by our group (Naumann, Pal et al. 2018, Pal, Glass et al. 2018).

Cortical cultures were splitted as described under 2.3.7.4 and plated on one site only of PLO/Laminin-coated MFCs (see section 2.3.2.2). Only neuronal axons can grow through the 900 μ m long micro channels, allowing the separation of distal vs. proximal axons for organelle trafficking analysis. To visualize mitochondria and lysosomes, cell cultures were incubated with 50 nM Mito- and LysoTracker in double for 1 h at 37°C, prior to imaging. Live cell imaging was performed without any further washing steps as described in section 2.4.3. Post-imaging,

medium was changed to normal NDM maintenance medium and cell could be further cultivated if needed.

Movie acquisitions was performed at strictly standardized readout positions (Figure 2.4). The readout windows were located either adjacent to the micro channels exits (distal) or the channel entries (proximal). Movies were analyzed with FIJI software using the TrackMate v2.7.4 plugin for object (lysosomes and mitochondria) recognition and tracking. Video properties were as shown in Table 2.30. Settings for TrackMate plugin are shown in **Fehler! Verweisquelle konnte nicht gefunden werden.** A minimum of 5 movies showing 2 micro channels each was analyzed at each readout positions (distal vs. proximal) per cell line. Typically, 200–500 tracks per movie were obtained and analyzed with respect to track displacement (measure for processive, i.e. straight, motility as opposed to undirected random walks) and mean speed. Results were assembled and post-filtered (threshold for track displacement $\geq 1.2 \mu\text{m}$) in KNIME and batch results were saved as MS Excel files. The bulk statistics were analyzed and displayed as box plots using GraphPad Prism 7 software (see section 2.6).

Table 2.30 Video properties for TrackMate analysis

Global	Yes
Channels (c)	1
Slices (z)	1
Frames (f)	400
Unit of length	Micron
Pixel width	0.23
Pixel high	0.23
Voxel depth	1
Frame interval	0.3 sec
Origin (pixel)	0.0

Table 2.31 Settings for TrackMate Plugin.

Detector	DoG detector
Diameter (DoG detector)	1.6
Threshold (DoG detector)	45
Median filter	No
Subpixel localization	Yes
Initial tresholding	45
View	HyperStack Displayer
Filters on spot	None
Tracker	Linear mition LAP tracker (Kalam tracker)

Initial search radius	2.0
Search radius	1.25
Max frame gap	2
Filters on track	Yes
Duration of track	3 sec

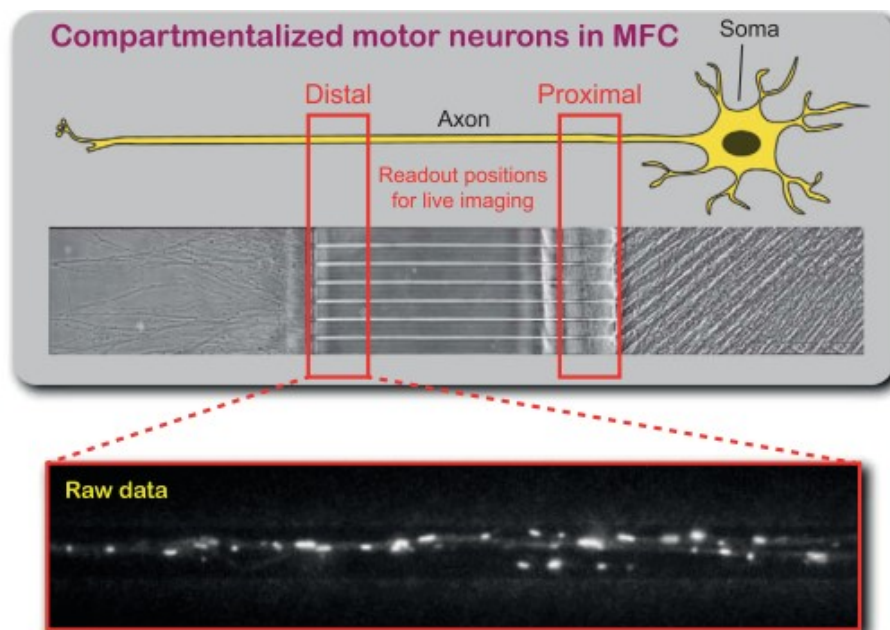


Figure 2.4 Overview of MFC culture system for axonal organelle trafficking analysis.

iPSC-derived neurons are plated on only one side of the microfluidic chambers (MFCs). Axons grow from the seeding site through 900 μm long microchannels. To distinguish between distal and proximal axonal parts, live cell imaging was implemented on defined readout positions as marked by red boxes. The illustration was adopted from Pal et al. 2018.

2.5.3 FUS-EGFP localization

The cellular localization of endogenously expressed FUS was aimed to be analyzed. For that isogenic iPSC lines FUS-WT and FUS-P525L, expressing EGFP-tagged FUS, were differentiated into cortical neurons and astrocytes and stained for either neuron marker MAP2 or astrocyte marker GFAP (Table 2.6). Apotome microscopy using a 63x oil objective was conducted to obtain Z-stack images (see section 2.4.2). A Z-stack of 7 images in 1 μm steps was acquired. A semi-automated workflow, using CellProfiler image analysis software (Table 2.14), was established to measure and quantify FUS-EGFP intensity within cytoplasm and nuclei of cortical neurons and astrocytes. Analysis pipeline was designed as follows:

1. For Apotome images stained for three markers (e.g. FUS-EGFP/ MAP2/ Hoechst)
 - a. Loading of maximum intensity projection images in czi- or tif-format
 - b. Extract metadata

- c. Split channels into its greyscale components
2. Identify nuclei automatically via Hoechst staining
3. Mask MAP2/GFAP channel with automatically detected nuclei from point 2
4. Identify MAP2/GFAP region automatically via MAP2/GFAP staining, excluding nuclei as masked in point 3
5. Mask FUS-EGFP channel with automatically detected MAP2/GFAP area from point 4
6. Overlay MAP2 and Hoechst channels with detected outlines in point 2 and 4
7. Manually select nuclei positive for MAP2/GFAP, using overlay created in point 6
8. Measure object intensity of MAP2/GFAP area excluding nuclei (point 4) and marker positive nuclei (point 7)
9. Overlay outlines of identified object to create merged images (e.g. overlay MAP2 area and MAP2 positive nuclei with outlines detected in point 4 and 7)
10. Save images of interest
11. Export measurements as excel spreadsheets

Results derived from semi-automated CellProfiler analysis were assembled and post-filtered in KNIME (Table 2.14). To determine the cytoplasmic shift of FUS-EGFP amount, the ratio of nucleus/cytoplasm was calculated using KNIME and exported as excel spreadsheets. Those results were further loaded in Graphpad PRISM 7 for creation of graphs and statistical analysis (see section 2.6).

2.5.4 Evaluation of C9ORF72-associated DPRs

In collaboration with Dr. Carina Schludi and Prof. Dr. Dieter Edbauer (DZNE Munich) three monoclonal antibodies were evaluated in iPSC-derived cortical neurons by ELISA and immunofluorescence staining. All three antibodies were generated individually by collaborators and shown to specifically detect DRPs in previous publications (Table 2.32). In this thesis work, partially different clones as published were used. According to Edbauer lab, used clones exposed to work best in ELISA and immunofluorescence staining of cell cultures.

Table 2.32 DPR antibodies

Antibody	Clone used	Clone published	Reference
Poly-GA	IAI2	5E9 + 5F2	(Mackenzie, Arzberger et al. 2013, Schludi, May et al. 2015)
Poly-GP	18H8	7A5	(Schludi, May et al. 2015)
Poly-GR	5H9	5H9 + 7H1	(Mori, Arzberger et al. 2013, Schludi, May et al. 2015)

For ELISA experiments, iPSCs were differentiated into cortical cells and cell pellets were collected at different maturation stages. To obtain pellets, 2w/6w or 3w/6w of cortical cells were washed once with DPBS, scraped off in DPBS, and collected in a 15 ml falcon. Cells were centrifuged briefly at full speed to collect pellet at the bottom of the tube. Supernatant was removed and cell pellets were directly frozen at -80°C. Frozen cell pellets were sent to Dr. Carina Schludi, who implemented protein extraction and ELISA experiments. Results received from Dr. C. Schludi were further loaded into Graphpad PRISM 7 for creation of graphs and statistical analysis (see section 2.6).

For immunofluorescence analysis, cortical cultures were co-stained with one of the three DPR antibodies and neurons marker MAP2 (Table 2.6). Apotome microscopy using a 63x oil objective was conducted to obtain images of one focal plane for analysis (see section 2.4.2). To identify and quantify cytoplasmic DPR granules, an automated workflow using CellProfiler image analysis software was established (Table 2.14). Analysis pipeline was designed as follows:

1. For Apotome images stained for three markers (e.g. Poly-GP/ MAP2/ Hoechst)
 - a. Loading of images in czi- or tif-format
 - b. Extract metadata
 - c. Split channels into its greyscale components
2. Identify nuclei automatically via Hoechst staining
3. Mask MAP2 channel with automatically detected nuclei from point 2
4. Identify MAP2 region automatically via MAP2 staining, excluding nuclei as masked in point 3
5. Mask Poly-GP/Poly-GA channel with automatically detected MAP2 area from point 4
6. Identify cytoplasmic Poly-GP/Poly-GA granules within MAP2 area (point 5) automatically by using a robust background thresholding within each assigned object (point 4)
7. Measure object size, shape, and number of identified Poly-GP/Poly-GA granules (point 6) and MAP2 region (point 4)
8. Relate identified objects: Poly-GP/Poly-GA granules (point 6) and MAP2 region (point 4)
9. Overlay outlines of identified object to create merged images (e.g. overlay MAP2 area and MAP2 positive nuclei with outlines detected in point 4 and 7)
10. Save images of interest
11. Export measurements as excel spreadsheets

Results derived from CellProfiler analysis were assembled and post-filtered in KNIME (Table 2.14). Further, the granule numbers per MAP2 area were calculated using KNIME and exported as excel spreadsheets. Those results were further loaded in Graphpad PRISM 7 for creation of graphs and statistical analysis (see section 2.6).

2.6 Quantifications and Statistics

Randomly assigned images of independent experiments were used for quantitative analysis. Independent experiments base on different (independent) differentiation pipelines and are depicted as sample size (n) in the main text and/ or figure legends.

Statistical analysis was performed using Graphpad/ PRISM 7 (Table 2.14). Graphs that are separated by dotted line always show: left non-isogenic lines and right isogenic ones.

Statistica analysis was performed as follows: T-test was conducted to analyze experiments with one independent variable and two groups only. Experimental setups with one independent variable but more than two groups were analyzed using a One-way ANOVA. Experimental set ups with two independent variables and more than two groups were analyzed by Two-way ANOVA. Tukey's post-hoc test was used if every mean was compared with every other mean. Dunnett's post-hoc test was used if every mean was compared to one control mean. Sidak post-hoc test was used if a selected set of means was compared. The individually used significance tests and post-hoc tests are indicated in the respective figure legends of results. Present statistical significances according to the adjustments are indicated in each graph and Figure legend. * $P \leq 0.05$, ** $P \leq 0.01$, *** $P \leq 0.001$, **** $P \leq 0.0001$ were considered as significant.

If not stated otherwise, the mean \pm SD of independent experiments was calculated, as represented in the main text or by bar/ line graphs and aligned dot plots. Error bars are only shown for data obtained from $n \geq 3$ experiments. Data obtained from $n \leq 2$ experiments is depicted without error bars. Box plots represent batch results (plotted raw data of individual detected objects) with following settings: whiskers from 1–99%, outliers as dots, boxes from 25–75 percentile, median as horizontal center line, mean as cross. Other settings are indicated in the legend of the individual Figure.

3 Results

3.1 Cortical differentiation of patient-specific iPSCs

The main focus of this thesis work was the analysis of disease-related pathologies within corticospinal motor neurons of cortical layer 5 and projection neurons of cortical layer 1/2 – 3 that are specifically affected in ALS and FTLD, respectively. Moreover, cortical astrocytes were aimed to be analyzed to compare their phenotypical characteristics to that of neurons. For this purpose, a differentiation protocol was used which recapitulates human neurogenesis (Burkhardt, Martinez et al. 2013), resulting in the derivation of heterogeneous cultures consisting of all cortical neuronal and glial cell types (Molyneaux, Arlotta et al. 2007). The protocol used was already established in the lab by me in a previous study, which showed that *FUS-NLS* mutant iPSCs are able to successfully differentiate into cortical neurons and astrocytes (Japtok, Lojewski et al. 2015).

Patient-specific iPSCs were used as starting material for neural differentiation (see section 2.3.7.3). After 70 to 120 day of maturation, cortical cells were ready for analysis. Altogether, eleven different control and mutant iPSC lines (*C9ORF72* and *FUS*), including non-isogenic and isogenic ones, were used for in-depth characterization of disease-associated phenotypes. Following is an overview of non-isogenic and isogenic lines (for details see Table 2.15):

- Non-isogenic control lines:
 - Ctrl 1
 - Ctrl 2
 - Ctrl 3
 - Ctrl 4
- Non-isogenic *C9ORF72* mutant lines:
 - C9-HRE 1
 - C9-HRE 3
- Isogenic *C9ORF72* lines:
 - C9-WT
 - C9-HRE 2
- Isogenic *FUS* lines:
 - FUS-WT (with EGFP-Tag)
 - FUS-R521C (without EGFP-Tag)
 - FUS-P525L (with EGFP-Tag)

In order to proof the neural differentiation capacity of control and mutant iPSC lines, the neuron types and cell morphologies were analyzed. For that, patient-specific iPSCs were differentiated and matured for at least 70 days after neural induction. Cortical neurons were then detected by immunofluorescence staining against microtubule-associated protein 2 (MAP2). Astrocytes were detected by staining against glial fibrillary acid protein (GFAP). Figure 3.1 shows that control as well as mutant lines were able to differentiate into cortical neurons and astrocytes. Representative images of only control cell lines (Ctrl 1, C9-WT) and mutant line C9-HRE 2 are shown as *FUS* lines were already published in Japtok et al. (2015). No gross morphological differences were observed between control and mutant neurons (Figure 3.1 A) and astrocytes (Figure 3.1 C) after 100 days maturation. Even though there was an effect of the cell line on neuron number in the determination of living MAP2 positive neurons, statistical post-hoc testing revealed that these differences were not statistically significant between the tested lines (Figure 3.1 B; $P=0.031$, $F(6, 12) = 3.48$, $n=1-3$, one-way ANOVA with Tukey's post-hoc test). Quantification of astrocytes was not possible due to cell morphology. Astrocytes can show star-like shape or spongiform morphology, while possessing long main processes in differentiation stage and acquiring complex morphologies at more mature stage (Schiweck, Eickholt et al. 2018, Zhou, Zuo et al. 2019). Moreover, they do not possess such a clear "cell body" surrounding the nucleus as observed in neurons (also called soma). Thus, nuclei positive for GFAP could not be determined with certainty. Furthermore, fragmented and pyknotic nuclei (independent of MAP2 staining) were counted in order to determine cell death in cortical cultures. Quantification revealed an effect of cell line on number of pyknotic nuclei. However, statistical post-hoc testing revealed that these differences were not statistically significant between the tested lines (Figure 3.1 B; $P=0.049$, $F(7, 12) = 2.94$, $n=1-3$, one-way ANOVA with Tukey's post-hoc test).

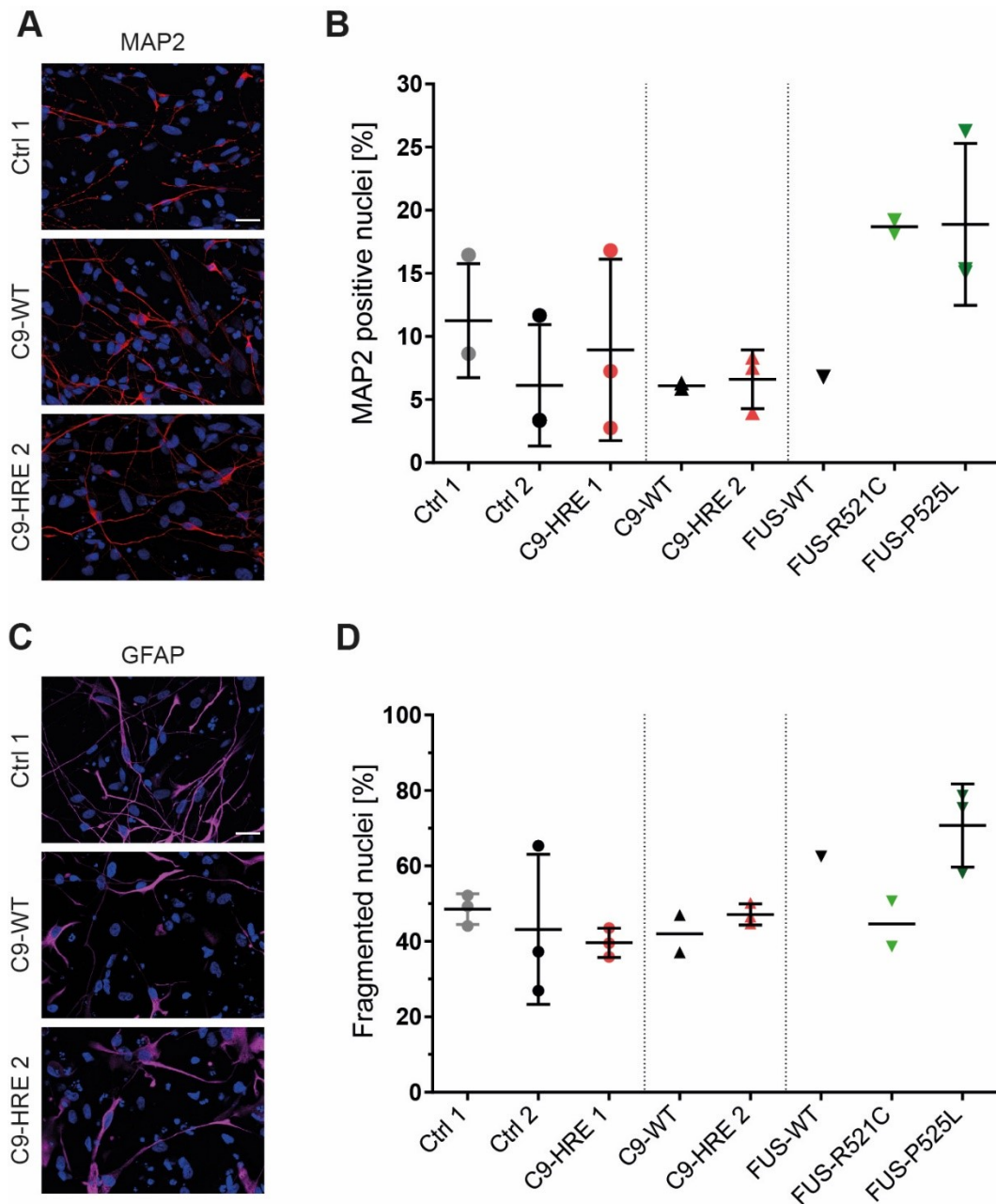


Figure 3.1 Derivation of patient-specific cortical neurons and astrocytes.

The differentiation protocol used in this study results in the derivation of cortical neurons (A) and astrocytes (B). **A** Neurons (MAP2) matured for 100 days show no morphological differences between controls and mutants. **B** Quantification of total MAP2 positive neuron soma from total living cell number (intact Hoechst) in % showed an effect of cell line ($P=0.031$, $F(6, 12) = 3.48$, $n=1-3$). However, *C9ORF72* (red) and *FUS* (green) mutants show no significant differences compared to controls (black and grey). **C** Cortical astrocytes (GFAP) at maturation day 100 show now morphological differences between controls and mutants. **D** Quantification of fragmented nuclei from total nuclei number (living and dead) in % showed an effect of cell line ($P=0.049$, $F(7, 12) = 2.94$, $n=1-3$). However, *C9ORF72* (red) and *FUS* (green) mutants show no significant differences compared to controls (black and grey). The effect of cell line in B+D was calculated by One-way ANOVA with Tukey's post-hoc test ($n=1-3$). Representative images of control cell lines (Ctrl 1, C9-WT) and mutant line C9-HRE 2 are shown (A+C). Nuclei were stained with Hoechst. Scale bars: 25 μm .

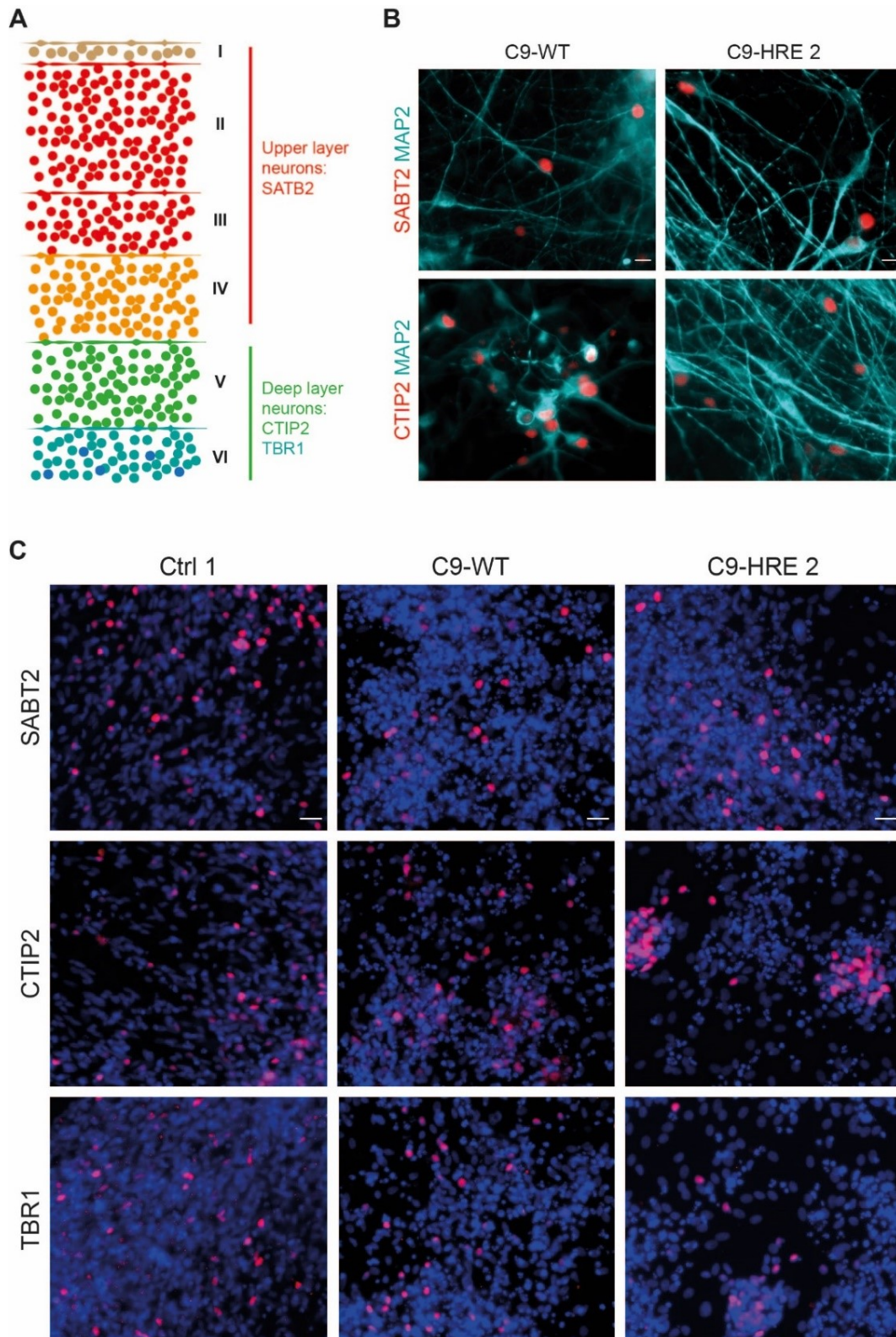


Figure 3.2 Derivation of patient-specific neurons from all cortical layers.

A The differentiation protocol results in the derivation of various neuronal cell types from all cortical layers. Upper layer neurons can be detected by SATB2 (layer 1/2-3), while deep layer neurons can be detected by CTIP2 (layer V) or TBR1 (layer VI). **B** Neurons stain positive for upper and lower neuron marker. Images display sections of 40x magnification. Scale bars: 10 μ m. **C** Control as well as mutant iPSC lines successfully differentiate into neurons of all cortical layers. Images display sections of 20x magnification. Scale bars: 25 μ m. Representative images of controls (Ctrl 1, C9-WT) and mutant C9-HRE 2 are shown (B-C). Nuclei were stained with Hoechst.

Cortical neurons of different laminar fates and projection types can be identified by analyzing expression of subtype specific markers (Molyneaux, Arlotta et al. 2007, Shi, Kirwan et al. 2012, Shi, Kirwan et al. 2012). Accordingly, immunofluorescence staining with different antibodies was used to detect distinct cerebral neuronal subtypes, including neurons of layer 6 (TBR1), layer 5 (CTIP2), and upper layer 1/2-3 (SATB2) (schematic overview: Figure 3.2 A). Figure 3.2 B+C shows that neurons positive for marker proteins of all cortical layers were detected, indicating that control as well as mutant lines were able to successfully differentiate into mixed cultures of the main cortical neuronal subtypes.

In summary, control and mutant iPSC lines showed similar capacities to differentiate into all cortical cell types that are of interest for further disease modeling purposes. Of note, a cell line dependent difference in neuron number was not observed. The absence of morphological pathologies at the analyzed time point for cortical neurons and astrocytes was verified for all control and mutant cultures. Thus a pathological action of *FUS* or *C9ORF72* mutation to cortical culture derivation/differentiation could be excluded.

3.2 CRISPR/Cas9n-mediated gene editing of *FUS*

3.2.1 Generation of isogenic WT and P525L *FUS*-EGFP iPSC lines

One aim of this thesis work was generation of isogenic *FUS*-EGFP lines for the study of *FUS*-related neuropathology in iPSC *in vitro* models. Two isogenic iPSC lines, *FUS*-WT and *FUS*-P525L were generated. As a parental line for gene editing, a patient-derived iPSC clone from a female patient carrying a heterozygous *FUS*-R521C mutation was used (see section 2.1.9). The patient-specific *FUS* sequence was corrected/ modified at its mutation site and simultaneously an *EGFP* sequence was introduced by CRISPR/Cas9n-mediated genome editing (Ran, Hsu et al. 2013) (Figure 3.3 A).

First, sgRNA for *FUS* targeting were designed and cloned into pX335B vector (see section 2.2.1.1 and 2.2.1.3). Next, using the CRISPR vector pX335B containing Cas9n and two sgRNAs, a DSB at the target site was introduced to trigger homology directed repair (HDR) (Figure 3.3 B). As a HDR template, a plasmid (pEX-K4) containing the *FUS* correction sequence (*WT* or *P525L*) plus *EGFP*-Tag was used. For codon specification that were modified see Table 3.1. The correction plasmids for CRISPR/Cas9n-mediated *FUS* editing were designed and generated as described under section 2.2.1.4.

For gene targeting, human iPSCs were transiently co-transfected with pX335B and pEX-K4 plasmids (either WT or P525L) (Figure 3.3 C)(see section 2.3.5). Successfully transfected cells were selected by Puromycin treatment. After 3-7 days of recovery, iPSCs were split on new plates in a single cell dilution. After another 7-14 days, EGFP-positive colonies were picked

and further expanded. Such single-cell-derived clones were then characterized and successfully gene edited clones were used for disease-modeling experiments.

Table 3.1 Codon specifications for gene editing of *FUS*

	WT codon	Mutant codon
R521C	Cgc	Tgc
P525L	cCg	cTg

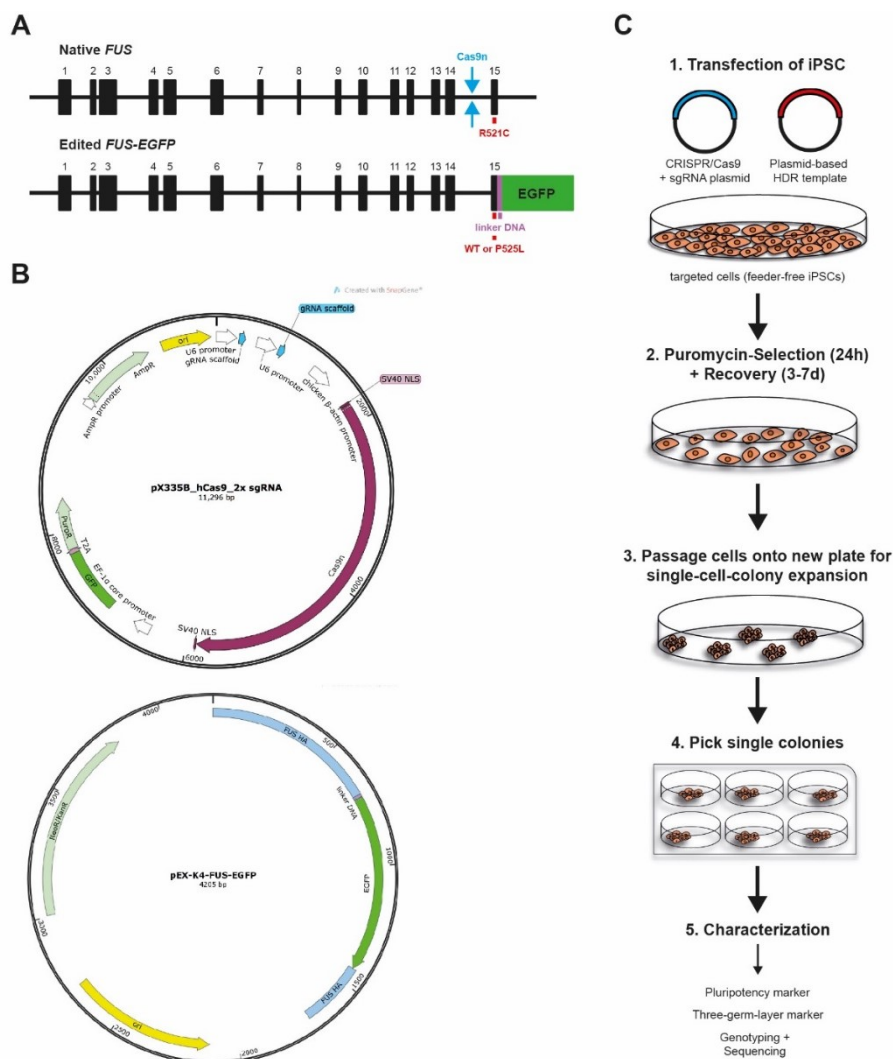


Figure 3.3 Generation of gene edited *FUS-EGFP* iPSC lines.

A Schematic representation of *FUS* before and after gene editing showing the Cas9n cut site and the mutation site of the parental line (upper panel). The native *R521C* mutation was corrected to *WT* or *P525L* coding sequence of *FUS* and C-terminally tagged with *EGFP* (lower panel). The illustration was adopted by Marrone et al. 2018 and modified by the author of this study. **B** Plasmid maps of CRISPR/Cas9n plasmid pX335B containing Cas9 nickase and 2x guide RNAs and pEX-K4 correction plasmid containing HDR template for *FUS* editing. **C** Workflow chart of CRISPR/Cas9n-mediated genome editing of human iPSCs. © Julia Japtok

3.2.2 Characterization of isogenic WT and P525L FUS-EGFP iPSC lines

3.2.2.1 Screening and Genotyping of isogenic FUS-EGFP iPSCs

The CRISPR/Cas9n-mediated gene editing of *FUS* resulted in generation of mixed cell population in which iPSCs that underwent gene editing were expressing EGFP-tagged *FUS*. This criterion was used for a first screening of single-cell-derived clones. Using widefield fluorescence microscopy 12-24 clones were examined for homogenous expression of *FUS-EGFP*. Figure 3.4 A shows representative clones for *FUS-WT* and *FUS-P525L* iPSCs which show an uniform expression of *FUS-EGFP* in all cells. The clones *FUS-WT* C4 and *FUS-P525L*-C21 were selected for further characterization.

By using CRISPR/Cas9n gene editing method described by Ran and colleagues, the risk of targeting unwanted genomic sites is reduced to a minimum (Ran, Hsu et al. 2013). Nevertheless, proper integration of *EGFP* into the targeted site of *FUS* needed to be confirmed on genomic DNA level. The presence of the *EGFP*-Tag within the genomic sequence of *FUS* was confirmed by Screening-PCR (Figure 3.4 B, lane 1+2). For this a forward primer (*FUS*-1.3-F) targeting *FUS* upstream of the used homology arms and a reverse primer (*EGFP* Rev 1) targeting *EGFP* were used (Table 2.9). The 909 bp amplified PCR product confirmed that integration of *EGFP* occurred on the targeted site of *FUS*.

After successful Screening-PCR the genotype of selected clones was determined by PCR and sequencing (see section 2.2.4.3). For the genotyping PCR, the primer pair *FUS*-2.1-F/-R was used targeting *FUS* up- and downstream of *EGFP* sequence, including the mutation site of the parental line. In this setup amplification should result in two PCR products (1257 bp for *FUS-EGFP* and 528 bp for untagged, endogenous *FUS*), if cells are heterozygous for the introduced modification. Figure 3.4 B (lane 2+4) shows that both selected clones, *FUS-WT* C4 and *FUS-P525L* C21, are heterozygous for the introduced genomic modification. To confirm the genotype by sequencing, PCR products were analyzed on a 1% agarose gel and the two different sized bands were purified from the gel (see section 2.2.7). In order to identify if correction of *FUS* occurred on the originally mutated allele and not on the WT allele of the parental line, both purified PCR products were sequenced (Figure 3.4 C, see section 2.2.5.1). The PCR products containing *FUS* with *EGFP* (*FUS-EGFP* Allele) were sequenced using the reverse primer (*EGFP* Rev 1). The smaller PCR products containing *FUS* without *EGFP* (*WT* Allele) were sequenced using the reverse primer (*FUS*-seq-R). The original genotype of the used patient-derived iPSC line was *FUS-R521C/FUS-WT*. The genotype of successfully modified clones *FUS-WT* C4 and *FUS-P525L* C21 was *FUS-WT-EGFP/FUS-WT* and *FUS-P525L-EGFP/FUS-WT* respectively, as confirmed by sequencing. Both clones were chosen

for in-depth characterization of pluripotency and are further referred to as FUS-WT and FUS-P525L.

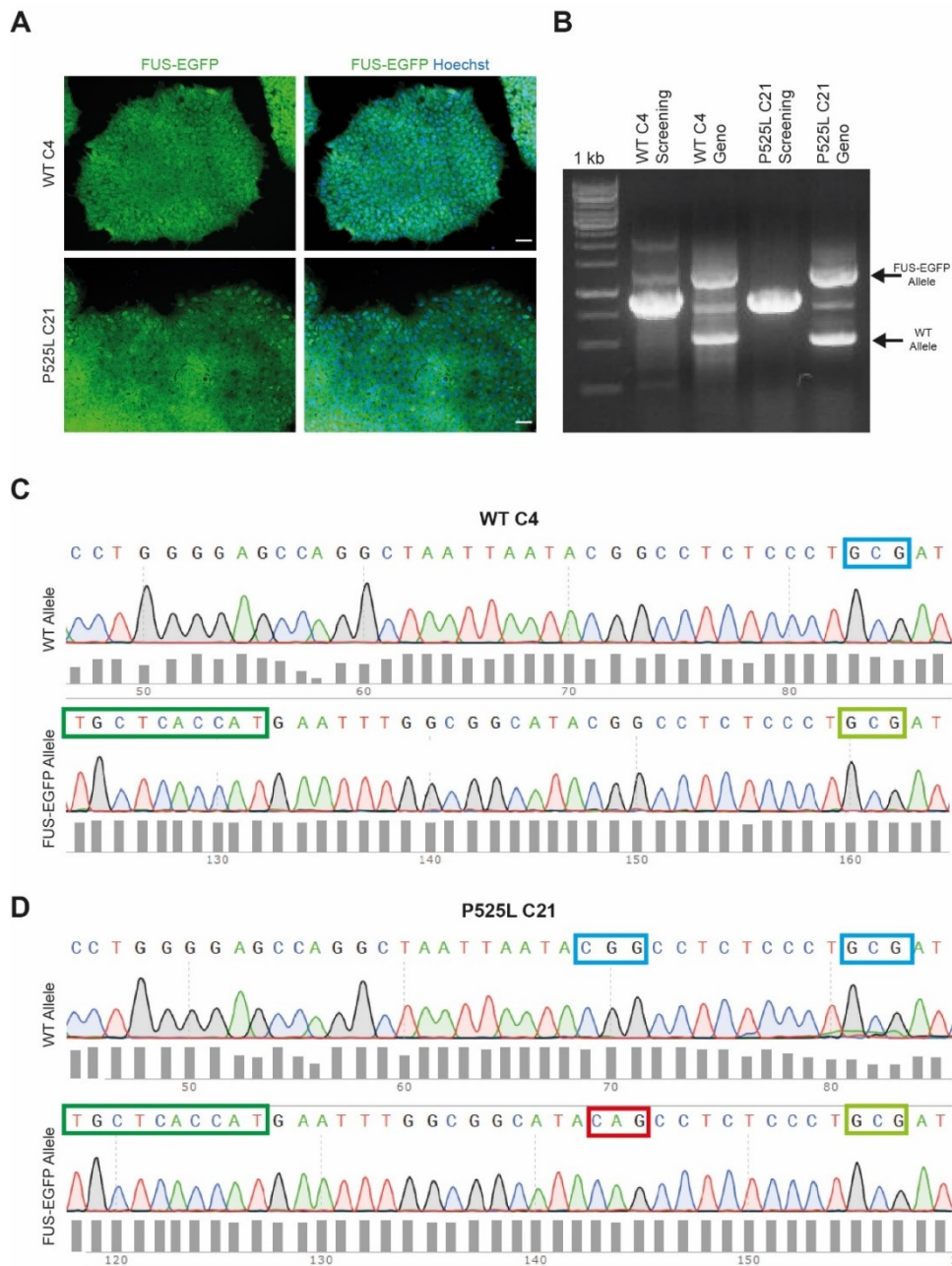


Figure 3.4 Screening and genotyping of FUS-EGFP positive clones.

A FUS-EGFP expression in WT and P525L clones after CRISPR/Cas9n-mediated gene editing. Nuclei are counter stained with Hoechst. Scale bars: 50 μ m. **B** Screening-PCR (lane 1+3) and Genotyping-PCR (lane 2+4). **C-D** In order to verify that correction of mutant *FUS-R521C* cell line (Table 2.15) was successful, the genotype of the derived isogenic cell lines was determined by Sanger sequencing. Shown are the reverse strands of both alleles. **C** Sequencing results of FUS-WT C4. The *FUS-EGFP* allele shows that *FUS* mutation at amino acid position 521 (light green box) is corrected to *WT* sequence and *EGFP* sequence is present (dark green box). The *WT* allele shows *FUS-WT* sequence at the same position (blue box). **D**. Sequencing results of FUS-P525L C21. The *FUS-EGFP* allele confirms presence of *EGFP* sequence (dark green box) and possesses the mutant sequence coding for *P525L* mutation at amino acid position 525 (red box) while the parental *FUS-R521C* mutation was corrected to *WT* sequence (light green box). The *WT* allele shows *FUS-WT* sequences (blue boxes) at both positions of interest.

3.2.2.2 Pluripotency of isogenic FUS-EGFP iPSCs

The parental line FUS-R521C which was used for CRISPR/Cas9n-mediated gene editing was previously characterized and published (Japtok, Lojewski et al. 2015). However, even though the introduced genomic modification is specific for the target site within *FUS*, there is still a possibility of off-targets that might affect pluripotency of generated iPSCs. Therefore, the confirmation of pluripotent state of the generated iPSC lines was necessary. Standard procedures for verification of pluripotency include immunofluorescence staining for known marker proteins and differentiation into the three germ layers, namely meso-, endo- and ectoderm.

To confirm pluripotency, iPSC clones were stained for proteins which are known to be expressed in pluripotent ESCs: OCT4, SOX2, TRA-1-60, and SSEA4. Figure 3.5 shows that both isogenic iPSC clones were stained positive for the pluripotency markers.

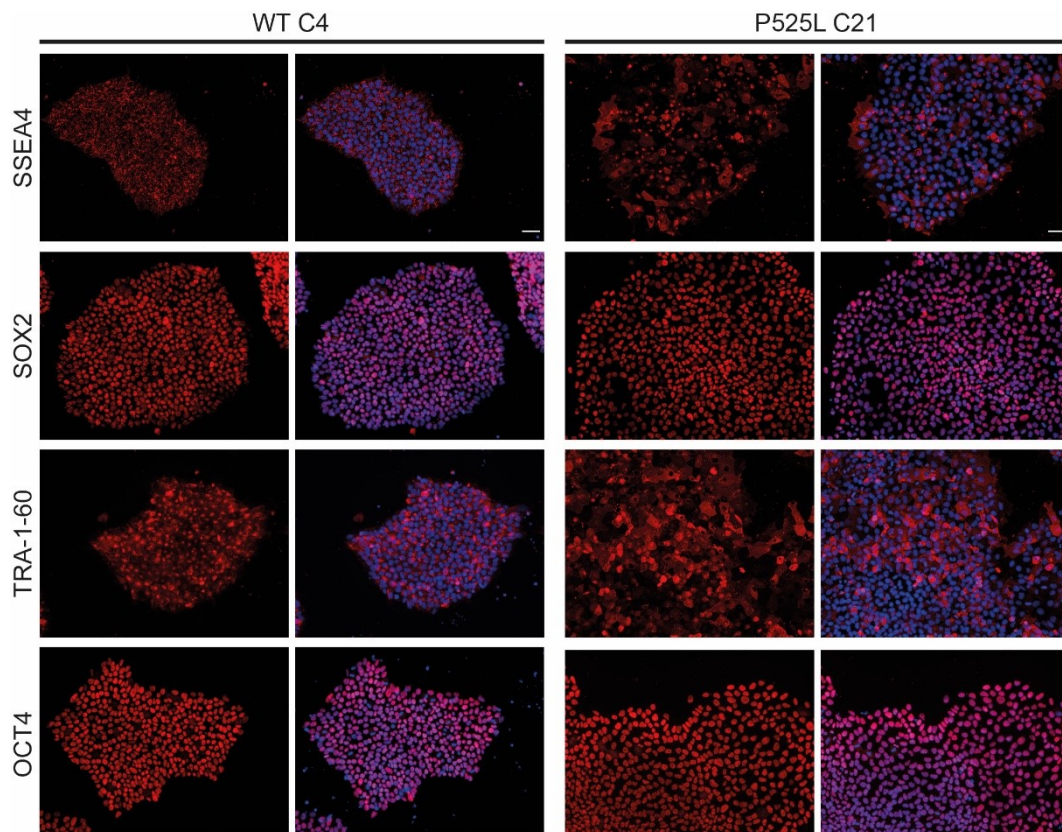


Figure 3.5 Isogenic WT and P525L iPSCs are positive for markers of pluripotency.

Isogenic WT and P525L iPSC clones show positive staining for pluripotency markers OCT4, SOX2, TRA-1-60, and SSEA4. Representative images in 40x magnification are shown. Nuclei are counter stained with Hoechst. Scale bars: 50µm.

Next, embryoid bodies (EBs) were formed from both iPSC clones. EBs were spontaneously differentiated into three germ layers for two weeks (see section 2.3.6). Figure 3.6 shows positive staining of iPSC clones for known marker proteins of mesoderm (alpha-smooth muscle

actin (SMA)), endoderm (GATA Binding Protein 4 (GATA4)), and ectoderm (neuron-specific class III beta-tubulin (TUJ1)), which further confirmed their pluripotent nature.

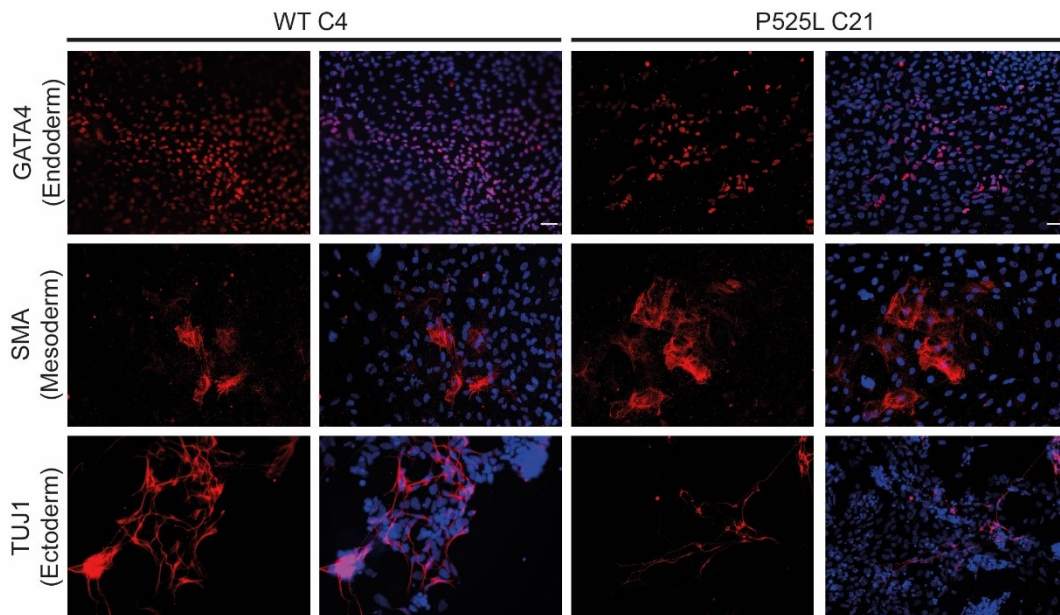


Figure 3.6 Isogenic WT and P525L iPSCs can differentiate into cells of all three germ layer.

Isogenic WT and P525L iPSC clones were spontaneously differentiated into cell types of the three germ layer to confirm pluripotent state of gene edited iPSCs. Both clones show positive staining for endoderm marker GATA, mesoderm marker SMA, and ectoderm marker TUJ1. Nuclei are counter stained with Hoechst. Scale bars: 50 μ m.

Taken together, the pluripotent state and successful recombination, as shown by genotyping and sequencing, were confirmed for both gene edited clones. In conclusion, the isogenic pair (FUS-WT and FUS-P525L) can be used for neural differentiation and disease-related experiments.

3.2.2.3 Off-targets

The CRISPR/Cas9n-mediated gene editing approach via double nicking is a powerful system to target precisely and reduce unintended interactions (off-targets) to a minimum. Nevertheless, cooperative nicking at off-target sites or individual off-target single-stranded nicks might still occur. Consequently, a computational approach was used to evaluate the likelihood of off-target sites for the given pair of sgRNAs.

To screen for possible off-target effects of Cas9n both target specific sgRNAs (T1 and T2, see Table 2.16) were checked via the “CRISPR Design” online tool from Zhang laboratory (<http://crispr.mit.edu>) and the “Off-spotter” tool from Pliatsika et al. (Pliatsika and Rigoutsos 2015). Both online tools confirmed that there are no genomic off-targets that are targeted from both sgRNAs in combination, which could result in the introduction of a DSB at any unintended site. Table 3.2 Table 3.3 and show possible off-target site of individual sgRNAs T1 and T2,

respectively, which could result in single-stranded nicks. The analysis of possible off-target site indicates a high specificity of the selected sgRNAs for *FUS* gene editing.

Table 3.2 Possible Off-targets of sgRNA Target 1 (GCGAGTATCTTATCTCAAGT)

Chr.	Strand	Position	# of mis-matches	Gene	Intron / Exon	Tool
7	-	82419483	3	PCLO	Intron	Off-spotter
3	-	10226296	4	IRAK2	Intron	Off-spotter
20	-	34778913	4	EPB41L1	Intron	Off-spotter
4	+	4304528	4	ZBTB49	Exon	Zhang Lab
20	-	18467412	4	RBBP9	Exon	Zhang Lab
2	-	171249076	3	MYO3B	Intron	Zhang Lab
4	-	124236784	4	SPATA5	Exon	Zhang Lab
8	-	14596389	4	SGCZ	Intron	Off-spotter
X	+	101979095	4	BHLHB9	Intron	Off-spotter
17	-	38548446	4	TOP2A	Intron	Zhang Lab

Table 3.3 Possible Off-targets of sgRNA Target 2 (GTTAGGTAGGAGGGGCAGAT)

Chr.	Strand	Position	# of mis-matches	Gene	Intron / Exon	Tool
2	+	241705216	4	KIF1A	Intron	Zhang Lab
20	+	3016619	4	PTPRA	Intron	Zhang Lab
16	-	2946266	4	FLYWCH2	Intron	Zhang Lab
11	-	16883955	4	PLEKHA7	Intron	Off-spotter
3	+	123823364	4	KALRN	Intron	Off-spotter
2	+	218750868	4	TNS1	Intron	Zhang Lab
15	+	91003806	3	IQGAP1	Intron	Off-spotter
6	+	152016039	3	ESR1	Intron	Off-spotter
7	-	154375887	3	DPP6	Intron	Off-spotter

15	+	93480077	4	CHD2	Intron	Off-spotter
9	-	35496488	4	RUSC2	Intron	Off-spotter
11	-	8909439	4	ST5	Intron	Off-spotter
3	-	67492286	4	SUCLG2	Intron	Off-spotter
15	-	45544391	4	SLC28A2	Intron	Zhang Lab
11	+	32457461	4	WT1-AS	Intron	Zhang Lab

3.3 Analysis disease-associated proteins

3.3.1 FUS-EGFP localization in cortical neurons and astrocytes

Mutations within the *NLS* of *FUS* are known to lead to a cytoplasmic mislocalization of FUS protein (Vance, Rogelj et al. 2009, Bosco, Lemay et al. 2010, Dormann, Rodde et al. 2010, Gal, Zhang et al. 2011, Kino, Washizu et al. 2011, Zhang and Chook 2012, Vance, Scotter et al. 2013, Wang, Pan et al. 2013). Previously, it could be shown that FUS mislocalization depends on aging and the severity of mutation in mutant cortical neurons (Japtok, Lojewski et al. 2015). Furthermore, our group showed that *FUS-P525L* mutation leads to a severe shift of FUS from the nucleus to cytoplasm in spinal MNs (Naumann, Pal et al. 2018). In this thesis work, the same isogenic FUS-EGFP iPSC lines were used to analyze FUS-EGFP cellular localization in iPSC-derived cortical neurons and astrocytes.

Cortical cultures derived from isogenic iPSC lines FUS-WT and FUS-P525L were matured for 100 days and stained for either neuron marker MAP2 or astrocyte marker GFAP. In both lines, a nuclear as well as cytoplasmic expression of FUS-EGFP could be observed. However, cytoplasmic mislocalization of FUS-EGFP seemed to be more severe in few *FUS-P525L* mutant neurons, but not astrocytes, compared to FUS-WT (Figure 3.7 A). To determine quantitative FUS-EGFP amounts, signals were semi-automatically detected using CellProfiler Software (see section 2.5.3). In brief, MAP2 or GFAP area was automatically detected and marker positive nuclei were manually selected. FUS-EGFP integrated intensity was measured within MAP2 or GFAP positive area (excluding nuclei) and within marker positive nuclei. To determine the cytoplasmic shift of FUS-EGFP amount the ratio of nucleus/cytoplasm was calculated. Figure 3.7 B shows that *FUS-P525L* mutant neurons showed a tendency of increased nuclear to cytoplasmic shift of FUS-EGFP amounts compared to FUS-WT. This was not observed in astrocytes. These results show that *FUS-NLS* mutation seems to specifically affect FUS cellular localization in neurons but not astrocytes.

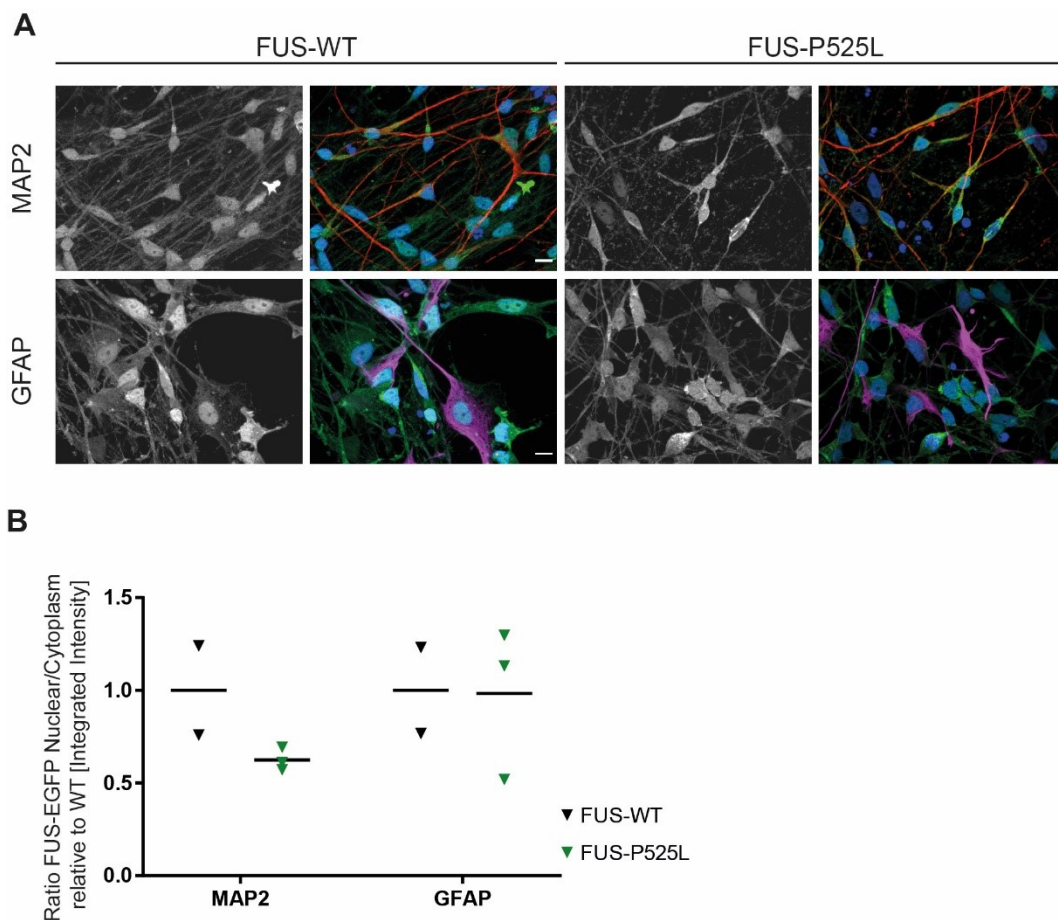


Figure 3.7 Analysis of FUS-EGFP cellular distribution in cortical neurons and astrocytes.

A Cortical cultures at maturation day 100 were stained for MAP2 or GFAP. FUS-EGFP was detected in nucleus and cytoplasm of both isogenic lines (FUS-WT and FUS-P525L). Nuclei were stained with Hoechst. Scale bars: 10 μ m. **B** FUS-EGFP integrated intensity was semi-automatically measured in cytoplasm and nuclei of either MAP2 or GFAP positive cells. *FUS-P525L* mutant neurons but not astrocytes showed a decreased FUS-EGFP amount compared to isogenic control. The ratio of FUS-EGFP integrated intensity nuclear/cytoplasmic in marker positive cells was calculated. Data is depicted relative to isogenic FUS-WT cell line.

3.3.2 Characterization of *C9ORF72*-associated DPRs

Aim of this thesis work was the recapitulation of *C9ORF72-HRE*-associated pathologies in the here used patient-specific *in vitro* model, using iPSC-derived cortical neurons. The accumulation of DPRs is a characteristic pathology in *C9ORF72*-associated disease. Studies using post mortem tissue of *C9ORF72-HRE* carriers showed, that DPRs are predominantly detectable within cortical region (Ash, Bieniek et al. 2013, Mackenzie, Arzberger et al. 2013, Schludi, May et al. 2015) and that the DPR species Poly-GA, Poly-GP, and Poly-GR are most abundant (Gendron, Bieniek et al. 2013, Mori, Weng et al. 2013). For that reason Poly-GA, Poly-GP, and Poly-GR were chosen to be analyzed. In collaboration with Dr. Carina Schludi and Prof. Dr. Dieter Edbauer (DZNE Munich) three monoclonal antibodies, which were already shown to specifically detect DRPs in various models (Mackenzie, Arzberger et al. 2013, Mori,

Arzberger et al. 2013, Schludi, May et al. 2015), were evaluated in iPSC-derived cortical neurons.

3.3.2.1 ELISA for Poly-GP

First, endogenous DPR levels of Poly-GP were determined utilizing enzyme linked immunosorbent assay (ELISA). Various control and *C9ORF72-HRE* mutant cell lines were differentiated into cortical cells. After 80 and 120 days of maturation whole cell lysates were collected for ELISA analysis. Analysis of the data showed that there seems to be no effect of aging on Poly-GP production (Figure 3.8). Also, there seemed to be no differences between distinct cell lines (Figure 3.8), although *C9ORF72-HRE* mutant lines showed a slightly higher Poly-GP production compared to controls (for descriptive statistics see Supplemental Table S 7). Non-isogenic mutants (C9-HRE 1+3) showed very low DPR amount, which can be expected to be non-pathogenic as it is comparable to control levels (below 400 arbitrary units). Moreover, those data is comparable to Poly-GP ELISA results obtained from control sMN cultures (Abo-Rady 2018). In contrast, C9-HRE 2 cell line showed much higher Poly-GP levels compared to its isogenic control. This data is comparable to data obtained from sMN cultures in which the same isogenic pair was used (Abo-Rady 2018). Overall, ELISA quantification does not show a clear *C9ORF72-HRE* caused effect on Poly-GP production but did confirm previous findings of excessive Poly-GP production in only one out of three *C9ORF72-HRE* mutant lines.

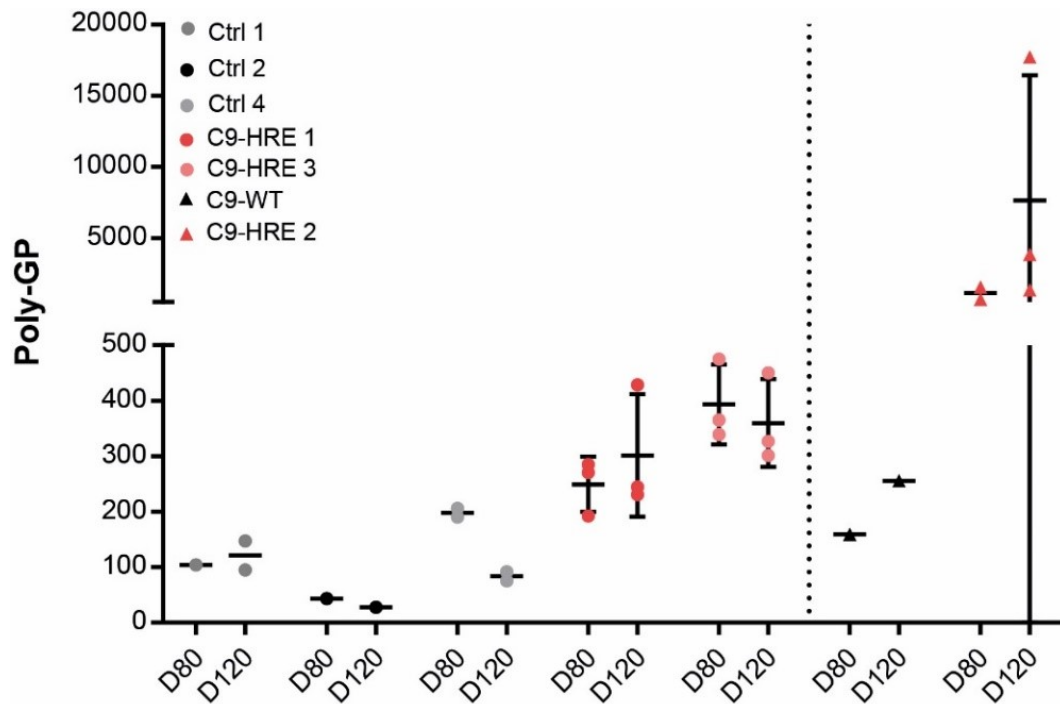


Figure 3.8 Production of Poly-GP in cortical cells is not affected by aging.

Production of endogenous Poly-GP was quantified utilizing ELISA. Mature (D80) iPSC-derived cortical cells were compared with aged (D120) ones. No difference in Poly-GP production between D80 and D120 old cortical cells was observed. Poly-GP production tended to be higher in C9-HRE mutant lines compared to controls. For descriptive statistics see Supplemental Table S 7 (n=1-3).

As already shown, the *in vitro* model used in this work results in the production of only 5-20% neurons (Figure 3.1). The Poly-GP levels detected by ELISA do not distinguish between different cortical cell types. This could be a reason for the unexpected low DPR detection levels. To specifically detect DPRs within cortical neurons, Poly-GP, Poly-GA, and Poly-GR were analyzed using co-immunofluorescence staining with the neuron marker MAP2. Because ELISA results showed no effect of aging on DPR production, only one maturation time point (100 days) was chosen to be analyzed.

3.3.2.2 Immunofluorescence staining for Poly-GP

Poly-GP was analyzed first. Small dot-like granules could be detected in control as well as *C9ORF72-HRE* mutant lines (Figure 3.9). The granules were distributed in the cytoplasm and neurites of cortical neurons. Additionally a nuclear staining could be detected, which confirms previous findings (Schludi, May et al. 2015, Yamakawa, Ito et al. 2015). Surprisingly, Poly-GP granules were also observable within control neurons as well. The qualitative analysis of the immunofluorescence staining revealed no clear difference between control and *C9ORF72-HRE* mutants. To evaluate this further, CellProfiler image analysis software was used (Carpenter, Jones et al. 2006, Kametsky, Jones et al. 2011). A pipeline was created to automatically detect Poly-GP granules within MAP2 positive area, excluding nuclear region

(see section 2.5.4). Detected granules were automatically counted and size was measured. Because the derivation of neurons, and thus MAP2 area, can vary between independent differentiations and cell lines, Poly-GP values were normalized to total MAP2 area per experiment.

Figure 3.10 A shows that no difference was observed regarding the number of detected Poly-GP granules between control and *C9ORF72-HRE* mutant cortical neurons relative to MAP2 area (for descriptive statistics see Supplemental Table S 8). In contrast, the total area of detected Poly-GP was significantly increased in both *C9ORF72-HRE* mutant cell lines compared to controls (Figure 3.10 B). Analysis of individual Poly-GP granules plotted as box plots, showed that granule size (area and radius) is significantly increased in *C9ORF72-HRE* mutant cortical neurons compared to controls (Figure 3.10 C+D; for descriptive statistics see Supplemental Table S 10 and Supplemental Table S 11). Taken together, immunofluorescence staining analysis of size parameters of detected Poly-GP granules revealed that granule size is increased in *C9ORF72-HRE* mutant cell lines.

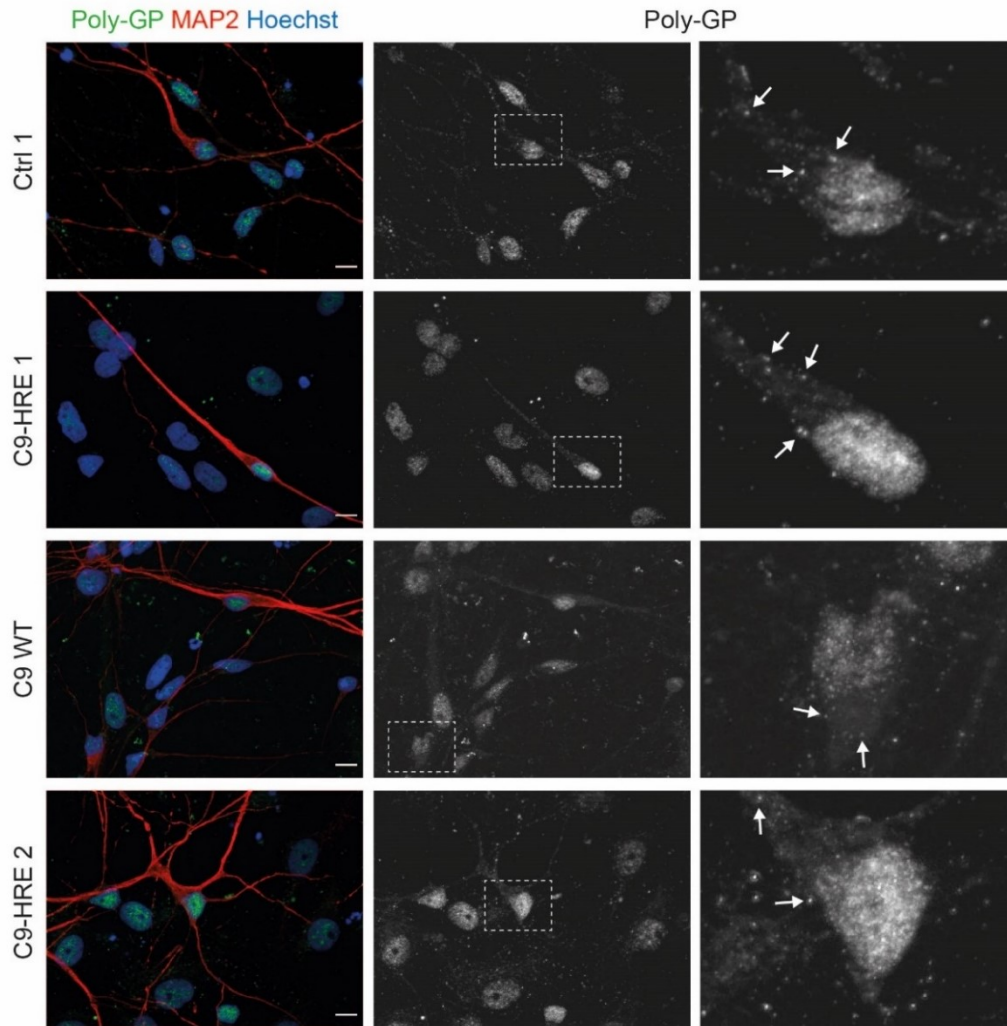


Figure 3.9 Detection of Poly-GP in cortical neurons.

Representative images of cortical neurons at maturation day 100 and stained for neuron marker MAP2 (red) and Poly-GP (green) are shown. Small cytoplasmic dot-like granules (white arrows) and nuclear staining were detected in non-isogenic (Ctrl 1 + C9-HRE 1) and isogenic lines (C9 WT + C9-HRE 2). Nuclei were stained with Hoechst. Scale bars: 10 μm .

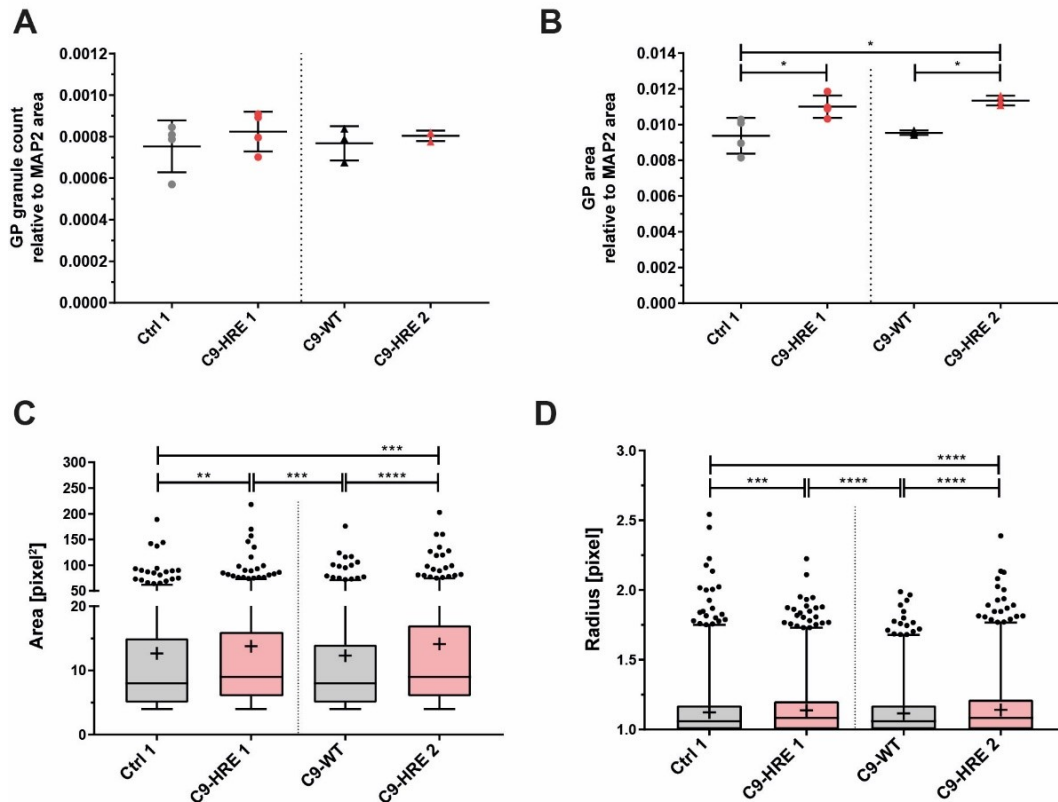


Figure 3.10 Characterization of Poly-GP within cortical neurons.

In cortical neurons matured for 100 days, Poly-GP granules were automatically detected within MAP2 positive area and excluding nuclei using CellProfiler software. **A** No difference in Poly-GP granule number was observed between control and C9-HRE mutants (Supplemental Table S 8). **B** Total Poly-GP area is significantly increased in C9-HRE mutants compared to controls (Supplemental Table S 9). Poly-GP measurements in A+B were normalized to MAP2 area. **C-D** The area (C) and radius (D) of individual Poly-GP granules is significantly increased in C9-HRE mutant cortical neurons compared to controls (Supplemental Table S 10+11). Values of individual detected Poly-GP granules are plotted. Box plots represent batch results merged from independent experiments. Statistics in A+B were calculated by One-way ANOVA with Tukey's post-hoc test and in C+ D by Kruskal-Wallis test with Dunn's post-hoc test (n=3-4).

3.3.2.3 Immunofluorescence staining for Poly-GA

After evaluation of Poly-GP in cortical neurons, a monoclonal antibody was used to detect Poly-GA. The same experimental setup as used for Poly-GP immunofluorescence staining and analysis was implemented. Similar to Poly-GP, small cytoplasmic inclusions and nuclear staining were observed for Poly-GA (Figure 3.11). This is consistent with previous findings (Schludi, May et al. 2015).

Software-based quantification of Poly-GA granule numbers revealed no difference between *C9ORF72-HRE* mutants and controls (Figure 3.12 A, for descriptive statistics see Supplemental Table S 12). Also for determination of total Poly-GA area, no difference between *C9ORF72-HRE* mutant and control cortical neurons was observed (Figure 3.12 B, for descriptive statistics see Supplemental Table S 13). Analysis of individual granule parameters showed varying results. Analyzing the non-isogenic cell lines, increased size of Poly-GA granule area was observed in C9-HRE 1 compared to Ctrl 2, but not to Ctrl 1 (Figure 3.12 C). Also, there was no difference in radius size (Figure 3.12 D). Overall, the results showed no differences in Poly-GA size parameters (area and radius) between C9-HRE 1 and Ctrl 1, which is in contrast to the results obtained previously for Poly-GP in the same cell lines. For descriptive statistics see Supplemental Table S 14 (area) and Supplemental Table S 15 (radius). Analysis of single Poly-GA granules in isogenic cortical neurons revealed no difference of granule area between C9-HRE 2 and its isogenic control C9-WT (Figure 3.12 C,) but the radius was significantly increased in C9-HRE 2 compared to C9-WT (Figure 3.12 D). Additionally, C9-HRE 2 Poly-GA granules showed significantly increased area and radius compared to all other non-isogenic lines. Moreover, the granule area between the three control lines differed significantly from each other. Taken together, quantitative determination of Poly-GA immunofluorescence staining revealed highly inconsistent results between non-isogenic and isogenic lines. No clear difference between *C9ORF72-HRE* mutants and controls was detected.

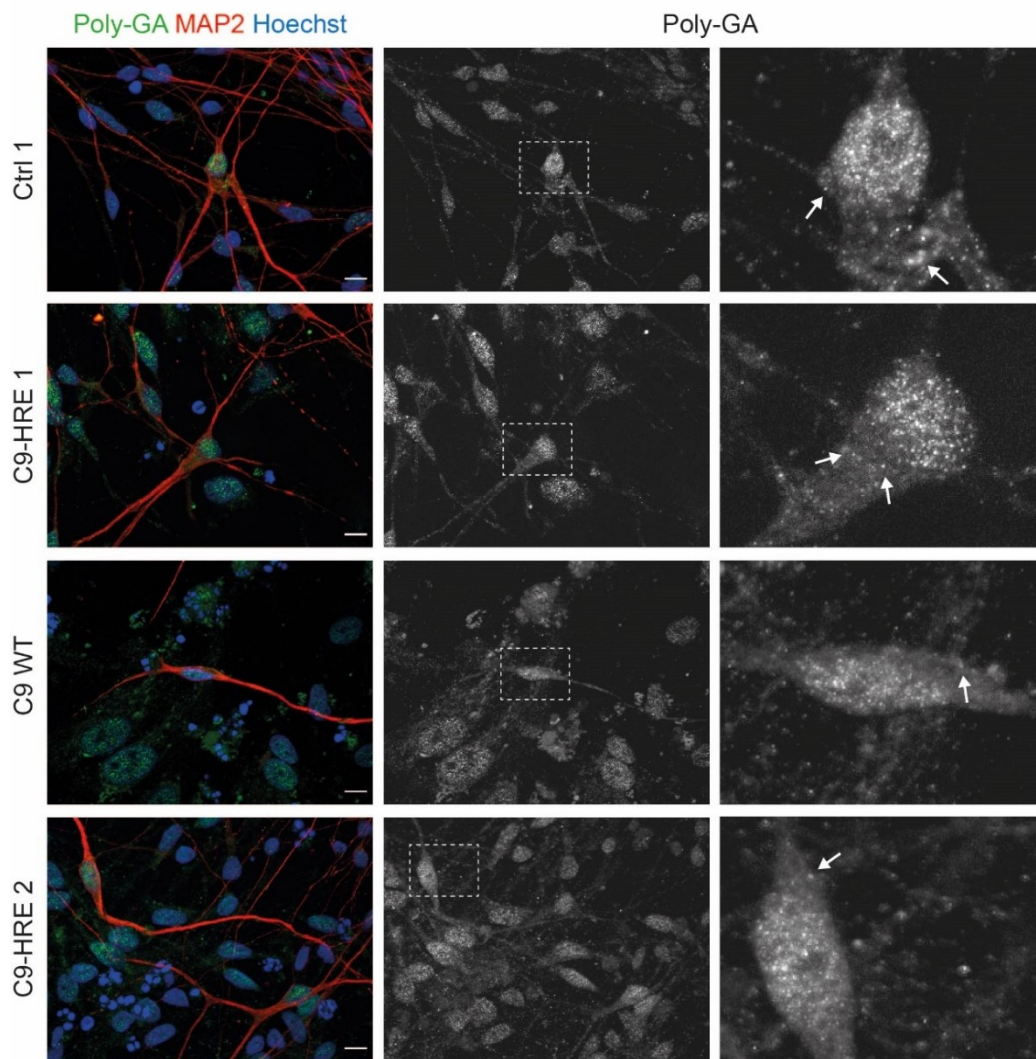


Figure 3.11 Detection of Poly-GA in cortical neurons.

Representative images of cortical neurons at maturation day 100 and stained for neuron marker MAP2 (red) and Poly-GA (green) are shown. Small cytoplasmic dot-like granules (white arrows) and nuclear staining were detected in non-isogenic (Ctrl 1 + C9-HRE 1) and isogenic lines (C9 WT + C9-HRE 2). Nuclei were stained with Hoechst. Scale bars: 10 μm .

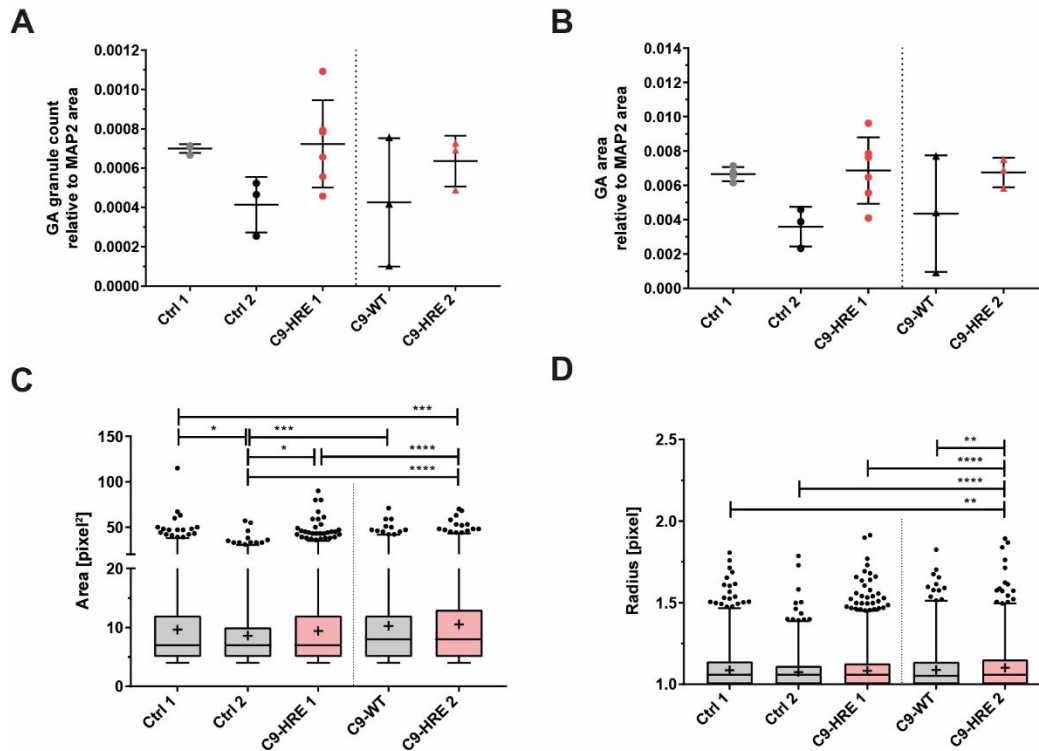


Figure 3.12 Characterization of Poly-GA within cortical neurons.

In cortical neurons matured for 100 days, Poly-GA granules were automatically detected within MAP2 positive area and excluding nuclei using CellProfiler software. **A-B** No difference in Poly-GA granule count (A, Supplemental Table S 12) or total area (B, Supplemental Table S 13) was observed between control and C9-HRE cortical neurons. Poly-GA measurements were normalized to MAP2 area. **C** An increased area of individual Poly-GA granules is observable in non-isogenic C9-HRE 1 mutant compared to Ctrl 2 but not Ctrl 1. C9-HR 2 shows no increased granule area compared to its isogenic control C9-WT but to all other non-isogenic lines (Ctrl 2, Ctrl 1, C9-HRE 1). For descriptive statistics see Supplemental Table S 14. **D** Analysis of radius showed no difference for non-isogenic cortical neurons (Ctrl 1, Ctrl2, and C9-HRE1). The radius of single granules in C9-HRE2 mutants was increased compared to its isogenic control C9-WT and also to all other non-isogenic lines (Ctrl 2, Ctrl 1, C9-HRE 1). For descriptive statistics see Supplemental Table S 15. In C+D, values of individual detected Poly-GP granules are plotted. Box plots represent batch results merged from independent experiments. Statistics in A+B were calculated by One-way ANOVA with Tukey's post-hoc test and in C+D by Kruskal-Wallis test with Dunn's post test (n=3-6).

3.3.2.4 Immunofluorescence staining for Poly-GR

In addition to Poly-GP and Poly-GA, Poly-GR was also aimed to be analyzed. However, preliminary test staining revealed a contingent un-specificity of the used monoclonal antibody. A strong cytoplasmic accumulation of Poly-GR in neurons and non-neuronal cells could be observed (Figure 3.13). However, even in the control line severe cytoplasmic aggregates positive for Poly-GR were detectable. Therefore, no further quantitative analysis of Poly-GR in cortical neurons was implemented.

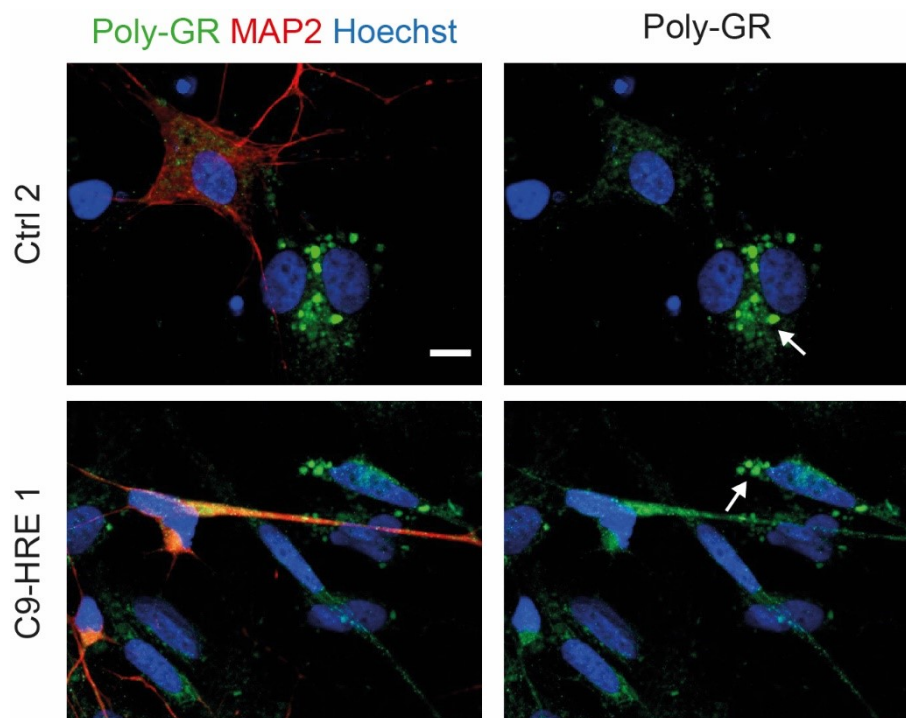


Figure 3.13 Detection of Poly-GR in cortical neurons.

Representative images of cortical neurons at maturation day 100 and stained for neuron marker MAP2 (red) and Poly-GR (green) are shown. Big cytoplasmic aggregates (white arrows) were detected in non-isogenic (Ctrl 2 + C9-HRE 1) neuronal and non-neuronal cells. Nuclei were stained with Hoechst. Scale bars: 10 μ m.

3.3.3 DPRs versus DNA damage

DDR is shown to be induced by *C9ORF72-HRE* in ALS and by overexpression of DPRs in cellular models (Farg, Konopka et al. 2017). In this thesis work, it was aimed to analyze a possible correlation between DPRs and DSBs using patient-specific iPSC-derived cortical neurons endogenously expressing *C9ORF72*. For this purpose, cortical neurons matured for 100 days were co-stained with either Poly-GP or Poly-GA antibody and the DSB marker 53BP1 and qualitative analysis was done to detect a possible correlation. It was not possible to perform automated analysis, since Poly-GP granules are localized in the cytoplasm while

53BP1 foci are situated in the nucleus and this kind of setup was incompatible with an automated Fiji or CellProfiler workflow.

No obvious correlation between Poly-GP nor Poly-GA and 53BP1 was observed. The formation of Poly-GP (Figure 3.14) and Poly-GA (Figure 3.15) granules was detected in both cortical neurons that showed nuclear 53BP1 foci (red arrows) as well as in neurons that did not show any DNA damage (white arrows). There was no clear difference in DPR levels between cells with high and low 53BP1 foci number. Thus, a direct correlation between DPR expression and DNA damage as shown by others could not be recapitulated in iPSC-derived cortical neurons carrying *C9ORF72-HRE* mutation.

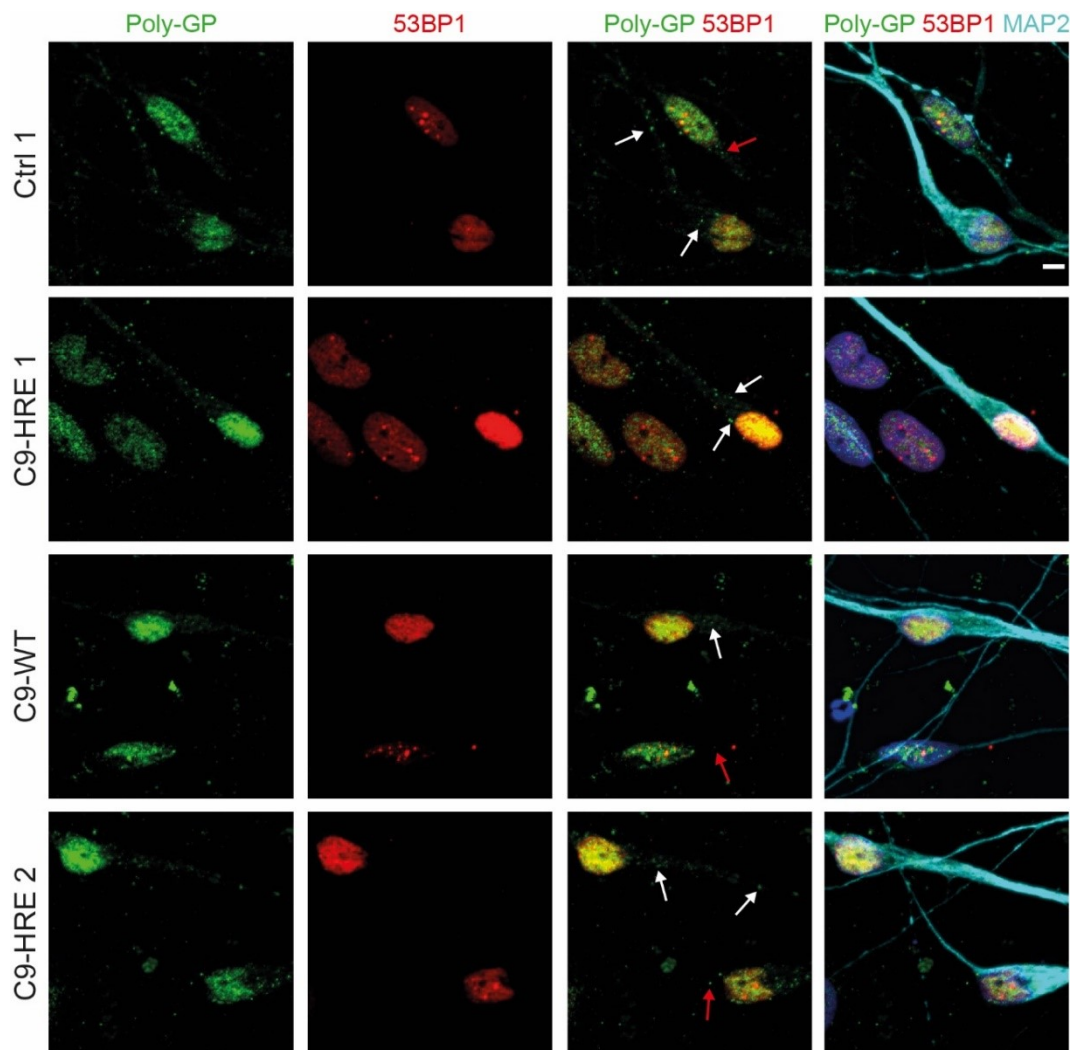


Figure 3.14 Poly-GP versus 53BP1.

Representative images of cortical neurons at maturation day 100 and stained for Poly-GP (green), 53BP1 (red) and neuron marker MAP2 (cyan) are shown. Small cytoplasmic Poly-GP granules could be detected in neurons without DNA damage (white arrows) and within neurons showing nuclear 53BP1 foci (red arrows). Nuclei were stained with Hoechst. Scale bars: 10 μ m.

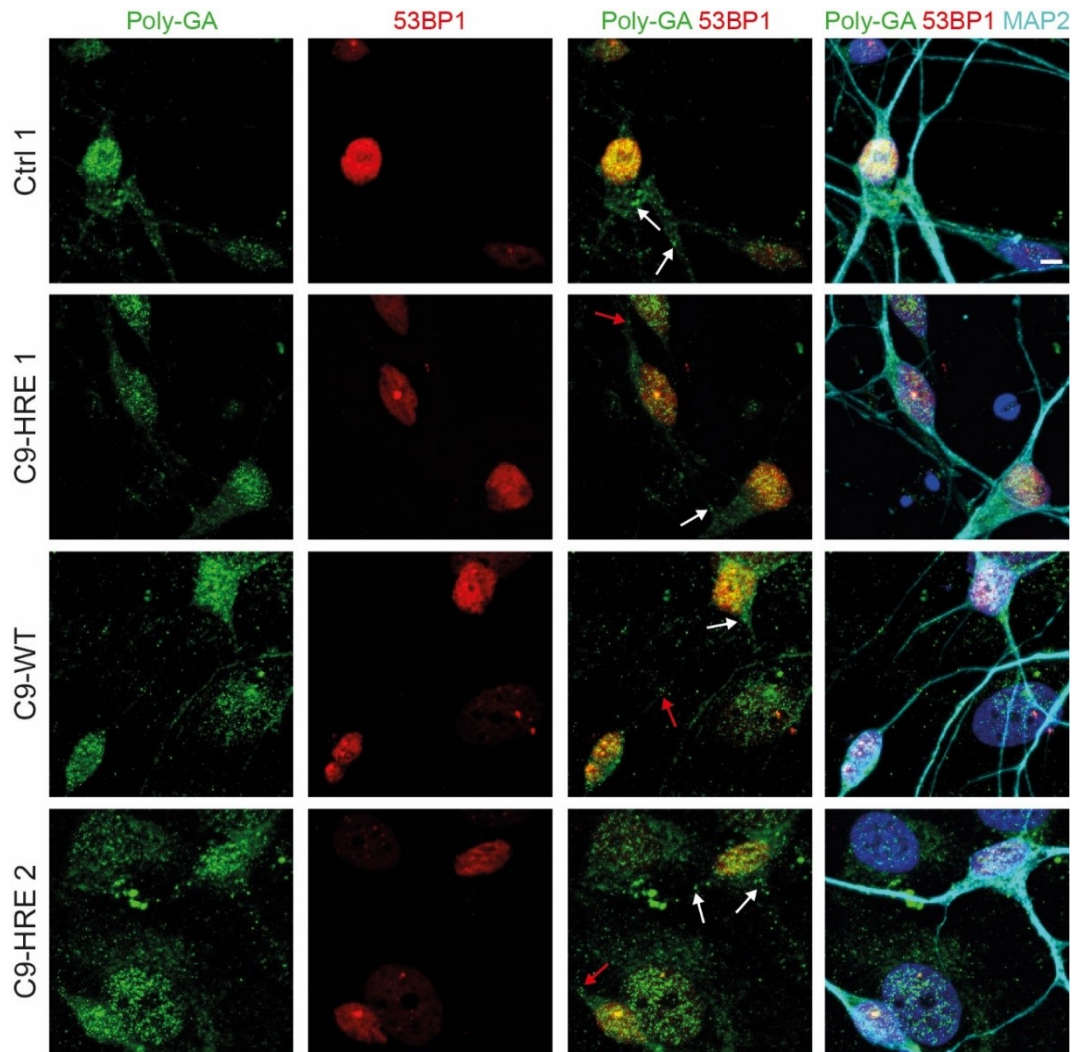


Figure 3.15 Poly-GA versus 53BP1.

Representative images of cortical neurons at maturation day 100 and stained for Poly-GA (green), 53BP1 (red) and neuron marker MAP2 (cyan) are shown. Small cytoplasmic Poly-GA granules could be detected in neurons without DNA damage (white arrows) and within neurons showing nuclear 53BP1 foci (red arrows). Nuclei were stained with Hoechst. Scale bars: 10 μ m.

3.3.4 TDP43 neuropathology in *C9ORF72-HRE* cortical cultures

To evaluate potential TDP43 neuropathology within the here used patient-specific *in vitro* model, 100 day matured iPSC-derived cortical neurons from healthy and *C9ORF72*-ALS patients were stained for TDP43.

No severe cytoplasmic accumulation of TDP43 was detectable. Only small cytoplasmic TDP43 granules were observed in control and in *C9ORF72-HRE* cortical neurons (Figure 3.16). TDP43 granules in *C9ORF72-HRE* mutant cortical neurons partially seemed to be bigger compared to control. Those granules, furthermore, did not co-localize with Poly-GA. In addition, nuclear loss of TDP43 was observed in a small number of cells. Also in these cells small cytoplasmic TDP43 granules were detected. However, qualitative screening revealed that mainly non-neuronal cells (MAP2 negative) showed a loss of nuclear TDP43 (Figure 3.17

A). Neuronal nuclear loss of TDP43 seemed to be very rare and was seen in only a few single MAP2 positive cells for C9-HRE 1 cell line (Figure 3.17 A, last panel). To determine if loss of nuclear TDP43 is associated with *C9ORF72-HRE* mutation, Hoechst positive and TDP43 negative nuclei were manually counted (independent of MAP2) and the percentages of cells with nuclear loss were determined. Quantification revealed that in *C9ORF72-HRE* mutant cortical cultures there were more cells with TDP43 negative nucleus compared to control (Figure 3.17). Because the percentages of TDP43 negative cells were highly variable between experiments, further quantification of additional experiments and cell lines need to be conducted.

Taken together, the detection of only small TDP43 granules in cortical neurons is consistent with previous reports which show that cytoplasmic TDP43 aggregation can be observed only at low amounts in cortical regions (Ash, Bieniek et al. 2013, Mackenzie, Arzberger et al. 2013, Mori, Arzberger et al. , Schludi, May et al. 2015). The nuclear clearance of TDP43 was accompanied by the cytoplasmic inclusion formation as previously shown (Neumann, Sampathu et al. 2006, Lee, Lee et al. 2011).

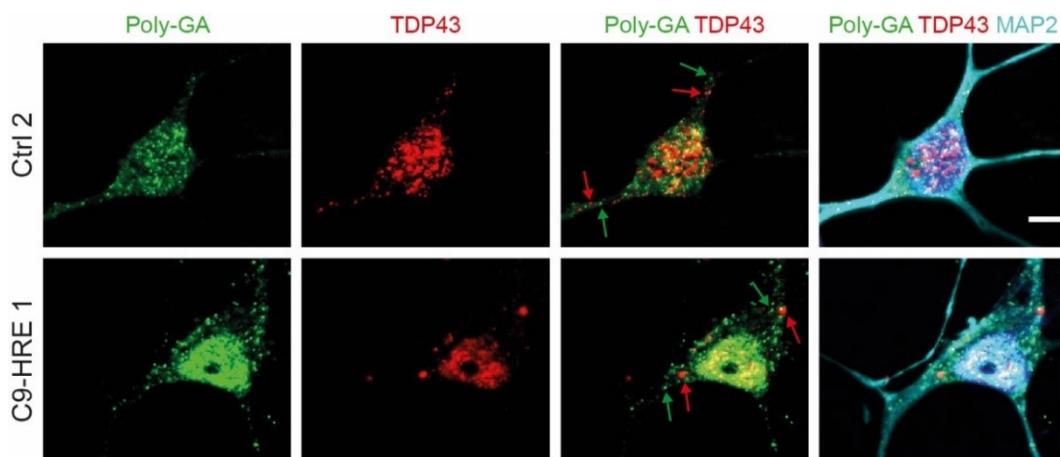


Figure 3.16 Detection of TDP43 versus Poly-GA in cortical neurons.

Representative images of cortical neurons at maturation day 100 and stained for Poly-GA (green), TDP43 (red) and MAP2 (cyan) are shown. Small cytoplasmic Poly-GA granules (green arrows) and TDP43 granules (red arrows) could be detected in non-isogenic (Ctrl 2 + C9-HRE 1) cortical neurons. Nuclei were stained with Hoechst. Scale bars: 5 μ m.

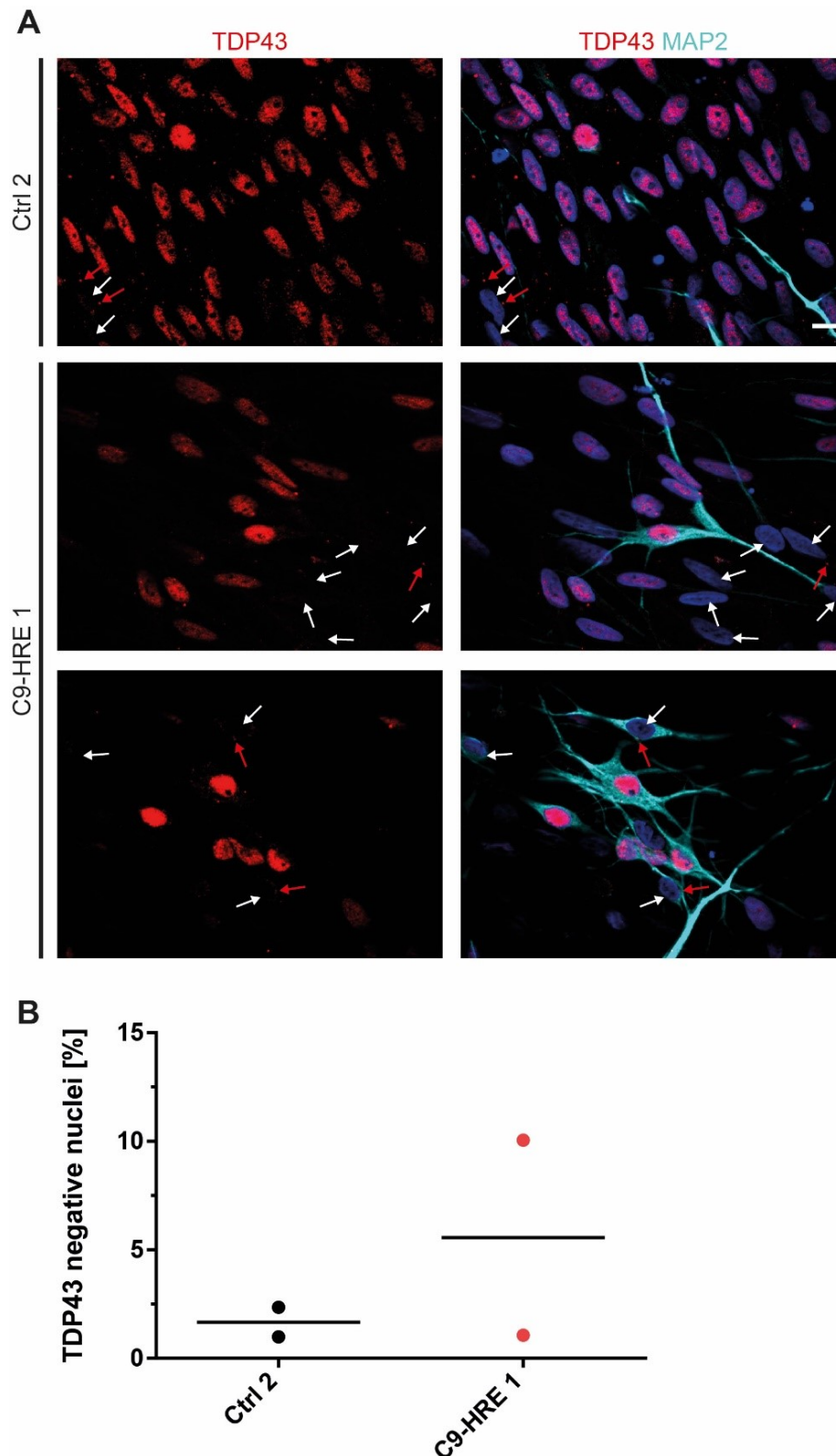


Figure 3.17 Loss of TDP43 in *C9ORF72-HRE* cortical neurons.

A Cortical neurons matured for 100 days were stained for TDP43 (red) and MAP2 (cyan). Depletion of nuclear TDP43 could be observed in control and *C9ORF72-HRE* mutant MAP2 negative cells (upper and middle panel) as well as in *C9ORF72-HRE* mutant MAP2 positive cells (lowest panel) as indicated by white arrows. Cell showing nuclear loss of TDP43 showed formation of cytoplasmic TDP43 granules (red arrows). Nuclei were stained with Hoechst. Scale bars: 10 μ m. **B** Percentages of cells showing depletion of nuclear TDP43 were determined manually. C9-HRE 1 showed increased loss of nuclear TDP43 compared to Ctrl 2.

3.4 Analysis of DNA damage in patient-specific *in vitro* models of ALS

3.4.1 Analysis of DNA damage marker γ H2AX and 53BP1

In order to detect DNA damage, patient-specific cultures were stained for DNA double strand break (DSB) marker proteins γ H2AX and 53BP1. Aim was the comparison of DNA damage levels in neurons and astrocytes. Because the *in vitro* models used in this thesis work showed variable differentiation potential (see section 3.1), the iPSC-derived neural cells were stained for neuron marker MAP2 or astrocyte marker GFAP to determine DNA damage specifically within marker positive nuclei. To evaluate the effect of patient-specific *C9ORF72* and *FUS* mutations on the amount of DNA damage, γ H2AX+ and 53BP1+ foci were determined at basal levels and using a pulse chase experiment after induction of DSBs by etoposide treatment and recovery. Cells were treated with 2 μ M etoposide for 1h to induce DNA damage and either fixed directly after treatment or etoposide was removed for 24h from the medium for DNA damage recovery (Figure 3.18 A). Furthermore, isogenic as well as non-isogenic lines were used.

3.4.1.1 Evaluation of DSB markers in cells with *C9ORF72-HRE* mutation

DSB markers γ H2AX and 53BP1 were analyzed in control and *C9ORF72-HRE* mutant spinal MNs, cortical neurons, and cortical astrocytes. Both markers were detected as nuclear dot-like pattern (foci) in spinal MNs (Figure 3.18), cortical neurons (Figure 3.19), and cortical astrocytes (Figure 3.20) under all implemented conditions (untreated, Eto 0h Recovery, and Eto 24h Recovery). Immunofluorescence staining revealed no obvious difference between examined cell lines or cell types. Therefore, CellProfiler software was used to semi-automatically detect and quantify nuclear foci (see section 2.5.1.1). In brief, MAP2 or GFAP positive nuclei were manually selected. Then, the software automatically detected nuclear γ H2AX and 53BP1 foci within neurons or astrocytes, following the quantification of DSBs under untreated and etoposide treated conditions.

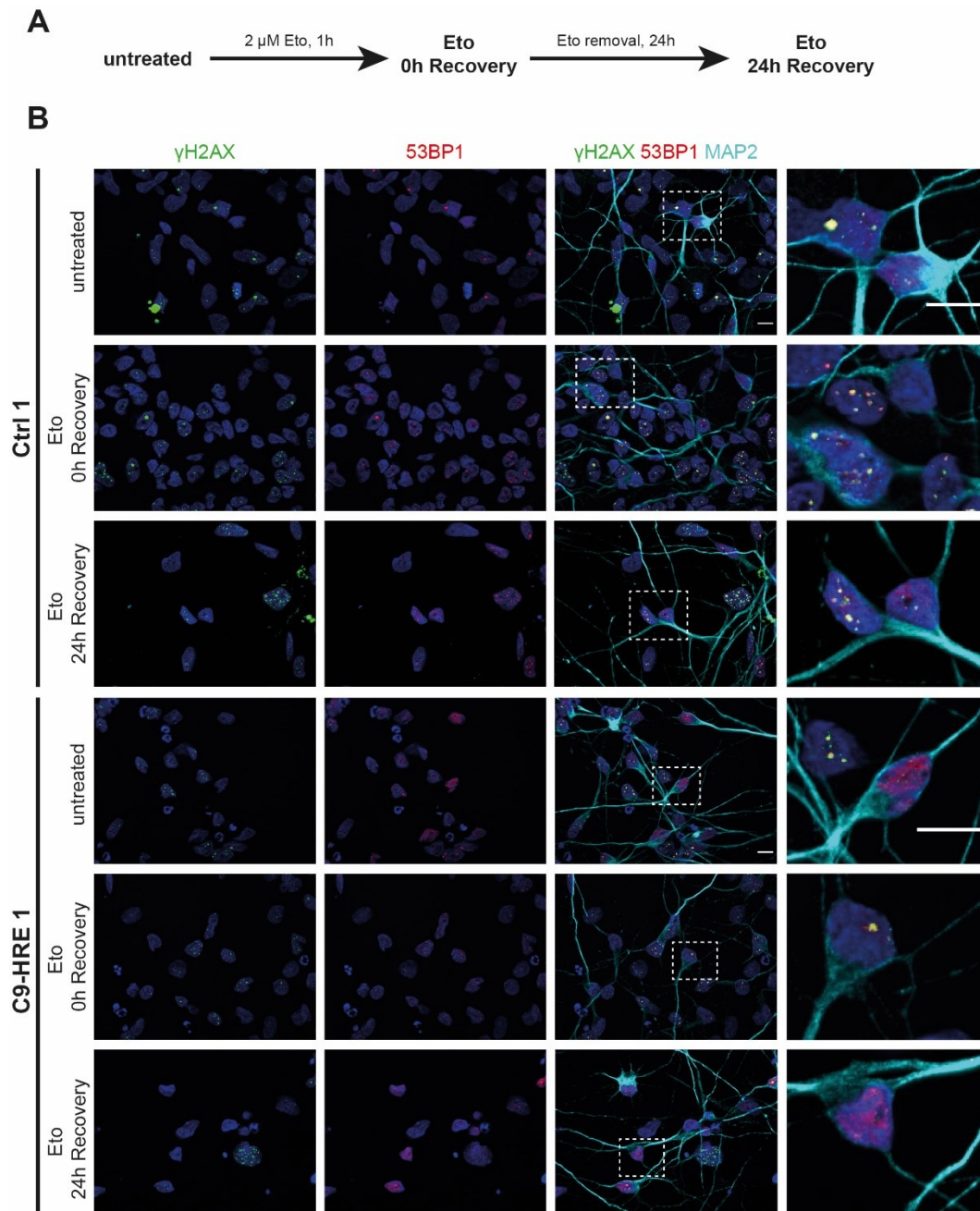


Figure 3.18 Detection of DSB markers in spinal MNs with *C9ORF72-HRE* mutation.

A Workflow chart of etoposide (Eto) treatment conditions with and without recovery. **B** Spinal MNs at maturation day 21 were stained for neuron marker MAP2 (cyan) and the two DSB markers γH2AX (green) and 53BP1 (red). DSBs were analyzed in untreated and etoposide treated cells without and after 24h recovery. Nuclear foci positive for both markers could be detected in all conditions and cell lines. Representative images of Ctrl 1 and C9-HRE1 are shown. Nuclei were stained with Hoechst. Scale bars: 10 μm .

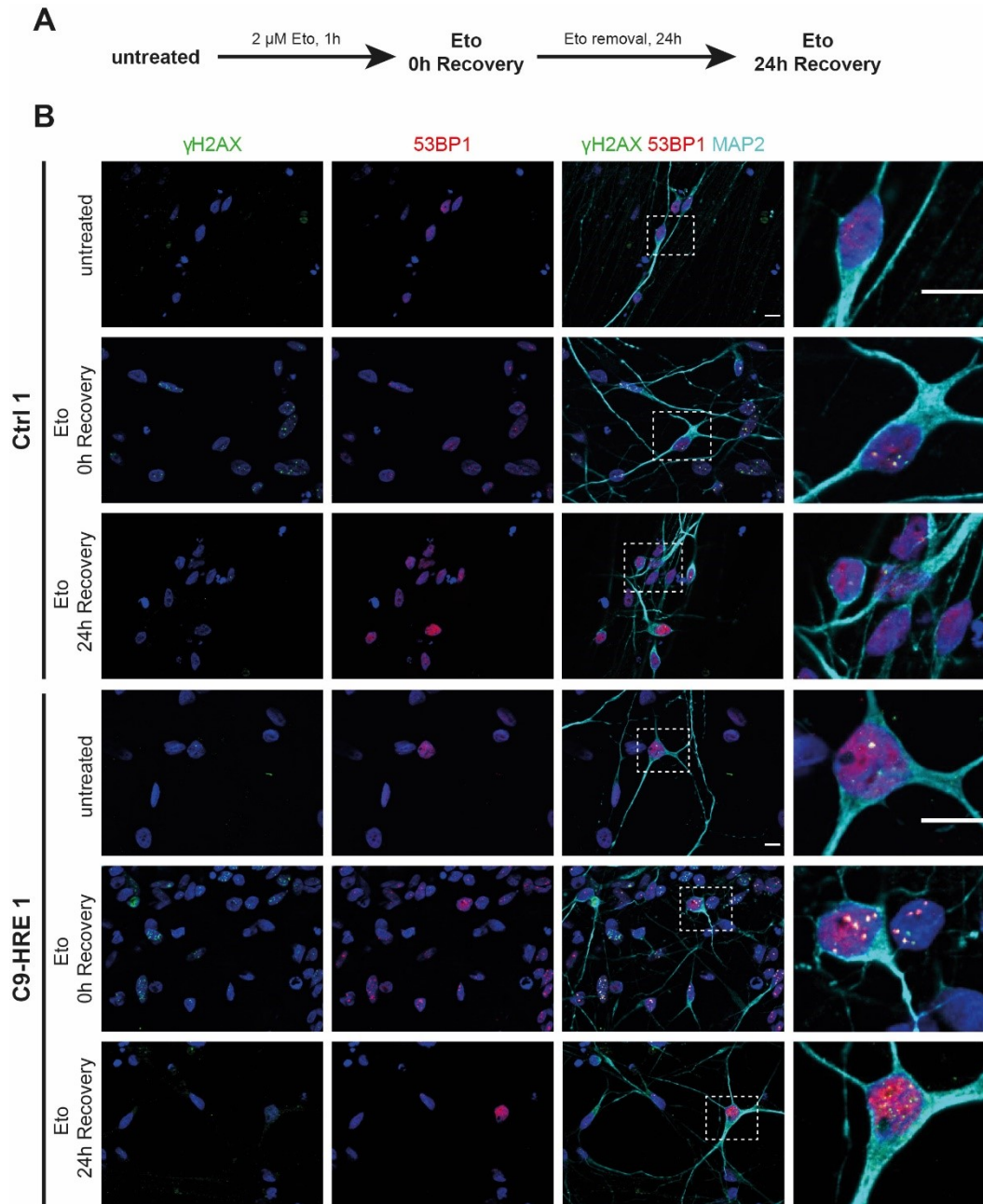


Figure 3.19 Detection of DSB markers in cortical neurons with *C9ORF72-HRE* mutation.

A Workflow chart of etoposide (Eto) treatment conditions with and without recovery. **B** Cortical cultures at maturation day 100 were stained for neuron marker MAP2 (cyan) and the two DSB markers γH2AX (green) and 53BP1 (red). DSBs were analyzed in untreated and Etoposide treated cells without and after 24h recovery. Nuclear foci positive for both markers could be detected in all conditions and cell lines. Representative images of Ctrl 1 and C9-HRE1 are shown. Nuclei were stained with Hoechst. Scale bars: 10 μm .

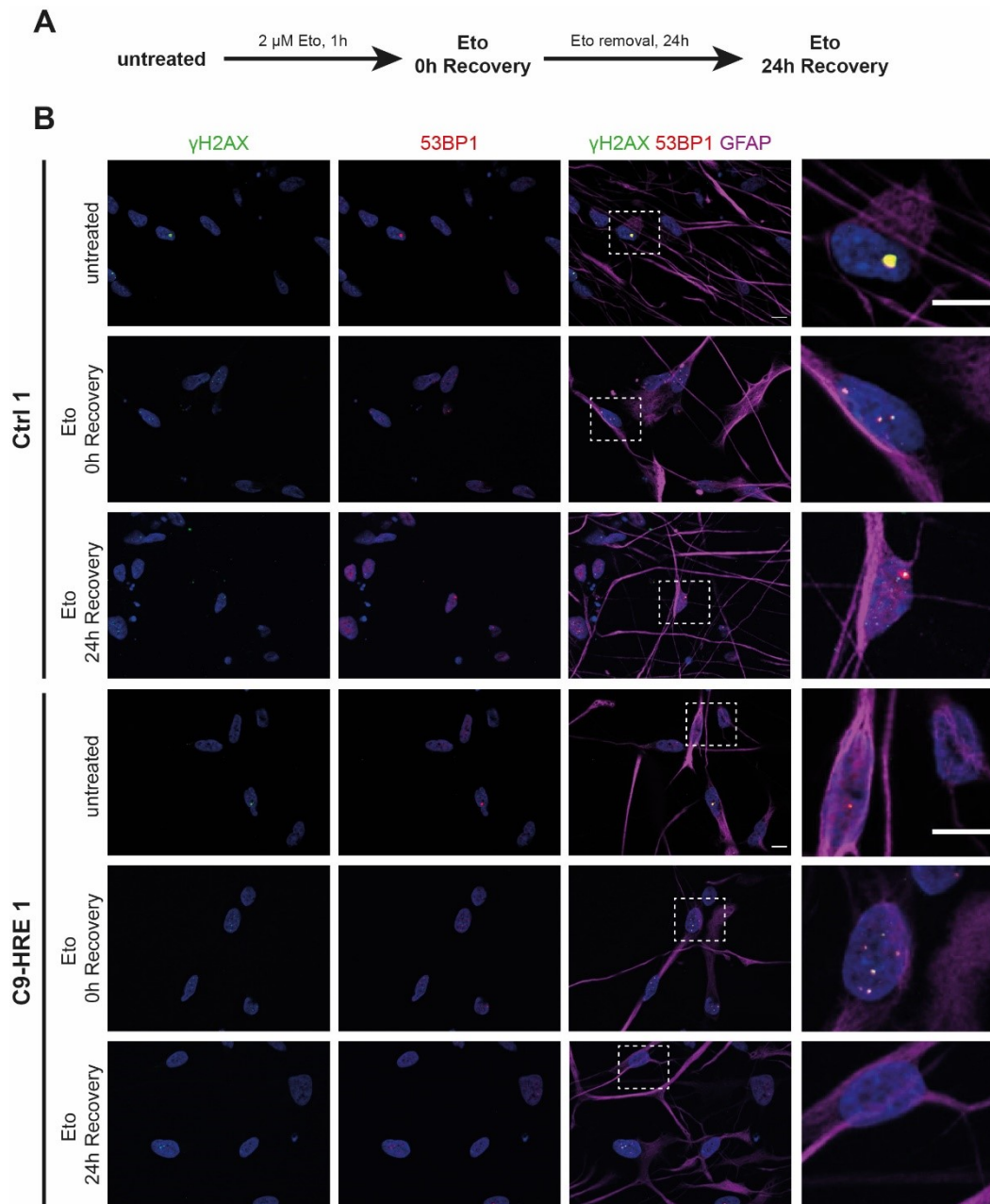


Figure 3.20 Detection of DSBs in cortical astrocytes with *C9ORF72-HRE* mutation.

A Workflow chart of etoposide (Eto) treatment conditions with and without recovery. **B** Cortical cultures at maturation day 100 were stained for astrocyte marker GFAP (magenta) and the two DSB markers γH2AX (green) and 53BP1 (red). DSBs were analyzed in untreated and Etoposide treated cells without and after 24h recovery. Nuclear foci positive for both markers could be detected in all conditions and cell lines. Representative images of Ctrl 1 and C9-HRE1 are shown. Nuclei were stained with Hoechst. Scale bars: 10 μm .

First, DSB levels were quantified in spinal MN cultures. For that, the non-isogenic lines Ctrl 1 and C9-HRE 1 were differentiated as described under section 2.3.7.2. Spinal MNs matured for 21 days were then stained for γ H2AX and 53BP1. In spinal MNs no difference of DNA damage between control and mutant was observed (Figure 3.21, γ H2AX: $P=0.124$, 53BP1: $P=0.123$, $n=3$, unpaired two-tailed t-test). This is contrast to previous findings which showed increased DSB levels in patient-specific spinal MNs with *C9ORF72-HRE* mutation (Higelin, Catanese et al. 2018) or in neuroblastoma cell and primary mouse neurons expressing *C9ORF72-HRE* (Farg, Konopka et al. 2017).

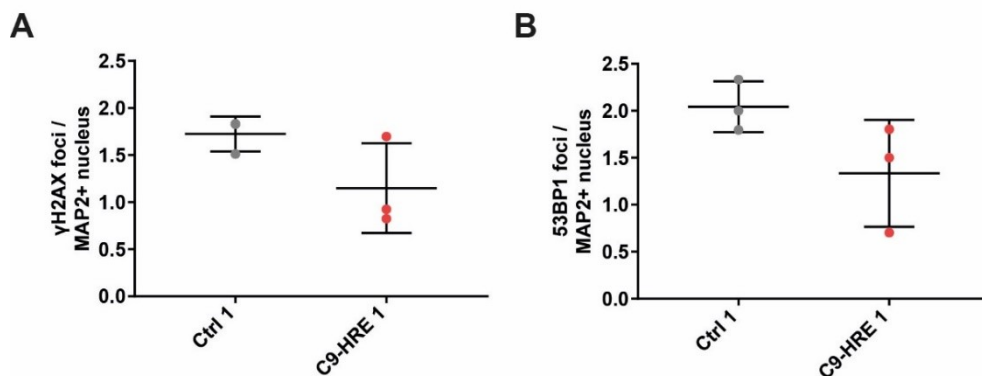


Figure 3.21 Characterization of DSB markers in untreated spinal MNs with *C9ORF72-HRE* mutation.

Nuclear foci of DSB markers γ H2AX and 53BP1 were semi-automatically detected within MAP2 positive nuclei in 21 day matured spinal MNs. **A-B** No difference of γ H2AX (A) or 53BP1 (B) foci number per MAP2+ nucleus was detected between control (Ctrl 1) and C9-HRE mutant (C9-HRE 1). Statistics were calculated by Unpaired two-tailed t-test ($n=3$).

Next, DSB numbers were determined within cortical cells. Figure 3.22 A and B show the quantification of DSB markers γ H2AX (A) and 53BP1 (B) in cortical neurons. An effect of cell line was observed on γ H2AX foci number ($P=0.013$, $F(4, 19) = 4.19$, $n=3-8$, One-way ANOVA) but not on 53BP1 foci count ($P=0.102$, $F(4, 16) = 2.31$, $n=3-6$, One-way ANOVA). In Figure 3.22 C and D the quantification of γ H2AX (C) and 53BP1 (D) in cortical astrocytes is demonstrated. The cell line showed an effect on both γ H2AX ($P=0.007$, $F(4,17)=5.18$, $n=3-7$, One-way ANOVA) and 53BP1 ($P<0.0001$, $F(4,17)=15.53$, $n=3-7$, One-way ANOVA) foci numbers. Statistical post-hoc testing revealed no significant differences when *C9ORF72-HRE* mutants were compared to their corresponding non-isogenic or isogenic controls (C9-HRE 1 vs. Ctrl 1+2 and C9-HRE 2 vs. C9-WT). Thus, *C9ORF72-HRE* mutation does not seem to drive the detected cell line effects. Taken together, it can be said, that no obvious effect of *C9ORF72-HRE* mutation on accumulation of DSBs in spinal or cortical neurons and astrocytes was observed.

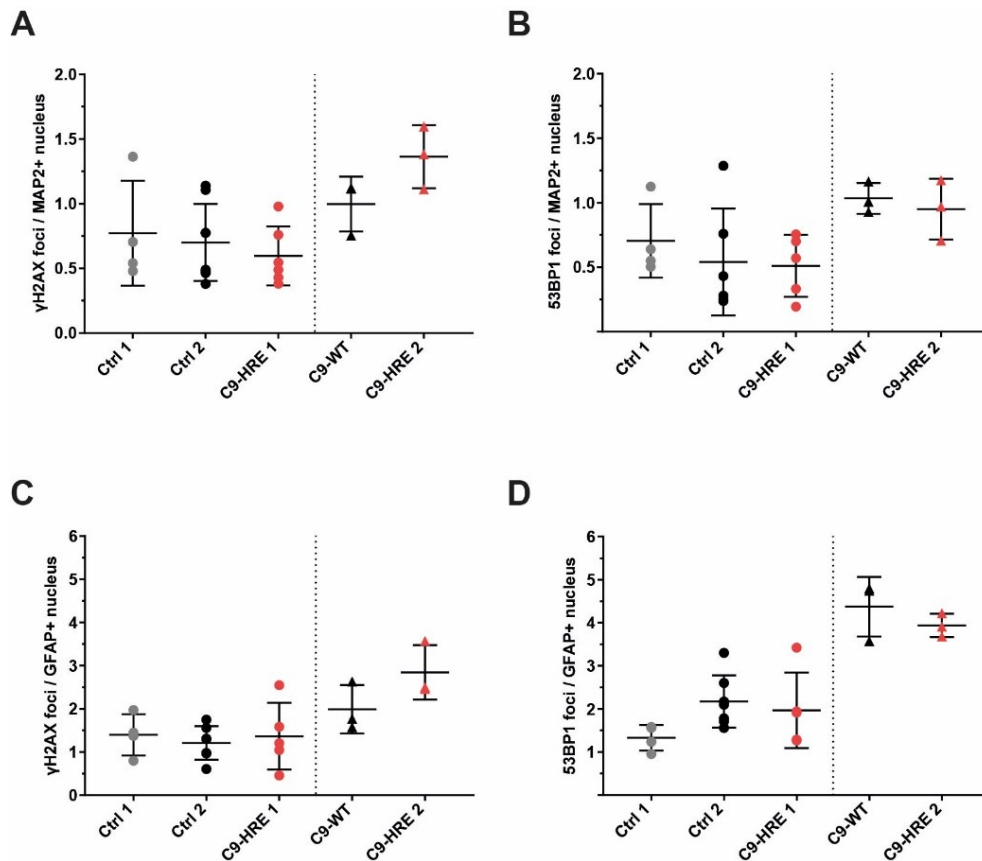


Figure 3.22 Characterization of DSB markers in untreated cortical neurons and astrocytes with *C9ORF72-HRE* mutation.

Nuclear foci of DSB markers γ H2AX and 53BP1 were semi-automatically detected within MAP2 and GFAP positive cells in 100 day matured cortical cultures. **A-B** In MAP2+ nuclei the cell line had an effect on γ H2AX foci number (A, $P=0.013$) but not on 53BP1 (B, $P=0.102$). **C-D** In GFAP+ nuclei the cell line had an effect on the foci number on both γ H2AX (C, $P=0.007$) and 53BP1 (D, $P<0.0001$). Multiple comparison revealed no significant difference between mutants compared to their corresponding controls (C9-HRE 1 vs. Ctrl 1+2; C9-HRE 2 vs. C9-WT). Statistics were calculated by one-way ANOVA with Tukey's post-hoc test ($n=3-8$).

We next asked the question whether there are differences in occurrence of DNA damage in cortical vs. spinal neurons. The neuronal cell type indeed showed an effect on basal γ H2AX (Figure 3.23 A, $P=0.001$, $F(1, 12) = 19.55$, $n=3-6$, Two-way ANOVA) and 53BP1 (Figure 3.23 B, $P<0.0001$, $F(1, 11) = 36.3$, $n=3-6$, Two-way ANOVA) levels. Thus, spinal MNs show significantly more DSBs compared to cortical neurons. Next, DSB levels were compared in cortical neurons versus astrocytes. Here the cell type also showed a strong effect on DSB levels for both γ H2AX (Figure 3.23 C, $P<0.0001$, $F(1, 36) = 39.97$, $n=3-8$, Two-way ANOVA) and 53BP1 (Figure 3.23 D, $P<0.0001$, $F(1, 33) = 160.7$, $n=3-6$, Two-way ANOVA). Neurons showed significantly less DNA damage than astrocytes in cortical cultures. Finally, the two DSB markers were compared amongst each other in cortical cells. In cortical neurons an effect of the marker on the foci number could not be detected (Figure 3.23 E, $P=0.147$, $F(1, 35) = 2.20$, $n=3-8$, Two-way ANOVA). In contrast, in cortical astrocytes an effect of the marker was detectable (Figure 3.23 F, $P<0.0001$, $F(1, 34) = 27.51$, $n=3-6$, Two-way ANOVA). However,

only two control lines showed significantly increased 53BP1 foci number compared to γ H2AX. In summary, spinal MNs showed significantly more basal DNA damage compared to cortical neurons while, in turn, cortical astrocytes presented significantly increased DSB levels compared to cortical neurons. Thus, the cell type showed a clear effect on basal DNA damage levels.

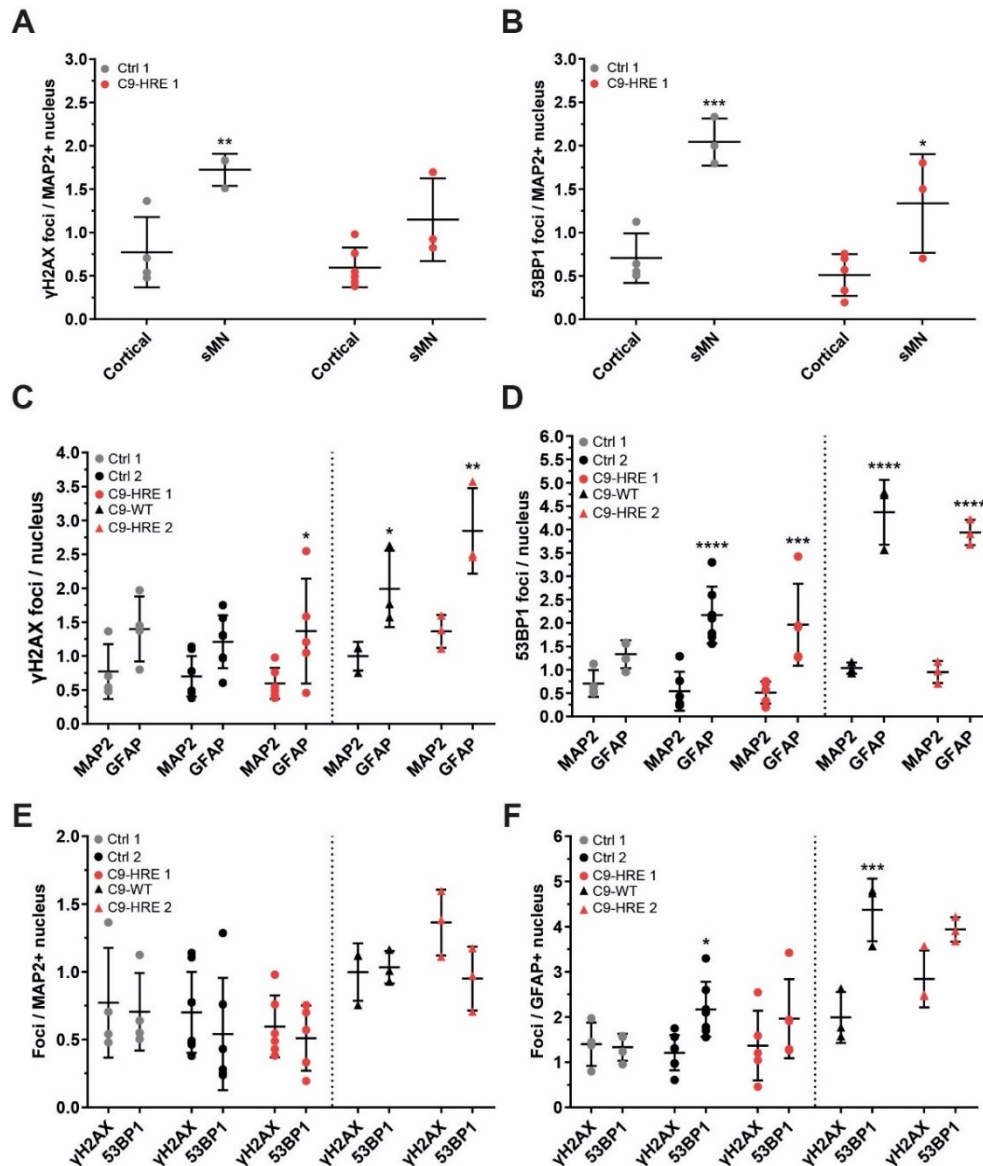


Figure 3.23 Comparison of DSB markers in untreated neural cell types with *C9ORF72-HRE* mutation.

After detection of nuclear foci of the DSB markers γ H2AX and 53BP1 in untreated spinal MNs and cortical neurons and astrocytes, the detected foci numbers were compared among each other. **A-B** Spinal MNs showed significantly higher basal levels of DNA damage for both γ H2AX (A) and 53BP1 (B) when compared to cortical neurons. **C-D** In cortical cultures, basal DNA damage levels for both γ H2AX (C) and 53BP1 (D) were significantly higher in astrocytes compared to neurons. **E-F** DSB marker 53BP1 showed similar basal levels of DNA damage in cortical neurons (E) and astrocytes (F) when compared to γ H2AX. Only in astrocytes (F), increased foci numbers of 53BP1 could be detected for Ctrl2 and C9-WT lines. Statistics were calculated by Two-way ANOVA with Sidak's post-hoc test to compare cortical vs. sMN (A-B), MAP2 vs. GFAP (C-D), or γ H2AX vs. 53BP1 (E-F) (n=3-8). Asterix indicate post-hoc significances.

No clear effect of patient-specific *C9ORF72-HRE* mutation on DNA damage could be observed in unstressed conditions. Therefore, we next investigated whether induction of DNA damage differs in mutants and controls. Thus spinal and cortical cultures were treated with etoposide to analyze the effect of DNA damage induction in mutant cells. Etoposide (Eto) is an inhibitor of topoisomerase II α which results in the formation and accumulation of DSBs as long as it is exposed to cell culture (Walker and Nitiss 2002). Spinal cultures at day 21 or cortical cultures at day 100 of maturation were treated with 2 μ M etoposide for 1h. Cells were either fixed directly after treatment or etoposide was removed to allow cells to recover for 24h (Figure 3.24 A). Aim was to evaluate if patient-specific cells react differentially to the treatment and if they are able to recover.

First, etoposide treated spinal MNs were analyzed. DSB levels after etoposide treatment and recovery were normalized to untreated values. No effect of treatment was neither observed for γ H2AX (Figure 3.24 B, $P=0.079$, $F(2, 11) = 3.22$, $n=2-3$, Two-way ANOVA) nor 53BP1 (Figure 3.24 C, $P=0.165$, $F(2, 11) = 2.136$, $n=2-3$, Two-way ANOVA).

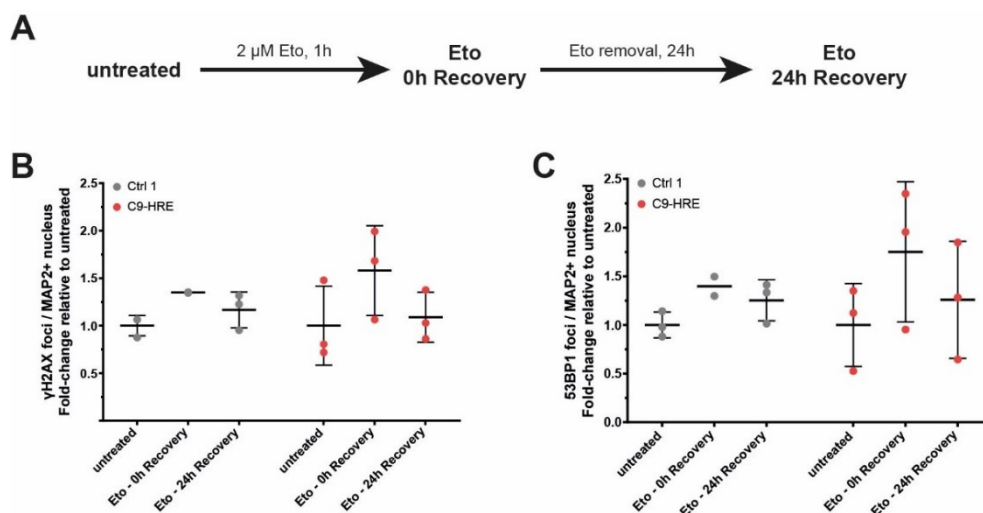


Figure 3.24 Characterization of DSB markers in etoposide treated spinal MNs with *C9ORF72-HRE* mutation.

A Workflow chart of etoposide (Eto) treatment conditions with and without recovery. Spinal MNs matured for 21 days were treated with etoposide to induce DNA damage. Foci number of γ H2AX and 53BP1 was determined in untreated, etoposide treated without recovery and etoposide treated with 24h recovery MAP2+ cells. **B+C** An effect of etoposide treatment on DSB foci levels could not be detected, neither for γ H2AX (B, $P=0.079$) nor 53BP1 (C, $P=0.165$). Data is depicted relative to untreated cell line. Statistics were calculated by Two-way ANOVA with Dunnett's post-hoc test to compare treatment effect with untreated condition ($n=2-3$).

Next, etoposide treated cortical cultures were analyzed. Because non-isogenic controls Ctrl 1 and Ctrl 2 did not significantly differ under untreated condition they were pooled for analysis. Evaluation of etoposide treatment and recovery was analyzed relative to untreated condition. In cortical neurons, etoposide treatment showed a strong effect on both γ H2AX (Figure 3.25 B, $P<0.0001$, $F(2, 46) = 47.33$, $n=2-12$, Two-way ANOVA) and 53BP1 (Figure 3.25 C,

$P < 0.0001$, $F(2, 43) = 16.02$, $n = 2-10$, Two-way ANOVA) foci number. Same in cortical astrocytes, a strong effect of treatment on γ H2AX (Figure 3.25 D, $P < 0.0001$, $F(2, 46) = 23.97$, $n = 2-11$, Two-way ANOVA) and 53BP1 (Figure 3.25 E, $P = 0.0004$, $F(2, 46) = 9.183$, $n = 2-11$, Two-way ANOVA) was observed. All examined cell lines and cell types were able to recover. Of note, similar as observed in untreated conditions non-isogenic lines behaved slightly differently compared to isogenic ones. Non-isogenic controls (Ctrl 1+2) and C9-HRE 1 mutant showed a stronger increase of DNA damage after treatment than isogenic control C9-WT and C9-HRE 2 mutant. This, in turn, is contrary to untreated conditions, in which the two isogenic lines showed increased basal DSB levels compared to non-isogenic lines (Figure 3.22).

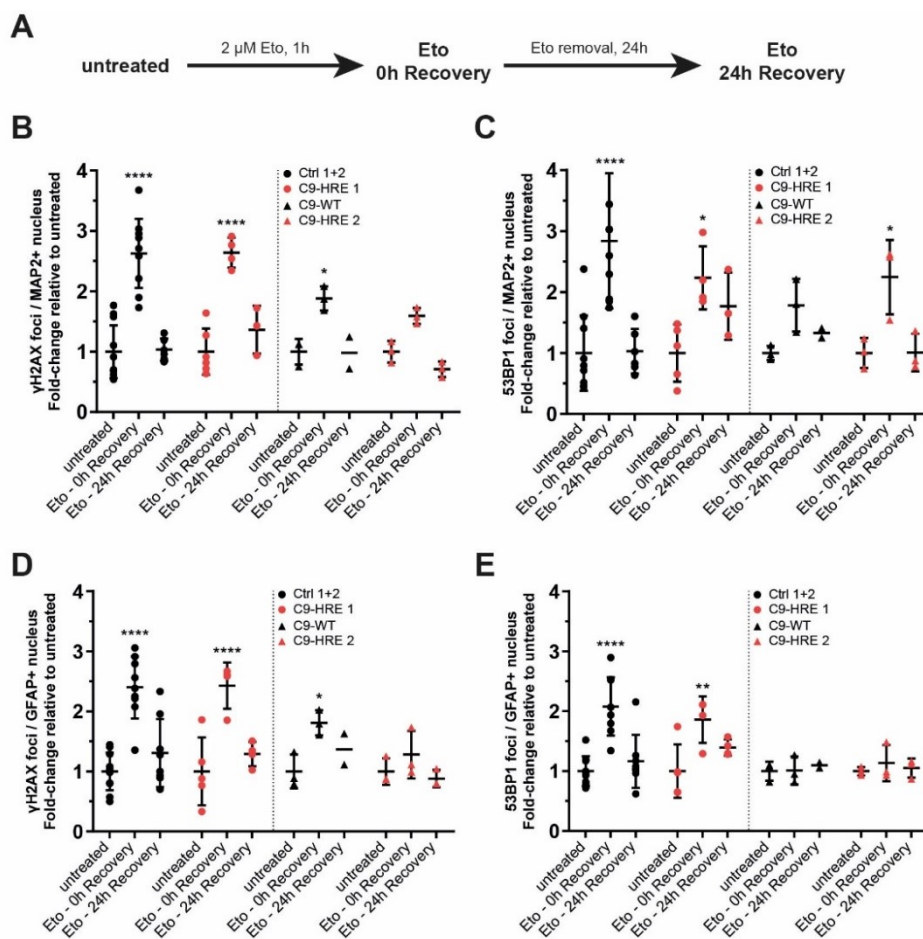


Figure 3.25 Characterization of DSB markers in etoposide treated cortical cultures with *C9ORF72*-HRE mutation.

A Workflow chart of etoposide (Eto) treatment conditions with and without recovery. Cortical cultures matured for 100 days were treated with etoposide to induce DNA damage. Foci number of γ H2AX and 53BP1 was determined in untreated, etoposide treated without recovery, and etoposide treated with 24h recovery MAP2+ and GFAP+ cells. **B-C** Etoposide treatment showed an effect in cortical neurons for both DSB markers γ H2AX (B, $P < 0.0001$) and 53BP1 (C, $P < 0.0001$). **D-E** An effect of treatment could also be detected in cortical astrocytes for both γ H2AX (D, $P < 0.0001$) and 53BP1 (E, $P = 0.0004$). Non-isogenic lines showed a stronger increase of DNA damage after etoposide treatment than isogenic lines. No difference between controls and C9-HRE mutants could be observed. All tested lines recover after DNA damage induction. Data is depicted relative to untreated cell line. Data of non-isogenic controls (Ctrl 1+2) were pooled. Statistics were calculated by Two-way ANOVA with Dunnett's post-hoc test to compare treatment effect with untreated condition ($n = 2-12$). Asterix indicate post-hoc significances.

Taken together, etoposide treatment and recovery showed an effect in cortical neurons and astrocytes but not in spinal MNs. Most importantly, there was no difference between control and mutant cells. Moreover, isogenic lines C9-WT and C9-HRE 2 showed a less strong increase of DSB number after treatment than non-isogenic lines. Both lines presented already higher DNA damage level in untreated condition in cortical cells. The same applies to spinal MNs, which showed increased DSB levels compared to cortical neurons. In conclusion, this implies that cells which already possess high basal levels of DNA damage, do not accumulate DSBs after etoposide treatment to the same extent as cells with lower basal DNA damage levels or cells with high basal DNA damage levels die of after treatment.

3.4.1.2 Evaluation of DSB marker in cells with *FUS-NLS* mutation

Increased levels of DNA damage, specifically DSBs, and increased vulnerability to DNA damage induction have been reported for various *in vitro* models carrying ALS-associated *FUS* mutations (Mastrocola, Kim et al. 2013, Qiu, Lee et al. 2014, Higelin, Demestre et al. 2016, Naumann, Pal et al. 2018). In our recent publication, using the same *FUS* lines as within this thesis work, we could show that *FUS* mutant NPCs and spinal MNs show higher DSB levels in untreated condition compared to control (Figure 3.26 A+B). However, nothing is yet known about cortical cells in *FUS* mutation carriers. Therefore, DSB levels were analyzed in *FUS* mutant cortical neurons and astrocytes under the same conditions as already described for *C9ORF72-HRE* mutant cells (see section 3.4.1.1). Only DSB marker 53BP1 was evaluated, as previous comparison of γ H2AX and 53BP1 revealed no significant difference between both markers in controls and *C9ORF72-HRE* mutants (Figure 3.23 E+F). Further, isogenic control (*FUS*-WT) and mutants (*FUS*-R521C and *FUS*-P525L) were compared to non-isogenic controls (Ctrl 1 and Ctrl 2). As described in section 3.2, the patient-specific line *FUS*-R521C was used to generate EGFP-tagged lines *FUS*-WT and *FUS*-P525L. Thus, all three lines are isogenic to each other, however only two possess an EGFP-Tag. To exclude a possible influence of the EGFP-Tag on DNA damage levels, *FUS*-R521C line was additionally compared to non-isogenic control lines Ctrl 1 and Ctrl 2.

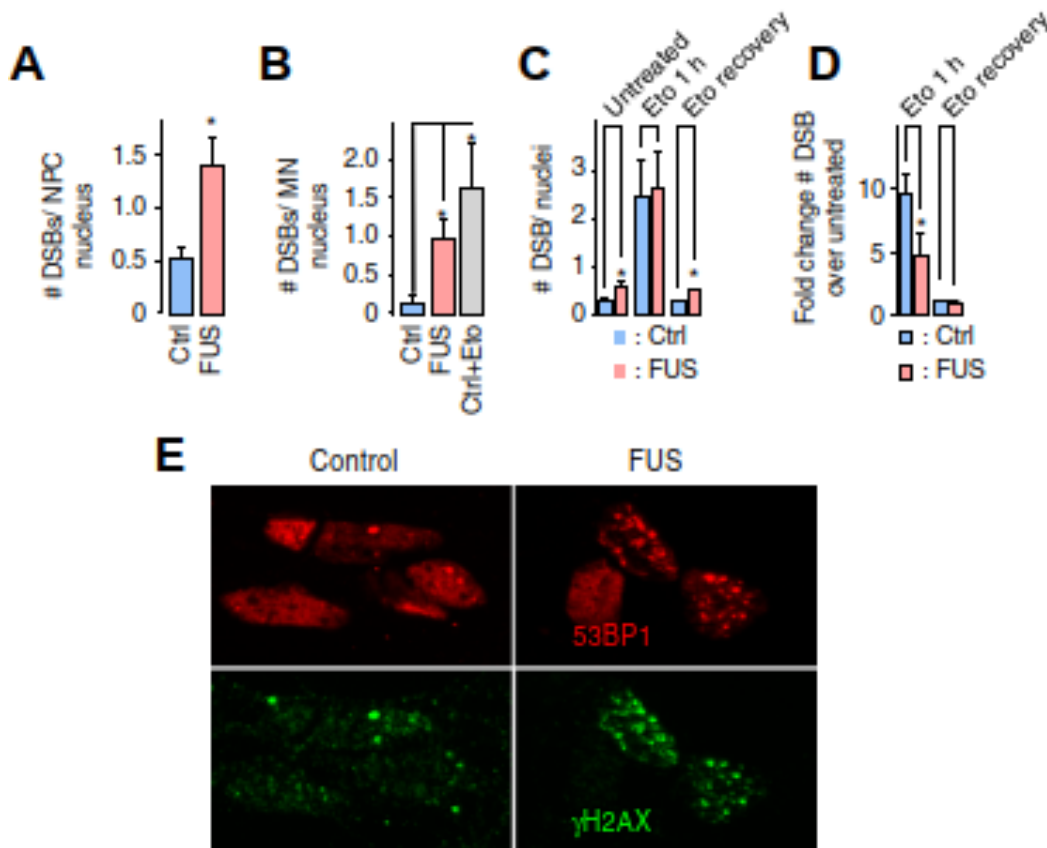


Figure 3.26 Characterization of DSB marker γ H2AX and 53BP1 in spinal MNs with *FUS* mutation.

A+B Both, *FUS*-NPCs (A) and mature sMNs (B) showed more DSBs per nucleus over controls (N = 3). **C** Untreated mature *FUS*-P525L (*FUS*) sMNs showed increased nuclear DSB foci over isogenic control cells, consistent with untagged *FUS* lines in **B**. 1 h etoposide treatment and 24 h withdrawal led to a similar response compared to control cells (i.e. transient increase of DSB foci and reversion to basal levels indicative of successful DSB repair). **D** Same as **C** but expressed as fold change over respective untreated control (N = 4). Statistics A-D: data are plotted as mean \pm SD, unpaired t-test (only A) or one-way ANOVA (B-D) with post-hoc Bonferroni test. **E** Validation of the γ H2AX antibody in *FUS*-P525L sMNs (without etoposide) by co-staining with 53BP1: Note the prominent colocalization (merge, yellow overlapping). The figure was adopted from Naumann & Pal 2018 and modified by the author of this study.

Small nuclear 53BP1 foci could be detected in all cell lines in untreated (Figure 3.27 A) and etoposide treated conditions (images not shown). Quantification of 53BP1 foci numbers in untreated cells showed no effect of the cell line on DSB levels in cortical neurons (Figure 3.27 B, $P=0.865$, $F(4, 11) = 0.31$, $n=1-6$, One-way ANOVA with Tukey's post-hoc test). In contrast, an effect of cell line on foci numbers was observed in cortical astrocytes (Figure 3.27 C, $P=0.047$, $F(4, 12) = 3.346$, $n=2-7$, One-way ANOVA with Tukey's post-hoc test). Statistical post-hoc testing, however, revealed no significant differences between *FUS* mutants and controls. This is different to spinal MNs, where *FUS* mutants showed significantly increased DSB levels compared to control (Figure 3.26 A-C). Furthermore, cortical astrocytes showed increased DSB levels in controls and *FUS* mutants when compared to cortical neurons (Figure 3.27 D). Thus, the cell type had an effect on 53BP1 foci number ($P<0.0001$, $F(1, 23) = 25.96$,

n=1-7, One-way ANOVA), which is consistent to previous findings in *C9ORF72-HRE* mutant lines (Figure 3.23 C+D).

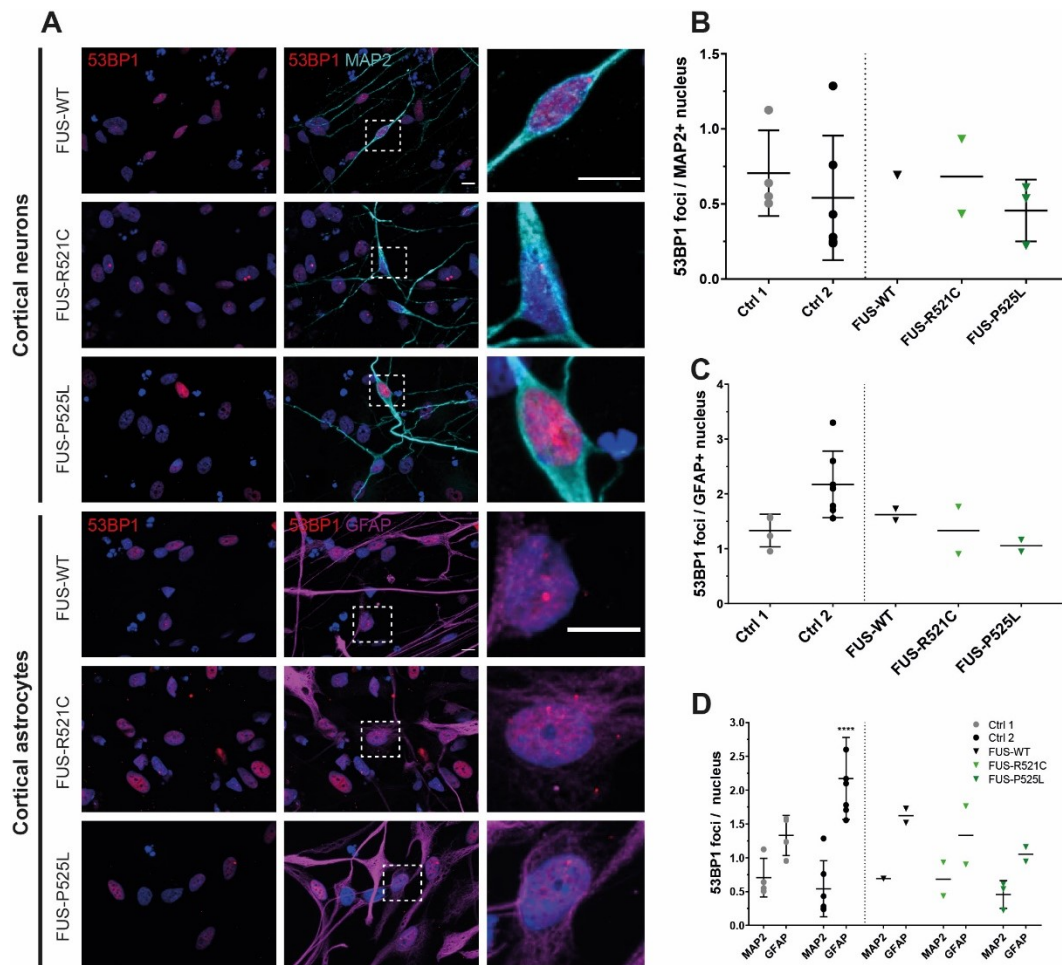


Figure 3.27 Characterization of DSB marker 53BP1 in untreated cortical cells with *FUS* mutation.

Cortical cultures at maturation day 100 were stained for DSB marker 53BP1 (red) and neuron marker MAP2 (cyan) or astrocyte marker GFAP (magenta). Nuclear foci were semi-automatically detected within MAP2 and GFAP positive nuclei. **A** Nuclear 53BP1 positive foci could be detected in all cell lines. Representative images of isogenic *FUS* control (*FUS*-WT) and mutant (*FUS*-R521C, *FUS*-P525L) lines are shown. Nuclei were stained with Hoechst. Scale bars: 10 μ m. **B-C** The cell line had no effect on basal 53BP1 foci numbers in cortical neurons (B, $P=0.865$) but showed an effect in astrocytes (C, $P=0.047$). Effect of cell line on 53BP1 foci numbers was calculated by One-way ANOVA with Tukey's post-hoc test ($n=1-7$). **D** The cell type had an effect on basal DSB levels ($P<0.0001$). The effect of cell type was calculated by Two-way ANOVA with Sidak's post-hoc test to compare MAP2 vs. GFAP ($n=1-7$). Asterix indicate post-hoc significances.

Evaluation of DSB levels after DNA damage induction revealed an effect of etoposide treatment on 53BP1 foci numbers in both cortical neurons (Figure 3.28 B, $P<0.0001$, $F(2, 33) = 18.96$, $n=1-10$, Two-way ANOVA) and astrocytes (Figure 3.28 C, $P<0.0001$, $F(2, 32) = 76.54$, $n=1-11$, Two-way ANOVA). Controls as well as mutants showed increased DSB numbers after treatment. All cell lines were able to recover after DNA damage induction. No differences were found between control and mutant cortical cells. Those results are consistent with DNA damage induction data obtained from spinal MNs. Figure 3.26 C+D shows, that both

control and *FUS* mutant spinal MNs show increased DSB levels after etoposide treatment and that both are able to recover DNA damage after etoposide retrieval.

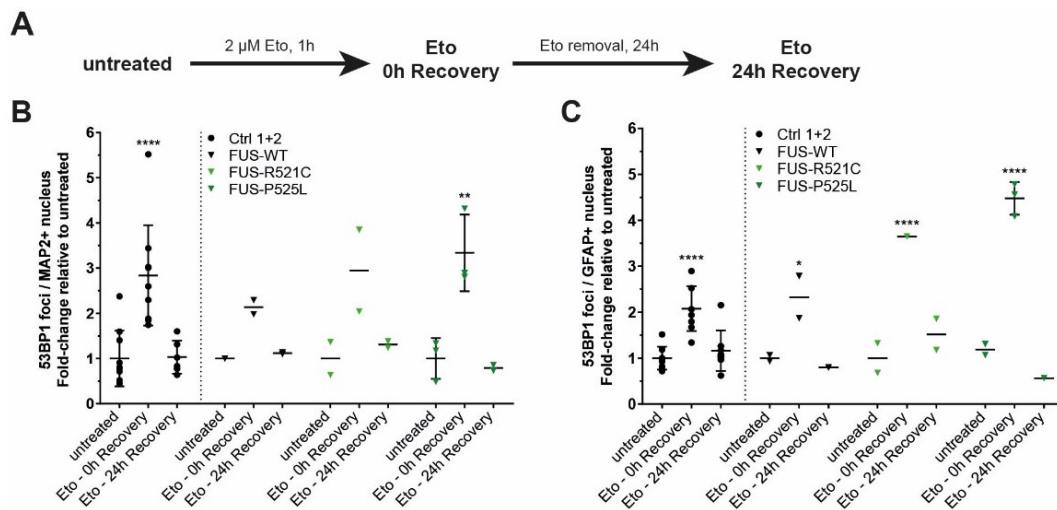


Figure 3.28 Characterization of DSB marker 53BP1 in etoposide treated cortical cells with *FUS* mutation.

A Workflow chart of etoposide (Eto) treatment conditions with and without recovery. Cortical cultures matured for 100 days were treated with etoposide to induce DNA damage. Foci number of 53BP1 was determined in untreated, etoposide treated without, and etoposide treated with 24h recovery MAP2+ and GFAP+ cells. **B-C** Etoposide treatment showed an effect on 53BP1 foci numbers in cortical neurons (B, $P < 0.0001$) and astrocytes (C, $P < 0.0001$). All tested lines recover after DNA damage induction. Data is depicted relative to untreated cell line. Data of non-isogenic controls (Ctrl 1+2) were pooled. Statistics were calculated by two-way ANOVA with Dunnett's post-hoc test to compare treatment effect with untreated condition ($n=1-11$). Asterix indicate post-hoc significances.

In summary, cortical cultures of *FUS* mutants show no increased accumulation of DNA damage in unstressed condition compared to controls, which is different to spinal MNs. Moreover, cortical astrocytes show increased basal levels of DNA damage compared to neurons. This results are consistent with aforementioned findings in *C9ORF72-HRE* mutant cortical cultures. Finally, cortical neurons and astrocytes are able to recover after DNA damage induction via etoposide, similar as observed in spinal MNs.

3.4.1.3 Effect of etoposide on cell survival

Previous findings showed that cortical neurons are able to recover DNA damage induced by etoposide (see section 3.4.1). However, single cells acquire different amounts of DSBs. Because neurons are supposed to be highly vulnerable to DSBs (Penndorf, Witte et al. 2018), cells with high DSB levels might rather die off instead of repairing the DNA damage. In turn, measured DSB levels after recovery might be related to cells that did not acquire high DSB levels after etoposide treatment. To validate this, fragmented nuclei were counted and MAP2 positive nuclei numbers were determined in cortical cultures before and after etoposide treatment with 24h recovery phase. Quantification of fragmented nuclei revealed no effect of

etoposide treatment on cell death (Figure 3.29 A, $P=0.094$, $F(1, 22) = 3.06$, $n=1-3$, Two-way ANOVA). Etoposide neither had an effect on neuron numbers (Figure 3.29 B, $P=0.133$, $F(1, 22) = 2.44$, $n=1-3$, Two-way ANOVA). Taken together, DNA damage induction via etoposide did not result in increased cell death or neuron loss.

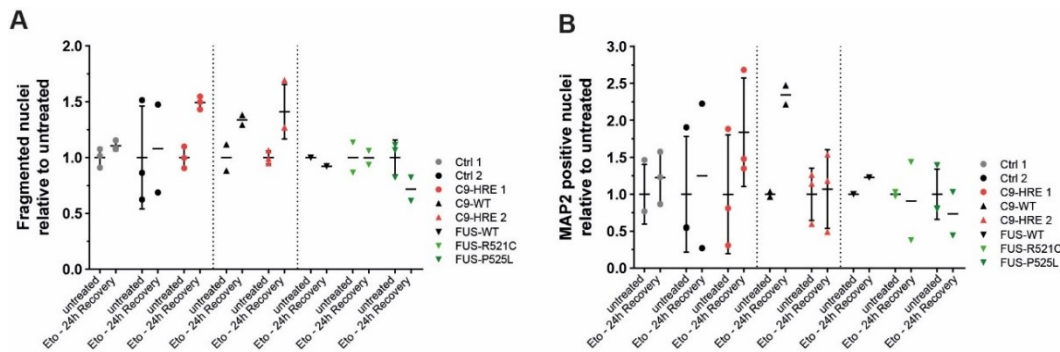


Figure 3.29 Effect of etoposide on cell survival.

Cortical cultures matured for 100 days were treated with etoposide to induce DNA damage and allowed to recover for 24h. **A-B** The effect of etoposide treatment on cell survival was analyzed by determining the numbers of fragmented nuclei (A) and living MAP2 positive nuclei (B). Etoposide treatment showed neither effect on fragmented nuclei numbers (A, $P=0.094$) nor on MAP2 positive nuclei (B, $P=0.1329$). Data is depicted relative to untreated cell line. Statistics were calculated by Two-way ANOVA with Sidak's post-hoc test to compare etoposide treated cells after recovery with untreated condition ($n=1-3$).

3.4.2 Analysis of laser-induced DNA damage

FUS is known to be involved in DDR and mutations within *FUS* gene were shown to lead to an impaired recruitment of the protein to DNA damage sites (DDS) (Mastrocola, Kim et al. 2013, Wang, Pan et al. 2013, Qiu, Lee et al. 2014, Rulten, Rotheray et al. 2014, Naumann, Pal et al. 2018). In particular, our group could show that P525L mutant FUS fails to be recruited to laser cut sites in spinal MNs (Figure 3.30)(Naumann, Pal et al. 2018). In this thesis work, the same isogenic WT and P525L EGFP-tagged FUS lines were used. Implementing the same UV laser-induced DNA damage, the recruitment of WT and P525L FUS-EGFP was analyzed in iPSCs and cortical neurons.

Both cell types (iPSC and cortical neurons) showed FUS-EGFP recruitment to DDS in WT as well as in P525L mutants (Figure 3.31 A). Of note, P525L mutant FUS is recruited to laser cut, which is contrary to previous findings in spinal MNs (Figure 3.30)(Naumann, Pal et al. 2018). Evaluation of FUS-EGFP fluorescence intensity on cutting site revealed, that P525L mutant cortical neurons showed delayed recruitment of FUS-EGFP and longer association to laser cut sites compared to controls (Figure 3.31 B, lower panel). This difference was not observed in iPSCs, in which control and P525L mutant cells show similar FUS-EGFP kinetics after laser irradiation (Figure 3.31 B, upper panel). In iPSCs, mutant FUS even seemed to be recruited slightly faster than WT FUS.

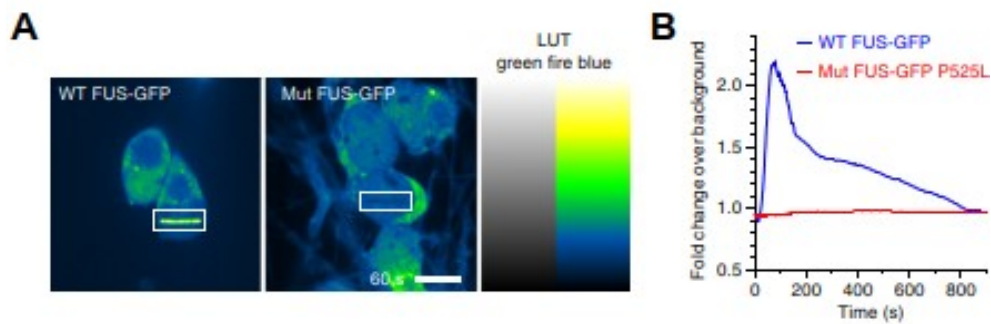


Figure 3.30 Recruitment of FUS-EGFP to laser-induced DNA damage sites in spinal MNs.

A Mutant FUS-P525L failed to be recruited to DNA damage sites. Recruitment-withdrawal to Laser cuts in spinal MN nuclei (boxed area) expressing normal (WT) or mutant P525L (Mut) FUS-EGFP was imaged live at maturation day 21. **B** Quantification of A, FUS-EGFP at cut over time. The figure was adopted from Naumann & Pal 2018 and modified by the author of this study.

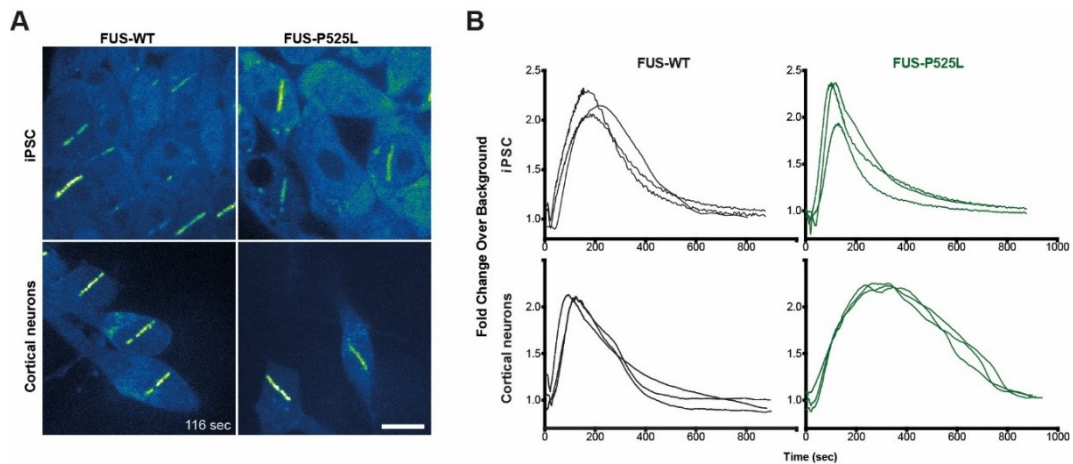


Figure 3.31 Recruitment of FUS-EGFP to laser-induced DNA damage sites in cortical neurons.

A Recruitment of WT or P525L FUS-EGFP to laser cut sites was analyzed in iPSCs and cortical neurons matured for 70-90 days. WT as well as P525L mutant cells showed recruitment of FUS-EGFP Scale bar: 10 μ m (Supplementary movie S1). **B** Graphic representation of A showed that FUS-EGFP recruitment of P525L mutant is delayed in cortical neurons compared to mutant iPSCs and compared to WT cortical neurons as well as iPSCs. Graphs represent FUS-EGFP signal at cut over time. Data from $n=3$ independent experiments is plotted. Data obtained from individual cells was pooled per experiment.

3.5 Axonal organelle trafficking analysis within patient-specific cortical neurons

Axonal organelle trafficking is known to be impaired in ALS (Wang, Li et al. 2013, Xia, Wang et al. 2016, Guo, Naujock et al. 2017, Kreiter, Pal et al. 2018, Naumann, Pal et al. 2018). Using compartmentalized microfluidics chambers (MFCs) for directed axonal growth, previous findings of our group show that *FUS* mutations lead to trafficking defects in the distal axon of

spinal MNs (Figure 3.32)(Naumann, Pal et al. 2018). In this thesis work, the same *FUS* mutant iPSC line as included in the publication (FUS-R521C) and one additional *FUS* mutant line (FUS-P525L) were used to analyze axonal organelle trafficking in iPSC-derived cortical neurons. Mitochondria and lysosome were visualized by the life dye treatments with Mito- and LysoTracker of cortical neurons cultured in MFCs (Pal, Glass et al. 2018). Videos from the distal (away from the soma) and proximal (near the soma) part of neuron axon were taken to determine organelle motility (schematic overview: Figure 3.34 A).

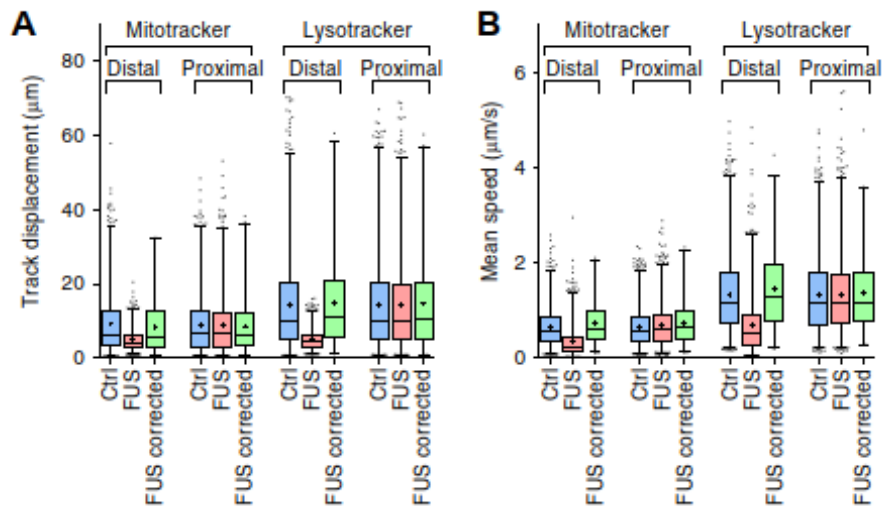


Figure 3.32 *FUS* mutant spinal MNs develop trafficking defects of mitochondria and lysosomes in distal axons.

Organelle displacement (A) and mean speed (B) analyses as box plots, batch analysis of three non-isogenic controls (Ctrl) and three *FUS* mutant (FUS) lines. The figure was adopted from Naumann & Pal 2018 and modified by the author of this study.

3.5.1 Directed axonal outgrowth of cortical neurons

Cortical cultures were matured for 40-45 days and plated into MFCs (see section 2.3.7.3). In order to determine if cortical neurons successfully grow within MFCs, cells were observed over time after splitting into MFCs. Brightfield imaging showed that control as well as *FUS* mutant lines successfully grow through micro channels from proximal to distal site (Figure 3.33 A, upper panel). Cortical astrocytes can also generate long cell processes that look similar to neuronal dendrites and axons (Figure 3.1 C, Figure 3.20). To verify that only neuronal axons grow through the micro channels and to distinguish neuronal and astrocytic cell processes, MFC cultures were stained for axon marker SMI32 (also known as neurofilament H) and astrocyte marker GFAP. SMI32 labels non-phosphorylated NF-H, including cell bodies, dendrites and subpopulation of pyramidal neurons in human and monkey neocortex (Campbell and Morrison 1989, Trapp, Peterson et al. 1998). Figure 3.33 A shows that only SMI32 positive axons grow through micro channel exit sites, while GFAP positive processes could not be observed.

Additionally, after splitting into MFCs the number of passed channel exits was counted 2 to 3 times a week for the isogenic *FUS* lines. In Figure 3.33 B the data of two independent differentiations is plotted. For all three cell lines a highly inter-experimental variability was observed. As shown in the upper panel of Figure 3.33 B, *FUS-R521C* neurons need more time to fully grow through the micro channels in one experiment (Exp. 1) which is the other way around in the second experiment (Exp.2). In contrast, *FUS-P525L* as well as *FUS-WT* neurons need approximately the same time to grow through MFCs in both independent experiments. Nevertheless, the data showed no growth differences caused by *FUS* mutations (*FUS-R521C* and *FUS-P525L*) compared to their isogenic control (*FUS-WT*). Moreover, the data showed that cortical neurons need at least 30 days after splitting into MFCs to fully grow through channel exit sites.

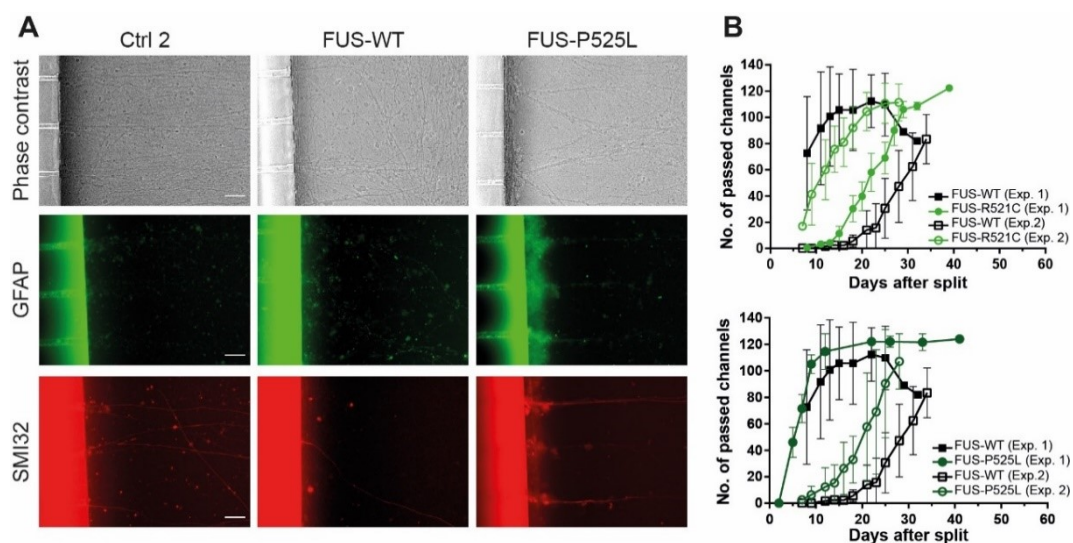


Figure 3.33 Characterization of distal axonal outgrowth of cortical neurons in MFCs.

Cortical cells were split into MFCs at maturation day 40-45. **A** To fully grow through the micro channels exit sites, neurons needed to be matured for at least further 40 days as shown by brightfield imaging (upper panel). Staining of distal exit sites of MFCs for axon marker SMI32 (red) and astrocyte marker GFAP (green) confirmed that only neuronal axons grow through the micro channels and not astrocytic processes. Representative images of non-isogenic line Ctrl 2 and isogenic lines *FUS-WT* and *FUS-P525L* are shown. Images display sections of 20x magnification. Scale bars: 25 μ m. **B** Quantitative determination of number of passed channel exits over time after split into MFCs. No difference of axonal outgrowth between isogenic control (black lines) and *FUS* mutants (*FUS-R521C*: light green, upper panel; *FUS-P525L*: dark green, lower panel) was observed. Shown is data of two independent differentiations (Exp. 1 + 2). For each experiment, values of three technical replicates (MFCs) were pooled.

3.5.2 Motility of mitochondria and lysosomes

Previous findings of our group and others could show, that axonal organelle trafficking is impaired in mutant *FUS* (Guo, Naujock et al. 2017, Naumann, Pal et al. 2018)(Figure 3.32) and *TDP43* (Kreiter, Pal et al. 2018) spinal MN cultures. To analyze organelle motility parameters in cortical cultures, mitochondria and lysosome were tracked with a live cell imaging approach (see section 2.4.3) and the mean speed and displacement (=extent of

movement radius) of tracked organelles was determined. Cortical MFC cultures were imaged earliest at maturation day 70 (~30 days after splitting into MFCs) to ensure that cortical neuron axons fully grow through micro channels. Latest imaging time point was 130 days after neural induction to ensure imaging before cortical neurons start to degenerate. Received data of the two isogenic *FUS* mutant lines FUS-R521C and FUS-P525L was pooled (FUSmt) and compared to pooled control data received from isogenic control FUS-WT and the non-isogenic control line Ctrl 2.

Live cell imaging movies and maximum intensity projections of Mito- and LysoTracker showed no obvious differences between controls and mutants in cortical neurons cultured in MFCs (Figure 3.34 B+E, Supplemental Movie S2+3). Quantitative assessment of mitochondrial and lysosomal track displacement revealed a significant increased track displacement of mitochondria and lysosomes in distal and proximal axons of *FUS* mutants compared to controls (Figure 3.34 C+F, Supplemental Table S 1, Supplemental Table S 3). Calculation of mitochondrial and lysosomal mean speed revealed that both organelle types are significantly slowed down in distal and proximal axons of *FUS* mutant cortical neurons compared to controls (Figure 3.34 D+G, Supplemental Table S 2, Supplemental Table S 4). Taken together, an effect of *FUS* mutations on axonal trafficking of mitochondria and lysosome could be observed in cortical neurons. However, mutant *FUS* affects cortical axonal trafficking differently as observed in spinal MNs in which a dramatic if not complete loss of motility has been described (Guo, Naujock et al. 2017, Naumann, Pal et al. 2018).

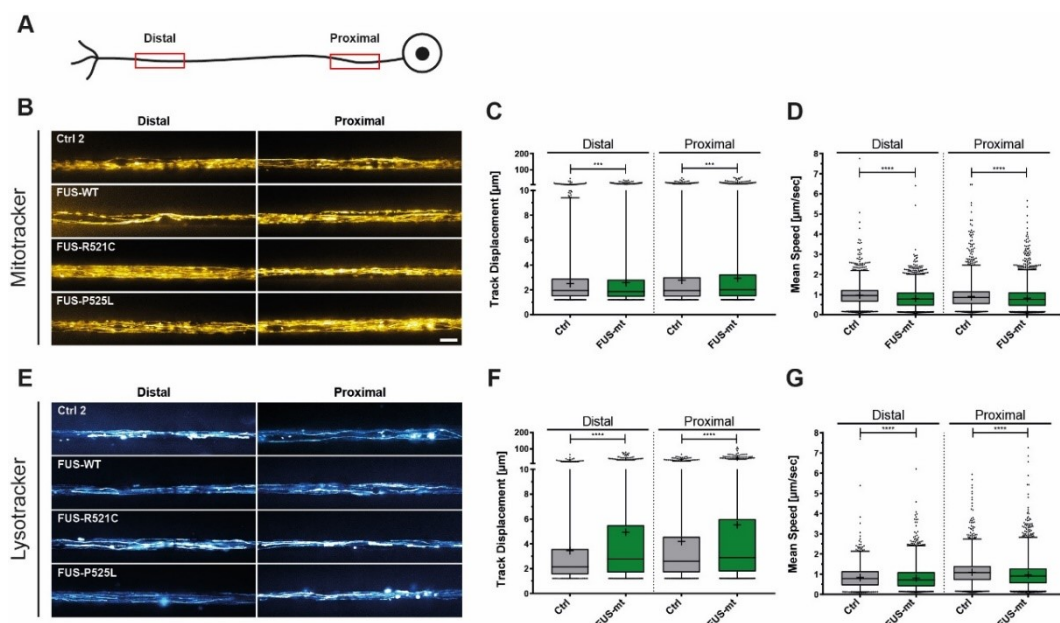


Figure 3.34 Live cell imaging analysis of mitochondrial and lysosomal motility.

A Schematic demonstration of distal and proximal areas of a neuron axon. **B+E** Representative images taken from live cell imaging show Mitotracker (B) and LysoTracker (E) in 900 µm MFC cortical cultures

matured for over 70 days (for movies see supplementary Movies S2+3). Images represent maximum projection intensities of one passed channel and display sections from 100 x magnifications. Scale bars: 10 μm . **C** Quantification of mitochondrial track displacement showed a significant increase of proximal and distal motility. **D** Quantification of mean speed revealed significantly decreased motility of mitochondria in proximal and distal axons. **F** Quantification of lysosomal track displacement showed a significant increase of proximal and distal motility. **G** Quantification of mean speed revealed significantly decreased lysosomal motility in both proximal and distal axons. Analysis as box plots. Control data was pooled from non-isogenic Ctrl 2 and isogenic FUS-WT. FUS mutant data was pooled from isogenic mutants FUS-R521C and FUS-P525L. For detailed statistics see Supplemental Table S 1-4. Statistics were calculated by Kolmogorov-Smirnov test (n=3-7 technical replicates from 2-4 independent differentiations).

Not all of the detected organelles are considered to be moving. To calculate the percentages of moving mitochondria and lysosome the ratio of non-moving versus moving organelle counts was determined. Tracked organelles with a displacement $\geq 1.2 \mu\text{m}$ were considered as moving tracks. Everything below was considered to be a non-moving organelle. Figure 3.35 shows the comparison of total moving mitochondria and lysosomes in distal versus proximal cortical neuron axon.

An effect of cell line on amount of moving mitochondria was neither detected for distal nor for proximal axon (Figure 3.35 A, Supplemental Table S 5). Similar amounts of moving mitochondria could be detected for mutants as well as controls with no detectable effect of *FUS* mutation. Consistent with this, no effect of cell line on amounts of moving lysosome in distal and proximal (Figure 3.35 B, Supplemental Table S 6) axon could be observed. Similar amounts of moving lysosomes were detected for both mutants and controls.

In summary, on average $20.61 \pm 6.56 \%$ moving organelles were detected within cortical axons. An effect of *FUS* mutation on amounts of moving organelles could not be observed.

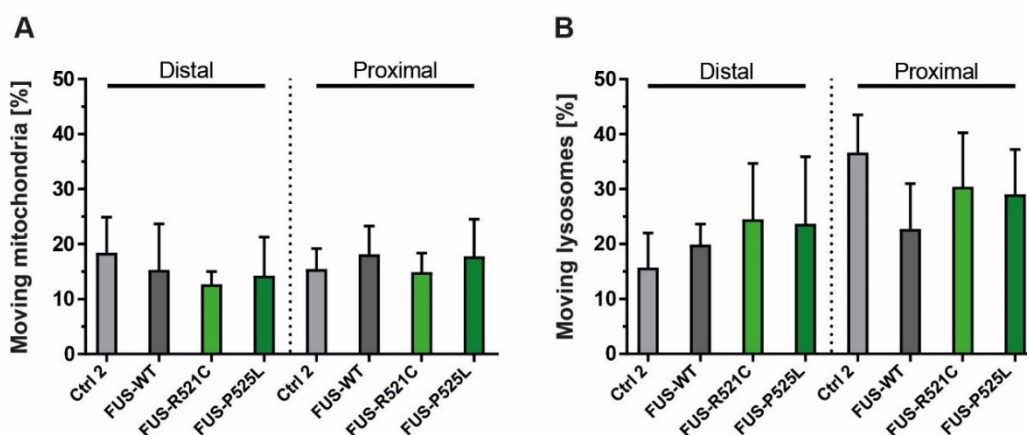


Figure 3.35 Quantification of mitochondrial and lysosomal moving tracks.

The amounts of moving organelles in distal and proximal parts of cortical neuron axon were determined by calculating the ratio of non-moving and moving tracks. Tracked organelles with a displacement $\geq 1.2 \mu\text{m}$ were considered as moving tracks. No effect of cell line on amounts of moving mitochondria (A) or lysosomes (B) could be observed. The effect of the cell line on organelle motility was calculated by One-way ANOVA with Tukey's post-hoc test (n=3-7 technical replicates from ≥ 2 independent differentiations). See Supplemental Table S 5+6 for descriptive statistics.

4 Discussion

The main subject of this thesis work is to model cortical neuropathology of *FUS*- and *C9ORF72*-associated ALS using patient-specific iPSCs. Thereby, this study concentrates on the importance of human cellular models and the consideration of the analyzed cell type. One issue in ALS research is still that our understanding of the disease is mainly based on human postmortem tissue, animal models, and overexpression model systems. Cellular models using heterologous expression in primary rodent cultures or human carcinoma-derived cell lines (HeLa, U2OS, NSC-34, etc.) are an important tool to decipher disease mechanism underlying disease, however they cannot fully represent physiological conditions. Moreover, in ALS specifically spinal and cortical motor neurons are affected by neurodegeneration (Van Langenhove, van der Zee et al. 2012) and also astrocytes have been proposed to contribute to disease (Di Giorgio, Carrasco et al. 2007, Marchetto, Muotri et al. 2008, Haidet-Phillips, Hester et al. 2011, Meyer, Ferraiuolo et al. 2014). Therefore, the analysis of those affected cell types is important to reveal mechanism causing particularly those cells to degenerate. Another issue in ALS research which is discussed in this thesis, is that various pathomechanisms have been proposed to cause ALS pathology and that those highly depend on the underlying gene mutation (Japtok, Lojewski et al. 2015, Higelin, Demestre et al. 2016, Pal, Glass et al. 2018).

To gather a deeper insight into this set of issues, patient-specific iPSC lines were used, which allow the analysis of pathological effects caused by physiological expressed mutant proteins. Moreover, iPSC-derived neural cultures allowed the direct comparison of cortical neurons vs. astrocytes and cortical vs. spinal neurons of the same patient. The additional use of isogenic iPSC lines further allowed the analysis of mutation-caused effects independent of patient's genetic background. To narrow down the many and various proposed cellular processes causing ALS, this thesis concentrated on the evaluation of cellular distribution of disease-associated proteins, DNA damage, and axonal organelle trafficking. Therewith and to the best of my knowledge, this study is the first to analyze iPSC-derived cortical cultures carrying either mutation within *FUS* or *C9ORF72* and directly comparing neurons vs. astrocytes as well as spinal vs. cortical lineage. Previous studies concentrating on those two ALS-associated genes focus only on the analysis of iPSC-derived spinal MNs or use rodent primary cultures of cortical neurons. Thus, this thesis work will contribute new knowledge in the context of cortical neuropathology in *FUS*- and *C9ORF72*-ALS.

4.1 Control and mutant iPSCs differentiate into cortical neurons and astrocytes

Patient-specific iPSCs derived from healthy controls and ALS patients with either *FUS* or *C9ORF72* mutation successfully differentiate in various cortical cell types, including neurons of all cortical layers and astrocytes. The protocol used here resulted in the derivation of heterogeneous cultures including differentiation into cortical neurons and astrocytes (Burkhardt, Martinez et al. 2013). The advantage of this protocol is that different cortical neural cell types are co-cultured and can be monitored simultaneously, closely mimicking physiological conditions. Increased cell death or variances of neuron count as hint for neurodegeneration could not be detected. By this I found no hint for a difference of differentiation behavior in healthy vs. diseased lines indicating no neurodevelopmental phenotype. In this thesis work, marker positive cells of all cortical deep and upper layers neurons (Figure 3.2) could be detected as well as astrocytes (Figure 3.1). This is consistent with a previously published study on *FUS-NLS* iPSC lines (Japtok, Lojewski et al. 2015).

A significant drawback of the used protocol is the long differentiation time which further only results in the derivation of 5 to 20% neurons. Because iPSCs are used as starting material, the differentiation process becomes more complex and cells need to be differentiated for 2 to 4 months to obtain fully mature cultures. However, fast protocols such as NGN2 driven cortical differentiation did not yield cortical subtype/layer subtype neurons (B. Szewczyk in our group, personal communication). In contrast to this, spinal MN protocols are easy to handle and highly efficient because NPCs can be used as starting material. The use of NPCs allows the derivation of greater than 90% of spinal MNs within 2 to 3 weeks of differentiation (Kreiter, Pal et al. 2018, Marrone, Poser et al. 2018). This may explain why ALS research, as yet, concentrates on studying patient-specific cellular models of spinal MNs and only few studies on cortical neurons exist (Burkhardt, Martinez et al. 2013, Japtok, Lojewski et al. 2015, Birger, Ottolenghi et al. 2018). In conclusion, control as well as mutant iPSCs successfully differentiate into cortical neurons and astrocytes, however showing a high variability between experiments and cells lines. This highlights the importance to evaluate disease-related phenotypes in the context of marker positivity such as MAP2 for neurons and GFAP for astrocytes.

4.2 Isogenic iPSC lines allow the analysis of mutation-dependent effects independent of patient's genetic background

In this study, non-isogenic patient-specific iPSC lines were used but also isogenic ones. All isogenic lines used, were generated using CRISPR/Cas9n technology for target gene editing.

As starting material for gene modification patient-derived iPSC lines with either *FUS* or *C9ORF72* mutation were used. As part of this thesis work, two *FUS EGFP*-tagged cell lines were generated. Using a parental line with *FUS-R521C* mutation, both a wild type and a new *FUS-P525L* iPSC line carrying an additional C-terminal EGFP tag were generated (Figure 3.3 A and Table 2.15). Two clones were selected for disease modeling purposes as they showed the intended genotypes (Figure 3.4) and pluripotency could be confirmed (Figure 3.5 and Figure 3.6). In addition to those *FUS* isogenic lines, *C9ORF72* isogenic lines were used, which were kindly provided by the lab of Jared Sternecker and generated by Dr. Masin Abo-Rady (Abo-Rady 2018). To derive the here used isogenic lines, a parental line with *C9ORF72-HRE* mutation was corrected to physiological repeat length (Table 2.15).

The use of isogenic lines is an important aspect of this thesis work because it allows the analysis of disease associated phenotypes resulting from the genotype and not the patient's genetic background. This is of great interest, as in ALS research it is already shown that pathological phenotypes depend on severity of underlying mutation (Huang, Zhou et al. 2011, Mitchell, McGoldrick et al. 2013, Japtok, Lojewski et al. 2015) and the gene affected (Pal, Glass et al. 2018). In this context, analyzed phenotypes can be very subtle or vary between non-isogenic lines. As an example, *FUS* mislocalization in *FUS-R521C* mutants was only detectable in aging cortical neurons while more severe *FUS-R495QfsX527* mutation led to mislocalization in all cells, independent of age and cell type (Japtok, Lojewski et al. 2015). Moreover, *C9ORF72-HRE* spinal MNs showed increased DNA damage compared to only one out of two non-isogenic controls (Higelin, Catanese et al. 2018). Therefore, one cannot rule out the possibility that such observations are putatively caused by the patient's genetic background, especially if only subtle observed phenotypes are detected. In conclusion, this highlights the importance of isogenic lines to rule out possible effects of unintended genetic background.

4.3 Disease-associated proteins

4.3.1 Cytoplasmic mislocalization of mutant *FUS* depends on cell type

Cytoplasmic mislocalization and aggregation of mutant *FUS* is a widely discussed disease mechanisms causing *FUS* pathology. In *FUS*-ALS, most disease-causing mutations cluster within the C-terminal part of the protein, which lead to a disrupted NLS and further resulting in nuclear to cytoplasmic shift of mutant *FUS* (Vance, Rogelj et al. 2009, Bosco, Lemay et al. 2010, Dormann, Rodde et al. 2010, Gal, Zhang et al. 2011, Kino, Washizu et al. 2011, Zhang and Chook 2012, Vance, Scotter et al. 2013, Wang, Pan et al. 2013). In the present work, it could be shown that *FUS-P525L* mutant cortical neurons show a nuclear to cytoplasmic shift

of FUS-EGFP localization compared to *FUS-WT* cells, which is consistent with a previous study on spinal MNs using the same isogenic lines (Naumann, Pal et al. 2018). This shift was not observed in mutant cortical astrocytes when compared to control (Figure 3.7). Those results indicate that FUS cellular localization is not only affected by mutation but also dependent on the cell type. Indeed, a study by Andersson and colleagues showed cell type-specific expression patterns of FUS by analyzing its cellular distribution in various organ tissues derived from healthy individuals (Andersson, Stahlberg et al. 2008). They found that 0 % of glial cells but 2 to 25 % of neurons showed FUS cytoplasmic expression. In addition, in my Master thesis work on cortical *in vitro* cultures I could show different effects of *FUS-R521C* mutation on cytoplasmic mislocalization. Accordingly, the percentage of neurons showing a mislocalization was higher (>40 %) than those of non-neuronal cells (<20 %) (Japtok, Lojewski et al. 2015). Moreover, the extent of FUS cytoplasmic mislocalization and aggregation was shown to depend on age and severity of mutation in spinal MNs (Higelin, Demestre et al. 2016) as well as cortical neurons (Japtok, Lojewski et al. 2015).

In conclusion, the present work and previous studies showed that FUS pathology in ALS is not simply caused by *FUS* mutation, but also depends on the severity of mutation, aging, and cell type. The precise underlying mechanism how FUS mislocalization and aggregation causes disease are still unclear. However, aforementioned factors seem to have a great influence on how underlying pathomechanism cause disease. Therefore, those factors need to be taken into account for future investigation.

4.3.2 C9ORF72-associated DPR pathology can only be recapitulated partially within iPSC-derived cortical neurons

DPRs are a hallmark characteristic of *C9ORF72*-associated ALS. DPRs can be detected throughout the CNS of *C9ORF72*-ALS patients, while predominantly localizing to cortical regions and cerebellum (Ash, Bieniek et al. 2013, Mackenzie, Arzberger et al. 2013, Schludi, May et al. 2015). DPR-conferred toxicity was shown in various overexpression models (Wen, Tan et al. 2014, Freibaum, Lu et al. 2015, Ohki, Wenninger-Weinzierl et al. 2017). The problem with these models is that they lead to accelerated protein levels, incomparable to ALS patient's pathology. Within this thesis work, immunocytochemistry assays were used to analyze whether endogenously expressed DPRs can be detected in iPSC-derived cortical neurons. Three monoclonal antibodies against Poly-GP, Poly-GA, and Poly-GR were evaluated in patient-specific *in vitro* cultures.

Poly-GA and Poly-GR antibodies were tested in immunofluorescence staining only. Staining for both antibodies reveal unexpected and possibly unspecific staining as also control lines show positive staining, which was unexpected. Quantitative analysis of Poly-GA revealed

highly inconsistent results between non-isogenic and isogenic lines and no clear effect of *C9ORF72-HRE* mutation was observed (Figure 3.12). Small cytoplasmic DPR granules as well as nuclear staining were detected in both control and *C9ORF72-HRE* mutant cortical neurons. In terms of Poly-GR antibody, a strong cytoplasmic accumulation in control and *C9ORF72-HRE* mutant neuronal in non-neuronal cells was observed (Figure 3.13). Both antibodies were previously shown to specifically detect DPR aggregation in *C9ORF72*-ALS cases but not in healthy individuals (Mackenzie, Arzberger et al. 2013, Mori, Arzberger et al. 2013, Schludi, May et al. 2015). However, the specificity of the two generated antibodies was tested in immunoblots and IHC staining on postmortem tissue. Protocols for preparation of protein samples and staining of human tissue are highly different from protocols used for *in vitro* staining, as used within this thesis. Such protocols can affect the antigen detected. If antibodies are then developed according to such protocols, staining patterns can look differently because staining protocols for *in vitro* culture might affect the antigen differently. Moreover, the tissue used was obtained from different patients as the patient-derived iPSC lines in the present study. Thus, it is still possible that the antibodies reveal partially unspecific staining in cellular models expressing DPRs endogenously. Therefore, both antibodies were considered to be unspecific within the here used model system. Further evaluations would be needed to confirm specificity also in cellular models such as testing additional patient-derived iPSC lines or different protocols for staining. In the present study only one to two control and *C9-HRE* lines were tested. Further on, antibodies could be tested in overexpression cellular models.

In contrast to Poly-GA and Poly-GR, Poly-GP antibody showed expected staining pattern (Figure 3.9). A diffuse staining with some nuclear enrichment and small cytoplasmic granules was observed, as previously published (Schludi, May et al. 2015, Yamakawa, Ito et al. 2015). Quantification of staining revealed that *C9ORF72-HRE* mutant cortical neurons did not show increased granule numbers, but size of granules was increased compared to controls (Figure 3.10). This is partially consistent with previous findings, showing increased area but not number of aggregates in DPR expressing cells (Zhou, Lehmer et al. 2017). However, Zhou and colleagues could observe increased aggregation only for Poly-GA and Poly-PR but not for Poly-GP and used, different to this work, rodent and human overexpression models. In addition to staining, ELISA was utilized to analyze Poly-GP levels at different maturation stages in cortical cells. ELISA evaluation revealed neither effect of aging nor genotype (Figure 3.8). The control lines and two *C9ORF72-HRE* lines (out of three) showed no increased Poly-GP levels. The detected levels (below 500 arbitrary units) can be considered to be not pathological as they are comparable to Poly-GP levels detected in control spinal MNs (Abo-Rady 2018). Only one out of three *C9ORF72-HRE* lines showed increased levels of Poly-GP in cortical cells (2000 to 4000 arbitrary units). This confirms previous studies using the same line and antibody

that showed higher Poly-GP levels in spinal MN cultures at approximately same detected Poly-GP levels (Abo-Rady 2018).

Within the here established *in vitro* model, using iPSC-derived cortical neurons, the hallmark pathology of C9ORF72-ALS can be recapitulated only partially. Only one out of three C9ORF72-HRE lines showed elevated Poly-GP levels. Further, immunofluorescence staining revealed increased Poly-GP aggregation, however yet only small dot-like granules could be observed. No big cytoplasmic star-shaped aggregates were detected, as they are reported to occur in C9ORF72 cases (Mackenzie, Arzberger et al. 2013, Mori, Arzberger et al. 2013, Freibaum, Lu et al. 2015, Schludi, May et al. 2015). DPRs are also shown to be primarily detected within cortical regions of C9ORF72-ALS tissue (Mackenzie, Arzberger et al. 2013, Schludi, May et al. 2015). Therefore, it was unexpected that here no such aggregation could be detected. A possible explanation could be an age-dependent effect as also discussed below in terms of DNA damage and axonal trafficking. This is plausible also in this case, especially as I already could show in my master thesis study on FUS-ALS, that severe cytoplasmic aggregation occurred only after 160 days *in vitro* differentiation within cortical neurons (Japtok 2014). However, no age-dependent effect between 80 and 120 days was observed. Yet, 40 more days of *in vitro* cultivation is a long time to obtain 160 day aged cortical cultures. Furthermore, an age-dependency was only tested by ELISA but not by staining, in which specifically neurons are detected. Thus, additional staining experiments on cortical neurons aged for more than 120 days are need to clarify if the used models is able to fully recapitulate disease pathology. Finally, similar to Poly-GA and Poly-GR, Poly-GP showed possibly unspecific staining and detection in ELISA. Same as discussed above, also control cortical cells showed positive staining and/ or antigen is maybe differently affected by different staining protocols used.

In conclusion, all three tested antibodies are possibly unspecific and results shown should be interpreted with care. Also not tested in this thesis is the influence of the C9RF72-HRE length on staining pattern and stability of repeat length. iPSC lines used in this study were genotyped once initially after reprogramming or gene modification but not after several passaging or differentiation. C9RF72-HRE length is thought to be unstable, meaning increase or decrease of size is possible. Reprogramming and differentiation was shown to affect repeat instability (Almeida, Gascon et al. 2013) and also repeat size can vary among neuronal and non-neuronal tissues of patients with C9ORF72-HRE (Nordin, Akimoto et al. 2015). Repeat length in cerebellum correlated with survival, disease onset, and progression (van Blitterswijk, DeJesus-Hernandez et al. 2013, Nordin, Akimoto et al. 2015), yet the exact relation between repeat length and phenotype is unclear (Rohrer, Isaacs et al. 2015). Thus future experiment might need to analyze repeat length on staining pattern and/ or also test exact repeat length on a regular basis.

4.3.3 DPR accumulation and DNA damage do not correlate in iPSC-derived cortical neurons

Accumulation of DPRs as well as DNA damage are both linked to C9ORF72-ALS individually but also in correlation with each other (Lopez-Gonzalez, Lu et al. 2016, Farg, Konopka et al. 2017, Higelin, Catanese et al. 2018). In this thesis work, both DPR formation and DNA damage were analyzed in C9ORF72-ALS patient-specific *in vitro* model. Neither severe DPR accumulation nor increased DNA damage could be observed in C9ORF72-HRE mutant cortical neurons, as already discussed above. Qualitative assessment of both factors neither revealed a correlation between both. This is in contrast to previous findings that show that accumulation of DNA damage is conferred by DPR production (Lopez-Gonzalez, Lu et al. 2016). Using C9ORF72-ALS patient-specific spinal MNs, Lopez-Gonzalez et al. could show that DPR production leads to mitochondrial dysfunction, which further results in increased oxidative stress and accumulation of DNA damage. However, they also showed that most severe DNA damage was only observed in 4-month-old cultures. This is even longer differentiation time than used in this thesis work. Thus, additional aging experiments would be needed to fully clarify if cortical neurons need more time to develop disease-associated phenotype or if underlying disease mechanism are different in spinal versus cortical neurons. Further, antibody specificity within the here used model is questionable.

4.3.4 ALS-associated TDP43 pathology can be recapitulated partially within iPSC-derived cortical neurons

Cytoplasmic aggregates containing non-mutated TDP43 are another hallmark in ALS (Neumann, Sampathu et al. 2006, Mackenzie, Bigio et al. 2007, Blokhuis, Groen et al. 2013). In terms of C9ORF72-ALS, neuronal and glial TDP43 positive inclusions can be observed in most cases (Mackenzie, Bigio et al. 2007, Rohrer, Isaacs et al. 2015). Within this thesis work, TDP43 was analyzed by immunofluorescence staining of control and C9ORF72-HRE mutant cortical neurons. Small cytoplasmic granules, which did not co-localize with Poly-GA, could be found in C9ORF72-HRE mutant cortical neurons (Figure 3.16). The missing co-localization is consistent with previous findings in human postmortem (Ash, Bieniek et al. , Mackenzie, Arzberger et al. 2013, Mori, Arzberger et al. , Schludi, May et al. 2015). However, also control cortical cells showed described pathology. TDP43 was shown to form beneficial and reversible aggregates under physiological condition in healthy muscle cells (Vogler, Wheeler et al. 2018). If cytoplasmic granules observed within healthy neurons possess beneficial effects needs to be proven. Moreover, TDP43 granules seemed to be slightly bigger in C9ORF72-HRE mutant neurons. However, granule numbers and size were not quantified due to technical reasons.

Thus, further evaluation is required to verify if *C9ORF72-HRE* mutant cortical neurons show increased TDP43 aggregation. In addition, the nuclear clearance of TDP43 accompanied by the formation of small cytoplasmic inclusions was observed (Figure 3.17). This is consistent with previous studies on TDP43 pathology in ALS (Neumann, Sampathu et al. 2006, Mackenzie, Bigio et al. 2007, Lee, Lee et al. 2011). In contrast to those findings is, that within this thesis work, TDP43 nuclear loss was mainly detected within MAP2 negative cells. Though glial inclusions formation and nuclear loss could already be shown in spinal cord postmortem tissue (Mackenzie, Bigio et al. 2007), it needs to be determined, yet, whether nuclear loss can be associated with astrocytes within iPSC-derived cortical cells. Furthermore, only two independent differentiations with high inter-experimental variability were analyzed. Accordingly, additional experiments will be needed to clarify if nuclear clearance of TDP43 is indeed increased in *C9ORF72-HRE* cortical cells within the here used model system.

In conclusion, known ALS-associated TDP43 pathology could be partially recapitulated within the here used model system. Additional experiments to increase sample size as well as additional quantifications need to be implemented to confirm that observed pathology indeed can be associated with *C9ORF72*-ALS.

4.4 Characterization of DNA damage

4.4.1 *C9ORF72-HRE* and *FUS-NLS* mutations do not affect DSB levels in unstressed cortical neurons and astrocytes

One aim of this study was the analysis of DSB markers γ H2AX and 53BP1 in cortical neurons and astrocytes to determine the effects of ALS-associated mutations on DNA damage. Evaluation of immunofluorescence staining revealed no increased accumulation of DNA damage in mutant cell lines compared to their corresponding controls. This could be shown for mature cortical neurons and astrocytes (day 100) with either *C9ORF72-HRE* (Figure 3.22) or *FUS-NLS* (Figure 3.27) mutation. In addition, young spinal MNs (day 21) did not showed an effect of *C9ORF72-HRE* mutation either (Figure 3.21). This is contradicting to published data for both ALS-associated genes. Both *FUS* and *C9ORF72* have clearly been linked to DNA damage and DDR (Wang, Pan et al. 2013, Hill, Mordes et al. 2016, Farg, Konopka et al. 2017). Accordingly, it is shown that cortical and spinal MNs with either *C9ORF72-HRE* (Lopez-Gonzalez, Lu et al. 2016, Farg, Konopka et al. 2017, Higelin, Catanese et al. 2018) or *FUS-NLS* (Wang, Pan et al. 2013, Qiu, Lee et al. 2014, Higelin, Demestre et al. 2016, Naumann, Pal et al. 2018) mutation show increased DSB levels. However, published data is either basing on h-iPSC-derived spinal MNs or primary mouse cortical neurons. None of them analyzed DNA damage in patient-specific iPSC-derived cortical cells. Following

paragraphs will give explanations for the differences between published and the here presented data.

In the context of *C9ORF72-HRE* mutation, an effect of the cell line, independent of genotype, on DSB levels in cortical cultures could be shown. This means that no obvious influence of the mutation was detected, however the two isogenic cell lines (C9-WT and C9-HRE 2) showed increased DNA damage levels compared to non-isogenic lines (Ctrl 1, Ctrl2, and C9-HRE 1). Overall the DSB levels between controls and mutants were rather similar. This fits together with data published by Higelin and colleagues (Higelin, Catanese et al. 2018). They could show significantly increased DSB levels within spinal MNs only between one analyzed *C9ORF72-HRE* patient-specific iPSC line compared to one out of two non-isogenic control lines. This indicates a potential participation of the patient's genetic background on DNA damage levels. In isogenic lines the patient's genetic background is the same and should not affect analyzed phenotypes. However, focusing only on isogenic iPSC lines used here, *C9ORF72-HRE* mutant cortical cultures did not show increased accumulation of DSBs compared to corresponding control either. This shows that in contrast to spinal MNs, DDR seems not to be different in healthy and *C9ORF72-HRE* cortical neurons as shown by particularly using isogenic lines.

There are, furthermore, some striking differences to published data. According to this, Farg and colleagues showed increased γ H2AX levels in human postmortem spinal cord tissue derived from *C9ORF72*-ALS patients (Farg, Konopka et al. 2017). Data obtained from postmortem tissue, however, is not comparable one to one to data basing on *in vitro* cultures. Histological preparation, paraffin embedding, and staining protocols are highly different to protocols used for immunofluorescence staining on cell cultures. Furthermore, postmortem tissue only recapitulates end stage of the disease. Thus, it might only represents an accelerated phenotype which would not be this obvious at an earlier stage of disease. Accordingly, Higelin as well as Lopez-Gonzalez et al. (Lopez-Gonzalez, Lu et al. 2016, Higelin, Catanese et al. 2018) showed an age-dependent increase of DNA damage in patient-derived spinal MNs with *C9ORF72-HRE* (Lopez-Gonzalez, Lu et al. 2016, Higelin, Catanese et al. 2018). As a conclusion from those studies it can be said that the maturation time points in the present study were possibly too early. Analysis of DSB marker at a later time point would need to be implemented to clarify this. This on the other side however means, that DNA damage seems not to be an early event in *C9ORF72-HRE* cortical neurodegeneration.

In the context of *FUS-NLS* mutations, DSB levels within cortical cultures were also not increased in mutant cell lines. Same as observed for *C9ORF72-HRE* lines, focusing on isogenic lines no difference of DNA damage levels between *FUS* mutant and control cells was observed. This is in striking contrast to a previous report of our group in which the same patient-specific iPSC lines (*FUS*-R521C and *FUS*-P525L) were used. The data clearly showed

increased γ H2AX levels in NPCs and spinal MNs, particularly we showed increased DSB levels already in young neurons (Naumann, Pal et al. 2018). Furthermore, two other studies exist which evaluated the same two *FUS-NLS* mutations as used here. Both studies showed an increase of γ H2AX positive cells in cortex tissue carrying either *FUS-NLS* mutation (Wang, Pan et al. 2013, Qiu, Lee et al. 2014). Of note, both studies either use patient or transgenic mouse postmortem tissue representing again end stage of disease. Corresponding to this, Higelin and colleagues could show an age-dependent increase of γ H2AX levels in *FUS-NLS* mutant patient-specific spinal MNs (Higelin, Demestre et al. 2016), similar as they already showed for *C9ORF72-HRE* (Higelin, Catanese et al. 2018). In conclusion, same as indicated for *C9ORF72-HRE*, the maturation time to analyze DNA damage in cortical neurons and astrocytes is possibly too early. However, in *FUS-NLS* spinal MNs DNA damage was shown to be an early event (Naumann, Pal et al. 2018). Both studies from Naumann (2018) and Higelin (2016) could show that increased DSB levels can already be detected in young spinal MNs or even NPCs. Interestingly, Higelin and colleagues used, similar to this thesis work, iPSCs as starting material for differentiation, while Naumann et al. used NPCs. That means different protocols for spinal MN derivation came to the same results. Thus, *FUS-NLS* mutation (as well as *C9ORF72-HRE*) seem to have different effects on DNA damage pathway in particular cortical neurons.

Besides analyzing the effects of ALS-associated mutations on DNA damage, another aim of this thesis work was to evaluate if the analyzed neural cell type matters. Remarkably, spinal MNs and cortical astrocytes showed higher DSB levels compared to cortical neurons, independent of genotype (Figure 3.23 A-D and Figure 3.27 D). Various studies exist that show a disease-associated increase of DNA damage in neurons as well as astrocytes. Increased DNA damage within neurons could already be related to AD (Mullaart, Boerrigter et al. 1990), PD (Zhang, Perry et al. 1999), and ALS (Qiu, Lee et al. 2014, Farg, Konopka et al. 2017) and in astrocytes related to AD (Myung, Zhu et al. 2008) and FTD (Su, Nichol et al. 2000). In the present work, no ALS-mutation-associated increase of DNA damage could be shown. DDR seems not to be different in healthy and *C9ORF72-HRE* or *FUS-NLS* cortical cells. However, to my knowledge there is no other literature existing which directly compares neuronal versus glial DNA damage. Thus, this study is the first showing increased basal level of DNA damage in a cell type but not genotype dependent manner. This strengthens the hypothesis, that cortical cells underlie different diseases mechanism as spinal ones and shows the need to further investigate disease-associated pathways in cell types affected by disease, particularly cortical versus spinal neurons and astrocytes in ALS.

4.4.2 *C9ORF72-HRE* and *FUS-NLS* mutations do not affect DDR signaling and DSB repair upon DNA damage induction

To further evaluate the effect of ALS-associated mutations on DNA damage accumulation, DSB levels were determined after DNA damage induction via etoposide. Etoposide indirectly induces DSBs via inhibition of topoisomerase II α (Walker and Nitiss 2002, Schonn, Hennesen et al. 2010). In this study, it served as a positive control for DNA damage. Indeed, a strong effect of etoposide treatment on cortical cultures, independent of genotype, could be detected. Thus, ALS-associated mutations within *FUS* or *C9ORF72* do not affect initiation of DDR signaling, as shown by increase of γ H2AX and 53BP1 foci numbers in cortical neurons and astrocytes (Figure 3.25 and Figure 3.28). In contrast, no effect of etoposide treatment within *C9ORF72-HRE* and control spinal MNs was observed (Figure 3.24). This was unexpected but might be explained with a dependency of DNA damage accumulation on basal DSB levels.

As discussed above, spinal MNs showed already increased DSB levels compared to cortical neurons under untreated conditions, however, contrary to cortical neurons, they do not react to the etoposide treatment. This leads to the assumption that cells possibly can acquire only a certain amount of DNA damage. This theory is strengthened by having a closer look on the reaction of isogenic *C9ORF72* cortical cultures towards DSB induction. Both C9-WT and C9-HRE 2 showed a less strong increase of DSBs upon etoposide treatment compared to non-isogenic lines (Figure 3.25). However, both lines also showed already increased DNA damage levels in untreated conditions, compared to non-isogenic lines (Figure 3.22). Similar observation could also be made in a previous study of our group. Under untreated conditions, *FUS-NLS* mutant spinal MNs showed increased DSBs numbers compared to control (Naumann, Pal et al. 2018). However, upon etoposide treatment *FUS-NLS* mutants showed a less strong accumulation of DSBs than the control. Taken together, this indicates that cells, independent of the genotype, accumulate DSB after etoposide depending on initial basal levels of DNA damage. If and how this correlates with cell death and neurodegeneration needs further exploration.

To evaluate the possible influence of *FUS* or *C9ORF72* mutations in DNA damage repair, the recovery of DNA damage was analyzed upon etoposide withdrawal. Cells were allowed to recover for 24 h without any additional DSB induction. Clearly, all analyzed cell lines and cell types were able to recover from DNA damage induction. Similar DSB levels as in untreated conditions were detected in spinal MNs (Figure 3.24) as well as in cortical neurons and astrocytes (Figure 3.25 and Figure 3.28). This is consistent with previous mentioned study of our group, which likewise showed that control as well as *FUS-NLS* mutant spinal MNs successfully repair etoposide induced DNA damage (Naumann, Pal et al. 2018).

To verify that the DSB recovery is not masked by increased cell death, the effect of etoposide on cell viability was analyzed 24h after treatment withdrawal. No effect of etoposide treatment could be detected (Figure 3.29). As a conclusion, this shows that analyzed cell cultures carrying ALS-associated mutations are able to repair induced DNA damage and observations made are not due to a loss of dead cells from the analysis.

4.4.3 Recruitment of FUS-EGFP to laser-induced DNA damage sites depends on cell- and genotype

The effect of ALS-associated mutation within *FUS* was further evaluated by analyzing the recruitment of FUS protein to laser-induced DNA damage sites. For that, two isogenic iPSC lines that endogenously express WT or P525L EGFP-tagged FUS were used and which were successfully generated as part of this thesis (see section 3.2). Previous studies, using cell models that heterologous express FUS protein showed that WT FUS is rapidly recruited to laser-induced DDS. (Mastrocola, Kim et al. 2013, Wang, Pan et al. 2013, Rulten, Rotheray et al. 2014, Aleksandrov, Dotchev et al. 2018). Our group could recapitulate this by showing rapid recruitment of WT FUS to DDS in spinal MNs while using the same isogenic FUS-EGFP iPSC lines that were generated as part of this thesis work (Figure 3.30)(Naumann, Pal et al. 2018). In the present study, FUS-EGFP recruitment was analyzed in iPSCs and cortical neurons. Consistent with previous reports, WT FUS-EGFP was recruited quickly to DDS in both iPSCs and cortical neurons. Interestingly, recruitment of P525L FUS-EGFP was unaffected in iPSCs but seemed to be slightly delayed in cortical neurons (Figure 3.31). This is in striking contrast to our aforementioned study, in which recruitment of FUS-P525L within spinal MNs was completely diminished (Naumann, Pal et al. 2018). Further detailed quantification of the fitted curves needs to be implemented to confirm the observed minor shift of the graphs in Figure 3.31.

The detection of described differences of mutant FUS recruitment to DDS between spinal and cortical neurons is a noticeable discovery of this thesis work that is strengthened due to the use of the same cell lines and techniques as published previously. That FUS-P525L showed hints for a marginal impaired recruitment might be explained by a possible age-dependent effect. As discussed above, aging affects DNA damage accumulation in neurons (Lopez-Gonzalez, Lu et al. 2016, Higelin, Catanese et al. 2018). This might also be the case for FUS recruitment to DDS within cortical neurons. Furthermore, cortical cultures consist of various neuron types (Figure 3.2). However, in ALS particularly MNs are affected by neurodegeneration. In cortical cultures MNs are rare and cannot be specifically detected within live cell imaging approaches. Thus, a FUS recruitment defect that is possibly specific to MNs, is perhaps masked by the functional recruitment of FUS within other neuronal subtypes.

Nevertheless, every single neuron analyzed in spinal cultures as well as their all neuroprogenitor cells did not respond to laser cutter (Naumann, Pal et al. 2018). Thus, undiscovered differential mechanisms in cortical vs. spinal neurons could affect FUS recruitment to DDS.

With respect to clinical features of FUS-ALS, it represents classical ALS neuropathology with showing a severe loss of MNs in the spinal cord and similar loss of neurons in the brainstem, however only mild to moderate loss of neurons in the motor cortex (Deng, Gao et al. 2014). In contrast thereto, ALS patients with *C9ORF72-HRE* more commonly show behavioral and/ or cognitive impairment compared to patients without repeat expansion and neurodegeneration can not only be observed in spinal cord but also cortical areas (Rohrer, Isaacs et al. 2015). Thus, one can say that in FUS-ALS predominantly lower MNs are affected by disease, while in *C9ORF72*-ALS upper MNs are affected or both upper and lower MNs. This, in conclusion, fits to the here presented data. Spinal MNs carrying mutations within *FUS* are more affected by disease and thus show severe effects on DDR, while cortical neurons are possibly less affected by disease and thus show a normal FUS recruitment to DDS. Consistent with that dependency on the neuronal cell type, Birger et al. showed that survival of cortical and spinal neurons is differently affected by expression of disease-relevant proteins (Birger, Ottolenghi et al. 2018). In summary, the present work shows that FUS recruitment to DDS is modulated by mutation but is also highly dependent on the analyzed cell type. This highlights the importance of the analyzed cell types, including subtypes of neurons, which are used for disease modeling.

4.5 *FUS*-NLS mutations affect axonal organelle trafficking differently as in spinal MNs

To further analyze ALS-associated disease mechanisms, axonal organelle transport in compartmentalized *FUS*-NLS mutant cortical neuron cultures was analyzed. Especially neurons depend on functional organelle transport for proper energy supply (mitochondrial transport) and waste removal (lysosomal transport) due to their highly asymmetric structure and long axons (Millecamps and Julien 2013, Taylor, Brown et al. 2016). Aim of this thesis was to evaluate trafficking in distal and proximal parts of neuron axon, implementing the same experimental set up as already published for spinal MNs (Naumann, Pal et al. 2018).

An effect of *FUS* mutation on axonal trafficking of mitochondria and lysosome could be observed within directed cortical neuron cultures. However, mutations within *FUS* affect cortical axonal trafficking differently as observed in spinal MNs (Guo, Naujock et al. 2017, Naumann, Pal et al. 2018). Accordingly, an increased organelle displacement of both

mitochondria and lysosomes was detected in distal and proximal axonal parts of *FUS-NLS* mutant cortical neurons (Figure 3.34 B + F). This is contrary to previous findings in spinal MNs, which showed significant decreased organelle displacement in only distal axons of *FUS-NLS* mutant spinal MNs (Naumann, Pal et al. 2018). Another parameter analyzed was the organelle mean speed. For this, within *FUS-NLS* mutant cortical neurons a significantly decreased lysosomal and mitochondrial mean speed within distal and proximal axons was observed (Figure 3.34 D + G). Thus, evaluation of mean speed is partially consistent to findings in spinal MNs, which showed decreased organelle mean speed only distal axonal parts. Of note, in spinal MNs a severe distal trafficking defect was observed, while cortical neurons show global trafficking effects that are, additionally, far less distinctive than observed in spinal MNs (Naumann, Pal et al. 2018). In summary it can be said, that *FUS-NLS* mutations affect cortical organelle trafficking much different and much less pronounced than observed in spinal MNs, fitting to above mentioned results on DNA damage and DDR response.

Evaluation of organelle trafficking in cortical neurons is rather inconclusive when compared to previous studies on spinal MNs. A possible explanation could be an underlying age-dependent effect as already discussed on DNA damage. Accordingly, impairment of axonal trafficking was shown to occur in an age-dependent manner in *FUS* (Guo, Naujock et al. 2017, Naumann, Pal et al. 2018) and *TARDBP* (Kreiter, Pal et al. 2018) mutant neurons. The timescale between spinal MN protocols and cortical differentiation protocols are different, ranging from 2 to 4 weeks for spinal and 2 to 4 months for derivation of cortical neurons. Interestingly, differently implemented protocols for spinal MN derivation come to the same observation of severe axonal trafficking defects in *FUS-NLS* mutant lines. While our group relies on NPCs for MN differentiation (Naumann, Pal et al. 2018), Guo et al. (2017) use, similar to this thesis work, iPSCs for directed differentiation into MNs. Yet, both studies could show that in spinal MNs no obvious trafficking defects can be observed in very young neurons (one week of differentiation) but that observable impairment occurs approximately after 2 to 3 weeks of differentiation. Thus, cortical neurons possibly need more time to develop more pronounced phenotypes because the range they need for differentiation, maturation, and aging is way longer.

Another issue is that movies from different maturation time points (day 70 to 130) were pooled for analysis of cortical organelle trafficking. This is because of the high inter-experimental variability of cortical MFC cultures as shown in Figure 3.33. Independent of the genotype but dependent on the individual experiment, cortical neurons need different times to fully grow through micro channels of MFCs. This means the same cell line might showed different growth behaviors in MFCs in independent differentiation pipelines. To ensure similar qualities of cortical MFC cultures, cells were imaged once the majority of channels were penetrated and before neurons showed obvious signs of neurodegeneration. Therefore, there

was no standardized imaging time point. This is different to spinal cultures in which cells were strictly imaged at one particular time point (Kreiter, Pal et al. 2018, Naumann, Pal et al. 2018, Pal, Glass et al. 2018). Thus, the high inter-experimental variability of cortical MFC cultures and the varying imaging time points might affect organelle trafficking results. To overcome this further experiments need to be implemented to increase the amount of independent experiments and narrow down the time range in which movies were taken (e.g. day 70 to 80). Nevertheless, phenotypes in sMNs did appear rather early, after 3 weeks of differentiation and also prior any obvious signs for neurodegeneration.

As aforementioned, in FUS-ALS specifically spinal MNs are affected by neurodegeneration, while cortical neurons are less affected (Deng, Gao et al. 2014). In our previous work on spinal MNs we also could show that axonal trafficking defects occur shortly prior to onset of neurodegeneration-related phenotypes such as axonal swellings and fragmentation of axons (Naumann, Pal et al. 2018). In this thesis work no obvious effects of neurodegeneration could be observed such as increased cell death or fragmentation of axons, even though this still needs to be proven by proper quantification and evaluation at different time points. Nevertheless, the present study is the first showing differential axonal trafficking defects in cortical neurons compared to spinal ones. Similar to DNA damage analysis, trafficking result show that the analyzed neuron type matters and indicates different underlying disease mechanism in cortical vs. spinal neurons.

4.6 Conclusion

ALS is devastating neurodegenerative disease specifically affecting upper and lower MNs (Van Langenhove, van der Zee et al. 2012, Vance, Scotter et al. 2013). The overall aim of this thesis work was the modeling of cortical neuropathology of *FUS*- and *C9ORF72*-associated ALS. Differential phenotypes between cortical neurons vs. astrocytes and cortical vs. spinal neurons were analyzed. For that, human iPSCs derived from healthy controls and ALS patients carrying mutations within *FUS* or *C9ORF72* were used for directed cortical differentiation. Immunofluorescence staining and live cell imaging approaches were implemented to analyze disease-associated proteins, DNA damage, and axonal trafficking. Until now, only few studies exist analyzing disease-associated pathology in human cortical *in vitro* models of ALS (Burkhardt, Martinez et al. 2013, Japtok, Lojewski et al. 2015, Birger, Ottolenghi et al. 2018). Most studies either concentrate on spinal MNs (Lenzi, De Santis et al. 2015, Higelin, Demestre et al. 2016, Lopez-Gonzalez, Lu et al. 2016, Higelin, Catanese et al. 2018, Marrone, Drexler et al. 2019) or rodent cortical cultures (Alami, Smith et al. 2014, Qiu, Lee et al. 2014, Farg, Konopka et al. 2017, Walker, Herranz-Martin et al. 2017). However, yet no proof exists that underlying mechanisms causing disease are the same in spinal vs. cortical MNs. For that

reason, experiments implemented within this thesis work should help to augment knowledge on particular cortical neurodegeneration in ALS and highlighting differences and importance of analyzed cell types.

Within this project, a clear cell type dependent effect on analyzed phenotypes was observed, while ALS-associated mutations seemed to have only minor effects. Accordingly, cell type dependent increased basal DNA damage levels in cortical astrocytes vs. neurons and spinal vs. cortical neurons were detected. However, *FUS* or *C9ORF72* mutant cortical cells do not recapitulate increased DNA damage levels observed in spinal MNs (Higelin, Demestre et al. 2016, Higelin, Catanese et al. 2018, Naumann, Pal et al. 2018). Furthermore, *FUS* mutation affected recruitment to DDS, axonal trafficking, and cytoplasmic mislocalization differently, depending on the analyzed cell type. Additionally, recruitment and trafficking of mutant *FUS*, showed only slight mutation dependent effects and also less pronounced phenotypes as observed in spinal MNs (Naumann, Pal et al. 2018). Those results show that in particular the analyzed cell type matters and that ALS-associated phenotypes differ between cortical and spinal neurons. Because known ALS-associated pathology could be recapitulated only partially and with less pronounced phenotypes as previously reported, further experiments need to be implemented to confirm findings of this thesis and evaluate other variables affecting phenotype. Accordingly, a putative age-dependency needs to be proven. Age-dependent effects are shown for various mechanisms including DNA damage (Higelin, Demestre et al. 2016, Lopez-Gonzalez, Lu et al. 2016, Higelin, Catanese et al. 2018), organelle trafficking (Guo, Naujock et al. 2017, Kreiter, Pal et al. 2018, Naumann, Pal et al. 2018), and protein aggregation (Japtok, Lojewski et al. 2015, Higelin, Demestre et al. 2016). Furthermore, comparison with spinal MNs showed differential results. This indicates that disease progression might be caused by differential mechanisms. This needs to be taken into account for future investigation and particular development of treatment.

A limiting factor of above mentioned results is that observations made in cortical neurons are possibly masked by various neuronal cell types. In ALS, specifically MNs are affected. However, within the here used cortical cultures it was difficult to differentiate cortical MNs from other neuron types. Furthermore, long differentiation times are required for the derivation of cortical neurons and astrocytes. This requires accurately planning of experiments on a long-term scale, in which also the high inter-experimental variability needs to be taken into account. The use of pluripotent stem cells as starting material for differentiation and the variable differentiation potential of each individual cell lines makes cortical differentiation more complex. Nevertheless, it could be shown that directed differentiation of patient-specific iPSCs into cortical neurons and astrocytes is a suitable model to study ALS in those types of cells. Moreover, studies from Guo et al. (2017) and Higelin et al. (2016 and 2018) also use iPSCs for directed differentiation into spinal MNs. Yet, they made contradictory observation regarding

DNA damage and organelle trafficking in spinal MNs compared to data presented within this thesis work. This highlights the importance of the analyzed cell type and strengthens the hypothesis that differential mechanisms in lower and upper MNs cause disease. In conclusion, patient-specific cellular models are an important tool in ALS research and particular differences between cortical and spinal MNs further need to be investigated to decipher underlying disease mechanism, the interplay of cell types affected by the disease, and how they participate in disease progression.

5 Summary

Amyotrophic lateral sclerosis (ALS) is a of neurodegenerative diseases, in which neurodegeneration specifically affects upper (corticospinal) and lower (spinal) motor neurons (MNs). At present, ALS remains an incurable disease. Death occurs on average 2 to 5 years after symptom onset. About 90% are sporadic cases (sALS) and 10% are familial cases (fALS). It is of great interest to investigate monogenetic forms causing fALS to understand its underlying disease pathologies and mechanisms. Over 20 genes have been linked to ALS until now, including Fused in sarcoma (*FUS*) and Chromosome 9 open reading frame 72 (*C9ORF72*). About 4% of fALS cases are caused by dominant mutations within *FUS*, representing the third most common fALS form in Germany. The G4C2 hexanucleotide repeat expansion (HRE) in the *C9ORF72* gene is the most common cause for ALS and Frontotemporal dementia (FTD). ALS patients differ significantly in their presentation of clinical symptoms, including site of onset, rate of progression, and presence of cognitive dysfunction. Those factors were also shown to highly depend on the underlying mutation in fALS cases. Aim of this thesis work is the modeling of *FUS*- and *C9ORF72*-associated ALS in a disease-related *in vitro* model of particularly cortical neuropathology using patient-derived iPSCs. The hypothesis of the current work is that underlying disease mechanisms do differentially affect cortical vs. spinal neurons and act in a cell type-dependent manner. Human iPSCs derived from healthy controls and ALS patients carrying mutations within *FUS* or *C9ORF72* were used for directed cortical and spinal differentiation. Additionally, two new *FUS*-WT- and *FUS*-P525L-EGFP-tagged isogenic iPSC lines were generated by CRISPR/Cas9n gene editing. Immunofluorescence staining and live cell imaging approaches were implemented to analyze disease-associated proteins, DNA damage, and axonal trafficking. Within this project, a clear cell type-dependent effect on analyzed phenotypes was observed, while ALS-associated mutations seemed to have only minor effects. Accordingly, cell type-dependent increased basal DNA damage levels in cortical astrocytes vs. neurons and spinal vs. cortical neurons were detected. However, *FUS* or *C9ORF72* mutant cortical cells do not recapitulate increased DNA damage levels as they have been observed in spinal MNs. Furthermore, *FUS* mutation affected recruitment to DNA damage sites, axonal trafficking, and cytoplasmic mislocalization differentially, depending on the analyzed cell type. In cortical neurons, recruitment and trafficking of mutant *FUS* showed only slight mutation-dependent effects and also less pronounced phenotypes than observed in spinal MNs. In conclusion, patient-specific cellular models are an important tool in ALS research and particularly differences between cortical and spinal MNs need to be further investigated to decipher underlying disease mechanisms, the interplay of cell types affected by the disease, and how they participate in disease progression.

6 Zusammenfassung

Amyotrophe Lateralsklerose (ALS) ist eine neurodegenerative Erkrankung, bei welcher speziell erste (kortikospinal) und zweite (spinal) Motorneurone (MN) von Neurodegeneration betroffen sind. Gegenwärtig bleibt ALS eine unheilbare Erkrankung. Der Tod tritt durchschnittlich 2 bis 5 Jahre nach Auftreten der Symptome ein. Circa 90% der Fälle treten sporadisch auf (sALS), während 10% familiär sind (fALS). Es ist von großem Interesse monogenetische Formen der fALS zu untersuchen um zugrundeliegende Pathologien und Mechanismen zu verstehen. Bislang wurden über 20 Gene mit ALS in Verbindung gebracht, einschließlich Fused in sarcoma (*FUS*) und Chromosome 9 open reading frame (*C9ORF72*). Circa 4% der fALS Fälle sind durch dominante Mutationen in *FUS* verursacht und repräsentieren damit die dritthäufigste Form der fALS in Deutschland. Die G4C2 hexanucleotide repeat expansion (HRE) in *C9ORF72* ist die häufigste Ursache für ALS und Frontotemporale Demenz (FTD). ALS Patienten unterscheiden sich erheblich in der Präsentation ihrer klinischen Symptome wie Ausbruchsort, Progressionsrate und Auftreten kognitiver Störungen. Diese Faktoren sind auch stark abhängig von der zugrundeliegenden Mutation in fALS. Ziel dieser Doktorarbeit ist die Modellierung von *FUS*- und *C9ORF72*-assoziierter ALS in einem krankheits-relevanten *in vitro* Model von speziell kortikaler Neuropathologie mit Hilfe von Patienten-spezifischen iPSCs. Die Hypothese der vorliegenden Arbeit ist das in einer Zelltyp-abhängigen Art und Weise zugrundeliegende Erkrankungsmechanismen in kortikalen vs. spinalen Neuronen unterschiedlich betroffen sind. Humane iPSC, generiert von gesunden Kontrollen und ALS Patienten mit *FUS* oder *C9ORF72* Mutation, wurden für die gerichtete kortikale und spinale Differenzierung genutzt. Zusätzlich wurden zwei neue *FUS*-WT- und *FUS*-P525L-EGFP-markierte isogene Linien mittels CRISPR/Cas9n Technik generiert. Methoden basierend auf Immunfluoreszenz Färbungen und Lebendzell-Mikroskopie wurden angewendet um Krankheits-relevante Proteine, DNA Schäden und axonale Organell-Mobilität zu analysieren. In diesem Projekt konnte ein deutlicher Zelltyp-abhängiger Effekt auf analysierte Phänotypen beobachtet werden, während ALS-assozierte Mutationen scheinbar nur geringfügige Effekte zeigten. Dementsprechend wurde ein Zelltyp-abhängiger Anstieg des basalen DNA Schadens in kortikalen Astrozyten vs. Neuronen und spinalen vs. kortikalen Neuronen detektiert. Jedoch konnte in *FUS* oder *C9ORF72* mutierten kortikalen Zellen kein erhöhter DNA Schaden nachgewiesen werden, wie es zuvor in spinalen MN beobachtet wurde. Des Weiteren beeinflussen *FUS* Mutationen die Rekrutierung von *FUS* zu DNA-geschädigten Stellen, die Organell-Mobilität und die zytoplasmatische Fehllokalisierung des Proteins in Abhängigkeit vom Zelltyp. In kortikalen Neuronen wurde in Bezug auf die Rekrutierung von mutiertem *FUS* und Organell-Mobilität nur leichte Mutations-abhängige und wesentlich schwächer ausgeprägte Effekte beobachtet als in

spinalen MN. Zusammenfassend kann gesagt werden, dass Patienten-spezifische Zellmodelle ein wichtiges Instrument in der ALS Forschung sind und dass vor allem Unterschiede zwischen kortikalen und spinalen MN weiter untersucht werden müssen, um zugrundeliegende Krankheits-relevante Mechanismen zu entschlüsseln und wie diese zum Fortschreiten der Erkrankung beitragen.

7 References

- Abe, K., Y. Itoyama, G. Sobue, S. Tsuji, M. Aoki, M. Doyu, C. Hamada, K. Kondo, T. Yoneoka, M. Akimoto, H. Yoshino and A. L. S. S. G. Eदारavone (2014). "Confirmatory double-blind, parallel-group, placebo-controlled study of efficacy and safety of edaravone (MCI-186) in amyotrophic lateral sclerosis patients." *Amyotroph Lateral Scler Frontotemporal Degener* **15**(7-8): 610-617.
- Abeliovich, A. and A. D. Gitler (2016). "Defects in trafficking bridge Parkinson's disease pathology and genetics." *Nature* **539**(7628): 207-216.
- Abo-Rady, M. (2018). Modeling C9ORF72-induced Amyotrophic Lateral Sclerosis using patient specific induced pluripotent stem cells. Ph.D Dissertation, Technische Universität Dresden.
- Al-Chalabi, A., A. Jones, C. Troakes, A. King, S. Al-Sarraj and L. H. van den Berg (2012). "The genetics and neuropathology of amyotrophic lateral sclerosis." *Acta Neuropathol* **124**(3): 339-352.
- Al-Chalabi, A., L. H. van den Berg and J. Veldink (2017). "Gene discovery in amyotrophic lateral sclerosis: implications for clinical management." *Nat Rev Neurol* **13**(2): 96-104.
- Alami, N. H., R. B. Smith, M. A. Carrasco, L. A. Williams, C. S. Winborn, S. S. W. Han, E. Kiskinis, B. Winborn, B. D. Freibaum, A. Kanagaraj, A. J. Clare, N. M. Badders, B. Bilican, E. Chaum, S. Chandran, C. E. Shaw, K. C. Eggan, T. Maniatis and J. P. Taylor (2014). "Axonal transport of TDP-43 mRNA granules is impaired by ALS-causing mutations." *Neuron* **81**(3): 536-543.
- Aleksandrov, R., A. Dotchev, I. Poser, D. Krastev, G. Georgiev, G. Panova, Y. Babukov, G. Danovski, T. Dyankova, L. Hubatsch, A. Ivanova, A. Ategin, M. N. Nedelcheva-Veleva, S. Hasse, M. Sarov, F. Buchholz, A. A. Hyman, S. W. Grill and S. S. Stoyanov (2018). "Protein Dynamics in Complex DNA Lesions." *Mol Cell* **69**(6): 1046-1061 e1045.
- Almeida, S., E. Gascon, H. Tran, H. J. Chou, T. F. Gendron, S. Degroot, A. R. Tapper, C. Sellier, N. Charlet-Berguerand, A. Karydas, W. W. Seeley, A. L. Boxer, L. Petrucelli, B. L. Miller and F. B. Gao (2013). "Modeling key pathological features of frontotemporal dementia with C9ORF72 repeat expansion in iPSC-derived human neurons." *Acta Neuropathol* **126**(3): 385-399.
- Andersson, M. K., A. Stahlberg, Y. Arvidsson, A. Olofsson, H. Semb, G. Stenman, O. Nilsson and P. Aman (2008). "The multifunctional FUS, EWS and TAF15 proto-oncoproteins show cell type-specific expression patterns and involvement in cell spreading and stress response." *BMC Cell Biol* **9**: 37.
- Aoki, Y., R. Manzano, Y. Lee, R. Dafinca, M. Aoki, A. G. L. Douglas, M. A. Varela, C. Sathyaprakash, J. Scaber, P. Barbagallo, P. Vader, I. Mager, K. Ezzat, M. R. Turner, N. Ito, S. Gasco, N. Ohbayashi, S. El Andaloussi, S. Takeda, M. Fukuda, K. Talbot and M. J. A. Wood (2017). "C9orf72 and RAB7L1 regulate vesicle trafficking in amyotrophic lateral sclerosis and frontotemporal dementia." *Brain* **140**(4): 887-897.
- Arai, T., M. Hasegawa, H. Akiyama, K. Ikeda, T. Nonaka, H. Mori, D. Mann, K. Tsuchiya, M. Yoshida, Y. Hashizume and T. Oda (2006). "TDP-43 is a component of ubiquitin-positive tau-negative inclusions in frontotemporal lobar degeneration and amyotrophic lateral sclerosis." *Biochem Biophys Res Commun* **351**(3): 602-611.
- Ash, P. E., K. F. Bieniek, T. F. Gendron, T. Caulfield, W. L. Lin, M. DeJesus-Hernandez, M. M. van Blitterswijk, K. Jansen-West, J. W. Paul, 3rd, R. Rademakers, K. B. Boylan, D. W. Dickson and L. Petrucelli (2013). "Unconventional translation of C9ORF72 GGGGCC expansion generates insoluble polypeptides specific to c9FTD/ALS." *Neuron* **77**(4): 639-646.
- Beck, J., M. Poulter, D. Hensman, J. D. Rohrer, C. J. Mahoney, G. Adamson, T. Campbell, J. Uphill, A. Borg, P. Fratta, R. W. Orrell, A. Malaspina, J. Rowe, J. Brown, J. Hodges, K. Sidle, J. M. Polke, H. Houlden, J. M. Schott, N. C. Fox, M. N. Rossor, S. J. Tabrizi, A. M. Isaacs, J. Hardy, J. D. Warren, J.

- Collinge and S. Mead (2013). "Large C9orf72 hexanucleotide repeat expansions are seen in multiple neurodegenerative syndromes and are more frequent than expected in the UK population." Am J Hum Genet **92**(3): 345-353.
- Bensimon, G., L. Lacomblez and V. Meininger (1994). "A controlled trial of riluzole in amyotrophic lateral sclerosis. ALS/Riluzole Study Group." N Engl J Med **330**(9): 585-591.
- Bentmann, E., M. Neumann, S. Tahirovic, R. Rodde, D. Dormann and C. Haass (2012). "Requirements for stress granule recruitment of fused in sarcoma (FUS) and TAR DNA-binding protein of 43 kDa (TDP-43)." J Biol Chem **287**(27): 23079-23094.
- Bento-Abreu, A., P. Van Damme, L. Van Den Bosch and W. Robberecht (2010). "The neurobiology of amyotrophic lateral sclerosis." Eur J Neurosci **31**(12): 2247-2265.
- Birger, A., M. Ottolenghi, L. Perez, B. Reubinoff and O. Behar (2018). "ALS-related human cortical and motor neurons survival is differentially affected by Sema3A." Cell Death Dis **9**(3): 256.
- Blair, I. P., K. L. Williams, S. T. Warraich, J. C. Durnall, A. D. Thoeng, J. Manavis, P. C. Blumbergs, S. Vucic, M. C. Kiernan and G. A. Nicholson (2010). "FUS mutations in amyotrophic lateral sclerosis: clinical, pathological, neurophysiological and genetic analysis." J Neurol Neurosurg Psychiatry **81**(6): 639-645.
- Blokhuis, A. M., E. J. Groen, M. Koppers, L. H. van den Berg and R. J. Pasterkamp (2013). "Protein aggregation in amyotrophic lateral sclerosis." Acta Neuropathol **125**(6): 777-794.
- Bohgaki, T., M. Bohgaki and R. Hakem (2010). "DNA double-strand break signaling and human disorders." Genome Integr **1**(1): 15.
- Boillee, S., C. Vande Velde and D. W. Cleveland (2006). "ALS: a disease of motor neurons and their nonneuronal neighbors." Neuron **52**(1): 39-59.
- Boillee, S., K. Yamanaka, C. S. Lobsiger, N. G. Copeland, N. A. Jenkins, G. Kassiotis, G. Kollias and D. W. Cleveland (2006). "Onset and progression in inherited ALS determined by motor neurons and microglia." Science **312**(5778): 1389-1392.
- Bosco, D. A., N. Lemay, H. K. Ko, H. Zhou, C. Burke, T. J. Kwiatkowski, Jr., P. Sapp, D. McKenna-Yasek, R. H. Brown, Jr. and L. J. Hayward (2010). "Mutant FUS proteins that cause amyotrophic lateral sclerosis incorporate into stress granules." Hum Mol Genet **19**(21): 4160-4175.
- Buchman, V. L., J. Cooper-Knock, N. Connor-Robson, A. Higginbottom, J. Kirby, O. D. Razinskaya, N. Ninkina and P. J. Shaw (2013). "Simultaneous and independent detection of C9ORF72 alleles with low and high number of GGGGCC repeats using an optimised protocol of Southern blot hybridisation." Mol Neurodegener **8**: 12.
- Burkhardt, M. F., F. J. Martinez, S. Wright, C. Ramos, D. Volfson, M. Mason, J. Garnes, V. Dang, J. Lievers, U. Shoukat-Mumtaz, R. Martinez, H. Gai, R. Blake, E. Vaisberg, M. Grskovic, C. Johnson, S. Irion, J. Bright, B. Cooper, L. Nguyen, I. Griswold-Prenner and A. Javaherian (2013). "A cellular model for sporadic ALS using patient-derived induced pluripotent stem cells." Mol Cell Neurosci **56**: 355-364.
- Byrne, S., M. Heverin, M. Elamin, C. Walsh and O. Hardiman (2014). "Intermediate repeat expansion length in C9orf72 may be pathological in amyotrophic lateral sclerosis." Amyotroph Lateral Scler Frontotemporal Degener **15**(1-2): 148-150.
- Campbell, M. J. and J. H. Morrison (1989). "Monoclonal antibody to neurofilament protein (SMI-32) labels a subpopulation of pyramidal neurons in the human and monkey neocortex." J Comp Neurol **282**(2): 191-205.
- Canter, R. G., J. Penney and L. H. Tsai (2016). "The road to restoring neural circuits for the treatment of Alzheimer's disease." Nature **539**(7628): 187-196.

- Carpenter, A. E., T. R. Jones, M. R. Lamprecht, C. Clarke, I. H. Kang, O. Friman, D. A. Guertin, J. H. Chang, R. A. Lindquist, J. Moffat, P. Golland and D. M. Sabatini (2006). "CellProfiler: image analysis software for identifying and quantifying cell phenotypes." Genome Biol **7**(10): R100.
- Cong, L., F. A. Ran, D. Cox, S. Lin, R. Barretto, N. Habib, P. D. Hsu, X. Wu, W. Jiang, L. A. Marraffini and F. Zhang (2013). "Multiplex genome engineering using CRISPR/Cas systems." Science **339**(6121): 819-823.
- Conte, A., S. Lattante, M. Zollino, G. Marangi, M. Luigetti, A. Del Grande, S. Servidei, F. Trombetta and M. Sabatelli (2012). "P525L FUS mutation is consistently associated with a severe form of juvenile amyotrophic lateral sclerosis." Neuromuscul Disord **22**(1): 73-75.
- Coppede, F. (2011). "An overview of DNA repair in amyotrophic lateral sclerosis." ScientificWorldJournal **11**: 1679-1691.
- Coppede, F. and L. Migliore (2015). "DNA damage in neurodegenerative diseases." Mutat Res **776**: 84-97.
- Crozat, A., P. Aman, N. Mandahl and D. Ron (1993). "Fusion of CHOP to a novel RNA-binding protein in human myxoid liposarcoma." Nature **363**(6430): 640-644.
- Debray, S., V. Race, V. Crabbe, S. Herdewyn, G. Matthijs, A. Goris, B. Dubois, V. Thijs, W. Robberecht and P. Van Damme (2013). "Frequency of C9orf72 repeat expansions in amyotrophic lateral sclerosis: a Belgian cohort study." Neurobiol Aging **34**(12): 2890 e2897-2890 e2812.
- DeJesus-Hernandez, M., I. R. Mackenzie, B. F. Boeve, A. L. Boxer, M. Baker, N. J. Rutherford, A. M. Nicholson, N. A. Finch, H. Flynn, J. Adamson, N. Kouri, A. Wojtas, P. Sengdy, G. Y. Hsiung, A. Karydas, W. W. Seeley, K. A. Josephs, G. Coppola, D. H. Geschwind, Z. K. Wszolek, H. Feldman, D. S. Knopman, R. C. Petersen, B. L. Miller, D. W. Dickson, K. B. Boylan, N. R. Graff-Radford and R. Rademakers (2011). "Expanded GGGGCC hexanucleotide repeat in noncoding region of C9ORF72 causes chromosome 9p-linked FTD and ALS." Neuron **72**(2): 245-256.
- Deltcheva, E., K. Chylinski, C. M. Sharma, K. Gonzales, Y. Chao, Z. A. Pirzada, M. R. Eckert, J. Vogel and E. Charpentier (2011). "CRISPR RNA maturation by trans-encoded small RNA and host factor RNase III." Nature **471**(7340): 602-607.
- Deng, H., K. Gao and J. Jankovic (2014). "The role of FUS gene variants in neurodegenerative diseases." Nat Rev Neurol **10**(6): 337-348.
- Deveau, H., J. E. Garneau and S. Moineau (2010). "CRISPR/Cas system and its role in phage-bacteria interactions." Annu Rev Microbiol **64**: 475-493.
- Di Giorgio, F. P., M. A. Carrasco, M. C. Siao, T. Maniatis and K. Eggan (2007). "Non-cell autonomous effect of glia on motor neurons in an embryonic stem cell-based ALS model." Nat Neurosci **10**(5): 608-614.
- Dion, P. A., H. Daoud and G. A. Rouleau (2009). "Genetics of motor neuron disorders: new insights into pathogenic mechanisms." Nat Rev Genet **10**(11): 769-782.
- Dobson-Stone, C., M. Hallupp, C. T. Loy, E. M. Thompson, E. Haan, C. M. Sue, P. K. Panegyres, C. Razquin, M. Seijo-Martinez, R. Rene, J. Gascon, J. Campdelacreu, B. Schmoll, A. E. Volk, W. S. Brooks, P. R. Schofield, P. Pastor and J. B. Kwok (2013). "C9ORF72 repeat expansion in Australian and Spanish frontotemporal dementia patients." PLoS One **8**(2): e56899.
- Dols-Icardo, O., A. Garcia-Redondo, R. Rojas-Garcia, R. Sanchez-Valle, A. Noguera, E. Gomez-Tortosa, P. Pastor, I. Hernandez, J. Esteban-Perez, M. Suarez-Calvet, S. Anton-Aguirre, G. Amer, S. Ortega-Cubero, R. Blesa, J. Fortea, D. Alcolea, A. Capdevila, A. Antonell, A. Llado, J. L. Munoz-Blanco, J. S. Mora, L. Galan-Davila, F. J. Rodriguez De Rivera, A. Lleo and J. Clarimon (2014). "Characterization of the repeat expansion size in C9orf72 in amyotrophic lateral sclerosis and frontotemporal dementia." Hum Mol Genet **23**(3): 749-754.

- Donnelly, C. J., P. W. Zhang, J. T. Pham, A. R. Haeusler, N. A. Mistry, S. Vidensky, E. L. Daley, E. M. Poth, B. Hoover, D. M. Fines, N. Maragakis, P. J. Tienari, L. Petrucelli, B. J. Traynor, J. Wang, F. Rigo, C. F. Bennett, S. Blackshaw, R. Sattler and J. D. Rothstein (2013). "RNA toxicity from the ALS/FTD C9ORF72 expansion is mitigated by antisense intervention." *Neuron* **80**(2): 415-428.
- Dormann, D. and C. Haass (2011). "TDP-43 and FUS: a nuclear affair." *Trends Neurosci* **34**(7): 339-348.
- Dormann, D. and C. Haass (2013). "Fused in sarcoma (FUS): an oncogene goes awry in neurodegeneration." *Mol Cell Neurosci* **56**: 475-486.
- Dormann, D., T. Madl, C. F. Valori, E. Bentmann, S. Tahirovic, C. Abou-Ajram, E. Kremmer, O. Ansorge, I. R. Mackenzie, M. Neumann and C. Haass (2012). "Arginine methylation next to the PY-NLS modulates Transportin binding and nuclear import of FUS." *EMBO J* **31**(22): 4258-4275.
- Dormann, D., R. Rodde, D. Edbauer, E. Bentmann, I. Fischer, A. Hruscha, M. E. Than, I. R. Mackenzie, A. Capell, B. Schmid, M. Neumann and C. Haass (2010). "ALS-associated fused in sarcoma (FUS) mutations disrupt Transportin-mediated nuclear import." *EMBO J* **29**(16): 2841-2857.
- Ederle, H. and D. Dormann (2017). "TDP-43 and FUS en route from the nucleus to the cytoplasm." *FEBS Lett* **591**(11): 1489-1507.
- Farg, M. A., A. Konopka, K. Y. Soo, D. Ito and J. D. Atkin (2017). "The DNA damage response (DDR) is induced by the C9orf72 repeat expansion in amyotrophic lateral sclerosis." *Hum Mol Genet* **26**(15): 2882-2896.
- Farg, M. A., V. Sundaramoorthy, J. M. Sultana, S. Yang, R. A. Atkinson, V. Levina, M. A. Halloran, P. A. Gleeson, I. P. Blair, K. Y. Soo, A. E. King and J. D. Atkin (2014). "C9ORF72, implicated in amyotrophic lateral sclerosis and frontotemporal dementia, regulates endosomal trafficking." *Hum Mol Genet* **23**(13): 3579-3595.
- Freibaum, B. D., Y. Lu, R. Lopez-Gonzalez, N. C. Kim, S. Almeida, K. H. Lee, N. Badders, M. Valentine, B. L. Miller, P. C. Wong, L. Petrucelli, H. J. Kim, F. B. Gao and J. P. Taylor (2015). "GGGGCC repeat expansion in C9orf72 compromises nucleocytoplasmic transport." *Nature* **525**(7567): 129-133.
- Gal, J., J. Zhang, D. M. Kwinter, J. Zhai, H. Jia, J. Jia and H. Zhu (2011). "Nuclear localization sequence of FUS and induction of stress granules by ALS mutants." *Neurobiol Aging* **32**(12): 2323 e2327-2340.
- Gasiunas, G., R. Barrangou, P. Horvath and V. Siksnys (2012). "Cas9-crRNA ribonucleoprotein complex mediates specific DNA cleavage for adaptive immunity in bacteria." *Proc Natl Acad Sci U S A* **109**(39): E2579-2586.
- Gendron, T. F., V. V. Belzil, Y. J. Zhang and L. Petrucelli (2014). "Mechanisms of toxicity in C9FTLD/ALS." *Acta Neuropathol* **127**(3): 359-376.
- Gendron, T. F., K. F. Bieniek, Y. J. Zhang, K. Jansen-West, P. E. Ash, T. Caulfield, L. Daugherty, J. H. Dunmore, M. Castanedes-Casey, J. Chew, D. M. Cosio, M. van Blitterswijk, W. C. Lee, R. Rademakers, K. B. Boylan, D. W. Dickson and L. Petrucelli (2013). "Antisense transcripts of the expanded C9ORF72 hexanucleotide repeat form nuclear RNA foci and undergo repeat-associated non-ATG translation in c9FTD/ALS." *Acta Neuropathol* **126**(6): 829-844.
- Gendron, T. F. and L. Petrucelli (2011). "Rodent models of TDP-43 proteinopathy: investigating the mechanisms of TDP-43-mediated neurodegeneration." *J Mol Neurosci* **45**(3): 486-499.
- GenScript (2019). CRISPR/Cas9 Plasmid Reagents for sgRNA Expression & Gene Editing.
- Giordana, M. T., M. Piccinini, S. Grifoni, G. De Marco, M. Vercellino, M. Magistrello, A. Pellerino, B. Buccinna, E. Lupino and M. T. Rinaudo (2010). "TDP-43 redistribution is an early event in sporadic amyotrophic lateral sclerosis." *Brain Pathol* **20**(2): 351-360.

- Glass, H., A. Pal, P. Reinhardt, J. Sternecker, F. Wegner, A. Storch and A. Hermann (2018). "Defective mitochondrial and lysosomal trafficking in chorea-acanthocytosis is independent of Src-kinase signaling." *Mol Cell Neurosci* **92**: 137-148.
- Gomez-Tortosa, E., J. Gallego, R. Guerrero-Lopez, A. Marcos, E. Gil-Neciga, M. J. Sainz, A. Diaz, E. Franco-Macias, M. J. Trujillo-Tiebas, C. Ayuso and J. Perez-Perez (2013). "C9ORF72 hexanucleotide expansions of 20-22 repeats are associated with frontotemporal deterioration." *Neurology* **80**(4): 366-370.
- Grabarz, A., A. Barascu, J. Guirouilh-Barbat and B. S. Lopez (2012). "Initiation of DNA double strand break repair: signaling and single-stranded resection dictate the choice between homologous recombination, non-homologous end-joining and alternative end-joining." *Am J Cancer Res* **2**(3): 249-268.
- Guo, W., M. Naujock, L. Fumagalli, T. Vandoorne, P. Baatsen, R. Boon, L. Ordovas, A. Patel, M. Welters, T. Vanwelden, N. Geens, T. Tricot, V. Benoy, J. Steyaert, C. Lefebvre-Omar, W. Boesmans, M. Jarpe, J. Sternecker, F. Wegner, S. Petri, D. Bohl, P. Vanden Berghe, W. Robberecht, P. Van Damme, C. Verfaillie and L. Van Den Bosch (2017). "HDAC6 inhibition reverses axonal transport defects in motor neurons derived from FUS-ALS patients." *Nat Commun* **8**(1): 861.
- Gurney, M. E., F. B. Cutting, P. Zhai, A. Doble, C. P. Taylor, P. K. Andrus and E. D. Hall (1996). "Benefit of vitamin E, riluzole, and gabapentin in a transgenic model of familial amyotrophic lateral sclerosis." *Ann Neurol* **39**(2): 147-157.
- Gurney, M. E., H. Pu, A. Y. Chiu, M. C. Dal Canto, C. Y. Polchow, D. D. Alexander, J. Caliendo, A. Hentati, Y. W. Kwon, H. X. Deng and et al. (1994). "Motor neuron degeneration in mice that express a human Cu,Zn superoxide dismutase mutation." *Science* **264**(5166): 1772-1775.
- Haidet-Phillips, A. M., M. E. Hester, C. J. Miranda, K. Meyer, L. Braun, A. Frakes, S. Song, S. Likhite, M. J. Murtha, K. D. Foust, M. Rao, A. Eagle, A. Kammesheidt, A. Christensen, J. R. Mendell, A. H. Burghes and B. K. Kaspar (2011). "Astrocytes from familial and sporadic ALS patients are toxic to motor neurons." *Nat Biotechnol* **29**(9): 824-828.
- Hasegawa, T., N. Sugeno, A. Kikuchi, T. Baba and M. Aoki (2017). "Membrane Trafficking Illuminates a Path to Parkinson's Disease." *Tohoku J Exp Med* **242**(1): 63-76.
- Heemels, M. T. (2016). "Neurodegenerative diseases." *Nature* **539**(7628): 179.
- Hewitt, C., J. Kirby, J. R. Highley, J. A. Hartley, R. Hibberd, H. C. Hollinger, T. L. Williams, P. G. Ince, C. J. McDermott and P. J. Shaw (2010). "Novel FUS/TLS mutations and pathology in familial and sporadic amyotrophic lateral sclerosis." *Arch Neurol* **67**(4): 455-461.
- Higelin, J., A. Catanese, L. L. Semelink-Sedlacek, S. Oeztuerk, A. K. Lutz, J. Bausinger, G. Barbi, G. Speit, P. M. Andersen, A. C. Ludolph, M. Demestre and T. M. Boeckers (2018). "NEK1 loss-of-function mutation induces DNA damage accumulation in ALS patient-derived motoneurons." *Stem Cell Res* **30**: 150-162.
- Higelin, J., M. Demestre, S. Putz, J. P. Delling, C. Jacob, A. K. Lutz, J. Bausinger, A. K. Huber, M. Klingenstein, G. Barbi, G. Speit, A. Huebers, J. H. Weishaupt, A. Hermann, S. Liebau, A. C. Ludolph and T. M. Boeckers (2016). "FUS Mislocalization and Vulnerability to DNA Damage in ALS Patients Derived hiPSCs and Aging Motoneurons." *Front Cell Neurosci* **10**: 290.
- Hill, S. J., D. A. Mordes, L. A. Cameron, D. S. Neuberg, S. Landini, K. Eggan and D. M. Livingston (2016). "Two familial ALS proteins function in prevention/repair of transcription-associated DNA damage." *Proc Natl Acad Sci U S A* **113**(48): E7701-E7709.
- Hoeijmakers, J. H. (2009). "DNA damage, aging, and cancer." *N Engl J Med* **361**(15): 1475-1485.

- Hsu, P. D., D. A. Scott, J. A. Weinstein, F. A. Ran, S. Konermann, V. Agarwala, Y. Li, E. J. Fine, X. Wu, O. Shalem, T. J. Cradick, L. A. Marraffini, G. Bao and F. Zhang (2013). "DNA targeting specificity of RNA-guided Cas9 nucleases." *Nat Biotechnol* **31**(9): 827-832.
- Huang, C., H. Zhou, J. Tong, H. Chen, Y. J. Liu, D. Wang, X. Wei and X. G. Xia (2011). "FUS transgenic rats develop the phenotypes of amyotrophic lateral sclerosis and frontotemporal lobar degeneration." *PLoS Genet* **7**(3): e1002011.
- Huang, E. J., J. Zhang, F. Geser, J. Q. Trojanowski, J. B. Strober, D. W. Dickson, R. H. Brown, Jr., B. E. Shapiro and C. Lomen-Hoerth (2010). "Extensive FUS-immunoreactive pathology in juvenile amyotrophic lateral sclerosis with basophilic inclusions." *Brain Pathol* **20**(6): 1069-1076.
- Iyama, T. and D. M. Wilson, 3rd (2013). "DNA repair mechanisms in dividing and non-dividing cells." *DNA Repair (Amst)* **12**(8): 620-636.
- Jackson, S. P. and J. Bartek (2009). "The DNA-damage response in human biology and disease." *Nature* **461**(7267): 1071-1078.
- Japtok, J. (2014). Modeling cortical neurodegeneration in FUS-ALS using patient-specific induced pluripotent stem cells. M. Sc. Master Thesis, Technische Universität Dresden.
- Japtok, J., X. Lojewski, M. Naumann, M. Klingenstein, P. Reinhardt, J. Sternecker, S. Putz, M. Demestre, T. M. Boeckers, A. C. Ludolph, S. Liebau, A. Storch and A. Hermann (2015). "Stepwise acquisition of hallmark neuropathology in FUS-ALS iPSC models depends on mutation type and neuronal aging." *Neurobiol Dis* **82**: 420-429.
- Jinek, M., K. Chylinski, I. Fonfara, M. Hauer, J. A. Doudna and E. Charpentier (2012). "A programmable dual-RNA-guided DNA endonuclease in adaptive bacterial immunity." *Science* **337**(6096): 816-821.
- Kabashi, E., P. N. Valdmanis, P. Dion, D. Spiegelman, B. J. McConkey, C. Vande Velde, J. P. Bouchard, L. Lacomblez, K. Pochigaeva, F. Salachas, P. F. Pradat, W. Camu, V. Meininger, N. Dupre and G. A. Rouleau (2008). "TARDBP mutations in individuals with sporadic and familial amyotrophic lateral sclerosis." *Nat Genet* **40**(5): 572-574.
- Kamentsky, L., T. R. Jones, A. Fraser, M. A. Bray, D. J. Logan, K. L. Madden, V. Ljosa, C. Rueden, K. W. Eliceiri and A. E. Carpenter (2011). "Improved structure, function and compatibility for CellProfiler: modular high-throughput image analysis software." *Bioinformatics* **27**(8): 1179-1180.
- Kaneb, H. M., P. A. Dion and G. A. Rouleau (2012). "The FUS about arginine methylation in ALS and FTLD." *EMBO J* **31**(22): 4249-4251.
- King, O. D., A. D. Gitler and J. Shorter (2012). "The tip of the iceberg: RNA-binding proteins with prion-like domains in neurodegenerative disease." *Brain Res* **1462**: 61-80.
- Kinner, A., W. Wu, C. Staudt and G. Iliakis (2008). "Gamma-H2AX in recognition and signaling of DNA double-strand breaks in the context of chromatin." *Nucleic Acids Res* **36**(17): 5678-5694.
- Kino, Y., C. Washizu, E. Aquilanti, M. Okuno, M. Kurosawa, M. Yamada, H. Doi and N. Nukina (2011). "Intracellular localization and splicing regulation of FUS/TLS are variably affected by amyotrophic lateral sclerosis-linked mutations." *Nucleic Acids Res* **39**(7): 2781-2798.
- Kiskinis, E., J. Sandoe, L. A. Williams, G. L. Boulting, R. Moccia, B. J. Wainger, S. Han, T. Peng, S. Thams, S. Mikkilineni, C. Mellin, F. T. Merkle, B. N. Davis-Dusenbery, M. Ziller, D. Oakley, J. Ichida, S. Di Costanzo, N. Atwater, M. L. Maeder, M. J. Goodwin, J. Nemes, R. E. Handsaker, D. Paull, S. Noggle, S. A. McCarroll, J. K. Joung, C. J. Woolf, R. H. Brown and K. Eggan (2014). "Pathways disrupted in human ALS motor neurons identified through genetic correction of mutant SOD1." *Cell Stem Cell* **14**(6): 781-795.
- Konopka, A. and J. D. Atkin (2018). "The Emerging Role of DNA Damage in the Pathogenesis of the C9orf72 Repeat Expansion in Amyotrophic Lateral Sclerosis." *Int J Mol Sci* **19**(10).

- Kreiter, N., A. Pal, X. Lojewski, P. Corcia, M. Naujock, P. Reinhardt, J. Sternecker, S. Petri, F. Wegner, A. Storch and A. Hermann (2018). "Age-dependent neurodegeneration and organelle transport deficiencies in mutant TDP43 patient-derived neurons are independent of TDP43 aggregation." *Neurobiol Dis* **115**: 167-181.
- Kwiatkowski, T. J., Jr., D. A. Bosco, A. L. Leclerc, E. Tamrazian, C. R. Vanderburg, C. Russ, A. Davis, J. Gilchrist, E. J. Kasarskis, T. Munsat, P. Valdmanis, G. A. Rouleau, B. A. Hosler, P. Cortelli, P. J. de Jong, Y. Yoshinaga, J. L. Haines, M. A. Pericak-Vance, J. Yan, N. Ticozzi, T. Siddique, D. McKenna-Yasek, P. C. Sapp, H. R. Horvitz, J. E. Landers and R. H. Brown, Jr. (2009). "Mutations in the FUS/TLS gene on chromosome 16 cause familial amyotrophic lateral sclerosis." *Science* **323**(5918): 1205-1208.
- Lagier-Tourenne, C., M. Polymenidou and D. W. Cleveland (2010). "TDP-43 and FUS/TLS: emerging roles in RNA processing and neurodegeneration." *Hum Mol Genet* **19**(R1): R46-64.
- Lagier-Tourenne, C., M. Polymenidou, K. R. Hutt, A. Q. Vu, M. Baughn, S. C. Huelga, K. M. Clutario, S. C. Ling, T. Y. Liang, C. Mazur, E. Wancewicz, A. S. Kim, A. Watt, S. Freier, G. G. Hicks, J. P. Donohue, L. Shiue, C. F. Bennett, J. Ravits, D. W. Cleveland and G. W. Yeo (2012). "Divergent roles of ALS-linked proteins FUS/TLS and TDP-43 intersect in processing long pre-mRNAs." *Nat Neurosci* **15**(11): 1488-1497.
- Lee, B. J., A. E. Cansizoglu, K. E. Suel, T. H. Louis, Z. Zhang and Y. M. Chook (2006). "Rules for nuclear localization sequence recognition by karyopherin beta 2." *Cell* **126**(3): 543-558.
- Lee, E. B., V. M. Lee and J. Q. Trojanowski (2011). "Gains or losses: molecular mechanisms of TDP43-mediated neurodegeneration." *Nat Rev Neurosci* **13**(1): 38-50.
- Lenzi, J., R. De Santis, V. de Turreis, M. Morlando, P. Laneve, A. Calvo, V. Caliendo, A. Chio, A. Rosa and I. Bozzoni (2015). "ALS mutant FUS proteins are recruited into stress granules in induced pluripotent stem cell-derived motoneurons." *Dis Model Mech* **8**(7): 755-766.
- Li, Y. R., O. D. King, J. Shorter and A. D. Gitler (2013). "Stress granules as crucibles of ALS pathogenesis." *J Cell Biol* **201**(3): 361-372.
- Lindahl, T. (1993). "Instability and decay of the primary structure of DNA." *Nature* **362**(6422): 709-715.
- Ling, S. C., M. Polymenidou and D. W. Cleveland (2013). "Converging mechanisms in ALS and FTD: disrupted RNA and protein homeostasis." *Neuron* **79**(3): 416-438.
- Lomen-Hoerth, C. (2011). "Clinical phenomenology and neuroimaging correlates in ALS-FTD." *J Mol Neurosci* **45**(3): 656-662.
- Lopez-Gonzalez, R., Y. Lu, T. F. Gendron, A. Karydas, H. Tran, D. Yang, L. Petrucelli, B. L. Miller, S. Almeida and F. B. Gao (2016). "Poly(GR) in C9ORF72-Related ALS/FTD Compromises Mitochondrial Function and Increases Oxidative Stress and DNA Damage in iPSC-Derived Motor Neurons." *Neuron* **92**(2): 383-391.
- Mackenzie, I. R., O. Ansorge, M. Strong, J. Bilbao, L. Zinman, L. C. Ang, M. Baker, H. Stewart, A. Eisen, R. Rademakers and M. Neumann (2011). "Pathological heterogeneity in amyotrophic lateral sclerosis with FUS mutations: two distinct patterns correlating with disease severity and mutation." *Acta Neuropathol* **122**(1): 87-98.
- Mackenzie, I. R., T. Arzberger, E. Kremmer, D. Troost, S. Lorenzl, K. Mori, S. M. Weng, C. Haass, H. A. Kretzschmar, D. Edbauer and M. Neumann (2013). "Dipeptide repeat protein pathology in C9ORF72 mutation cases: clinico-pathological correlations." *Acta Neuropathol* **126**(6): 859-879.
- Mackenzie, I. R., E. H. Bigio, P. G. Ince, F. Geser, M. Neumann, N. J. Cairns, L. K. Kwong, M. S. Forman, J. Ravits, H. Stewart, A. Eisen, L. McClusky, H. A. Kretzschmar, C. M. Monoranu, J. R. Highley, J. Kirby, T. Siddique, P. J. Shaw, V. M. Lee and J. Q. Trojanowski (2007). "Pathological TDP-43 distinguishes sporadic amyotrophic lateral sclerosis from amyotrophic lateral sclerosis with SOD1 mutations." *Ann Neurol* **61**(5): 427-434.

- Mackenzie, I. R., M. Neumann, E. H. Bigio, N. J. Cairns, I. Alafuzoff, J. Kril, G. G. Kovacs, B. Ghetti, G. Halliday, I. E. Holm, P. G. Ince, W. Kamphorst, T. Revesz, A. J. Rozemuller, S. Kumar-Singh, H. Akiyama, A. Baborie, S. Spina, D. W. Dickson, J. Q. Trojanowski and D. M. Mann (2009). "Nomenclature for neuropathologic subtypes of frontotemporal lobar degeneration: consensus recommendations." Acta Neuropathol **117**(1): 15-18.
- Mackenzie, I. R., R. Rademakers and M. Neumann (2010). "TDP-43 and FUS in amyotrophic lateral sclerosis and frontotemporal dementia." Lancet Neurol **9**(10): 995-1007.
- Madabhushi, R., L. Pan and L. H. Tsai (2014). "DNA damage and its links to neurodegeneration." Neuron **83**(2): 266-282.
- Mann, D. M. (2015). "Dipeptide repeat protein toxicity in frontotemporal lobar degeneration and in motor neurone disease associated with expansions in C9ORF72-a cautionary note." Neurobiol Aging **36**(2): 1224-1226.
- Marchetto, M. C., A. R. Muotri, Y. Mu, A. M. Smith, G. G. Cezar and F. H. Gage (2008). "Non-cell-autonomous effect of human SOD1 G37R astrocytes on motor neurons derived from human embryonic stem cells." Cell Stem Cell **3**(6): 649-657.
- Mariani, J., M. V. Simonini, D. Palejev, L. Tomasini, G. Coppola, A. M. Szekely, T. L. Horvath and F. M. Vaccarino (2012). "Modeling human cortical development in vitro using induced pluripotent stem cells." Proc Natl Acad Sci U S A **109**(31): 12770-12775.
- Marrone, L., H. C. A. Drexler, J. Wang, P. Tripathi, T. Distler, P. Heisterkamp, E. N. Anderson, S. Kour, A. Moraiti, S. Maharana, R. Bhatnagar, T. G. Belgard, V. Tripathy, N. Kalmbach, Z. Hosseinzadeh, V. Crippa, M. Abo-Rady, F. Wegner, A. Poletti, D. Troost, E. Aronica, V. Busskamp, J. Weis, U. B. Pandey, A. A. Hyman, S. Alberti, A. Goswami and J. Sternecker (2019). "FUS pathology in ALS is linked to alterations in multiple ALS-associated proteins and rescued by drugs stimulating autophagy." Acta Neuropathol **138**(1): 67-84.
- Marrone, L., I. Poser, I. Casci, J. Japtok, P. Reinhardt, A. Janosch, C. Andree, H. O. Lee, C. Moebius, E. Koerner, L. Reinhardt, M. E. Cicardi, K. Hackmann, B. Klink, A. Poletti, S. Alberti, M. Bickle, A. Hermann, U. B. Pandey, A. A. Hyman and J. L. Sternecker (2018). "Isogenic FUS-eGFP iPSC Reporter Lines Enable Quantification of FUS Stress Granule Pathology that Is Rescued by Drugs Inducing Autophagy." Stem Cell Reports **10**(2): 375-389.
- Mastrocola, A. S., S. H. Kim, A. T. Trinh, L. A. Rodenkirch and R. S. Tibbetts (2013). "The RNA-binding protein fused in sarcoma (FUS) functions downstream of poly(ADP-ribose) polymerase (PARP) in response to DNA damage." J Biol Chem **288**(34): 24731-24741.
- Matus, S., D. B. Medinas and C. Hetz (2014). "Common ground: stem cell approaches find shared pathways underlying ALS." Cell Stem Cell **14**(6): 697-699.
- Maury, Y., J. Come, R. A. Piskorowski, N. Salah-Mohellibi, V. Chevalere, M. Peschanski, C. Martinat and S. Nedelec (2015). "Combinatorial analysis of developmental cues efficiently converts human pluripotent stem cells into multiple neuronal subtypes." Nat Biotechnol **33**(1): 89-96.
- McGeer, P. L. and E. G. McGeer (2002). "Inflammatory processes in amyotrophic lateral sclerosis." Muscle Nerve **26**(4): 459-470.
- Meyer, K., L. Ferraiuolo, C. J. Miranda, S. Likhite, S. McElroy, S. Renusch, D. Ditsworth, C. Lagier-Tourenne, R. A. Smith, J. Ravits, A. H. Burghes, P. J. Shaw, D. W. Cleveland, S. J. Kolb and B. K. Kaspar (2014). "Direct conversion of patient fibroblasts demonstrates non-cell autonomous toxicity of astrocytes to motor neurons in familial and sporadic ALS." Proc Natl Acad Sci U S A **111**(2): 829-832.
- Millecamps, S., S. Boillee, I. Le Ber, D. Seilhean, E. Teyssou, M. Giraudeau, C. Moigneu, N. Vandenberghe, V. Danel-Brunaud, P. Corcia, P. F. Pradat, N. Le Forestier, L. Lacomblez, G. Bruneteau, W. Camu, A. Brice, C. Cazeneuve, E. Leguern, V. Meininger and F. Salachas (2012). "Phenotype

difference between ALS patients with expanded repeats in C9ORF72 and patients with mutations in other ALS-related genes." *J Med Genet* **49**(4): 258-263.

Millecamps, S. and J. P. Julien (2013). "Axonal transport deficits and neurodegenerative diseases." *Nat Rev Neurosci* **14**(3): 161-176.

Mitchell, J. C., P. McGoldrick, C. Vance, T. Hortobagyi, J. Sreedharan, B. Rogelj, E. L. Tudor, B. N. Smith, C. Klasen, C. C. Miller, J. D. Cooper, L. Greensmith and C. E. Shaw (2013). "Overexpression of human wild-type FUS causes progressive motor neuron degeneration in an age- and dose-dependent fashion." *Acta Neuropathol* **125**(2): 273-288.

Molyneaux, B. J., P. Arlotta, J. R. Menezes and J. D. Macklis (2007). "Neuronal subtype specification in the cerebral cortex." *Nat Rev Neurosci* **8**(6): 427-437.

Montuschi, A., B. Iazzolino, A. Calvo, C. Moglia, L. Lopiano, G. Restagno, M. Brunetti, I. Ossola, A. Lo Presti, S. Cammarosano, A. Canosa and A. Chio (2015). "Cognitive correlates in amyotrophic lateral sclerosis: a population-based study in Italy." *J Neurol Neurosurg Psychiatry* **86**(2): 168-173.

Mori, K., T. Arzberger, F. A. Grasser, I. Gijssels, S. May, K. Rentzsch, S. M. Weng, M. H. Schludi, J. van der Zee, M. Cruts, C. Van Broeckhoven, E. Kremmer, H. A. Kretzschmar, C. Haass and D. Edbauer (2013). "Bidirectional transcripts of the expanded C9orf72 hexanucleotide repeat are translated into aggregating dipeptide repeat proteins." *Acta Neuropathol* **126**(6): 881-893.

Mori, K., S. M. Weng, T. Arzberger, S. May, K. Rentzsch, E. Kremmer, B. Schmid, H. A. Kretzschmar, M. Cruts, C. Van Broeckhoven, C. Haass and D. Edbauer (2013). "The C9orf72 GGGGCC repeat is translated into aggregating dipeptide-repeat proteins in FTLD/ALS." *Science* **339**(6125): 1335-1338.

Mullaart, E., M. E. Boerrigter, R. Ravid, D. F. Swaab and J. Vijg (1990). "Increased levels of DNA breaks in cerebral cortex of Alzheimer's disease patients." *Neurobiol Aging* **11**(3): 169-173.

Myung, N. H., X. Zhu, Kruman, II, R. J. Castellani, R. B. Petersen, S. L. Siedlak, G. Perry, M. A. Smith and H. G. Lee (2008). "Evidence of DNA damage in Alzheimer disease: phosphorylation of histone H2AX in astrocytes." *Age (Dordr)* **30**(4): 209-215.

Naumann, M., A. Pal, A. Goswami, X. Lojewski, J. Japtok, A. Vehlow, M. Naujock, R. Gunther, M. Jin, N. Stanslowsky, P. Reinhardt, J. Sternecker, M. Frickenhaus, F. Pan-Montojo, E. Storkebaum, I. Poser, A. Freischmidt, J. H. Weishaupt, K. Holzmann, D. Troost, A. C. Ludolph, T. M. Boeckers, S. Liebau, S. Petri, N. Cordes, A. A. Hyman, F. Wegner, S. W. Grill, J. Weis, A. Storch and A. Hermann (2018). "Impaired DNA damage response signaling by FUS-NLS mutations leads to neurodegeneration and FUS aggregate formation." *Nat Commun* **9**(1): 335.

Neumann, M., D. M. Sampathu, L. K. Kwong, A. C. Truax, M. C. Micsenyi, T. T. Chou, J. Bruce, T. Schuck, M. Grossman, C. M. Clark, L. F. McCluskey, B. L. Miller, E. Masliah, I. R. Mackenzie, H. Feldman, W. Feiden, H. A. Kretzschmar, J. Q. Trojanowski and V. M. Lee (2006). "Ubiquitinated TDP-43 in frontotemporal lobar degeneration and amyotrophic lateral sclerosis." *Science* **314**(5796): 130-133.

Nishihira, Y., C. F. Tan, O. Onodera, Y. Toyoshima, M. Yamada, T. Morita, M. Nishizawa, A. Kakita and H. Takahashi (2008). "Sporadic amyotrophic lateral sclerosis: two pathological patterns shown by analysis of distribution of TDP-43-immunoreactive neuronal and glial cytoplasmic inclusions." *Acta Neuropathol* **116**(2): 169-182.

Niu, C., J. Zhang, F. Gao, L. Yang, M. Jia, H. Zhu and W. Gong (2012). "FUS-NLS/Transportin 1 complex structure provides insights into the nuclear targeting mechanism of FUS and the implications in ALS." *PLoS One* **7**(10): e47056.

Nolan, M., K. Talbot and O. Ansorge (2016). "Pathogenesis of FUS-associated ALS and FTD: insights from rodent models." *Acta Neuropathol Commun* **4**(1): 99.

- Nordin, A., C. Akimoto, A. Wuolikainen, H. Alstermark, P. Jonsson, A. Birve, S. L. Marklund, K. S. Graffmo, K. Forsberg, T. Brannstrom and P. M. Andersen (2015). "Extensive size variability of the GGGGCC expansion in C9orf72 in both neuronal and non-neuronal tissues in 18 patients with ALS or FTD." Hum Mol Genet **24**(11): 3133-3142.
- Ohki, Y., A. Wenninger-Weinzierl, A. Hruscha, K. Asakawa, K. Kawakami, C. Haass, D. Edbauer and B. Schmid (2017). "Glycine-alanine dipeptide repeat protein contributes to toxicity in a zebrafish model of C9orf72 associated neurodegeneration." Mol Neurodegener **12**(1): 6.
- Pal, A., H. Glass, M. Naumann, N. Kreiter, J. Japtok, R. Sczech and A. Hermann (2018). "High content organelle trafficking enables disease state profiling as powerful tool for disease modelling." Sci Data **5**: 180241.
- Pasinelli, P. and R. H. Brown (2006). "Molecular biology of amyotrophic lateral sclerosis: insights from genetics." Nat Rev Neurosci **7**(9): 710-723.
- Penndorf, D., O. W. Witte and A. Kretz (2018). "DNA plasticity and damage in amyotrophic lateral sclerosis." Neural Regen Res **13**(2): 173-180.
- Perlson, E., G. B. Jeong, J. L. Ross, R. Dixit, K. E. Wallace, R. G. Kalb and E. L. Holzbaur (2009). "A switch in retrograde signaling from survival to stress in rapid-onset neurodegeneration." J Neurosci **29**(31): 9903-9917.
- Perrot, R. and J. P. Julien (2009). "Real-time imaging reveals defects of fast axonal transport induced by disorganization of intermediate filaments." FASEB J **23**(9): 3213-3225.
- Philips, T. and J. D. Rothstein (2015). "Rodent Models of Amyotrophic Lateral Sclerosis." Curr Protoc Pharmacol **69**: 5 67 61-21.
- Pliatsika, V. and I. Rigoutsos (2015). "'Off-Spotter': very fast and exhaustive enumeration of genomic lookalikes for designing CRISPR/Cas guide RNAs." Biol Direct **10**: 4.
- Polymenidou, M. and D. W. Cleveland (2011). "The seeds of neurodegeneration: prion-like spreading in ALS." Cell **147**(3): 498-508.
- Powers, C. A., M. Mathur, B. M. Raaka, D. Ron and H. H. Samuels (1998). "TLS (translocated-in-liposarcoma) is a high-affinity interactor for steroid, thyroid hormone, and retinoid receptors." Mol Endocrinol **12**(1): 4-18.
- Qiu, H., S. Lee, Y. Shang, W. Y. Wang, K. F. Au, S. Kamiya, S. J. Barmada, S. Finkbeiner, H. Lui, C. E. Carlton, A. A. Tang, M. C. Oldham, H. Wang, J. Shorter, A. J. Filiano, E. D. Roberson, W. G. Tourtellotte, B. Chen, L. H. Tsai and E. J. Huang (2014). "ALS-associated mutation FUS-R521C causes DNA damage and RNA splicing defects." J Clin Invest **124**(3): 981-999.
- Rademakers, R., H. Stewart, M. Dejesus-Hernandez, C. Krieger, N. Graff-Radford, M. Fabros, H. Briemberg, N. Cashman, A. Eisen and I. R. Mackenzie (2010). "Fus gene mutations in familial and sporadic amyotrophic lateral sclerosis." Muscle Nerve **42**(2): 170-176.
- Ran, F. A., P. D. Hsu, C. Y. Lin, J. S. Gootenberg, S. Konermann, A. E. Trevino, D. A. Scott, A. Inoue, S. Matoba, Y. Zhang and F. Zhang (2013). "Double nicking by RNA-guided CRISPR Cas9 for enhanced genome editing specificity." Cell **154**(6): 1380-1389.
- Ran, F. A., P. D. Hsu, J. Wright, V. Agarwala, D. A. Scott and F. Zhang (2013). "Genome engineering using the CRISPR-Cas9 system." Nat Protoc **8**(11): 2281-2308.
- Rao, K. S. (1993). "Genomic damage and its repair in young and aging brain." Mol Neurobiol **7**(1): 23-48.
- Reinhardt, P., M. Glatza, K. Hemmer, Y. Tsytsyura, C. S. Thiel, S. Hoing, S. Moritz, J. A. Parga, L. Wagner, J. M. Bruder, G. Wu, B. Schmid, A. Ropke, J. Klingauf, J. C. Schwamborn, T. Gasser, H. R.

- Scholer and J. Sternecker (2013). "Derivation and expansion using only small molecules of human neural progenitors for neurodegenerative disease modeling." *PLoS One* **8**(3): e59252.
- Renton, A. E., A. Chio and B. J. Traynor (2014). "State of play in amyotrophic lateral sclerosis genetics." *Nat Neurosci* **17**(1): 17-23.
- Renton, A. E., E. Majounie, A. Waite, J. Simon-Sanchez, S. Rollinson, J. R. Gibbs, J. C. Schymick, H. Laaksovirta, J. C. van Swieten, L. Myllykangas, H. Kalimo, A. Paetau, Y. Abramzon, A. M. Remes, A. Kaganovich, S. W. Scholz, J. Duckworth, J. Ding, D. W. Harmer, D. G. Hernandez, J. O. Johnson, K. Mok, M. Ryten, D. Tratzuni, R. J. Guerreiro, R. W. Orrell, J. Neal, A. Murray, J. Pearson, I. E. Jansen, D. Sondervan, H. Seelaar, D. Blake, K. Young, N. Halliwell, J. B. Callister, G. Toulson, A. Richardson, A. Gerhard, J. Snowden, D. Mann, D. Neary, M. A. Nalls, T. Peuralinna, L. Jansson, V. M. Isoviita, A. L. Kaivorinne, M. Holtta-Vuori, E. Ikonen, R. Sulkava, M. Benatar, J. Wu, A. Chio, G. Restagno, G. Borghero, M. Sabatelli, I. Consortium, D. Heckerman, E. Rogaeva, L. Zinman, J. D. Rothstein, M. Sendtner, C. Drepper, E. E. Eichler, C. Alkan, Z. Abdullaev, S. D. Pack, A. Dutra, E. Pak, J. Hardy, A. Singleton, N. M. Williams, P. Heutink, S. Pickering-Brown, H. R. Morris, P. J. Tienari and B. J. Traynor (2011). "A hexanucleotide repeat expansion in C9ORF72 is the cause of chromosome 9p21-linked ALS-FTD." *Neuron* **72**(2): 257-268.
- Rohrer, J. D., A. M. Isaacs, S. Mizielinska, S. Mead, T. Lashley, S. Wray, K. Sidle, P. Fratta, R. W. Orrell, J. Hardy, J. Holton, T. Revesz, M. N. Rossor and J. D. Warren (2015). "C9orf72 expansions in frontotemporal dementia and amyotrophic lateral sclerosis." *Lancet Neurol* **14**(3): 291-301.
- Rosen, D. R. (1993). "Mutations in Cu/Zn superoxide dismutase gene are associated with familial amyotrophic lateral sclerosis." *Nature* **364**(6435): 362.
- Rowland, L. P. and N. A. Shneider (2001). "Amyotrophic lateral sclerosis." *N Engl J Med* **344**(22): 1688-1700.
- Rulten, S. L. and G. J. Grundy (2017). "Non-homologous end joining: Common interaction sites and exchange of multiple factors in the DNA repair process." *Bioessays* **39**(3).
- Rulten, S. L., A. Rotheray, R. L. Green, G. J. Grundy, D. A. Moore, F. Gomez-Herreros, M. Hafezparast and K. W. Caldecott (2014). "PARP-1 dependent recruitment of the amyotrophic lateral sclerosis-associated protein FUS/TLS to sites of oxidative DNA damage." *Nucleic Acids Res* **42**(1): 307-314.
- Saberi, S., J. E. Stauffer, D. J. Schulte and J. Ravits (2015). "Neuropathology of Amyotrophic Lateral Sclerosis and Its Variants." *Neurol Clin* **33**(4): 855-876.
- Sances, S., L. I. Bruijn, S. Chandran, K. Eggan, R. Ho, J. R. Klim, M. R. Livesey, E. Lowry, J. D. Macklis, D. Rushton, C. Sadegh, D. Sareen, H. Wichterle, S. C. Zhang and C. N. Svendsen (2016). "Modeling ALS with motor neurons derived from human induced pluripotent stem cells." *Nat Neurosci* **19**(4): 542-553.
- Schindelin, J., I. Arganda-Carreras, E. Frise, V. Kaynig, M. Longair, T. Pietzsch, S. Preibisch, C. Rueden, S. Saalfeld, B. Schmid, J. Y. Tinevez, D. J. White, V. Hartenstein, K. Eliceiri, P. Tomancak and A. Cardona (2012). "Fiji: an open-source platform for biological-image analysis." *Nat Methods* **9**(7): 676-682.
- Schiweck, J., B. J. Eickholt and K. Murk (2018). "Important Shapeshifter: Mechanisms Allowing Astrocytes to Respond to the Changing Nervous System During Development, Injury and Disease." *Front Cell Neurosci* **12**: 261.
- Schludi, M. H., S. May, F. A. Grasser, K. Rentzsch, E. Kremmer, C. Kupper, T. Klopstock, D. German Consortium for Frontotemporal Lobar, A. Bavarian Brain Banking, T. Arzberger and D. Edbauer (2015). "Distribution of dipeptide repeat proteins in cellular models and C9orf72 mutation cases suggests link to transcriptional silencing." *Acta Neuropathol* **130**(4): 537-555.
- Schonn, I., J. Hennesen and D. C. Dartsch (2010). "Cellular responses to etoposide: cell death despite cell cycle arrest and repair of DNA damage." *Apoptosis* **15**(2): 162-172.

- Sheetz, M. P., K. K. Pfister, J. C. Bulinski and C. W. Cotman (1998). "Mechanisms of trafficking in axons and dendrites: implications for development and neurodegeneration." *Prog Neurobiol* **55**(6): 577-594.
- Shelkovnikova, T. A., H. K. Robinson, N. Connor-Robson and V. L. Buchman (2013). "Recruitment into stress granules prevents irreversible aggregation of FUS protein mislocalized to the cytoplasm." *Cell Cycle* **12**(19): 3194-3202.
- Shi, Y., P. Kirwan and F. J. Livesey (2012). "Directed differentiation of human pluripotent stem cells to cerebral cortex neurons and neural networks." *Nat Protoc* **7**(10): 1836-1846.
- Shi, Y., P. Kirwan, J. Smith, H. P. Robinson and F. J. Livesey (2012). "Human cerebral cortex development from pluripotent stem cells to functional excitatory synapses." *Nat Neurosci* **15**(3): 477-486, S471.
- Simon-Sanchez, J., E. G. Dopper, P. E. Cohn-Hokke, R. K. Hukema, N. Nicolaou, H. Seelaar, J. R. de Graaf, I. de Koning, N. M. van Schoor, D. J. Deeg, M. Smits, J. Raaphorst, L. H. van den Berg, H. J. Schelhaas, C. E. De Die-Smulders, D. Majoor-Krakauer, A. J. Rozemuller, R. Willemsen, Y. A. Pijnenburg, P. Heutink and J. C. van Swieten (2012). "The clinical and pathological phenotype of C9ORF72 hexanucleotide repeat expansions." *Brain* **135**(Pt 3): 723-735.
- Sivadasan, R., D. Hornburg, C. Drepper, N. Frank, S. Jablonka, A. Hansel, X. Lojewski, J. Sternecker, A. Hermann, P. J. Shaw, P. G. Ince, M. Mann, F. Meissner and M. Sendtner (2016). "C9ORF72 interaction with cofilin modulates actin dynamics in motor neurons." *Nat Neurosci* **19**(12): 1610-1618.
- Sreedharan, J., I. P. Blair, V. B. Tripathi, X. Hu, C. Vance, B. Rogelj, S. Ackerley, J. C. Durnall, K. L. Williams, E. Buratti, F. Baralle, J. de Belleruche, J. D. Mitchell, P. N. Leigh, A. Al-Chalabi, C. C. Miller, G. Nicholson and C. E. Shaw (2008). "TDP-43 mutations in familial and sporadic amyotrophic lateral sclerosis." *Science* **319**(5870): 1668-1672.
- StemCell, A. (2018). "Genetically Modified Cell Lines / Isogenic Cell Lines." Retrieved May, 2019, from <https://www.appliedstemcell.com/research/products/isogenic-cell-lines>.
- Su, J. H., K. E. Nichol, T. Sitch, P. Sheu, C. Chubb, B. L. Miller, K. J. Tomaselli, R. C. Kim and C. W. Cotman (2000). "DNA damage and activated caspase-3 expression in neurons and astrocytes: evidence for apoptosis in frontotemporal dementia." *Exp Neurol* **163**(1): 9-19.
- Sun, Z., Z. Diaz, X. Fang, M. P. Hart, A. Chesi, J. Shorter and A. D. Gitler (2011). "Molecular determinants and genetic modifiers of aggregation and toxicity for the ALS disease protein FUS/TLS." *PLoS Biol* **9**(4): e1000614.
- Suzuki, N., M. Aoki, H. Warita, M. Kato, H. Mizuno, N. Shimakura, T. Akiyama, H. Furuya, T. Hokonohara, A. Iwaki, S. Togashi, H. Konno and Y. Itoyama (2010). "FALS with FUS mutation in Japan, with early onset, rapid progress and basophilic inclusion." *J Hum Genet* **55**(4): 252-254.
- Suzuki, N., S. Kato, M. Kato, H. Warita, H. Mizuno, M. Kato, N. Shimakura, H. Akiyama, Z. Kobayashi, H. Konno and M. Aoki (2012). "FUS/TLS-immunoreactive neuronal and glial cell inclusions increase with disease duration in familial amyotrophic lateral sclerosis with an R521C FUS/TLS mutation." *J Neuropathol Exp Neurol* **71**(9): 779-788.
- Swarup, V. and J. P. Julien (2011). "ALS pathogenesis: recent insights from genetics and mouse models." *Prog Neuropsychopharmacol Biol Psychiatry* **35**(2): 363-369.
- Takahashi, K., K. Tanabe, M. Ohnuki, M. Narita, T. Ichisaka, K. Tomoda and S. Yamanaka (2007). "Induction of pluripotent stem cells from adult human fibroblasts by defined factors." *Cell* **131**(5): 861-872.
- Taylor, J. P., R. H. Brown, Jr. and D. W. Cleveland (2016). "Decoding ALS: from genes to mechanism." *Nature* **539**(7628): 197-206.

- Trapp, B. D., J. Peterson, R. M. Ransohoff, R. Rudick, S. Mork and L. Bo (1998). "Axonal transection in the lesions of multiple sclerosis." N Engl J Med **338**(5): 278-285.
- Turner, B. J. and K. Talbot (2008). "Transgenics, toxicity and therapeutics in rodent models of mutant SOD1-mediated familial ALS." Prog Neurobiol **85**(1): 94-134.
- van Blitterswijk, M., M. DeJesus-Hernandez, E. Niemantsverdriet, M. E. Murray, M. G. Heckman, N. N. Diehl, P. H. Brown, M. C. Baker, N. A. Finch, P. O. Bauer, G. Serrano, T. G. Beach, K. A. Josephs, D. S. Knopman, R. C. Petersen, B. F. Boeve, N. R. Graff-Radford, K. B. Boylan, L. Petrucelli, D. W. Dickson and R. Rademakers (2013). "Association between repeat sizes and clinical and pathological characteristics in carriers of C9ORF72 repeat expansions (Xpansize-72): a cross-sectional cohort study." Lancet Neurol **12**(10): 978-988.
- Van Damme, P., W. Robberecht and L. Van Den Bosch (2017). "Modelling amyotrophic lateral sclerosis: progress and possibilities." Dis Model Mech **10**(5): 537-549.
- Van Deerlin, V. M., J. B. Leverenz, L. M. Bekris, T. D. Bird, W. Yuan, L. B. Elman, D. Clay, E. M. Wood, A. S. Chen-Plotkin, M. Martinez-Lage, E. Steinbart, L. McCluskey, M. Grossman, M. Neumann, I. L. Wu, W. S. Yang, R. Kalb, D. R. Galasko, T. J. Montine, J. Q. Trojanowski, V. M. Lee, G. D. Schellenberg and C. E. Yu (2008). "TARDBP mutations in amyotrophic lateral sclerosis with TDP-43 neuropathology: a genetic and histopathological analysis." Lancet Neurol **7**(5): 409-416.
- Van Langenhove, T., J. van der Zee and C. Van Broeckhoven (2012). "The molecular basis of the frontotemporal lobar degeneration-amyotrophic lateral sclerosis spectrum." Ann Med **44**(8): 817-828.
- Vance, C., B. Rogelj, T. Hortobagyi, K. J. De Vos, A. L. Nishimura, J. Sreedharan, X. Hu, B. Smith, D. Ruddy, P. Wright, J. Ganesalingam, K. L. Williams, V. Tripathi, S. Al-Saraj, A. Al-Chalabi, P. N. Leigh, I. P. Blair, G. Nicholson, J. de Belleruche, J. M. Gallo, C. C. Miller and C. E. Shaw (2009). "Mutations in FUS, an RNA processing protein, cause familial amyotrophic lateral sclerosis type 6." Science **323**(5918): 1208-1211.
- Vance, C., E. L. Scotter, A. L. Nishimura, C. Troakes, J. C. Mitchell, C. Kathe, H. Urwin, C. Manser, C. C. Miller, T. Hortobagyi, M. Dragunow, B. Rogelj and C. E. Shaw (2013). "ALS mutant FUS disrupts nuclear localization and sequesters wild-type FUS within cytoplasmic stress granules." Hum Mol Genet **22**(13): 2676-2688.
- Verbeeck, C., Q. Deng, M. DeJesus-Hernandez, G. Taylor, C. Ceballos-Diaz, J. Kocerha, T. Golde, P. Das, R. Rademakers, D. W. Dickson and T. Kukar (2012). "Expression of Fused in sarcoma mutations in mice recapitulates the neuropathology of FUS proteinopathies and provides insight into disease pathogenesis." Mol Neurodegener **7**: 53.
- Vogler, T. O., J. R. Wheeler, E. D. Nguyen, M. P. Hughes, K. A. Britson, E. Lester, B. Rao, N. D. Betta, O. N. Whitney, T. E. Ewachiw, E. Gomes, J. Shorter, T. E. Lloyd, D. S. Eisenberg, J. P. Taylor, A. M. Johnson, B. B. Olwin and R. Parker (2018). "TDP-43 and RNA form amyloid-like myo-granules in regenerating muscle." Nature **563**(7732): 508-513.
- Walker, C., S. Herranz-Martin, E. Karyka, C. Liao, K. Lewis, W. Elsayed, V. Lukashchuk, S. C. Chiang, S. Ray, P. J. Mulcahy, M. Jurga, I. Tsagakis, T. Iannitti, J. Chandran, I. Coldicott, K. J. De Vos, M. K. Hassan, A. Higginbottom, P. J. Shaw, G. M. Hautbergue, M. Azzouz and S. F. El-Khamisy (2017). "C9orf72 expansion disrupts ATM-mediated chromosomal break repair." Nat Neurosci **20**(9): 1225-1235.
- Walker, J. V. and J. L. Nitiss (2002). "DNA topoisomerase II as a target for cancer chemotherapy." Cancer Invest **20**(4): 570-589.
- Wang, W., L. Li, W. L. Lin, D. W. Dickson, L. Petrucelli, T. Zhang and X. Wang (2013). "The ALS disease-associated mutant TDP-43 impairs mitochondrial dynamics and function in motor neurons." Hum Mol Genet **22**(23): 4706-4719.

- Wang, W. Y., L. Pan, S. C. Su, E. J. Quinn, M. Sasaki, J. C. Jimenez, I. R. Mackenzie, E. J. Huang and L. H. Tsai (2013). "Interaction of FUS and HDAC1 regulates DNA damage response and repair in neurons." Nat Neurosci **16**(10): 1383-1391.
- Wen, X., W. Tan, T. Westergard, K. Krishnamurthy, S. S. Markandiah, Y. Shi, S. Lin, N. A. Shneider, J. Monaghan, U. B. Pandey, P. Pasinelli, J. K. Ichida and D. Trotti (2014). "Antisense proline-arginine RAN dipeptides linked to C9ORF72-ALS/FTD form toxic nuclear aggregates that initiate in vitro and in vivo neuronal death." Neuron **84**(6): 1213-1225.
- Williamson, T. L. and D. W. Cleveland (1999). "Slowing of axonal transport is a very early event in the toxicity of ALS-linked SOD1 mutants to motor neurons." Nat Neurosci **2**(1): 50-56.
- Worms, P. M. (2001). "The epidemiology of motor neuron diseases: a review of recent studies." J Neurol Sci **191**(1-2): 3-9.
- Writing, G. and A. L. S. S. G. Edaravone (2017). "Safety and efficacy of edaravone in well defined patients with amyotrophic lateral sclerosis: a randomised, double-blind, placebo-controlled trial." Lancet Neurol **16**(7): 505-512.
- Wyss-Coray, T. (2016). "Ageing, neurodegeneration and brain rejuvenation." Nature **539**(7628): 180-186.
- Xia, Q., H. Wang, Z. Hao, C. Fu, Q. Hu, F. Gao, H. Ren, D. Chen, J. Han, Z. Ying and G. Wang (2016). "TDP-43 loss of function increases TFEB activity and blocks autophagosome-lysosome fusion." EMBO J **35**(2): 121-142.
- Yamakawa, M., D. Ito, T. Honda, K. Kubo, M. Noda, K. Nakajima and N. Suzuki (2015). "Characterization of the dipeptide repeat protein in the molecular pathogenesis of c9FTD/ALS." Hum Mol Genet **24**(6): 1630-1645.
- Yamanaka, K., S. J. Chun, S. Boillee, N. Fujimori-Tonou, H. Yamashita, D. H. Gutmann, R. Takahashi, H. Misawa and D. W. Cleveland (2008). "Astrocytes as determinants of disease progression in inherited amyotrophic lateral sclerosis." Nat Neurosci **11**(3): 251-253.
- Yu, J., M. A. Vodyanik, K. Smuga-Otto, J. Antosiewicz-Bourget, J. L. Frane, S. Tian, J. Nie, G. A. Jonsdottir, V. Ruotti, R. Stewart, Slukvin, II and J. A. Thomson (2007). "Induced pluripotent stem cell lines derived from human somatic cells." Science **318**(5858): 1917-1920.
- Zhang, H., C. F. Tan, F. Mori, K. Tanji, A. Kakita, H. Takahashi and K. Wakabayashi (2008). "TDP-43-immunoreactive neuronal and glial inclusions in the neostriatum in amyotrophic lateral sclerosis with and without dementia." Acta Neuropathol **115**(1): 115-122.
- Zhang, J., G. Perry, M. A. Smith, D. Robertson, S. J. Olson, D. G. Graham and T. J. Montine (1999). "Parkinson's disease is associated with oxidative damage to cytoplasmic DNA and RNA in substantia nigra neurons." Am J Pathol **154**(5): 1423-1429.
- Zhang, Z. C. and Y. M. Chook (2012). "Structural and energetic basis of ALS-causing mutations in the atypical proline-tyrosine nuclear localization signal of the Fused in Sarcoma protein (FUS)." Proc Natl Acad Sci U S A **109**(30): 12017-12021.
- Zhou, B., Y. X. Zuo and R. T. Jiang (2019). "Astrocyte morphology: Diversity, plasticity, and role in neurological diseases." CNS Neurosci Ther **25**(6): 665-673.
- Zhou, Q., C. Lehmer, M. Michaelsen, K. Mori, D. Alterauge, D. Baumjohann, M. H. Schludi, J. Greiling, D. Farny, A. Flatley, R. Feederle, S. May, F. Schreiber, T. Arzberger, C. Kuhm, T. Klopstock, A. Hermann, C. Haass and D. Edbauer (2017). "Antibodies inhibit transmission and aggregation of C9orf72 poly-GA dipeptide repeat proteins." EMBO Mol Med **9**(5): 687-702.
- Zhou, Y., S. Liu, G. Liu, A. Ozturk and G. G. Hicks (2013). "ALS-associated FUS mutations result in compromised FUS alternative splicing and autoregulation." PLoS Genet **9**(10): e1003895.

Zinszner, H., J. Sok, D. Immanuel, Y. Yin and D. Ron (1997). "TLS (FUS) binds RNA in vivo and engages in nucleo-cytoplasmic shuttling." J Cell Sci **110** (Pt **15**): 1741-1750.

Zu, T., Y. Liu, M. Banez-Coronel, T. Reid, O. Pletnikova, J. Lewis, T. M. Miller, M. B. Harms, A. E. Falchook, S. H. Subramony, L. W. Ostrow, J. D. Rothstein, J. C. Troncoso and L. P. Ranum (2013). "RAN proteins and RNA foci from antisense transcripts in C9ORF72 ALS and frontotemporal dementia." Proc Natl Acad Sci U S A **110**(51): E4968-4977.

8 List of Figures

Figure 1.1 FUS domain structure.....	13
Figure 1.2 The <i>C9ORF72</i> gene and transcript variants.	14
Figure 1.3 Potential mechanism of neurodegeneration due to <i>C9ORF72</i> G4C2 repeat expansion.	16
Figure 1.4 Potential mechanisms of <i>FUS</i> -associated neuropathology.	18
Figure 1.5 Discovery of molecular mechanisms underlying ALS pathology using patient-specific iPSC-derived motor neurons.	24
Figure 1.6 CRISPR/Cas9-mediated gene editing.	26
Figure 1.7 D10A mutant nickase version of Cas9 (Cas9n).	26
Figure 2.1 Design of sgRNAs targeting <i>FUS</i>	38
Figure 2.2 Workflow chart of smNPC differentiation into spinal MNs.	54
Figure 2.3 Workflow chart of iPSC differentiation into cortical cells.	55
Figure 2.4 Overview of MFC culture system for axonal organelle trafficking analysis.	61
Figure 3.1 Derivation of patient-specific cortical neurons and astrocytes.	67
Figure 3.2 Derivation of patient-specific neurons from all cortical layers.	68
Figure 3.3 Generation of gene edited <i>FUS-EGFP</i> iPSC lines.	70
Figure 3.4 Screening and genotyping of <i>FUS-EGFP</i> positive clones.	72
Figure 3.5 Isogenic WT and P525L iPSCs are positive for markers of pluripotency.	73
Figure 3.6 Isogenic WT and P525L iPSCs can differentiate into cells of all three germ layer.	74
Figure 3.7 Analysis of <i>FUS-EGFP</i> cellular distribution in cortical neurons and astrocytes.	77
Figure 3.8 Production of Poly-GP in cortical cells is not affected by aging.	79
Figure 3.9 Detection of Poly-GP in cortical neurons.	81
Figure 3.10 Characterization of Poly-GP within cortical neurons.	82
Figure 3.11 Detection of Poly-GA in cortical neurons.	84
Figure 3.12 Characterization of Poly-GA within cortical neurons.	85
Figure 3.13 Detection of Poly-GR in cortical neurons.	86
Figure 3.14 Poly-GP versus 53BP1.	87
Figure 3.15 Poly-GA versus 53BP1.	88
Figure 3.16 Detection of TDP43 versus Poly-GA in cortical neurons.	89
Figure 3.17 Loss of TDP43 in <i>C9ORF72-HRE</i> cortical neurons.	90
Figure 3.18 Detection of DSB markers in spinal MNs with <i>C9ORF72-HRE</i> mutation.	92
Figure 3.19 Detection of DSB markers in cortical neurons with <i>C9ORF72-HRE</i> mutation.	93

Figure 3.20 Detection of DSBs in cortical astrocytes with <i>C9ORF72-HRE</i> mutation.	94
Figure 3.21 Characterization of DSB markers in untreated spinal MNs with <i>C9ORF72-HRE</i> mutation.	95
Figure 3.22 Characterization of DSB markers in untreated cortical neurons and astrocytes with <i>C9ORF72-HRE</i> mutation.	96
Figure 3.23 Comparison of DSB markers in untreated neural cell types with <i>C9ORF72-HRE</i> mutation.	97
Figure 3.24 Characterization of DSB markers in etoposide treated spinal MNs with <i>C9ORF72-HRE</i> mutation.	98
Figure 3.25 Characterization of DSB markers in etoposide treated cortical cultures with <i>C9ORF72-HRE</i> mutation.	99
Figure 3.26 Characterization of DSB marker γ H2AX and 53BP1 in spinal MNs with <i>FUS</i> mutation.	101
Figure 3.27 Characterization of DSB marker 53BP1 in untreated cortical cells with <i>FUS</i> mutation.	102
Figure 3.28 Characterization of DSB marker 53BP1 in etoposide treated cortical cells with <i>FUS</i> mutation.	103
Figure 3.29 Effect of etoposide on cell survival.	104
Figure 3.30 Recruitment of FUS-EGFP to laser-induced DNA damage sites in spinal MNs.	105
Figure 3.31 Recruitment of FUS-EGFP to laser-induced DNA damage sites in cortical neurons.	105
Figure 3.32 <i>FUS</i> mutant spinal MNs develop trafficking defects of mitochondria and lysosomes in distal axons.	106
Figure 3.33 Characterization of distal axonal outgrowth of cortical neurons in MFCs. ...	107
Figure 3.34 Live cell imaging analysis of mitochondrial and lysosomal motility.	108
Figure 3.35 Quantification of mitochondrial and lysosomal moving tracks.	109

9 List of Tables

Table 2.1 Instruments.....	28
Table 2.2 Chemicals and reagents	29
Table 2.3 Commercial available kits	30
Table 2.4 Enzymes for cell culture.....	30
Table 2.5 Restriction enzymes for cloning	30
Table 2.6 Primary antibodies	31
Table 2.7 Secondary antibodies	31
Table 2.8 Fluorescence reporters.....	32
Table 2.9 List of primer.....	32
Table 2.10 List of plasmids.....	32
Table 2.11 Cell culture media and supplements	33
Table 2.12 Growth factors and small molecules	33
Table 2.13 Consumables.....	33
Table 2.14 Software	35
Table 2.15 Cell lines.....	36
Table 2.16 Target specific sgRNA sequences for <i>FUS</i> gene editing.....	37
Table 2.17 Online tools for Off-target detection	38
Table 2.18 Materials for cloning.....	39
Table 2.19 Mixture for restriction digestion	39
Table 2.20 Mixture for annealing of oligos	39
Table 2.21 Mixture for ligation	40
Table 2.22 Mixture for degradation of unspecific recombination products.....	40
Table 2.23 Mixture for Colony PCR	44
Table 2.24 Program for Colony PCR	44
Table 2.25 Mixture for Screening PCR	44
Table 2.26 Program for Screening PCR	45
Table 2.27 Possible PCR products of <i>FUS</i> -EGFP Genotyping PCR.....	45
Table 2.28 Mixture for Genotyping PCR	45
Table 2.29 Program for Genotyping PCR	45
Table 2.30 Video properties for TrackMate analysis	60
Table 2.31 Settings for TrackMate Plugin.....	60
Table 2.32 DPR antibodies.....	62
Table 3.1 Codon specifications for gene editing of <i>FUS</i>	70
Table 3.2 Possible Off-targets of sgRNA Target 1 (GCGAGTATCTTATCTCAAGT).....	75
Table 3.3 Possible Off-targets of sgRNA Target 2 (GTTAGGTAGGAGGGGCAGAT)	75

Supplemental Table S 1: Box plot statistics of Figure 3.34 C - mitochondrial track displacement in μm	151
Supplemental Table S 2: Box plot statistics of Figure 3.34 D - mitochondrial mean speed in $\mu\text{m}/\text{sec}$	152
Supplemental Table S 3: Box plot statistics of Figure 3.34 F - lysosomal track displacement in μm	153
Supplemental Table S 4: Box plot statistics of Figure 3.34 G - lysosomal mean speed in $\mu\text{m}/\text{sec}$	154
Supplemental Table S 5: Descriptive statistics related to related to Figure 3.35 A - Percentages moving mitochondria.....	154
Supplemental Table S 6: Descriptive statistics related to related to Figure 3.35 B - Percentages moving lysosomes.....	155
Supplemental Table S 7: Descriptive statistics related to Figure 3.8 - Poly-GP ELISA. .	155
Supplemental Table S 8: Descriptive statistics related to Figure 3.10 A – Poly-GP granules relative to MAP2 area.	156
Supplemental Table S 9: Descriptive statistics related to Figure 3.10 B – Poly-GP area relative to MAP2 area.	156
Supplemental Table S 10: Descriptive statistics related to Figure 3.10 C – Poly-GP granule area in pixel^2	157
Supplemental Table S 11: Descriptive statistics related to Figure 3.10 D – Poly-GP granule radius in pixel.....	158
Supplemental Table S 12: Descriptive statistics related to Figure 3.12 A – Poly-GA granules relative to MAP2 area.	159
Supplemental Table S 13: Descriptive statistics related to Figure 3.12 B – Poly-GA area relative to MAP2 area.	159
Supplemental Table S 14: Descriptive statistics related to Figure 3.12 C – Poly-GA granule area in pixel^2	160
Supplemental Table S 15: Descriptive statistics related to Figure 3.12 D – Poly-GA granule radius in pixel.....	161

10 Acknowledgments

I want to express my gratitude to my supervisor Prof. Dr. Dr. Andreas Hermann for offering me the opportunity to undertake my doctoral thesis work in his lab. I like to thank him for his positivity, motivation, ideas, and discussions we had which considerably contributed to the project. I also would like to thank Prof. Dr. Marius Ader for his interest and assessment of this thesis.

The work was supported in part by the “Deutsche Gesellschaft für Muskelerkrankungen (He 2/2)”, the Roland Ernst Stiftung Saxony (03/14), the MeDDrive program of the Medical Faculty at the Technische Universität Dresden, BIOCREA GMBH, the Helmholtz Virtual Institute (VH-VI-510) “RNA dysmetabolism in ALS and FTD”, the Federal Ministry of Education and Research (BMBF FKZ: 01GM1303) under the frame of E-Rare-2, the ERA-Net for Research on Rare Diseases (EMINA2 consortium), the Project “Dementia in PARKINSON’S Disease: 3-Year Prospective-Longitudinal course and outcome of Parkinson’s disease” (Landscape-PD), and an unrestricted grant by the family of a deceased ALS patient.

I also want to thank Dr. J. Sternecker, Dr. P. Reinhardt, and Dr. R. M. Abo-Rady from CRTD (group for iPSCs and neurodegenerative disease) as well as Prof. Dr. S. Liebau from university Tübingen (institute for neuroanatomy and developmental biology) and Prof Dr. T. M. Böckers from university Ulm (institute for anatomy and cell biology) for providing the iPSC lines used here and Dr. Xenia Lowjeski for the generation of these. Especially, I thank Peter and Masin for their support by establishing the CRISPR/Cas9n method in our lab. Thanks also go to Prof. Dr. D. Edbauer and Dr. C. Schludi from DZNE Munich (group for cell biology of neurodegeneration) for the provision of DPR-specific antibodies and implementation of ELISA experiments.

Thanks go to the Light Microscopy Facility (a Core Facility of the CMCB Technology Platform at TU Dresden) for providing needed equipment and invaluable support whenever it was needed and to Dr. Arun Pal for the implementation of live cell imaging and his support by analyzing the resulting data.

Very special thanks go to the lab members of AG Hermann for all the special time we had together. I want to thank Katja, Sylvia, Andrea, Anett, and Conny for their experimental help, motivation, and sympathy. Special thanks go to Barbra, Yu, Annelie, Marie, Hannes, Sumi, and René for always being there, for your support, for cheering me up, listening to frustrations, and for the ideas and discussion we had.

Zum Schluss möchte ich noch meiner Familie und engen Freunden danken die immer an meiner Seite waren. Ein großes Dankeschön an meinen René für seine Geduld und der mich immer ermutigte vorwärtszugehen. Vor allem danke ich meiner Mutti, die mich bei jedem einzelnen Schritt unterstützte um meinen Weg zu gehen und meine Träume zu erfüllen.

11 Appendix

11.1 Supplementary Movies

Supplementary Movie S1

Refers to Figure 3.31 A, showing movie frame at 116 sec of FUS-EGFP recruited to Laser cut in untreated iPSCs and cortical neurons. Recruitment-withdrawal of nuclear FUS-EGFP to DNA Laser ablation cuts in hiPSC-derived mature neurons and iPSCs expressing WT or mutant P525L FUS-EGFP (isogenic control lines, Table 2.15). Confocal spinning disc fluorescence imaging at 100x magnification, NA 1.45 oil immersion, over 15 min upon Laser irradiation with 1 fps for frame 1-150 and 0.2 fps beyond, LUT Green Fire Blue.

Supplementary Movie S2-3 (general remarks)

All movies were recorded at 100x magnification, NA 1.45 oil immersion, at 3.3 fps per channel over 2 min (400 frames in total per channel) in epifluorescence mode if not stated otherwise below with illumination and filter settings as detailed in Material and Methods. Organelle motility revealed with LysoTracker Red DND-99 (LUT Yellow Hot), Mitotracker Deep Red FM (LUT Cyan Hot) or Mitotracker JC-1 (composite overlays of the red channel, LUT Red, and green channel, LUT green.) at standardized microchannel readout positions distal versus proximal in compartmentalized iPSC-derived MN cultures

Supplementary Movie S2

Refers to Figure 3.34 B showing maximum intensity projections of Mitotracker Deep Red FM. Moving mitochondria in distal and proximal axonal parts can be observed for controls (Ctrl 2 = AKC5, FUS-WT = KG WT) and FUS mutants (FUS-R521C = KG25C1, FUS-P525L = KG P525L).

Supplementary Movie S3

Refers to Figure 3.34 E showing maximum intensity projections of LysoTracker Red DND-99. Moving lysosomes in distal and proximal axonal parts can be observed for controls (Ctrl 2 = AKC5, FUS-WT = KG WT) and FUS mutants (FUS-R521C = KG25C1, FUS-P525L = KG P525L).

11.2 Supplementary Tables

Supplemental Table S 1: Box plot statistics of Figure 3.34 C - mitochondrial track displacement in μm .

	Distal		Proximal	
	Ctrl	FUSmt	Ctrl	FUSmt
	P=0.0001		P=0.0003	
Number of values	6194	7644	6411	9623
Minimum	1.20	1.20	1.20	1.20
25% Percentile	1.48	1.44	1.46	1.49
Median	1.95	1.86	1.94	2.01
75% Percentile	2.90	2.82	3.01	3.24
Maximum	47.09	37.57	51.75	55.60
Mean	2.51	2.58	2.77	2.93
Std. Deviation	1.84	2.27	2.65	2.91
Std. Error of Mean	0.02	0.03	0.03	0.03
Lower 95% CI of mean	2.46	2.53	2.70	2.87
Upper 95% CI of mean	2.55	2.63	2.83	2.99

Statistics were calculated by Kolmogorov-Smirnov test (n=3-7 technical replicates from 2-4 independent differentiations).

Supplemental Table S 2: Box plot statistics of Figure 3.34 D - mitochondrial mean speed in $\mu\text{m}/\text{sec}$.

	Distal		Proximal	
	Ctrl	FUSmt	Ctrl	FUSmt
	P<0.0001		P<0.0001	
Number of values	6194	7644	6411	9623
Minimum	0.08	0.06	0.02	0.05
25% Percentile	0.65	0.45	0.52	0.44
Median	0.95	0.77	0.86	0.76
75% Percentile	1.23	1.10	1.16	1.11
Maximum	7.75	6.41	6.46	5.66
Mean	0.96	0.81	0.90	0.82
Std. Deviation	0.46	0.44	0.51	0.48
Std. Error of Mean	0.01	0.01	0.01	0.00
Lower 95% CI of mean	0.95	0.80	0.88	0.81
Upper 95% CI of mean	0.97	0.82	0.91	0.83

Statistics were calculated by Kolmogorov-Smirnov test (n=3-7 technical replicates from 2-4 independent differentiations).

Supplemental Table S 3: Box plot statistics of Figure 3.34 F - lysosomal track displacement in μm .

	Distal		Proximal	
	Ctrl	FUSmt	Ctrl	FUSmt
	P<0.0001		P<0.0001	
Number of values	2657	5047	4907	6913
Minimum	1.20	1.20	1.20	1.20
25% Percentile	1.54	1.69	1.70	1.77
Median	2.14	2.77	2.60	2.89
75% Percentile	3.59	5.49	4.57	5.99
Maximum	64.66	79.53	66.21	109.40
Mean	3.45	4.93	4.19	5.53
Std. Deviation	3.95	6.29	4.95	7.35
Std. Error of Mean	0.08	0.09	0.07	0.09
Lower 95% CI of mean	3.30	4.76	4.05	5.36
Upper 95% CI of mean	3.60	5.11	4.33	5.70

Statistics were calculated by Kolmogorov-Smirnov test (n=3-7 technical replicates from 2-4 independent differentiations).

Supplemental Table S 4: Box plot statistics of Figure 3.34 G - lysosomal mean speed in $\mu\text{m}/\text{sec}$.

	Distal		Proximal	
	Ctrl	FUSmt	Ctrl	FUSmt
	P<0.0001		P<0.0001	
Number of values	2657	5047	4907	6913
Minimum	0.06	0.08	0.08	0.05
25% Percentile	0.44	0.40	0.71	0.55
Median	0.78	0.71	1.08	0.92
75% Percentile	1.15	1.10	1.41	1.29
Maximum	7.70	6.22	5.94	9.35
Mean	0.84	0.81	1.10	0.98
Std. Deviation	0.50	0.52	0.56	0.58
Std. Error of Mean	0.01	0.01	0.01	0.01
Lower 95% CI of mean	0.82	0.79	1.08	0.97
Upper 95% CI of mean	0.85	0.82	1.12	0.99

Statistics were calculated by Kolmogorov-Smirnov test (n=3-7 technical replicates from 2-4 independent differentiations).

Supplemental Table S 5: Descriptive statistics related to related to Figure 3.35 A - Percentages moving mitochondria.

	Distal				Proximal			
	Ctrl 2	FUS-WT	FUS-R521C	FUS-P525L	Ctrl 2	FUS-WT	FUS-R521C	FUS-P525L
One way ANOVA	F (3, 18) = 0.61		P=0.616		F (3, 18) = 0.62		P=0.613	
Number of values	3	6	7	6	3	6	7	6
Mean	18.42	15.31	12.70	14.29	15.48	18.15	14.90	17.79
Std. Deviation	6.46	8.38	2.33	7.00	3.69	5.13	3.46	6.72
Std. Error of Mean	3.73	3.42	0.88	2.86	2.13	2.10	1.31	2.74
Lower 95% CI	2.36	6.51	10.54	6.95	6.31	12.77	11.69	10.74
Upper 95% CI	34.47	24.10	14.85	21.63	24.64	23.54	18.10	24.83

The effect of the cell line on organelle motility was calculated by One-way ANOVA with Tukey's post-hoc test (n=3-7 technical replicates from ≥ 2 independent differentiations).

Supplemental Table S 6: Descriptive statistics related to related to Figure 3.35 B - Percentages moving lysosomes.

	Distal				Proximal			
	Ctrl 2	FUS- WT	FUS- R521C	FUS- P525L	Ctrl 2	FUS- WT	FUS- R521C	FUS- P525L
One way ANOVA	F (3, 18) = 0.81 P=0.506				F (3, 18) = 1.89 P=0.168			
Number of values	3	6	7	6	3	6	7	6
Mean	15.72	19.91	24.51	23.67	36.66	22.76	30.43	29.08
Std. Deviation	6.30	3.73	10.19	12.22	6.88	8.25	9.83	8.17
Std. Error of Mean	3.64	1.52	3.85	4.99	3.97	3.37	3.71	3.33
Lower 95% CI	0.07	15.99	15.08	10.85	19.58	14.10	21.35	20.51
Upper 95% CI	31.38	23.82	33.93	36.49	53.74	31.42	39.52	37.65

The effect of the cell line on organelle motility was calculated by One-way ANOVA with Tukey's post-hoc test (n=3-7 technical replicates from ≥ 2 independent differentiations).

Supplemental Table S 7: Descriptive statistics related to Figure 3.8 - Poly-GP ELISA.

	D80			D120		
	Mean	SD	n	Mean	SD	n
Ctrl 1	104.00	0.00	1	121.00	36.77	2
Ctrl 2	43.50	0.00	1	27.50	0.00	1
Ctrl 4	198.00	11.31	2	83.75	11.67	2
C9-WT	159.00	0.00	1	255.50	0.00	1
C9-HRE 1	249.17	50.04	3	301.17	110.50	3
C9-HRE 2	1121.50	625.79	2	7638.33	8817.01	3
C9-HRE 3	393.00	72.19	3	359.50	79.41	3

Supplemental Table S 8: Descriptive statistics related to Figure 3.10 A – Poly-GP granules relative to MAP2 area.

	Ctrl 1	C9-HRE 1	C9-WT	C9-HRE 2
One-way ANOVA	F (3, 10) = 0.456		P=0.7178	
Number of values	4	4	3	3
Minimum	0.0006	0.0007	0.0007	0.0008
25% Percentile	0.0006	0.0007	0.0007	0.0008
Median	0.0008	0.0008	0.0008	0.0008
75% Percentile	0.0008	0.0009	0.0008	0.0008
Maximum	0.0008	0.0009	0.0008	0.0008
Mean	0.00075	0.00082	0.00077	0.00080
Std. Deviation	0.00012	0.00010	0.00008	0.00002
Std. Error of Mean	0.0001	0.0000	0.0000	0.0000
Lower 95% CI	0.0006	0.0007	0.0006	0.0007
Upper 95% CI	0.0010	0.0010	0.0010	0.0009

Statistics were calculated by One-way ANOVA with Tukey's post-hoc test (n=3-4).

Supplemental Table S 9: Descriptive statistics related to Figure 3.10 B – Poly-GP area relative to MAP2 area.

	Ctrl 1	C9-HRE 1	C9-WT	C9-HRE 2
One-way ANOVA	F (3, 10) = 7.93		P=0.005	
Post-hoc		*		* +
Number of values	4	4	3	3
Minimum	0.0082	0.0103	0.0094	0.0111
25% Percentile	0.0084	0.0105	0.0094	0.0111
Median	0.0095	0.0109	0.0095	0.0113
75% Percentile	0.0102	0.0116	0.0097	0.0116
Maximum	0.0103	0.0119	0.0097	0.0116
Mean	0.0094	0.0110	0.0095	0.0114
Std. Deviation	0.0010	0.0006	0.0001	0.0003
Std. Error of Mean	0.0005	0.0003	0.0001	0.0002
Lower 95% CI	0.0078	0.0100	0.0092	0.0107
Upper 95% CI	0.0110	0.0120	0.0099	0.0120

Statistics were calculated by One-way ANOVA with Tukey's post-hoc test (n=3-4).

Asterix (*) indicates statistical significances when compared to Ctrl 1.

Plus sign (+) indicates statistical significances when compared to C9-WT.

Supplemental Table S 10: Descriptive statistics related to Figure 3.10 C – Poly-GP granule area in pixel².

	Ctrl 1	C9-HRE 1	C9-WT	C9-HRE 2
Kruskal-Wallis test	P<0.0001			
Post-hoc		**		***
		+++		++++
Number of values	2223	2480	1678	2113
Minimum	4.00	4.00	4.00	4.00
25% Percentile	5.00	6.00	5.00	6.00
Median	8.00	9.00	8.00	9.00
75% Percentile	15.00	16.00	14.00	17.00
Maximum	189.00	218.00	176.00	203.00
Mean	12.70	13.80	12.30	14.10
Std. Deviation	13.10	14.40	12.80	14.80
Std. Error of Mean	0.28	0.29	0.31	0.32
Lower 95% CI	12.10	13.20	11.70	13.50
Upper 95% CI	13.20	14.30	12.90	14.70

Statistics were calculated by Kurskal-Wallis test with Dunn's post-hoc test (n=3-4).

Asterix (*) indicates statistical significances when compared to Ctrl 1.

Plus sign (+) indicates statistical significances when compared to C9-WT.

Supplemental Table S 11: Descriptive statistics related to Figure 3.10 D – Poly-GP granule radius in pixel.

	T12-9	KDC28	MHC30-GC	33-1
Kruskal-Wallis test	P<0.0001			
Post-hoc		***		****
		++++		++++
Number of values	2223	2480	1678	2113
Minimum	1.00	1.00	1.00	1.00
25% Percentile	1.00	1.00	1.00	1.00
Median	1.06	1.08	1.06	1.08
75% Percentile	1.17	1.20	1.17	1.21
Maximum	2.54	2.23	1.99	2.39
Mean	1.12	1.14	1.12	1.14
Std. Deviation	0.17	0.17	0.15	0.17
Std. Error of Mean	0.00	0.00	0.00	0.00
Lower 95% CI	1.12	1.13	1.11	1.13
Upper 95% CI	1.13	1.14	1.12	1.15

Statistics were calculated by Kurskal-Wallis test with Dunn's post-hoc test (n=3-4).

Asterix (*) indicates statistical significances when compared to Ctrl 1.

Plus sign (+) indicates statistical significances when compared to C9-WT.

Supplemental Table S 12: Descriptive statistics related to Figure 3.12 A – Poly-GA granules relative to MAP2 area.

	Ctrl 1	Ctrl 2	C9-HRE 1	C9-WT	C9-HRE 2
One-way ANOVA	F (4, 14) = 2.14		P=0.130		
Number of values	4	3	6	3	3
Minimum	0.00067	0.00025	0.00046	0.00010	0.00049
25% Percentile	0.00068	0.00025	0.00053	0.00010	0.00049
Median	0.00071	0.00047	0.00072	0.00042	0.00069
75% Percentile	0.00071	0.00052	0.00087	0.00076	0.00073
Maximum	0.00071	0.00052	0.00109	0.00076	0.00073
Mean	0.00070	0.00041	0.00072	0.00043	0.00064
Std. Deviation	0.00002	0.00014	0.00022	0.00033	0.00013
Std. Error of Mean	0.00001	0.00008	0.00009	0.00019	0.00007
Lower 95% CI	0.00066	0.00006	0.00049	-0.00039	0.00032
Upper 95% CI	0.00074	0.00077	0.00096	0.00124	0.00096

Statistics were calculated by One-way ANOVA with Tukey's post-hoc test (n=3-6).

Supplemental Table S 13: Descriptive statistics related to Figure 3.12 B – Poly-GA area relative to MAP2 area.

	Ctrl 1	Ctrl 2	C9-HRE 1	C9-WT	C9-HRE 2
One-way ANOVA	F (4, 14) = 2.49		P=0.091		
Number of values	4	3	6	3	3
Minimum	0.0062	0.0023	0.0041	0.0009	0.0058
25% Percentile	0.0063	0.0023	0.0052	0.0009	0.0058
Median	0.0067	0.0039	0.0071	0.0044	0.0069
75% Percentile	0.0070	0.0046	0.0083	0.0077	0.0075
Maximum	0.0071	0.0046	0.0096	0.0077	0.0075
Mean	0.0067	0.0036	0.0069	0.0044	0.0067
Std. Deviation	0.0004	0.0012	0.0019	0.0034	0.0009
Std. Error of Mean	0.0002	0.0007	0.0008	0.0020	0.0005
Lower 95% CI	0.0060	0.0007	0.0048	-0.0041	0.0046
Upper 95% CI	0.0073	0.0065	0.0089	0.0128	0.0089

Statistics were calculated by One-way ANOVA with Tukey's post-hoc test (n=3-6).

Supplemental Table S 14: Descriptive statistics related to Figure 3.12 C – Poly-GA granule area in pixel².

	Ctrl 1	Ctrl 2	C9-HRE 1	C9-WT	C9-HRE 2
Kruskal-Wallis test	P<0.0001				
Post-hoc					***
	#		#	###	#### ****
Number of values	2091	1246	3582	1207	1699
Minimum	4.00	4.00	4.00	4.00	4.00
25% Percentile	5.00	5.00	5.00	5.00	5.00
Median	7.00	7.00	7.00	8.00	8.00
75% Percentile	12.00	10.00	12.00	12.00	13.00
Maximum	115.00	57.00	90.00	71.00	70.00
Mean	9.62	8.62	9.41	10.30	10.50
Std. Deviation	7.19	5.55	6.79	7.95	7.75
Std. Error of Mean	0.16	0.16	0.11	0.23	0.19
Lower 95% CI	9.31	8.31	9.19	9.81	10.20
Upper 95% CI	9.93	8.93	9.63	10.70	10.90
Mean ranks	4881	4557	4841	5056	5263

Statistics were calculated by Kruskal-Wallis test with Dunn's post-hoc test (n=3-6).

Asterix (*) indicates statistical significances when compared to Ctrl 1.

Double cross (#) indicates statistical significances when compared to Ctrl 2.

Asterix (*) indicates statistical significances when compared to C9-HRE 1.

Supplemental Table S 15: Descriptive statistics related to Figure 3.12 D – Poly-GA granule radius in pixel.

	Ctrl 1	Ctrl 2	C9-HRE 1	C9-WT	C9-HRE 2
Kruskal-Wallis test	P<0.0001				
Post-hoc					**
					####
					++

Number of values	2091	1246	3582	1207	1699
Minimum	1.00	1.00	1.00	1.00	1.00
25% Percentile	1.00	1.00	1.00	1.00	1.00
Median	1.06	1.06	1.06	1.05	1.06
75% Percentile	1.14	1.11	1.13	1.14	1.15
Maximum	1.81	1.79	1.91	1.83	1.89
Mean	1.09	1.07	1.08	1.09	1.10
Std. Deviation	0.11	0.09	0.10	0.12	0.12
Std. Error of Mean	0.00	0.00	0.00	0.00	0.00
Lower 95% CI	1.08	1.07	1.08	1.08	1.09
Upper 95% CI	1.09	1.08	1.09	1.09	1.11
Mean ranks	4903	4715	4857	4867	5222

Statistics were calculated by Kurskal-Wallis test with Dunn's post-hoc test (n=3-6).

Asterix (*) indicates statistical significances when compared to Ctrl 1.

Double cross (#) indicates statistical significances when compared to Ctrl 2.

Plus sign (+) indicates statistical significances when compared to C9-WT.

Asterix (*) indicates statistical significances when compared to C9-HRE 1.

11.3 Declarations

11.3.1 Erklärungen zur Eröffnung des Promotionsverfahrens

Technische Universität Dresden
Medizinische Fakultät Carl Gustav Carus
Promotionsordnung vom 24. Juli 2011

1. Hiermit versichere ich, dass ich die vorliegende Arbeit ohne unzulässige Hilfe Dritter und ohne Benutzung anderer als der angegebenen Hilfsmittel angefertigt habe; die aus fremden Quellen direkt oder indirekt übernommenen Gedanken sind als solche kenntlich gemacht.
2. Bei der Auswahl und Auswertung des Materials sowie bei der Herstellung des Manuskripts habe ich Unterstützungsleistungen von folgenden Personen erhalten:
Prof. Dr. Dr. Andreas Hermann
Dr. Arun Pal
Yu Niu
Barbara Szewczyk
Anne Seifert
3. Weitere Personen waren an der geistigen Herstellung der vorliegenden Arbeit nicht beteiligt. Insbesondere habe ich nicht die Hilfe eines kommerziellen Promotionsberaters in Anspruch genommen. Dritte haben von mir weder unmittelbar noch mittelbar geldwerte Leistungen für Arbeiten erhalten, die im Zusammenhang mit dem Inhalt der vorgelegten Dissertation stehen.
4. Die Arbeit wurde bisher weder im Inland noch im Ausland in gleicher oder ähnlicher Form einer anderen Prüfungsbehörde vorgelegt.
5. Die Inhalte dieser Dissertation wurden in folgender Form veröffentlicht:
Nicht zutreffend.
6. Ich bestätige, dass es keine zurückliegenden erfolglosen Promotionsverfahren gab.
7. Ich bestätige, dass ich die Promotionsordnung der Medizinischen Fakultät der Technischen Universität Dresden anerkenne.
8. Ich habe die Zitierrichtlinien für Dissertationen an der Medizinischen Fakultät der Technischen Universität Dresden zur Kenntnis genommen und befolgt.

Ort, Datum

Unterschrift des Doktoranden

11.3.2 Erklärung über Einhaltung gesetzlicher Vorgaben

Hiermit bestätige ich die Einhaltung der folgenden aktuellen gesetzlichen Vorgaben im Rahmen meiner Dissertation:

- das zustimmende Votum der Ethikkommission bei Klinischen Studien, epidemiologischen Untersuchungen mit Personenbezug oder Sachverhalten, die das Medizinproduktegesetz betreffen Aktenzeichen der zuständigen Ethikkommission EK 45022009

- die Einhaltung der Bestimmungen des Tierschutzgesetzes Aktenzeichen der Genehmigungsbehörde zum Vorhaben/zur Mitwirkung
Entfällt

- die Einhaltung des Gentechnikgesetzes
Projektnummer Az. 55-8811.71/170; Projekt 7 + 17

- die Einhaltung von Datenschutzbestimmungen der Medizinischen Fakultät und des Universitätsklinikums Carl Gustav Carus.

Ort, Datum

Unterschrift des Doktoranden